

UC San Diego

UC San Diego Electronic Theses and Dissertations

Title

Colloidal Lanthanide Nanoparticles: Doping, Epitaxy, and Photon Management

Permalink

<https://escholarship.org/uc/item/399100sr>

Author

He, Sha

Publication Date

2017

Peer reviewed|Thesis/dissertation

UNIVERSITY OF CALIFORNIA, SAN DIEGO

Colloidal Lanthanide Nanoparticles: Doping, Epitaxy, and Photon Management

A dissertation submitted in partial satisfaction of the
requirements for the degree Doctor of Philosophy

in

NanoEngineering

by

Sha He

Committee in charge:

Professor Adah Almutairi, Chair
Professor Guy Bertrand
Professor Darren J. Lipomi
Professor Ying Shirley Meng
Professor Liangfang Zhang

2017

Copyright

Sha He, 2017

All rights reserved

The Dissertation of Sha He is approved, and it is acceptable in quality and form for publication on microfilm and electronically:

Chair

University of California, San Diego

2017

DEDICATION

I dedicate this doctoral dissertation to my mother, Fang, who firmly believes education can change my life and made it happen.

TABLE OF CONTENTS

Signature Page.....	iii
Dedication.....	iv
Table of Contents.....	v
List of Abbreviations.....	vii
List of Figures.....	x
List of Schemes.....	xix
List of Tables.....	xx
Acknowledgements.....	xx
Vita.....	xxiv
Abstract of the Dissertation.....	xxvi
Chapter 0 Introduction.....	1
0.1 What are Lanthanides.....	1
0.2 Basic Physical and Chemical Properties of Lanthanides.....	3
0.3 Applications of Lanthanides in Industry.....	13
0.3.1 Lighting.....	14
0.3.2 Lasers.....	16
0.3.3 Telecommunications.....	17
0.4 Colloidal Nanoparticles: General.....	18
0.5 Lanthanide Colloidal Nanoparticles.....	20
0.5.1 Why Colloidal Lanthanide Nanoparticles.....	20
0.5.2 Basics of Colloidal Lanthanide Nanoparticles.....	21
0.5.3 Synthesis of Colloidal Lanthanide Nanoparticles.....	22
0.5.4 Characterization of Colloidal Lanthanide Nanoparticles.....	27
0.5.5 Applications of Colloidal Lanthanide Nanoparticles.....	31
0.6 Major Challenges in the Field.....	36
0.7 Scope of This Thesis.....	37
0.8 References.....	40
Chapter 1 Direct Evidence for Coupled Surface and Concentration Quenching Dynamics in Lanthanide-Doped Nanocrystals.....	52
1.1 Abstract.....	52
1.2 Introduction.....	52
1.3 Results and Discussion.....	55
1.4 Conclusion.....	73
1.5 Materials and Methods.....	74
1.6 References.....	79

Chapter 2 On the Critical Role of Optically Inert Epitaxial Shell in Enhancing Upconversion Luminescence of Core-Shell Nanoparticles.....	82
2.1 Abstract.....	82
2.2 Introduction.....	83
2.3 Results and Discussion.....	85
2.4 Conclusions.....	101
2.5 Materials and Methods.....	101
2.6 References.....	105
Chapter 3 Leveraging Spectral Matching between Photosensitizers and Upconversion Nanoparticles for 808 nm-Activated Photodynamic Therapy.....	110
3.1 Abstract.....	110
3.2 Introduction.....	111
3.3 Results and Discussion.....	117
3.4 Conclusions.....	136
3.5 Materials and Methods.....	137
3.6 References.....	148
Chapter 4 Simultaneous Enhancement of Photoluminescence, MRI Relaxivity, and CT Contrast by Tuning the Interfacial Layer of Lanthanide Heteroepitaxial Nanoparticles.....	154
4.1 Abstract.....	154
4.2 Introduction.....	155
4.3 Results and Discussion.....	158
4.4 Conclusions.....	188
4.5 Materials and Methods.....	189
4.6 References.....	199
Chapter 5 Compact Micellization: A Strategy for Ultrahigh T1 Magnetic Resonance Contrast with Gadolinium-Based Nanocrystals.....	205
5.1 Abstract.....	205
5.2 Introduction.....	206
5.3 Results and Discussion.....	208
5.4 Conclusions.....	230
5.5 Materials and Methods.....	231
5.6 References.....	238

LIST OF ABBREVIATIONS

ASM	American Society of Metals
CAs	Contrast Agents
3D	Three-Dimensional
Ce6	Chlorin e6
CS	Core-Shell
CSS	Core-Shell-Shell
CT	Computed Tomography
CW	Continuous Wave
DCFH-DA	2', 7'-Dichlorofluorescein Diacetate
DI	De-Ionized
DLS	Dynamic Light Scattering
DMEM	Dulbecco's Modified Eagle's medium
DMSO	Dimethyl sulfoxide
DPBF	1,3-Diphenylisobenzofuran
DMPE-PEG	1,2-dimyristoyl-sn-glycero-3-phosphoethanolamine-N-[methoxy(polyethylene glycol)-2000] (ammonium salt)
DSPE-PEG	1,2-distearoyl-sn-glycero-3-phosphoethanolamine-N-[methoxy(polyethylene glycol)-2000] (ammonium salt)
EDFA	Erbium-Doped Fiber Amplifiers
EDS	Energy-dispersive X-ray spectroscopy
EtOH	Ethanol
FBS	Fetal Bovine Serum

Gd-DOTA	Gd(III)-1,4,7,10-tetraazacyclododecane-1,4,7,10-tetraacetic acid
HD	Hydrodynamic
HR-TEM	High-Resolution Transmission Electron Microscopy
HU	Hounsfield Unit
ICP-AES	Inductively Coupled Plasma Atomic Emission Spectroscopy
IS	Inner Sphere
JCPDS	Joint Committee on Powder Diffraction Standards
LED	Light-Emitting Diode
Ln	Lanthanide
LSPR	Localized Surface Plasmon Resonance
MB	Methylene Blue
MCS	Multichannel Scaling
MRI	Magnetic Resonance Imaging
NCs	Nanocrystals
NIR	Near-Infrared
NPs	Nanoparticles
PDT	Photodynamic Therapy
PEG	Polyethylene Glycol
PES	Polyethersulfone
OS	Outer Sphere
PL	Photoluminescence
QY	Quantum Yield
RE	Rare Earth

ROI	Region of Interest
SC	Sodium Cacodylate
SEM	Scanning Electron Microscopy
SHG	Second Harmonic Generation
SS	Secondary Sphere
S/V	Surface-to-Volume
TEM	Transmission Electron Microscopy
TPA	Two-Photon Absorption
UC	Upconversion
UCNPs	Upconversion Nanoparticles
UV	Ultraviolet
XRD	X-Ray Diffraction
YAG	Yttrium Aluminate Garnet
ZnPc	Zinc Phthalocyanine

LIST OF FIGURES

Figure 0.1.	The seventeen elements in the periodic table.....	2
Figure 0.2.	Memorial plaque of the American Society for Metals (ASM) international society at the entrance of Ytterby mine.....	2
Figure 0.3.	The 4f ⁿ electronic configuration splits into many energy sublevels.....	4
Figure 0.4.	First Principle calculation of the possible 4f energy levels in lanthanide ions.....	5
Figure 0.5.	Lower part of the energy levels that are relevant to most of the studies.....	6
Figure 0.6.	Wavelength of the main emissive transitions of the trivalent lanthanides in the UV to NIR range.....	7
Figure 0.7.	Electron filling in different orbitals.....	7
Figure 0.8.	Simplified scheme showing the breaking/splitting of degeneracies of electron orbital states in 5d and 4f orbitals of lanthanides.....	8
Figure 0.9.	Comparison of lanthanides and d-block transition metals.....	9
Figure 0.10.	Configurational coordinate diagram for emission.....	10
Figure 0.11.	Schematic illustrations of second harmonic generation, two-photon absorption, and upconversion.....	11
Figure 0.12.	Triplet states are quenched by lanthanide trivalent ions when they are brought to close proximity.....	12
Figure 0.13.	The impact of lanthanides on solid-state lighting, particularly improving lighting efficiency.....	15
Figure 0.14.	The historical development of three generations of solid state white-light emitting devices since 1970.....	16
Figure 0.15.	Simplified workflow for erbium-doped fiber amplifiers.....	18
Figure 0.16.	Bandgap structure of semiconductor nanoparticles and localized surface plasmon resonance of noble metal nanoparticles.....	19
Figure 0.17.	Schematic illustration of the free energy for the controlled synthesis of NaLnF ₄ nanocrystals.....	23

Figure 0.18.	TEM images of NaYF ₄ :Yb, Er nanospheres.....	24
Figure 0.19.	Schematic presentation of cubic- and hexagonal-phase NaLnF ₄ structures, and doping-induced phase transformation.....	25
Figure 0.20.	TEM of NaYF ₄ :Yb ³⁺ /Er ³⁺ NPs and ripening-induced formation of core-shell NPs.....	26
Figure 0.21.	The effect of epitaxial shell in enhancing the luminescence of lanthanide-doped nanoparticles with different sizes.....	28
Figure 0.22.	Luminescence intensity of single UCNPs under different laser excitation power density.....	29
Figure 0.23.	Schematic illustrations of the simplified energy levels in the active-core/active-shell approach.....	30
Figure 0.24.	Comparison of water absorption at 980 nm and 808 nm. TEM image and the simplified energy level diagrams of the Nd ³⁺ -doped nanoparticles.....	31
Figure 0.25.	Schematic illustration of the lanthanide-doped NPs and their energy levels emphasizing the emission > 1000 nm, falling into the biological imaging window.....	32
Figure 0.26.	TEM images of the mesoporous silica-coated lanthanide-doped NPs and their use for PDT.....	34
Figure 0.27.	Schematic illustration of the improved bifacial solar cells with the upconverting contributions from the Er ³⁺ -doped lanthanides.....	35
Figure 1.1.	TEM images and size distribution of representative core NCs with different doping level.....	55
Figure 1.2.	TEM images and size distribution of representative core-shell NCs with different doping level.....	56
Figure 1.3.	Schematic illustration of the core-shell NCs structural composition and their energy level diagrams of Er ³⁺	57
Figure 1.4.	SEM image of NaErF ₄ /NaLuF ₄ core-shell NCs demonstrating high size uniformity.....	58
Figure 1.5.	Representative XRD pattern of the NaYF ₄ :25% Er ³⁺ /NaLuF ₄ core/shell NCs confirming the hexagonal phase.....	59
Figure 1.6.	Upconversion emission spectra and decay lifetime of the core NCs with variable Er ³⁺ dopant concentrations.....	60

Figure 1.7.	Upconversion emission spectra and decay lifetime of the core-shell NCs with variable Er^{3+} dopant concentrations.....	61
Figure 1.8.	Luminescence decay of the $^4\text{S}_{3/2}$ level at 540 nm of the core-shell nanocrystals with variable erbium dopant concentration in the core and their corresponding lifetime values.....	62
Figure 1.9.	Upconversion spectra of the core-shell nanocrystals with variable Er^{3+} dopant concentrations in the core ($\text{NaYF}_4\text{:X mol\% Er}^{3+}$, X: 5, 25, 50, and 100 mol%) excited at 800 nm.....	63
Figure 1.10.	Energy level diagram of Er^{3+} showing the excitation (808 nm) and the downshifted emission (1550 nm) levels.....	65
Figure 1.11.	Energy level diagram of Er^{3+} showing the excitation (658 nm) and the downshifted emission (1550 nm) levels.....	66
Figure 1.12.	TEM images of core (NaErF_4) and $\text{NaErF}_4/\text{NaLuF}_4$ core-shell nanocrystals with increasing shell thickness.....	67
Figure 1.13.	Upconversion emission spectra of NaErF_4 core (d: 0 nm), and $\text{NaErF}_4\text{-NaLuF}_4$ core-shell nanocrystals with increasing shell thickness.....	69
Figure 1.14.	Digital photographs of the $\text{NaErF}_4\text{-NaLuF}_4$ core-shell reaction mixture at various stages of the reaction and the observed red upconversion emission using a handheld 980 nm laser.....	70
Figure 1.15.	TEM images of core-shell nanocrystals with dopants in shell.....	71
Figure 1.16.	Energy levels and emission spectra of core-shell nanocrystals with dopants in the shell.....	72
Figure 2.1.	TEM images of the $\text{NaYF}_4\text{:Gd/Yb/Er}$ core UCNPs with different shell doping levels.....	87
Figure 2.2.	Ionic concentration of the dopants in the core and shells of the core-shell UCNPs shown in Figure 2.1.....	88
Figure 2.3.	Internal UCQY and luminescence decay lifetime of 540 nm, 654 nm, and 980 nm levels of the core-shell UCNPs with 980 nm excitation.....	90
Figure 2.4.	Internal UCQY enhancement by normalizing the QY of core@ NaYbF_4 to 100% and the corresponding red-to-green ratio of all five core-shell UCNPs.....	92

Figure 2.5.	Schematics and luminescence decay lifetime of downshifting luminescence at 1530 nm with 1500 nm excitation.....	94
Figure 2.6.	Schematics and luminescence decay lifetime of downshifting luminescence at 1530 nm with 980 nm excitation.....	96
Figure 2.7.	Schematic illustration of the core/inert shell, core/active shell, and core/active shell/inert shell UCNP.....	97
Figure 2.8.	TEM images of the core@NaGdF ₄ , core@NaGdF ₄ :Yb(50%), and core@NaGdF ₄ :Lu(50%) core-shell UCNP.....	100
Figure 3.1.	Energy level diagram of the conventional Nd ³⁺ -doped NPs absorbing 808 nm and emitting 540 nm.....	112
Figure 3.2.	Energy level diagram of the β-NaErF ₄ @NaLuF ₄ CS-NPs absorbing 808 nm and emitting 654 nm in this study.....	115
Figure 3.3.	Characterization β-NaErF ₄ @NaLuF ₄ CS-NPs including TEM, XRD, and spectra.....	117
Figure 3.4.	EDX spectra of NaErF ₄ core and NaErF ₄ @NaLuF ₄ CS-NPs showing only Er in the core and both Er and Lu in the CS-NPs.....	118
Figure 3.5.	TEM images, size distribution, and XRD pattern of NaErF ₄ core NPs.....	119
Figure 3.6.	Low-magnification TEM images of (a) NaErF ₄ core and (b) NaErF ₄ @NaLuF ₄ CS-NPs showing their excellent uniformity and monodispersity.....	120
Figure 3.7.	Low-magnification SEM image of NaErF ₄ @NaLuF ₄ CS-NPs.....	121
Figure 3.8.	The log-to-log plot of red upconversion emission peak intensity (integrated through 600 – 700 nm) to the 808 nm laser excitation power.....	122
Figure 3.9.	TEM image of β-NaYF ₄ :Yb(18%)/Er(2%)/@NaLuF ₄ :Nd(10%) NPs.....	122
Figure 3.10.	Spectral matching between the UCNP and the photosensitizers ZnPc.....	124
Figure 3.11.	The red-to-green ratio <i>versus</i> the 808 nm laser excitation at different pump power density.....	125

Figure 3.12.	Phase transfer of NaErF ₄ @NaLuF ₄ CS-NPs into water with ZnPc and DSPE-PEG 2000 surface coating.....	125
Figure 3.13.	Determination of singlet oxygen generation of ZnPc@PEG in the dark.....	127
Figure 3.14.	<i>in vitro</i> PDT on HeLa cells.....	128
Figure 3.15.	TEM of HeLa cells with the intracellular uptake of the CS-NP@ZnPc@PEG.....	129
Figure 3.16.	Confocal microscopy images of HeLa cells with the intracellular uptake of the CS-NP@ZnPc@PEG.....	130
Figure 3.17.	Toxicity of CS-NP@ZnPc@PEG to HeLa cells in the dark with different NP concentration and different incubation time.....	130
Figure 3.18.	<i>in vitro</i> cell viability of RAW264.7 cells incubated with CS-NP@ZnPc@PEG at different concentrations for 24 h.....	131
Figure 3.19.	Cell viability under 808 nm laser irradiation with different power density to determine the safe threshold for laser working in the PDT experiments.....	132
Figure 3.20.	Confocal microscopy images of HeLa cells showing intracellular visualization of singlet oxygen in split and merged imaging channels.....	133
Figure 3.21	PDT on cancer cell spheroids.....	135
Figure 4.1	TEM image and size distribution of the α -NaLuF ₄ NPs.....	160
Figure 4.2	TEM image and size distribution of the α -NaGdF ₄ NPs.....	160
Figure 4.3	Schematic illustration for the synthesis procedure for β -NaYb/ErF ₄ @NaLuF ₄ @NaGdF ₄ CSS NPs.....	161
Figure 4.4	TEM images and XRD patterns of the synthesized β -NaYb/ErF ₄ core, β -NaYb/ErF ₄ @NaLuF ₄ CS and β -NaYb/ErF ₄ @NaLuF ₄ @NaGdF ₄ CSS NPs.....	162
Figure 4.5	Low magnification TEM images of the core, CS and CSS NPs.....	163
Figure 4.6	Low magnification SEM image of the β -NaYb/ErF ₄ @NaLuF ₄ @NaGdF ₄ CSS NPs showing their excellent uniformity and monodispersity.....	164

Figure 4.7	EDS of (a) β -NaYb/ErF ₄ core, (b) β -NaYb/ErF ₄ @NaLuF ₄ CS, and (c) β -NaYb/ErF ₄ @NaLuF ₄ @NaGdF ₄ CSS NPs.....	166
Figure 4.8	Morphological characterization of the (a) core, (b) CS, and (c) CSS NPs.....	167
Figure 4.9	Photoluminescent properties of the β -NaYb/ErF ₄ @NaLuF ₄ CS NPs.....	168
Figure 4.10	Power density-dependent PL intensity of Yb/Er core and Yb/Er@Lu CS NPs.....	169
Figure 4.11	PL spectra of NaYF ₄ :Yb(20%)/Er(2%) NPs excited at 980 nm, showing major emission in the visible green regime instead of visible red and NIR regime.....	170
Figure 4.12	Absorbance at 980 nm and integrated PL intensity of Er@Lu CS NPs and Yb/Er@Lu CS NPs.....	170
Figure 4.13	Simplified energy level diagram of Yb ³⁺ /Er ³⁺ luminescent pair showing excitation at 808 nm.....	171
Figure 4.14	PL spectra across the visible and NIR regime of the Yb/Er core NPs and Yb/Er@Lu CS NPs with 808 nm excitation.....	172
Figure 4.15	Schemes, relaxivity plot, and phantom images of the β -NaYb/ErF ₄ @NaLuF ₄ @NaGdF ₄ CSS NPs.....	173
Figure 4.16	r_1 relaxivity of different samples at different field strength 1.5 T and 7 T.....	174
Figure 4.17	Hydrodynamic diameters (HD) of the α -NaGdF ₄ and β -Yb/Er@Lu@Gd CSS NPs.....	176
Figure 4.18	Comparison of image contrast between β -NaYb/ErF ₄ @NaLuF ₄ @NaGdF ₄ CSS NPs and Hexarbit in the same CT construct.....	177
Figure 4.19	TEM images, size distribution, and imaging properties of the β -NaYb/ErF ₄ @NaLuF ₄ @NaGdF ₄ CSS NPs with increasing thickness of the interfacial NaLuF ₄ layer.....	179
Figure 4.20	Low magnification TEM images of the (a) core, (b) CS, (c) CSS NPs with tunable thickness of the interfacial NaLuF ₄ layer.....	181
Figure 4.21	Morphological characterization of the (a) core, (b) CS, and (c) CSS NPs with increased interfacial NaLuF ₄ layer thickness.....	182

Figure 4.22	Comparison of PL intensity, MRI relaxivity, and CT contrast with increasing thickness of the interfacial NaLuF ₄ layer.....	184
Figure 4.23	Mass percentile change of the interfacial NaLuF ₄ layer in the Yb/Er@Lu@Gd CSS NPs with increased amount of Lu.....	184
Figure 4.24	TEM images of the β -NaYb/ErF ₄ @NaGdF ₄ CS NPs with increasing thickness of the NaGdF ₄ layer at the absence of the interfacial NaLuF ₄ layer.....	185
Figure 4.25	Low magnification TEM images of the Yb/Er@Gd1, Yb/Er@Gd2 and Yb/Er@Gd3 CS-NPs with increasing NaGdF ₄ shell thickness and no NaLuF ₄ layer.....	186
Figure 4.26	Morphological characterization of the (a) core, (b) CS and (c) CSS NPs shown in Figure 4. 24.....	188
Figure 5.1	TEM image and negative-stained TEM images of as synthesized ultrasmall (3 nm) oleate-stabilized NaGdF ₄ NCs.....	208
Figure 5.2	TEM) images and size distribution of oleate stabilized NaGdF ₄ NCs 3 nm, 4 nm, and 5 nm NaGdF ₄ :15% Ce ³⁺ /5% Tb ³⁺ NCs.....	210
Figure 5.3	Hydrodynamic size of the DSPE-PEG-2000 empty micelles in water prepared at different concentrations measured by DLS.....	211
Figure 5.4	Representative concentration dependent T ₁ ionic relaxivity plots.....	213
Figure 5.5	NC-micelles with variable NCs to DSPE-PEG ratio (weight/weight ratio) prepared by thin-film hydration method.....	214
Figure 5.6	Representative concentration dependent T ₁ ionic relaxivity plots (1.41 T) of NC-micelles prepared by thin-film hydration method with variable NCs to DSPE-PEG ratio.....	215
Figure 5.7	Comparison of thin-film hydration and solvent-exchange method with variable NCs to DSPE-PEG ratio.....	216
Figure 5.8	Sucrose gradient ultracentrifugation to remove empty micelles.....	216
Figure 5.9	Longitudinal T ₁ relaxivity (per Gd ³⁺) of the NaGdF ₄ NC-micelles at 1.41 T.....	217
Figure 5.10	Compact NC-micelles prepared from 3 nm NaGdF ₄ at NC to DSPE-PEG loading ratio of 1:40 measured by DLS.....	218

Figure 5.11	Representative concentration dependent ionic relaxivity plots (1.41 T) of compact NC-micelles (NCs to DSPE-PEG ratio weight/weight 1:40).....	219
Figure 5.12	Stability of compact-NC micelles stored at 4 °C.....	219
Figure 5.13	Representative concentration dependent T ₁ ionic relaxivity plots (7 T) compact NC-micelles (NCs to DSPE-PEG ratio weight/weight 1:40).....	221
Figure 5.14	Scheme and relaxivity of NaGdF ₄ NCs (3 nm) confined within DSPE-PEG micelles with variable PEG chain length and their respective average HD size.....	222
Figure 5.15	Representative concentration dependent ionic relaxivity plots (1.41 T) of NC-micelles with variable DSPE-PEG chain length (2000, 3000, and 5000).....	223
Figure 5.16	Schematic illustration of NaGdF ₄ NCs confined within DSPE-PEG micelles with variable core NC size (3, 4, 5 nm) and their respective average HD size.....	224
Figure 5.17	Representative concentration dependent ionic relaxivity plots (1.41 T) of NC-micelles with variable core NC size.....	225
Figure 5.18	Schematic illustration of NaGdF ₄ NCs (3 nm) coated with phospholipid-PEG micelles with variable hydrophobic chain length.....	226
Figure 5.19	Representative concentration dependent ionic relaxivity plot (1.41 T) of NC-micelles with DMPE-PEG-2000 coating.....	227
Figure 5.20	<i>In vitro</i> cell viability of HeLa cells incubated with compact NaGdF ₄ :DSPE-PEG-2000 micelles at different concentrations for 24 h.....	227
Figure 5.21	Representative optical microscopic images of HeLa cells incubated with and without the NaGdF ₄ NPs.....	228
Figure 5.22	MRI phantom images (top) and color contrasted images (bottom) of the HeLa cells incubated with NaGdF ₄ NC-micelles with different incubation times.....	229
Figure 5.23	<i>In vitro</i> cell viability of RAW264.7 cells incubated with compact NaGdF ₄ :DSPE-PEG-2000 micelles at different concentrations for 24 h.....	230

LIST OF SCHEMES

Scheme 2.1.	Lanthanide-doped core and core-shell UCNPs with different shell compositions.....	86
Scheme 3.1	The characteristics of the UCNP-PDT platforms.....	114
Scheme 4.1.	Schematic illustration for the β -Yb/Er@Lu@Gd hetero-epitaxial CSS NPs and their use as CAs for PL imaging, MRI, and CT.....	158

LIST OF TABLES

Table 0.1	Electron configuration and all possible energy levels in lanthanide trivalent ions.....	4
Table 0.2	Applications of each lanthanide element in industry.....	14
Table 0.3	Common laser-active rare earth ions and host media and important emission wavelengths.....	17
Table 3.1	Spectral features of the UCNPs and photosensitizers used in this work and other various studies.....	137
Table 4.1	Ionic properties of all four Ln ³⁺ ions incorporated in the CSS NPs in this study.....	159
Table 4.2	Calculated molar equivalency of each Ln ³⁺ for the synthesis of Yb/Er core, Yb/Er@Lu CS, and Yb/Er@Lu@Gd CSS NPs.....	161
Table 4.3	Calculated molar equivalency of compositions in the Yb/Er@Lu@Gd CSS NPs by measuring the size of each sample on a representative TEM image.....	165
Table 4.4	Elemental concentrations of different Ln ³⁺ in core, CS, and CSS NPs obtained from ICP-AES.....	165
Table 4.5	Paramagnetic properties of all four Ln ³⁺ ions incorporated in the CSS NPs in this study.....	174
Table 4.6	The amount of sacrificial α -NaLuF ₄ and α -NaGdF ₄ NPs used to synthesize β -Yb/Er@Lu@Gd CSS NPs with increasing thickness of interfacial NaLuF ₄ layers.....	180
Table 4.7	Molar equivalency of each component in the β -NaYb/ErF ₄ @NaLuF ₄ @NaGdF ₄ CSS NPs with tunable interfacial NaLuF ₄ layers.....	182
Table 5.1	Average hydrodynamic diameter (HD) sizes (number-weighted) and polydispersity index (PDI) of the micelles investigated in this study measured by DL.....	212
Table 5.2	Average relaxivity values per Gd ³⁺ of the micelles investigated in this study.....	220
Table 5.3	ICP-AES analysis summary of HeLa cells incubated with NaGdF ₄ NC-micelles.....	229

ACKNOWLEDGEMENTS

I would like to acknowledge Prof. Adah Almutairi for her work as the chair of my committee and the thesis advisor for the past five years. This incredible journey started in October 2012 with Adah and finally came to the point where I can stop and appreciate what Adah has done for me. I thank her for providing me the freedom to explore rough water in the new research field, excite myself with unexpected results, and shape myself to be a better researcher.

I acknowledge all the other members of my doctoral dissertation committee, Prof. Guy Bertrand, Prof. Darren J. Lipomi, Prof. Ying Shirley Meng, and Prof. Liangfang Zhang for their great help, guidance, suggestions, and scientific insights during the past several years.

I would like to thank the entire Almutairi lab including both the current and former members for their help and support during my work toward this doctoral dissertation. In particular, I gratefully thank Dr. Noah J. J. Johnson for his incredible mentorship during the early years of my Ph.D. studies, for him equipping me with all the necessary scientific skills I employed to complete this thesis, and for his unique inspiration to me for my scientific journey. Dr. Viet Anh Nguyen Huu sat next to me in the lab for almost entire five years. Viet was not only the co-author for three papers included in this thesis and made seminal contribution to the work, but also had plentiful discussion with me of topics ranging from philosophy, culture, and foreign languages. Dr. Wangzhong Sheng inspired me a lot for different discussions at group meetings, at late-night post-working chatting, and at coffee time! We also wrote a review article together and his working style impressed me. Carina Arboleda was the first junior student I mentored and worked with in the lab. Carina contributed significantly to the research work done in this thesis, and she also helped me to improve my communication and mentoring skills. Dr. Mathieu Lessard-Viger firstly introduced me to the lanthanide nanoparticle world right after I joined the lab. Dr. Carl-Johan Carling supervised me for simple organic synthesis in my first year when I worked on the nanoparticle/dye

conjugates. Dr. Ali Alhasan showed me about nanoparticle-DNA conjugates. Dr. Minnie Chan introduced me to the MRI studies. I also mentored several undergrads, Melinda Chan, Zhiyuan Ruan, and Johnny Kyo Koo, and all of them added great value to my doctoral research work.

The work included in this thesis spans a broad spectrum of topics which cannot possibly be organized here without the collaborative effort from numerous collaborators. Prof. Jesse V. Jokerst, Prof. Robert L. Sah, and Dr. Esther Cory at the UCSD campus made significant contribution on several related projects.

I reached out to a lot of researchers outside of UCSD for help with the work presented in this thesis. Notably, I thank Dr. Emory M. Chan and Dr. Thomas Bischof from the Molecular Foundry, Lawrence Berkeley National Lab for their help on optical measurements, discussion on the synthesis and modeling, and technical writing. I thank Dr. Stefan Fischer from Prof. A. Paul Alivisatos group from University of California Berkeley for their collaboration on lifetime measurements and their physics expertise well compensating all the chemistry work done in this thesis. I thank Prof. Hongjie Dai, Dr. Shuo Diao, Dr. Guosong Hong, and Dr. Alexander L. Antaris from Stanford University for their collaboration on downshifting luminescence characterization and application for NIR animal imaging. I thank Prof. Mercedeh Khajavikhan and Ahmed El Halawany from University of Central Florida for their collaboration on plasmon-enhanced luminescence.

The work in this thesis cannot be completed without the great execution and support from the technical staff all over UCSD. Particularly, I thank Dr. James Bower Cryo-Electron Microscopy Facility for the TEM characterization, Jennifer Santini and Ying Jones from the UCSD School of Medicine Microscopy Core for the confocal microscopy characterization, Paterno Castillo from Scripps Institution of Oceanography for the ICP characterization, Ryan Anderson

from Nano3 Cleanroom for the SEM characterization, Dr. Zhengjie Zhang from Prof. Seth Cohen group for their help on XRD characterization, and Robert Bussell from Center for Functional MRI for the magnetic characterization.

The Department of NanoEngineering at UCSD is an incredible environment for my career development and personal growth. I thank Prof. Joseph Wang, Prof. Darren J. Lipomi, Prof. Andrea R. Tao, Prof. Eric Fullerton, Prof. Gaurav Arya, Prof. Donald J. Sirbuly, Prof. Sadik C. Esener, Prof. Michael Berns, Prof. Michael J. Heller, Prof. Shaochen Chen, Prof. Liangfang Zhang, Prof. Jesse V. Jokerst, and Prof. Sungho Jin for their excellent teaching on various required and elective courses. Among all the peers, I would like to thank Dr. Jinxing Li, Yufeng Shen, and Chuanrui Chen from Prof. Joseph Wang group, Dr. Brandon Marin and Dr. Suchol Savagatrup from Prof. Darren J. Lipomi group, Dr. Wei Zhu from Prof. Shaochen Chen group, Dr. Chuze Ma from Prof. Shirley Meng group, Yunfeng Jiang, Haoliang Qian, and Qian Ma from Prof. Zhaowei Liu group, Zhao Wang, Dr. Yiwen Li, Ziyang Hu from Prof. Nathan Gianneschi group, Yue Zhang from Prof. Liangfang Zhang group, Junxing Wang from Prof. Jesse Jokerst group, James Wang from Prof. Andy Kummel group, Tiaohao Jiang, and Aoran Xu for invaluable camaraderie. I also thank Prof. Kanyi Pu from Nanyang Technological University and Prof. Zhen Gu from UNC Chapel Hill for giving me suggestions on writing.

Chapter of introduction, is unpublished work. Sha He and Adah Almutairi. The dissertation author was the primary investigator and author of this material.

Chapter 1, in full, is a reprint of the material as it appears in *J. Am. Chem. Soc.* 2017. Noah J. J. Johnson, Sha He, Shuo Diao, Emory M. Chan, Hongjie Dai, Adah Almutairi, American Chemical Society Press, 2017. The dissertation author was the primary investigator and author of this paper.

Chapter 2, is unpublished work. Sha He and Adah Almutairi. The dissertation author was the primary investigator and author of this material.

Chapter 3, is unpublished work. Sha He and Adah Almutairi. The dissertation author was the primary investigator and author of this material.

Chapter 4, is a reprint of the material as it appears in *Nano Lett.* Sha He, Noah J. J. Johnson, Viet Anh Nguyen Huu, Esther Cory, Yuran Huang, Robert L. Sah, Jess V. Jokerst, and Adah Almutairi, American Chemical Society Press, 2017. The dissertation author was the primary investigator and author of this paper.

Chapter 5, is a reprint of the material as it appears in *ACS Nano*. Noah J. J. Johnson, Sha He, Viet Anh Nguyen Huu, and Adah Almutairi, American Chemical Society Press, 2016. The dissertation author was the primary investigator and author of this paper.

VITA

- 2009 Bachelor of Science, Huazhong University of Science & Technology
- 2012 Master of Science, Chongqing University
- 2017 Doctor of Philosophy, University of California, San Diego

PUBLICATIONS

1. Surface-Dependent Optical and Magnetic Properties of Lanthanide-Doped Nanoparticles, He, S., Almutairi, A., *Acc. Chem. Soc.* 2017, *Invited Review*, in preparation.
2. On the Critical Role of Inert Epitaxial Shell in Enhancing Luminescence of Lanthanide-doped Core-Shell Nanocrystals, He, S., Fischer, S., Johnson, N. J. J., Bischof, T., Chan, E. M., Alivisatos, A. P., Almutairi, A., 2017, in preparation.
3. High Relaxivity Gadolinium-Polydopamine Nanoparticles, Wang, Z., Carniato, F., Huang, Y., Xie, Y., Li, Y., He, S., Zang, N., Rinehart, J., Botta, M., Gianneschi, N., *Small* 2017, accepted.
4. Sperm Motors with Chemotactic Property as Active Delivery Vehicles, Chen, C., Chang, X., Angsantikul, P., Li, J., Esteban-Fernandez de Avila, B., Karshalev, E., Liu, W., He, S., Castillo, R., Liang, Y., Guan, J., Zhang, L., Wang, J., *Adv. Mater.* 2017, revised.
5. Simultaneous Enhancement of Photoluminescence, MRI Relaxivity, and CT Contrast by Tuning the Interfacial Layer of Lanthanide Heteroepitaxial Nanoparticles, He, S., Johnson, N. J. J., Huu, V. A. N., Cory, E., Huang, Y., Sah, R. L., Jokerst, J. V., Almutairi, A., *Nano Lett.* 2017, *acs.nanolett.7b01753*, in press.
6. Leveraging Spectral Matching between Photosensitizers and Upconversion Nanoparticles for 808 nm-Activated Photodynamic Therapy, He, S., Johnson, N. J. J., Huu, V. A. N., Huang, Y., Almutairi, A., *ACS Nano* 2017, revised.
7. Heat Confinement: the Holy Grail of Near-Infrared Laser-based Therapy, Sheng, W., He, S., Seare, W., Almutairi, A., *J. Biomed. Opt.* 2017, *jbo-170036vr*, in press.
8. Nanoconfined Atomic Layer Deposition of TiO₂/Pt Nanocavities: Towards Ultra-Small Highly Efficient Catalytic Nanorockets, Li, J. X., Liu, W., Wang, J., Rozen, I., He, S., Chen, C., Kim, H., Lee, H., Li, T., Li, L., Mei, Y.-F., Wang, J., *Adv. Funct. Mater.* 2017, 27, 1700598 (*Highlighted as journal cover*).

9. Direct Evidence for Coupled Surface and Concentration Quenching Dynamics in Lanthanide-Doped Nanocrystals, Johnson, N. J. J., # He, S., # Diao, S., Chan, E. M., Dai, H. J., Almutairi, A., *J. Am. Chem. Soc.* 2017, 139, 3275–3282. (# denotes equal contribution)
10. Compact Micellization: A Strategy for Ultra-high T₁ MRI Contrast with Gadolinium-based Nanocrystals, Johnson, N. J. J., He, S., Huu, V. A. N., Almutairi, A., *ACS Nano* 2016, 10, 8299-8307.
11. Enhanced UV Upconversion Emission Using Plasmonic Nanocavities, El-Halawany, A., He, S., Hodaei, H., Bakry, A., Razvi, M. A. N., Alshahrie, A., Johnson, N. J. J., Christodoulides, D. N., Almutairi, A., Khajavikhan, M., *Opt. Exp.* 2016, 24, 13999-14009.
12. Light-triggered Chemical Amplification to Accelerate Degradation and Release from Polymeric Particles, Olejniczak, J., Huu, V. A. N., Lux, J., Grossman, M., He, S., Almutairi, A., *Chem. Commun*, 2015, 51, 16980-16983.
13. Short Soluble Coumarin Crosslinkers for Light-Controlled Release of Cells and Proteins from Hydrogels, de Gracia Lux, C., Lux, J., Collet, G., He, S., Chan, M., Olejniczak, J., Collet, A.-F., Almutairi, A., *Biomacromolecules*, 2015, 16, 3286-3296.
14. Engineering Upconversion Emission Spectra Using Plasmonic Nanocavities, Lantigua, C., He, S., Bouzan, M., Hayenga, W., Johnson, N. J. J., Almutairi, A., Khajavikhan, M., *Opt. Lett.* 2014, 39, 3710-3713.

FIELDS OF STUDY

Major Field: NanoEngineering

Studies in Colloidal chemistry and luminescence materials
Professor Adah Almutairi

ABSTRACT OF THE DISSERTATION

Colloidal Lanthanide Nanoparticles: Doping, Epitaxy, and Photon Management

by

Sha He

Doctor of Philosophy in NanoEngineering

University of California, San Diego, 2017

Professor Adah Almutairi, Chair

Lanthanides, known as the “vitamin of industry”, have been playing a pivotal role in a wealth of advanced materials and modern technologies including catalysts, magnets, lasers, economical lighting, and solar-energy conversion. With the development of nanoscience, lanthanide nanoparticles have been attracting increasing research interest as a new form of the old materials since 2000. These nanoparticles not only bring properties previously thought impossible in bulk lanthanide materials, but also raise concerns and challenges (e.g. quenching) that were not considered towards practical applications. This dissertation is dedicated to understanding and

tackling these challenges with designed colloidal lanthanide nanoparticles. Particularly, the first theme explains how the dopants in the nanoparticle matrix contribute to the size and shape of nanoparticles (doping). The second theme explores the growth behavior of core-shell nanoparticles with controlled interfacial strains (epitaxy). The third theme introduces how to address the quenching challenges and enhance the photoluminescence on nanoparticles with the optimized doping and epitaxy (photon management). We show that the optimized lanthanide nanoparticles have record-high emission efficiency, provide insight for future nanoparticle designs, and can be used as a promising toolset for a wide ranges of research topics including bioimaging, therapeutics, photocatalysis, and optical energy conversion.

Chapter of introduction starts with the fundamental physics and chemistry of lanthanides, discusses the unique features of colloidal lanthanide nanoparticles, summarizes the cutting-edge research directions in the lanthanide nanoparticle field, touches on the current daunting challenges in the field, and justifies the theme for this doctoral dissertation.

Chapter 1 reveals the interdependence of surface and concentrating quenching dynamics in lanthanide-doped nanoparticles. We show that the major quenching mechanism for nanoparticles with high doping levels is the energy migration to surface defects, as opposed to the commonly accepted cross-relaxation between neighboring dopants.

Chapter 2 analyzes the critical effect of the doped epitaxial shells in enhancing the upconversion luminescence in one of the most widely studied system— $\text{Yb}^{3+}/\text{Er}^{3+}$ co-doped β - NaYF_4 nanoparticles. We show that the core nanoparticles coated with the inert epitaxial shell have the highest emission intensity and luminescence quantum yield, and the both emission intensity and quantum yield monotonously drops with the increasing doping level in the shell.

Chapter 3 develops a photocatalysis/photodynamic therapy platform by engineering the spectral feature of the upconversion nanoparticles. The nanoparticles can be excited by the biobeneign 808 nm laser at extremely low irradiance, and emit visible red light centered at 654 nm that further activates the highly efficient photosensitizers ZnPc.

Chapter 4 develops a class of multimodal imaging contrast agents that work for optical imaging, magnetic resonance imaging, and computed tomography with high performance. Importantly, the optical emission, MRI relaxivity, and CT contrast are simultaneously enhanced by tuning the interfacial layer thickness in the heteroepitaxial structure, overcoming the conundrum that putting two imaging functions on the single entity often compromises the overall performance.

Chapter 5 introduces a surface-engineering strategy to enhance the MRI contrast remarkably approaching the known theoretical limit. Using monodispersed and ultrasmall NaGdF₄ nanoparticles and dual-solvent exchange-induced micellization, we demonstrate that the modified nanoparticles can be steadily dispersed in water, individually encapsulated, and does not coagulate. These features enhance the interaction between Gd³⁺ magnetic centers and the surrounding water protons and we obtain a MRI relaxivity as high as $\sim 80 \text{ mM}^{-1}\text{s}^{-1}$.

Introduction

0.1 What are Lanthanides?

Lanthanides are a series of fifteen elements with atomic numbers ranging from 57 to 71 in the periodic table—lanthanum (La, #57), cerium (Ce), praseodymium (Pr), neodymium (Nd), promethium (Pm), samarium (Sm), europium (Eu), gadolinium (Gd), terbium (Tb), dysprosium (Dy), holmium (Ho), erbium (Er), thulium (Tm), ytterbium (Yb), and lutetium (Lu, #71).¹⁻² Alternatively, these fifteen elements along with the two chemically similar elements sitting in diagonal of La in the periodic table, yttrium (Y, #39) and scandium (Sc, #21), are often referred together as rare earth elements or rare earth metals (Figure 0.1). They were first discovered in the late 18th century in Ytterby, a small village in Sweden (Figure 0.2). Several scientists and inventors including Gadolin, Berzelius, and Klaproth have contributed significantly to the discovery and purification of these metals from the earth minerals.² This series of elements were first named as ‘rare earth’ because they were purified from reasonably rare, low-abundance minerals in Europe. However, this was later proved misleading because these elements were in a practically unlimited abundance in the earth crust of East Asia, particularly in China. The term lanthanide was adopted, originating from the first element of the series, Lanthanum (La) to represent the series of the elements. In contemporary science and technology, the terms of lanthanides and rare earths are usually interchangeable and by default refer to the total seventeen elements.

Rare Earth Elements

H																	He
Li	Be											B	C	N	O	F	Ne
Na	Mg											Al	Si	P	S	Cl	Ar
K	Ca	Sc	Ti	V	Cr	Mn	Fe	Co	Ni	Cu	Zn	Ga	Ge	As	Se	Br	Kr
Rb	Sr	Y	Zr	Nb	Mo	Tc	Ru	Rh	Pd	Ag	Cd	In	Sn	Sb	Te	I	Xe
Cs	Ba	*	Hf	Ta	W	Re	Os	Ir	Pt	Au	Hg	Tl	Pb	Bi	Po	At	Rn
Fr	Ra	**	Rf	Db	Sg	Bh	Hs	Mt	Ds	Rg	Cn	Uut	Fl	Uup	Lv	Uus	Uuo
		*	La	Ce	Pr	Nd	Pm	Sm	Eu	Gd	Tb	Dy	Ho	Er	Tm	Yb	Lu
		**	Ac	Th	Pa	U	Np	Pu	Am	Cm	Bk	Cf	Es	Fm	Md	No	Lr

Light Rare Earth Element
 Heavy Rare Earth Element

Figure 0.1 The seventeen elements in the periodic table.

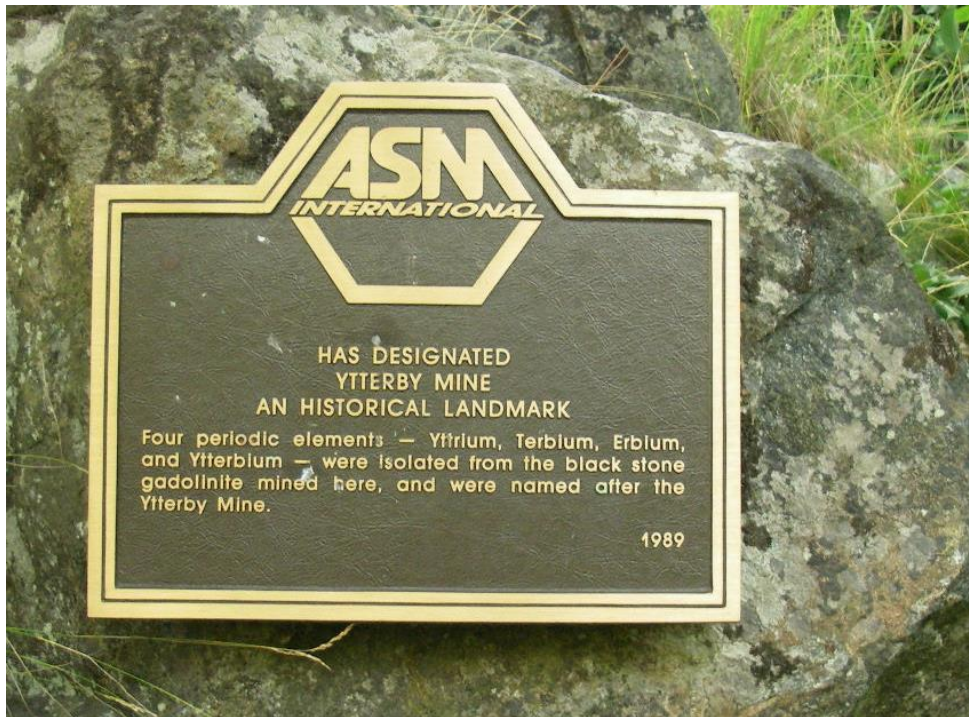


Figure 0.2 Memorial plaque of the American Society for Metals (ASM) international society at the entrance of Ytterby mine, Ytterby, Sweden.

0.2 Basic Physical and Chemical Properties of Lanthanides

Lanthanides are classified as inner transition metals with partially filled 4f electron configurations in the periodic table, and they are different from conventionally known transition metals whose d orbitals are partially filled. This is the most fundamental property of lanthanide ions (typically +3), and it enables several important features that set lanthanide ions apart from other transition metal ions and make lanthanides unique in the industry.^{1, 3-7} Y^{3+} and Sc^{3+} do not have any f orbitals, so they are often used as host materials to allow other lanthanides be doped in. Four important characteristics of lanthanide trivalent ions (Ln^{3+}) are listed below.

(1). There are fourteen electrons in total to occupy the 4f orbitals (Table 0.1). With the degree of fillings in the orbitals, there are numerous possible electron configurations, and they can be further split into many energy sublevels (Figure 0.3) with the influence of Coulombic interactions, spin-orbital coupling, and crystal field perturbation (very weak).⁸ Using first principle calculation, all the possible 4f energy levels in lanthanide ions can be roughly summarized in Figure 0.4, with the energy gap spanning from $0 - 2 \times 10^5 \text{ cm}^{-1}$. The 4f for La^{3+} is empty while for Lu^{3+} is full. Therefore both of these two ions do not allow and optical transitions.⁹ For other thirteen lanthanide ions, their electrons can be promoted to higher energy upon absorption of photons.

Table 0.1 Electron configuration and all possible energy levels in lanthanide trivalent ions.⁹

Atomic number	Ion	Ground configuration	Ground state $2S+1L_J$	Total number of states in ground configuration	Excited configuration	Total number of states in excited configuration
57	La ³⁺	4f ⁰	¹ S ₀	1	–	–
58	Ce ³⁺	4f ¹	² F _{5/2}	14	5d	10
59	Pr ³⁺	4f ²	³ H ₄	91	4f ¹ 5d	231
60	Nd ³⁺	4f ³	⁴ I _{9/2}	364	4f ² 5d	1274
61	Pm ³⁺	4f ⁴	⁵ I ₄	1001	4f ³ 5d	4641
62	Sm ³⁺	4f ⁵	⁶ H _{5/2}	2002	4f ⁴ 5d	12012
63	Eu ³⁺	4f ⁶	⁷ F ₀	3003	4f ⁵ 5d	23023
64	Gd ³⁺	4f ⁷	⁸ S _{7/2}	3432	4f ⁶ 5d	33462
65	Tb ³⁺	4f ⁸	⁷ F ₆	3003	4f ⁷ 5d	37323
66	Dy ³⁺	4f ⁹	⁶ H _{15/2}	2002	4f ⁸ 5d	32032
67	Ho ³⁺	4f ¹⁰	⁵ I ₈	1001	4f ⁹ 5d	21021
68	Er ³⁺	4f ¹¹	⁴ I _{15/2}	364	4f ¹⁰ 5d	10374
69	Tm ³⁺	4f ¹²	³ H ₆	91	4f ¹¹ 5d	3731
70	Yb ³⁺	4f ¹³	² F _{7/2}	14	4f ¹² 5d	924
71	Lu ³⁺	4f ¹⁴	¹ S ₀	1	4f ¹³ 5d	141

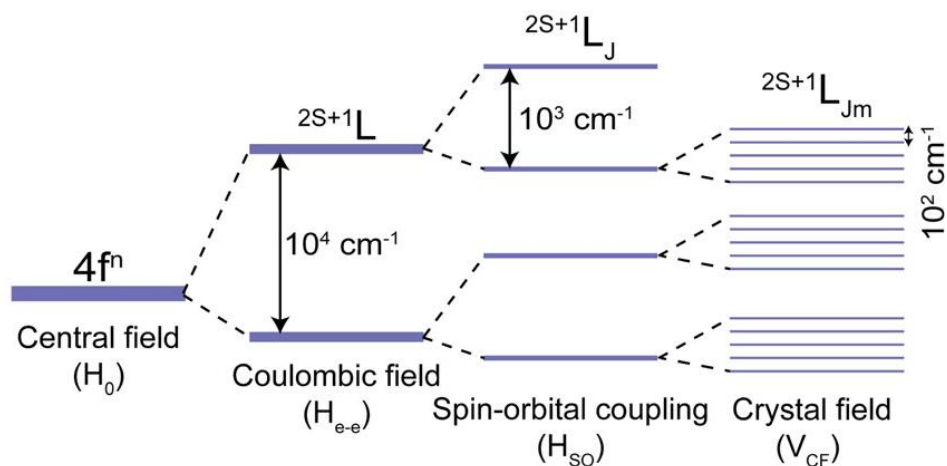


Figure 0.3 The 4fⁿ electronic configuration splits into many energy sublevels due to the strong effects of the Coulombic interaction and spin-orbit coupling as well as very weak crystal-field perturbation.⁸

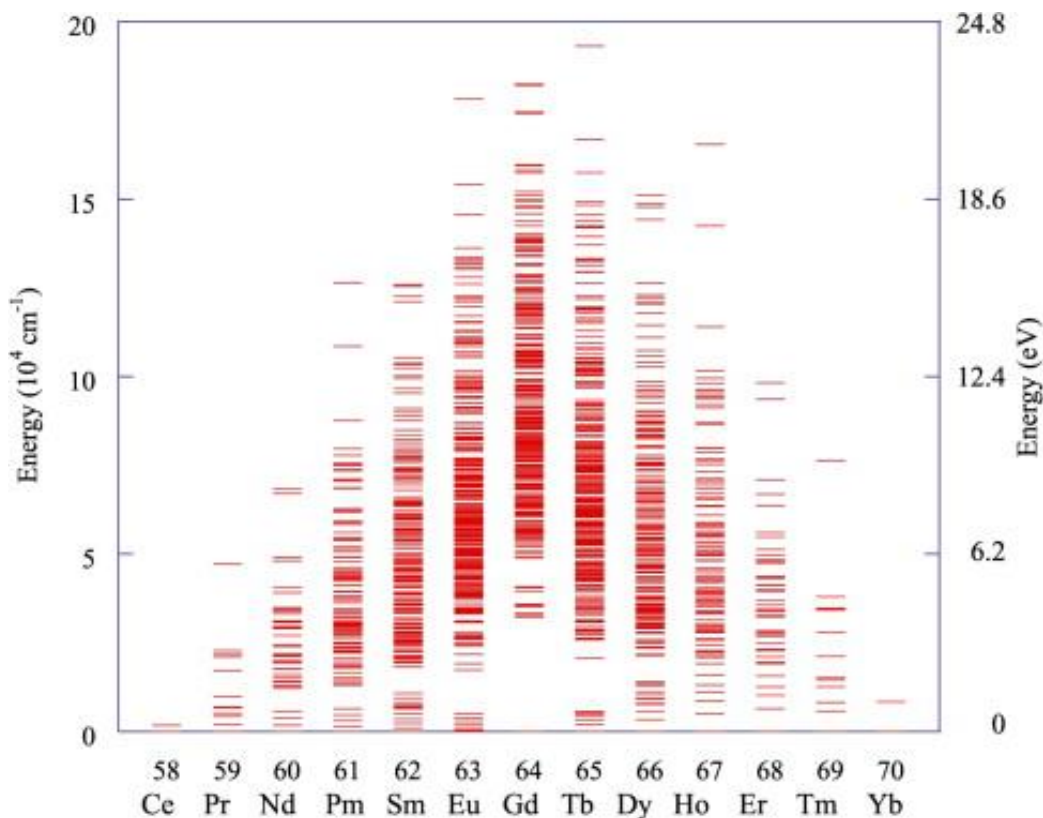


Figure 0.4 First Principle calculation of the possible 4f energy levels in lanthanide ions highlighting the abundance of major energy levels.⁹

(2). For the thirteen lanthanides rather than La^{3+} and Lu^{3+} , they can absorb excitation at different energies and relax the energy through the emission of photons. When X-rays are absorbed and visible photons are emitted on lanthanide ions, it is known as scintillation. However, in most cases, the lanthanides are excited by ultraviolet (UV) or visible light and emit visible or near-infrared (NIR) light, and this is known as photoluminescence. The wavelengths of UV to NIR light lies within 200-2000 nm, corresponding to $10^3 - 10^4 \text{ cm}^{-1}$ in wavenumbers.⁸ Therefore, the lower part of the energy levels in Figure 0.4 is often studied and it is known as the classical Dieke diagram (Figure 0.5).¹⁰ Due to the rich energy levels, the emission bands for the lanthanide ions cover the UV to NIR spectrum (Figure 0.6).¹¹

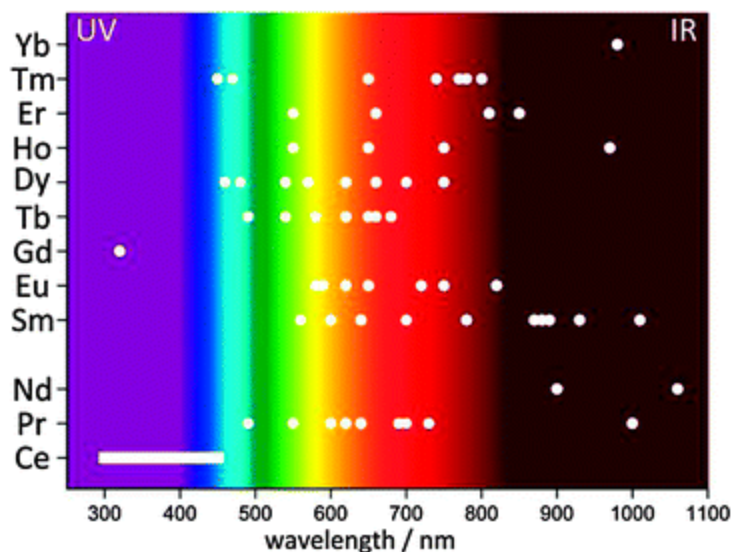


Figure 0.6 Wavelength of the main emissive transitions of the trivalent lanthanide coordination compounds in the UV to NIR range.¹¹

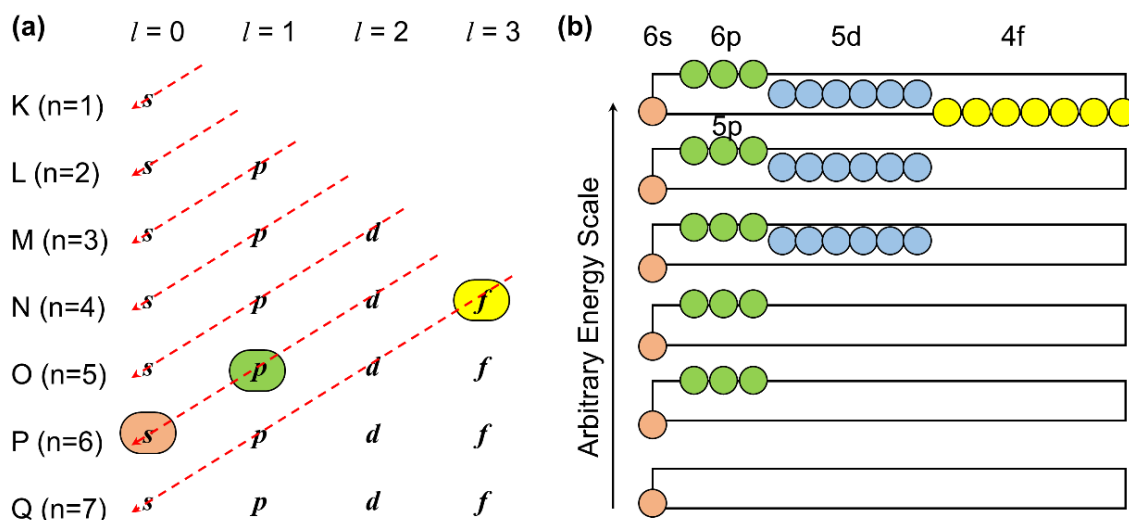


Figure 0.7 Electron filling in different orbitals. (a) The order of filling in orbitals and (b) the simplified energy level diagrams.

(3). Electrons fill the orbitals from the lowest to the highest energy (Figure 0.7a). The energy of 4f orbital is higher than that of 5p and 6s orbitals, and they are only occupied after both 5p and 6s have been filled (Figure 0.7b). The 4f orbitals are shielded by 5p and 6s orbitals, do not

participate chemical bond formation, and unlike 5d orbitals in lanthanides, are weakly influenced by the crystal field splitting (Figure 0.8). Therefore, the optical transitions, including the absorption and emission maximum and their colors, usually stays the same for a specific type of lanthanide ions wherever they are doped (Figure 0.9).

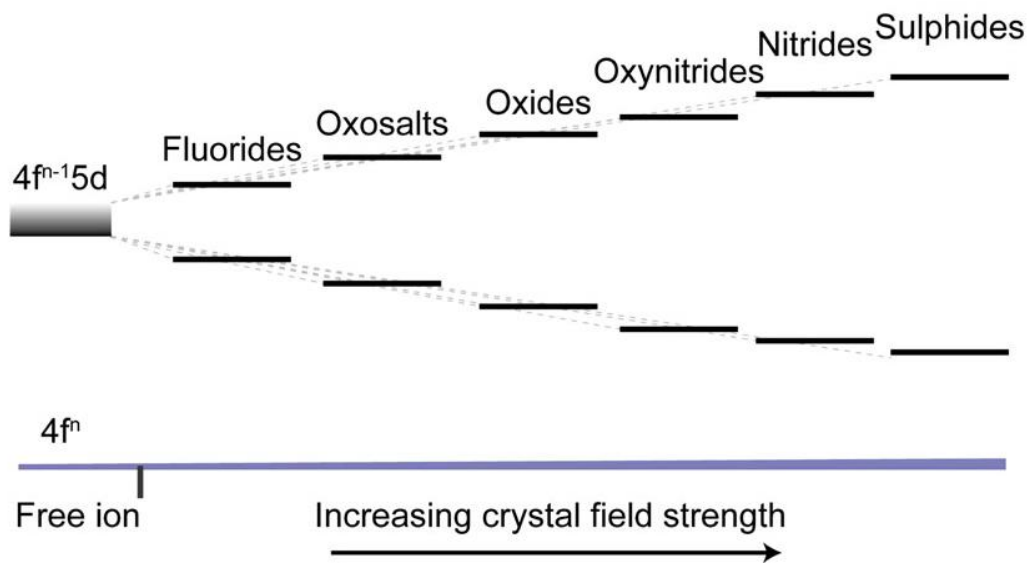


Figure 0.8 Simplified scheme showing the breaking/splitting of degeneracies of electron orbital states in 5d and 4f orbitals of lanthanides when they are doped into different types of inorganic host materials and are affected by the different surrounding charge distribution in various crystal field.⁸

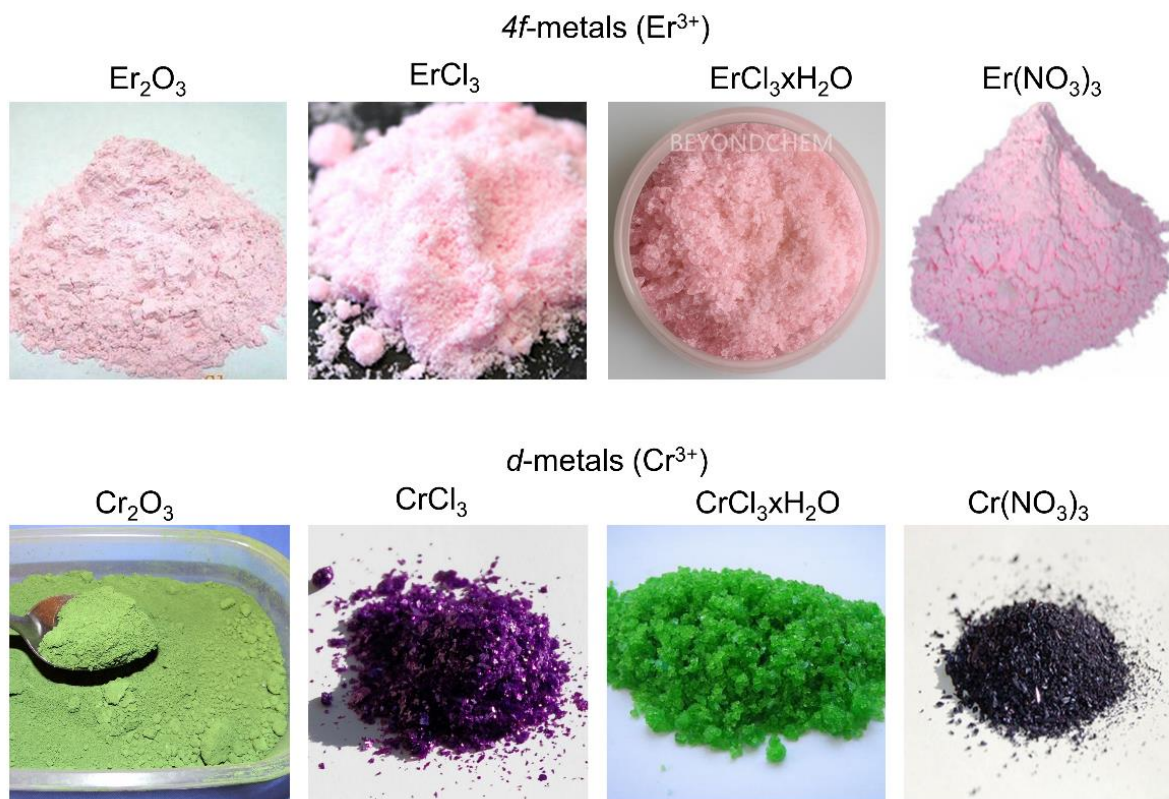


Figure 0.9 Comparison of lanthanides (upper panel) and d-block transition metals (lower panel).

(4). The 4f electrons are shielded from the surrounding chemical environment and the lanthanide element nuclei. Therefore, upon absorption of an incident photon, the promotion of an electron into a 4f orbital of higher energy from lower energy within the 4f shell does not perturb much the binding pattern between the lanthanide ions and the surrounding crystal field. As a result, the internuclear distances remain almost the same in the excited state, which generates very narrow emission bands (Figure 0.10). This is very different from organic fluorophores with broad emission peaks and provides very pure emission colors, benefiting emission multiplexing.

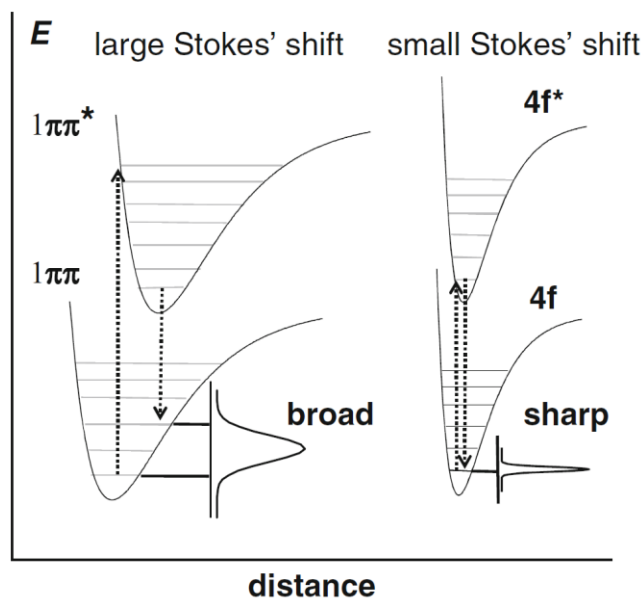


Figure 0.10 Configurational coordinate diagram for emission from (left) an organic fluorophore and (right) a lanthanide ion.⁹

(5). The intra-4f optical transitions are parity-forbidden, and therefore the excited electrons have relatively longer lifetime (μs to ms) at the excited states, giving possibility for persistent luminescence, multiphoton absorption, and anti-Stokes emission. Notably, the multiphoton absorption and anti-Stokes emission in lanthanide ions can be different from the previous mechanisms such as second harmonic generation (SHG) and two-photon absorption (TPA) (Figure 0.11). In SHG and TPA, two photons need to be absorbed simultaneously to reach the higher energy, and therefore it necessitates the extremely high excitation irradiance from lasers (usually femtosecond pulsing lasers). In lanthanide-based systems, the electron is able to absorb one photon, be excited to the first excited state, *sequentially* absorb the second photon to reach the second excited state, and finally emit. This is known as upconversion (UC) (Figure 0.11) and requires much lower excitation irradiance, which has received considerable research interest in the past decade. Also, the long lifetime of the luminescence from lanthanides evokes their use in time-resolved spectroscopies.¹²

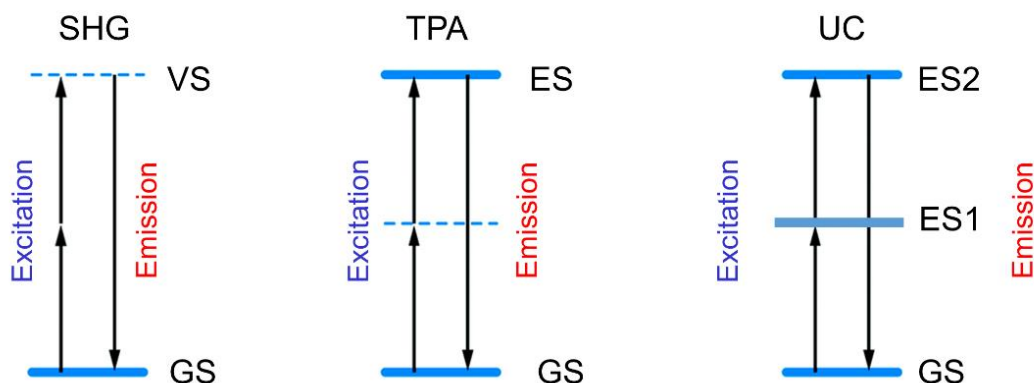


Figure 0.11 (from left to right) schematic illustrations of second harmonic generation (SHG), two-photon absorption (TPA), and upconversion (UC). GS, ground state; ES, excited state; VS, virtual state.

(6). Photobleaching refers to the destructions of a light-emitting entity (usually organic fluorophores) and permanent loss of light-emitting capability by high-intensity light irradiation. It is often caused by cleaving of covalent bonds or non-specific reactions between the fluorophores and surrounding molecules or within the fluorophores themselves. Such permanent, irreversible change leads to the transition of the light-emitting entity from singlet state to the triplet state and stops them from fluorescing. Photobleaching is a major challenge particularly for long-term imaging when green fluorescence proteins or typical organic fluorophores are used as imaging probes. However, in lanthanide-based luminescent materials, lanthanide ions are good quenchers to the triplet states (Figure 0.12).¹³ Therefore, the detrimental triplet states can be eliminated, and the photobleaching is significantly suppressed when lanthanide-based materials are under high-intensity light irradiation. Therefore, lanthanide-based optical probes can be used for long-term monitoring of various targets with high accuracy and reliability.

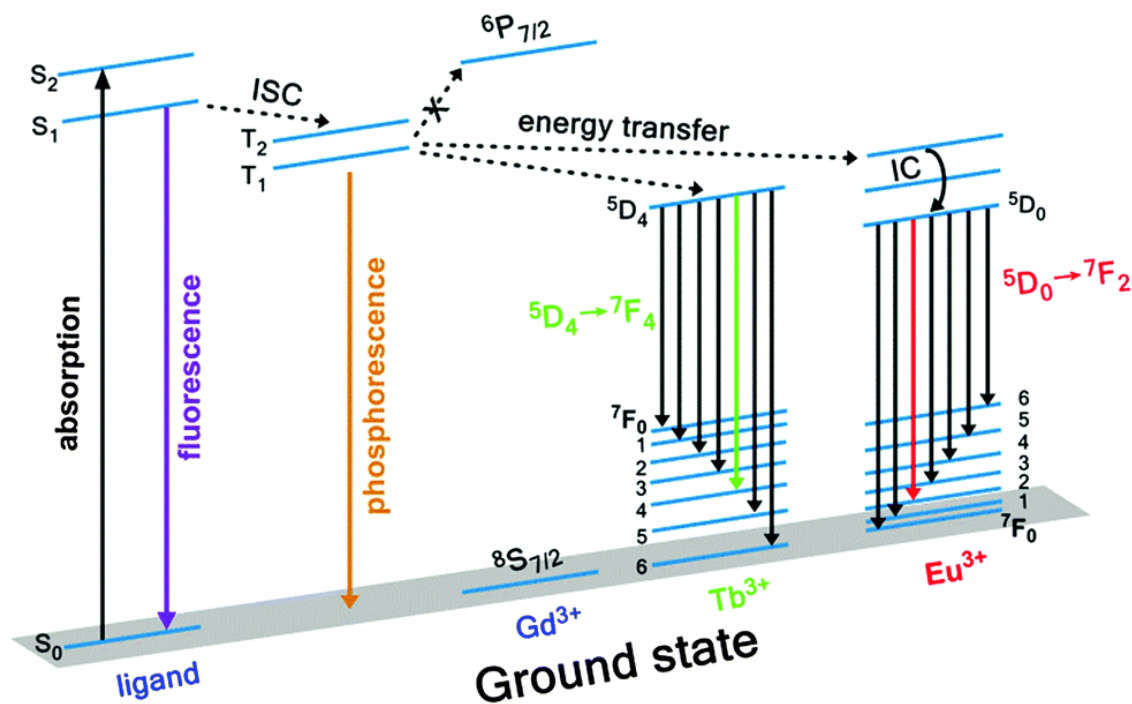


Figure 0.12 Triplet states are quenched by lanthanide trivalent ions when they are brought to close proximity.¹³

(7). The 4f electrons make the lanthanide trivalent ions highly paramagnetic. Paramagnetism refers to the susceptibility of materials to external magnetic field, and it is caused by the angular momentum of the unpaired electrons.¹⁴⁻¹⁸ As repeatedly stated above, the unpaired electrons occupy the 4f orbitals, and they behave like free electrons, making orbital and spin angular momentum together contributing to magnetic moment significantly higher than that of most other transition metal ions.¹⁹ Among all lanthanides, Gd³⁺ has the highest paramagnetism because it has seven unpaired electrons in the 4f orbitals, the most of all ions in the periodic table. Therefore, lanthanide ions respond to external magnetic fields more dramatically, and it also inspires a variety of applications such as magnets and magnetic resonance imaging contrast agents.²⁰⁻²⁷

0.3 Applications of Lanthanides in Industry

Lanthanides did not find any exciting applications in the span of more than a hundred years since its discovery, and it was dramatically changed when Carl Auer Freiherr von Welsbach, an Austrian inventor developed lanthanide-based flint and gas mantle around the 1900s. The flint was composed of a trace amount of Ce, and it was considered as the inspiration of ignition source or lighters (ferrocium) later, while the gas mantle was composed of La, Ce, Nd, and Sm, and it is now widely used in portable lanterns and lamps. Since then, lanthanide materials have evoked considerable interest in both academia and industry due to their unique properties.

Since its discovery and the early applications demonstrated a century ago, it has been realized that the lanthanides have particular merit in optics related applications, i.e. they can be effective toolset to manage photons in various ways. In modern industry, lanthanides are a vital piece of many advanced technologies and platforms. Some of the well-developed applications can be found in Table 0.2. Among all these applications, three representative applications using lanthanide materials, i.e. lighting, lasers, and telecommunications are highlighted below.

Table 0.2 Applications of each lanthanide element in industry²⁸

Element	Current Uses
Sc	Structural alloys, medical lasers, metal-halide lamps
Y	Phosphors, catalysts, propane gas mantles, oxygen sensors, structural metal alloys, structural ceramics, thermal barrier coatings, microwave filters
La	Ni-M-H rechargeable batteries, lighter flints, electron emitters, fiber-optic glasses, scintillators for radiation detection, abrasives, steels, welding
Ce	Structural metal alloys, polishing, fuel cracking catalysts, self-cleaning ovens, automotive catalytic converters, phosphors, pigment stabilization
Pr	Pigments, magnets, structural metal alloys, lighting, welders' goggles, fiber-optic amplifiers, catalysts, lighter flints
Nd	Pigments, magnets, lasers, cryocoolers, fertilizers, rear-view mirrors
Sm	Magnets, cancer treatment, nuclear reactor control rods, IR absorbers
Eu	Phosphors
Gd	Cancer treatment, neutron radiography, MRI contrast agents, neutron shielding, structural metal alloys
Tb	Phosphors, magnets (vs. Dy), magnetostrictive actuators, SOFCs (vs. Y)
Dy	Magnetostrictive actuators, thermal neutron absorbers, lasers, IR sources, metal-halide lamps, radiation dosimeters, catalysts, adiabatic refrigeration,
Ho	Magnetic flux concentrators, neutron absorbers, lasers, fiber-optics
Er	Lasers, optical amplifiers, medical lasers, neutron absorbers, vanadium alloys, pigments for artificial gemstones, cryocoolers
Tm	Portable X-ray sources, lasers (especially in surgery), radiation dosimeters, fluorescent anticounterfeiting banknote dyes
Yb	Gamma-ray sources, stainless steels, lasers, fiber-optics
Lu	Metal alloys, catalysts, cancer treatment

0.3.1 Lighting

Since Thomas Edison's pioneering work, the incandescent light bulb had dominated the lighting market for a century before it was replaced in the 1970s by fluorescent lamps with improved lighting efficiency. The inner side of the fluorescent lamps was usually coated with

lanthanide-containing phosphors (Figure 0.13). The lanthanide phosphors were typically composed of Eu, Tb, and Ce for tunable red, green, and blue luminescence under the 245 nm excitation from mercury, and the combination can be tuned to emit white luminescence for efficient lighting (Figure 0.14).⁸ However, its application was played down due to the environmental concern of mercury. With the development of GaN blue light-emitting diodes (LEDs) as the alternative of mercury excitation, the lanthanide-based phosphors have revived as the lighting options and their emission efficiency has been significantly improved.

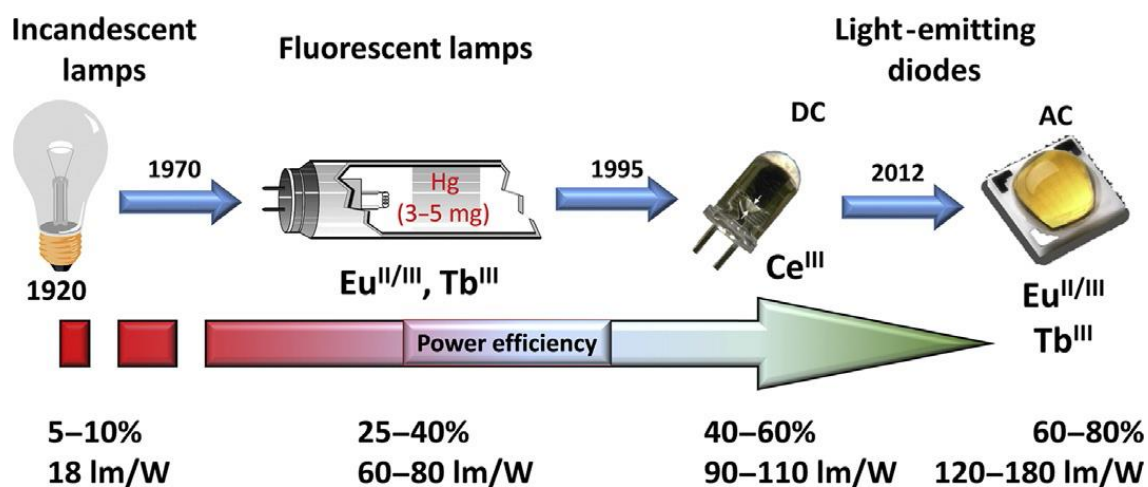


Figure 0.13 The impact of lanthanides on solid-state lighting, particularly improving lighting efficiency. Efficiencies in this figure are "typical" values for these devices in the market. Luminous efficiency (lm/W) refers to an input electric power of 100 W.²⁹

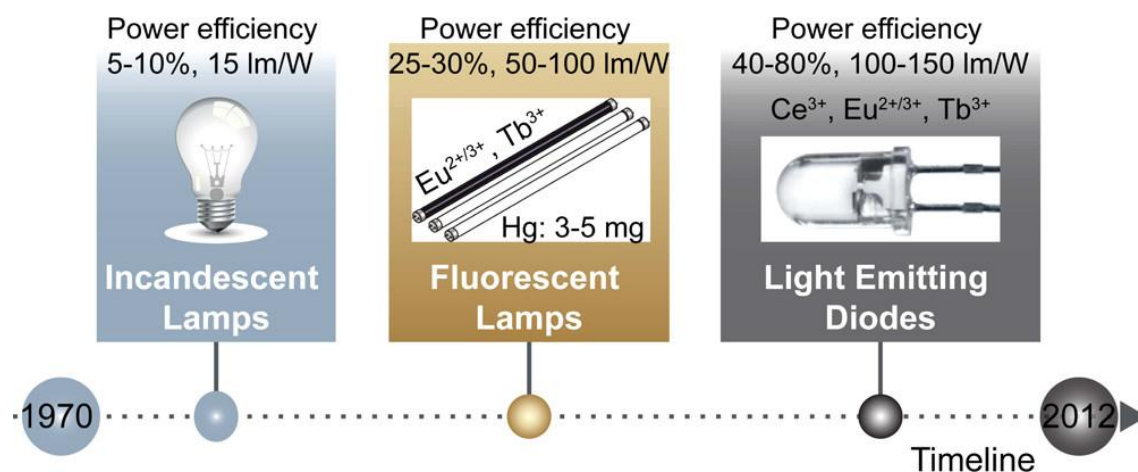


Figure 0.14 The historical development of three generations of solid state white-light emitting devices since 1970.⁸

0.3.2 Lasers

The active materials of solid state lasers are among the very early applications of lanthanides with high purity since the purification procedures were well developed. Lanthanide cations are ideally applied as the active material for solid-state lasers with emission spanning from UV, visible to the NIR region (Table 0.3).

With no doubt, one of the most widely used lanthanide-based lasers is the Nd-YAG (yttrium aluminate garnet as the host media, doped with 1% of Nd^{3+} as the active ions, usually $\text{Nd}:\text{Y}_3\text{Al}_5\text{O}_{12}$) laser with the strong emission line at 1060 nm in the NIR region. This wavelength (or frequency) can be facilely doubled (532 nm, green), tripled (355 nm, purple), or quadrupled (266 nm, UV) resulting in multi-line lasers for excitation of luminescence spectra. These lasers are essential to various aspects of our daily lives from slide presentations, manufacturing, optical tweezers, and medical surgeries to military laser designators.

Table 0.3 Common laser-active rare earth ions and host media and important emission wavelengths.³⁰⁻³¹

Lanthanide Ion	Common host media	Important emission wavelengths
Nd ³⁺	YAG, YVO ₄ , YLF, silica	1.03–1.1 μm, 0.9–0.95 μm, 1.32–1.35 μm
Yb ³⁺	YAG, tungstates, silica	1.0–1.1 μm
Er ³⁺	YAG, silica	1.5–1.6 μm, 2.7 μm, 0.55 μm
Tm ³⁺	YAG, silica, fluoride glasses	1.7–2.1 μm, 1.45–1.53 μm, 0.48 μm, 0.8 μm
Ho ³⁺	YAG, YLF, silica	2.1 μm, 2.8–2.9 μm
Pt ³⁺	silica, fluoride glasses	1.3 μm, 0.635 μm, 0.6 μm, 0.52 μm, 0.49 μm
Ce ³⁺	YLF, LiCAF, LiLuF, LiSAF, and similar fluorides	0.28–0.33 μm

0.3.3 Telecommunications

Telecommunication is the transmission of information or intelligence of any nature by wire, radio, optical or other electromagnetic systems. In modern telecommunication systems, information is transported by light that is guided in silica optical fibers. Despite its excellent transparency, the signals are usually attenuated over distance (~100 km) and need amplification for accurate transmission. A well-developed amplification system is the erbium-doped fiber amplifiers (EDFAs), and it has been deployed over all world since its first proposal in 1987 (Figure 0.15). All Er³⁺ have a typical emission peak around 1530 nm upon excitation at various wavelengths, and this wavelength falls well within the third communication window (or C band, 1530-1565 nm) featuring lowest attenuation losses and longest transmission range.

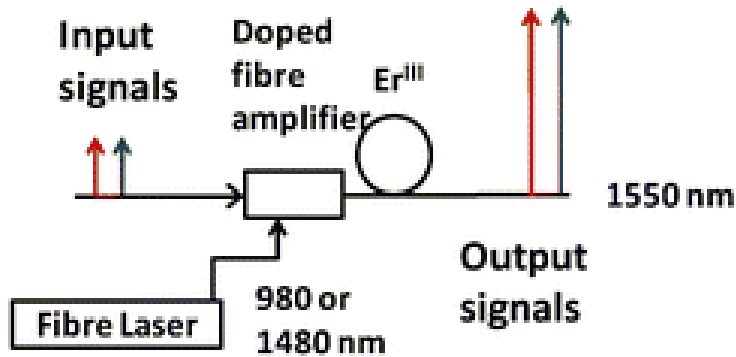


Figure 0.15 Simplified workflow for erbium-doped fiber amplifiers (EDFAs).²

0.4 Colloidal Nanoparticles: General

Colloids are defined as, particularly in chemical sciences, mixtures in which one substance is dispersed throughout another substance. Therefore, the colloids are composed of two different phases, the solute and the solvent. To be qualified as colloids, the mixture must not settle towards phase separation or would take a very long time for the settling to be observed. Typical colloids in daily life include milk, coffee, blood, ink, and soap water, etc.

To fulfill the requirement of long-time suspension instead of settlement, the solutes usually have a size between 1-1000 nm. Particularly, the colloids are specified as nanocolloids or colloidal nanoparticles if the sizes of the solute fall between 1 and 100 nm. More often, the colloidal nanoparticles are suspended in a various liquid solvent, and all the discussion below refers to colloidal nanoparticles dispersed in either organic or aqueous solvent by default.³²⁻³³ The colloidal nanoparticles are particularly interesting because (i) their nanoscale sizes bring numerous novel electrical, optical, magnetic, mechanical, and thermal properties that can only be observed at this scale, (ii) nanoparticles in the solvent are more easily to synthesize and fabricate with high uniformity, and (iii) these nanoparticles dispersed as the form of suspension in the solvent are more convenient to characterize and engineer for surface modification.³⁴⁻³⁶ As a result, the colloidal

nanoparticles including a broad range of materials such as metals, metal oxides, semiconductors, silica, titania, and polymers have been the cutting-edge research topics for several decades.³⁷⁻⁴⁵

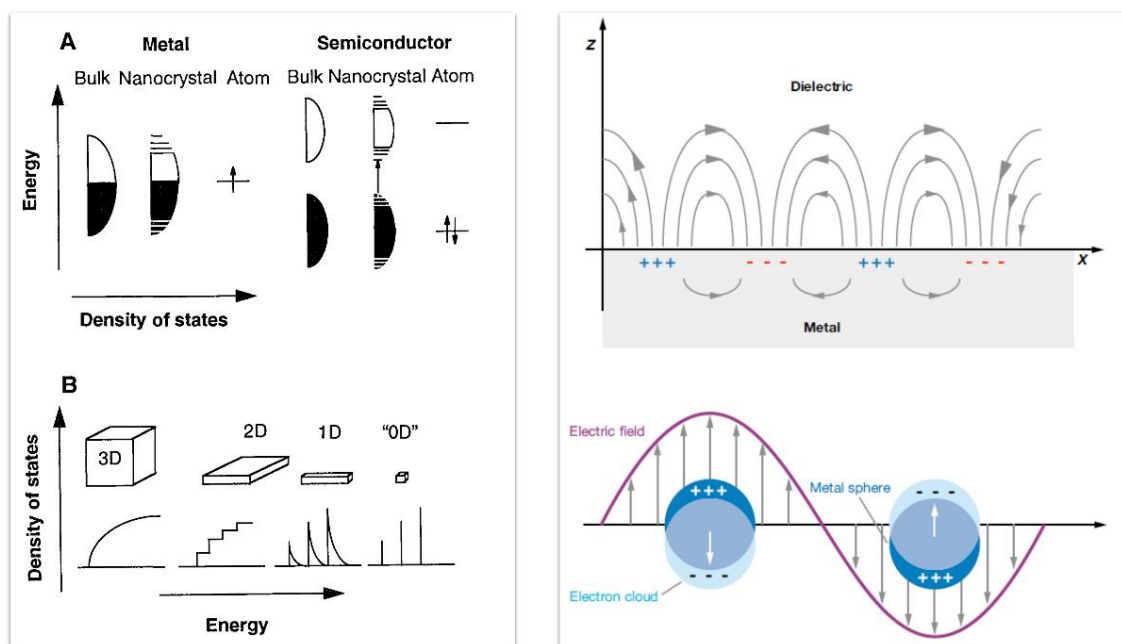


Figure 0.16 Bandgap structure of semiconductor nanoparticles (left) and localized surface plasmon resonance of noble metal nanoparticles (right).⁴⁶⁻⁴⁸

Two major classes of colloidal nanoparticles are transition metal-based semiconducting nanoparticles (CdSe, PbS, InP, etc. usually referred as quantum dots)^{46, 49-53} and noble metal-based plasmonic nanoparticles (Au, Ag, Cu, etc.).^{47-48, 52-54} Semiconductor nanoparticles have highly tunable, size-dependent band gap structures (Figure 0.16) generating tunable photoluminescence covering a broad range of the spectrum. Noble metal nanoparticles have tunable, size- and shape-dependent localized surface plasmon resonances (LSPR) (Figure 0.16) also spanning from UV to NIR region. In either case, the development of synthesis strategies enables the scientists to create a plethora of nanoparticles of various sizes, shapes, and assemblies, and these nanoparticles have been tailored to fit for myriad applications such as manufacturing, biomedicine, energy, environment, and catalysis, etc.^{34, 39, 47, 55-63}

0.5 Colloidal Lanthanide Nanoparticles

0.5.1 Why Colloidal Lanthanide Nanoparticles

The semiconductor- and noble metal-based nanoparticles have received considerable research interest and significantly contributed to different research topics, particularly light manipulation and photon management. However, the size- and shape-dependent optical properties can also be a double-edged sword because it might bring new challenges in practical applications. For example, significantly different sizes (2-10 nm) must be precisely controlled to obtain photoluminescence at different wavelengths, and it is difficult to collectively process nanoparticles with different sizes. Also, the susceptibility to surface oxidation in some nanoparticles such as PbS or Ag might alter their optical properties. Therefore, there is a demand to develop new toolsets that manipulate light in various ways but are insensitive to the physiochemical parameters such as sizes, shapes, and chemical environment. As stated above, lanthanides are such a class of materials, and lanthanide-based nanoparticles can be the new toolset that fulfills the requirements.^{1, 12, 64-65} On the other hand, with the versatility of lanthanide in modern industry and the development of nanoscience, it is natural to consider narrowing down the sizes of lanthanide bulk materials to the nanoscale and discovering new properties. The research on colloidal lanthanide nanoparticles is relatively new, and it has only been popular in the past ten to fifteen years.

One of the most heavily studied properties of lanthanide-based nanoparticles is upconversion (UC) (Figure 0.11), one type of anti-Stokes emission that usually refers to converting low energy photons to high energy photons under sequential instead of simultaneous absorption of multiple photons.^{1, 12} UC processes are a missing piece of the photoluminescence research and are a powerful platform to benefit studies from bioimaging to anticounterfeiting and solar energy

conversion.^{64, 66-69} UC processes are possible and most convenient in lanthanide-based materials because of the unique properties of lanthanides discussed above, such as multiple ladder-like energy levels, insensitivity to chemical environment, and long lifetime at the intermediate energy levels. The research interest in UC has been steadily growing when nanoscale lanthanide materials, i.e. lanthanide nanoparticles emerged because nanoparticulate form enables the precise control and tuning of different dopants and make studying interactions of lanthanide ions more convenient.

0.5.2 Basics of Colloidal Lanthanide Nanoparticles

There are several fundamental properties pertinent to all lanthanide nanoparticles that need to be touched on before the discussion goes into detail.

(1). Lanthanide nanoparticles are usually composed of a host matrix that are optically inert ions such as Sc^{3+} , Y^{3+} , La^{3+} , Gd^{3+} , and Lu^{3+} and optically active dopants of different doping concentration.¹²

(2). There are two major types of optically active dopants involved in the photoluminescence—sensitizers and activators. Sensitizers such as Nd^{3+} and Yb^{3+} , have relatively higher absorption cross-sections. Activators such as Eu^{3+} , Tb^{3+} , Ho^{3+} , Er^{3+} , Tm^{3+} have well-spaced energy levels that are suitable for sequential photon absorption. A sensitizer-activator pair could benefit from both and generate bright photoluminescence especially when their energy levels are matched.⁷⁰

(3). One of the most frequently used host matrix for lanthanide doping and luminescence is sodium yttrium tetrafluoride (NaYF_4) because of their relatively low phonon energy and low non-radiative energy loss.¹² There are two different crystalline phases for NaYF_4 , cubic (α) and hexagonal (β), and hexagonal phase promotes the lanthanide luminescence efficiency more than

the cubic phase with the same doping condition.⁷¹⁻⁷² This is because hexagonal phase NaYF₄ is a more asymmetric host and symmetry breaking enhances the parity-forbidden intra-4f transitions in the lanthanide dopants.

(4). In lanthanide colloidal nanoparticles, the epitaxial growth behavior can be controlled much more precisely and conveniently, generating core-shell nanoparticles or multilayer heteroepitaxial nanoparticles with distinctly defined structures with different dopants.⁷³ This makes lanthanide nanoparticles a much more versatile platform to investigate the fundamental photophysical processes and interactions between different lanthanide ions, which is challenging for lanthanide bulk materials.

0.5.3 Synthesis of Colloidal Lanthanide Nanoparticles

Prior to lanthanide nanoparticles, colloidal nanoparticles based on other materials have been designed and fabricated through many different strategies. One of the most well-developed, versatile, and reliable approaches is the thermal decomposition method, and it was proposed by Hyeon et al. in 2004.⁷⁴ In this approach, the metal precursors are mixed with high-boiling point solvent such as 1-octadecane, oleic acid, and oleylamine, etc., heated to high temperature (~300 °C) to generate colloidal nanoparticles under supersaturation conditions.⁷⁵⁻⁷⁹ This method was later adopted to synthesize lanthanide-based nanoparticles using lanthanide trifluoroacetate, acetate or chloride as the metal precursors, and have enabled a broad family of lanthanide-based nanoparticles with various lanthanide dopants.⁸⁰⁻⁸²

In 2006, Yan et al. systematically investigated the growth behavior of both cubic and hexagonal phase sodium lanthanide tetrafluoride (NaLnF₄, Ln = La to Lu) nanoparticles, which was the first comprehensive “synthesis tutorial” in the field.⁸³ Using a combination of different

metal precursors ($\text{Ln}(\text{CF}_3\text{COO})_3$ and $\text{Na}(\text{CF}_3\text{COO})$), coordinating solvent/ligands, reaction temperature, and reaction time, they demonstrated how different phases of nanoparticles formed and progressed by overcoming multiple energy barriers in the solution (Figure 0.17). It was revealed that the light lanthanides (Nd, Pr, etc.) tended to directly form as hexagonal phase while the heavy lanthanides (Y, Er, Tm, Yb, etc.) firstly form as cubic phase and transform to hexagonal phase with prolonged heating.⁸⁴⁻⁸⁵ This work provides an insightful yet general overview of NaLnF_4 nanoparticles with dopants across the whole lanthanide series, and it is of fundamental importance to all the synthesis work done in this thesis.

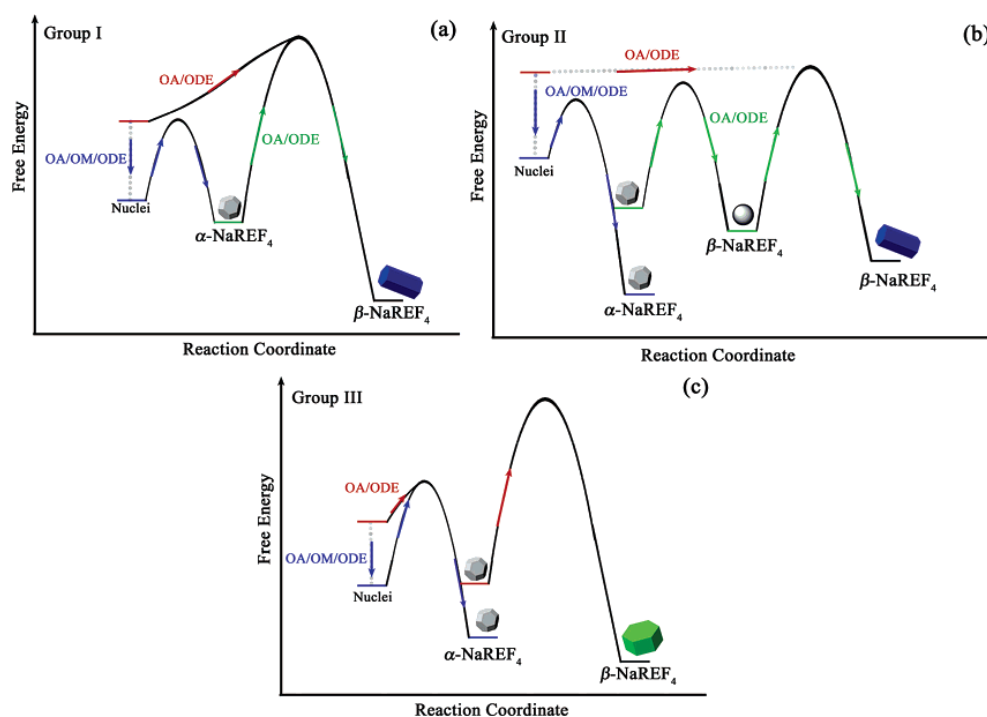


Figure 0.17 Schematic illustration of the free energy for the controlled synthesis of NaLnF_4 nanocrystals (I: Pr and Nd; II: Sm to Tb; III: Dy to Lu, Y).⁸³

In 2008, Zhang et al. developed an efficient strategy to synthesize NaYF_4 nanoparticles doped with various combination of sensitizers and activators, and significantly improved the yield of the hexagonal phase products.⁸⁶ Different from the commonly used $\text{Ln}(\text{CF}_3\text{COO})_3$ and

Na(CF₃COO), they used LnCl₃, NaOH, and NH₄F with well-matched stoichiometry (Figure 0.18), which greatly simplified the synthesis process and made the reaction more user-friendly because there were no more excess toxic fluorides at high temperatures. This strategy had received great attention, quickly became the mainstream synthesis protocol for lanthanide nanoparticles, and is the major synthesis method used in this thesis.

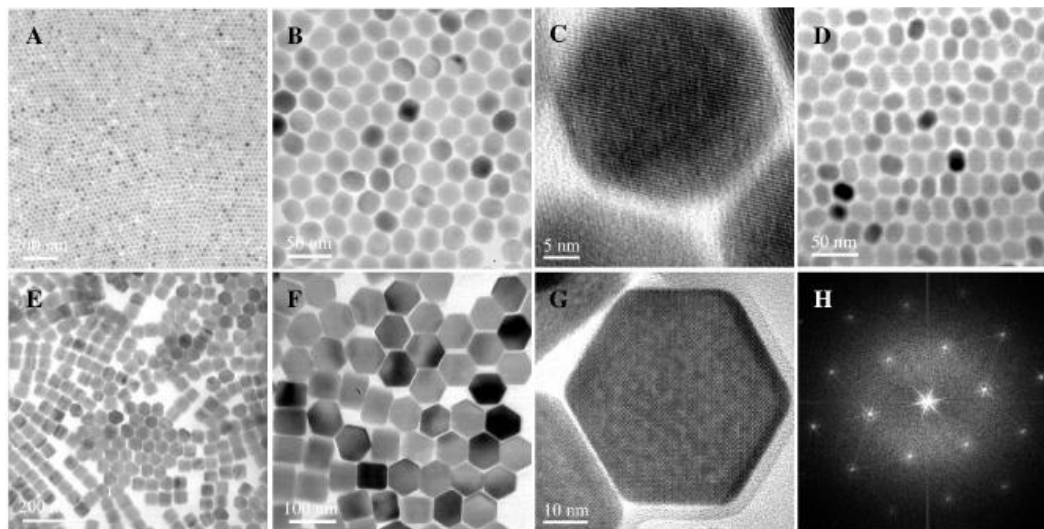


Figure 0.18 TEM images of NaYF₄:Yb, Er nanospheres ((A)–(C), at different magnifications), nanoellipses (D), and nanoplates ((E)–(G), at different magnifications) and Fourier transform of the TEM image in G (H).⁸⁶

In 2010, Liu et al. discovered the doping-dependent size and phase transformation for NaLnF₄ nanoparticles, which is one of most critical discovery in modern colloidal lanthanide nanoparticles.⁷² They showed that lanthanide ions with smaller atomic number have larger ionic radii and larger polarizability, favoring the formation of symmetry-breaking hexagonal phase NaLnF₄ nanoparticles (Figure 0.19). While the nanoparticles majorly composed of heavier lanthanides prefer the cubic phases, they can be readily transformed to hexagonal phases with 10–20% doping of lighter lanthanide ions in the nanoparticle matrix.

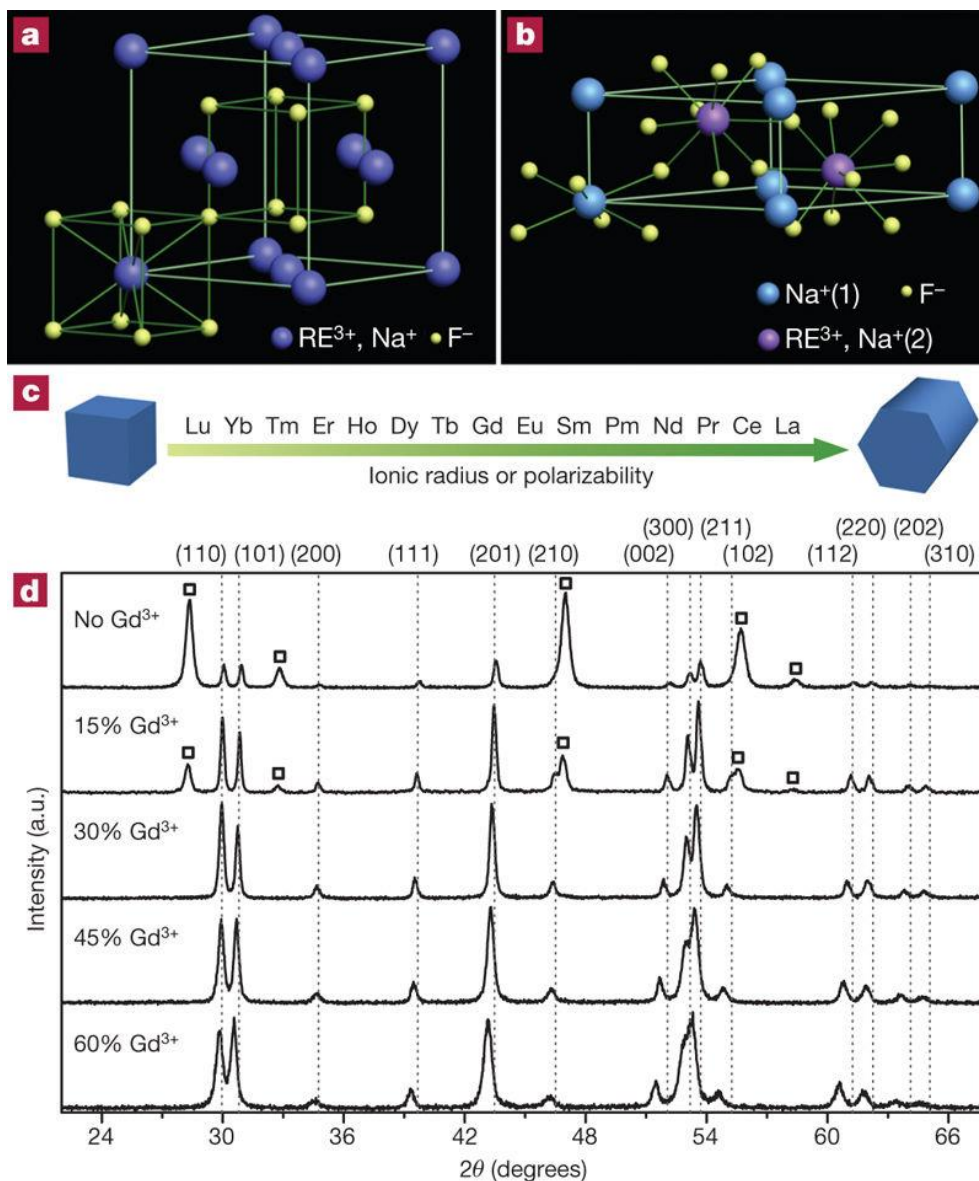


Figure 0.19 (a, b) Schematic presentation of cubic- and hexagonal-phase NaLnF₄ structures, respectively (RE, rare earth). In the hexagonal phase, an ordered array of F ions offers two types of cation sites (asymmetric): one occupied by Na⁺ and the other occupied randomly by Ln³⁺ and Na⁺. (c). General trend of phase transition from cubic to hexagonal as a function of ionic radius (or polarizability) of the lanthanide dopant ions. (d). X-ray powder diffraction patterns of the NaYF₄:Yb/Er (18/2 mol%) nanocrystals obtained in the presence of 0, 15, 30, 45 and 60 mol% Gd³⁺ dopant ions, respectively. Diffraction peaks corresponding to cubic NaYF₄ are marked with square boxes. A gradual decrease in diffraction peak intensities for cubic phase is observed as a function of increased Gd³⁺ dopant content.⁷²

With this strategy, the synthesis condition is much less stringent, and the hexagonal phases of lanthanide nanoparticles across the whole series can be easily synthesized with almost the same

synthesis parameters. This work laid the foundation for all the discussion about doping in this thesis.

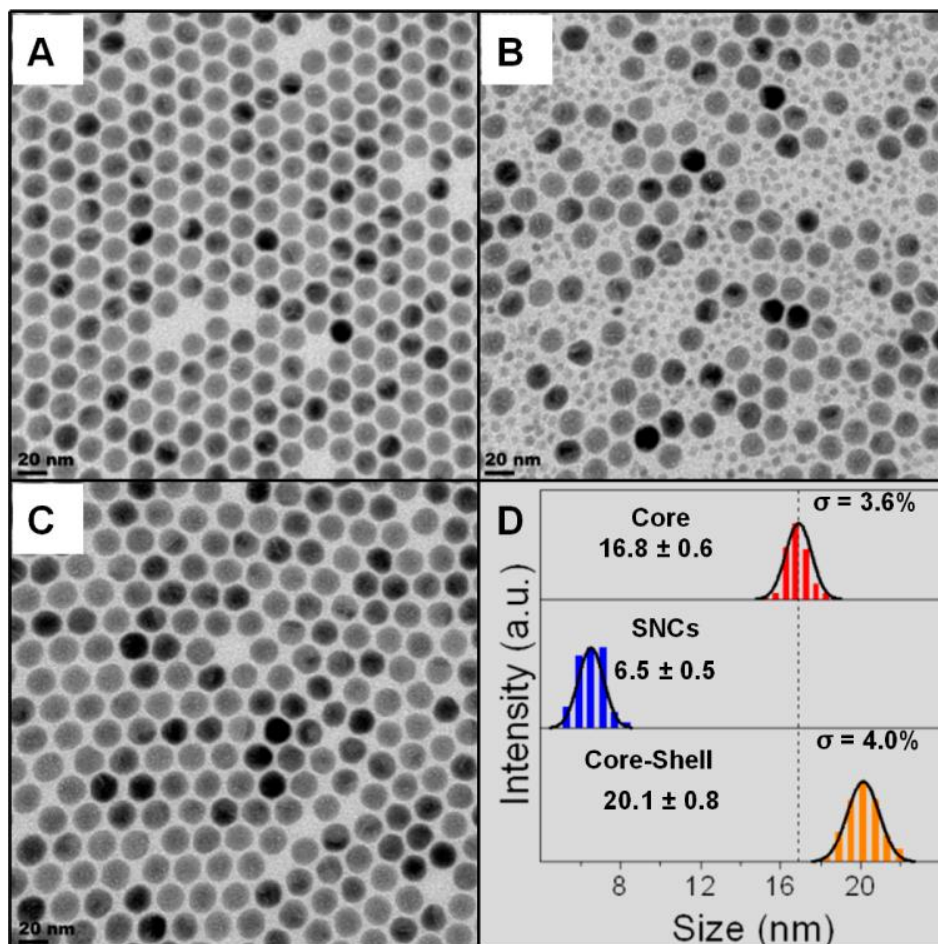


Figure 0.20 (A–C) TEM of NaYF₄:Yb³⁺/Er³⁺ (15/2%) core NCs, 15 s after injection of sacrificial α -NaYF₄ NCs and after 10 min self-focusing NaYF₄:Yb³⁺/Er³⁺ (15/2%) core-shell NCs, respectively, and (D) size distribution of the NCs.⁸⁷

In 2012, van Veggel et al. proposed a strategy to synthesize lanthanide nanoparticles with well-defined core-shell architectures using Ostwald ripening-based self-focusing (Figure 0.20).⁸⁷ Ostwald ripening is the “coalescence” of nanoparticles, typically as the growth of bigger nanoparticles (smaller surface-to-volume ratio and lower energy) at the expense of smaller nanoparticles (larger surface-to-volume ratio and higher energy) to lower the overall energy of the entire system. Ostwald ripening is a common phenomenon for various types of colloidal

systems,⁸⁸⁻⁸⁹ but it has not been deliberately used as a strategy to grow nanoparticles until this particular work. In this work, the hexagonal nanoparticles were first synthesized as the thermodynamically stable cores with sizes of 16 nm, and cubic phase kinetically stable nanoparticles with sizes of 6.5 nm dispersed in volatile solvents (hexane) were rapidly injected into the reaction solution at high temperature. Upon mixing, the cubic phase nanoparticles were dissolved and deposited onto the hexagonal phase cores to form core-shell structures with sizes of 20 nm because the cubic phase nanoparticles are less stable. This work is the major reference for all the epitaxial work (core-shell, multilayer structures) done in this thesis.

0.5.4 Characterization of Colloidal Lanthanide Nanoparticles

Due to the small sizes and large surface-to-volume ratios of colloidal lanthanide nanoparticles, the effect of surface on the photoluminescence of lanthanide-based nanoparticles are much more prominent. Colloidal lanthanide nanoparticles have much weaker luminescence than their bulk counterpart because of the possible presence of more surface defects and easy accessibility of quenchers in the surrounding of nanoparticles to the excited states. This is one of the most daunting challenges in research field after the focus of lanthanides has been shifted to the nanoscale. Liu et al. investigated the size-dependent optical properties of sensitizer and activator co-doped core nanoparticles and show that the luminescence intensity decreases proportionally to the size reduction from 25 nm to 10 nm (Figure 0.21).⁹⁰ When the core nanoparticles were coated with epitaxial shells at the same thickness, all groups of core-shell nanoparticles had increased luminescence intensity. Notably, the enhancement factor after epitaxial shell growth in the smallest nanoparticles was the highest, which indicates that the shells contribute most to the mostly quenched small nanoparticles. This work demonstrates the direct evidence of size-dependent

optical properties for both core and core-shell nanoparticles, and is the foundation to most of the discussion about core-shell structures in this thesis.

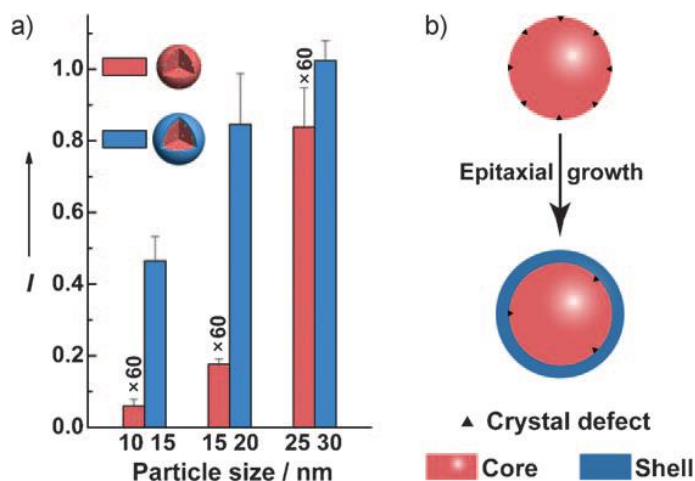


Figure 0.21 The effect of epitaxial shell in enhancing the luminescence of lanthanide-doped nanoparticles with different sizes.⁹⁰

With the understanding of surface-dependent luminescence quenching, there is another issue associated with quenching and doping in the lanthanide-doped nanoparticles. Doping inevitably increases the cross-relaxation of excitation energy between neighboring ions and also possibly drains the excitation energy to the surface defects. In either way, the luminescence intensity drops significantly with the increasing doping concentration and it is referred as concentration quenching. It has been generally accepted that the doping concentration of activators (Ho^{3+} , Er^{3+} , Tm^{3+} , etc.) in most of the lanthanide-based nanoparticles should be kept below 5% to maintain bright emission.^{1, 19, 27, 65-70, 91-93} Schuck et al. investigated the luminescence as a function of the doping concentration of activators (Er^{3+}) and the excitation power density at 980 nm laser (Figure 0.22).⁹⁴ They found that the nanoparticles with 20% activators doping were dimmer than that with 2% doping at low excitation power density (several W/cm^2), but the former ones were much brighter than the latter ones at significantly elevated power density ($10^6 \text{ W}/\text{cm}^2$). This

suggests that the concentration quenching can be alleviated with increased irradiance and the limit of 5% doping can be overcome.

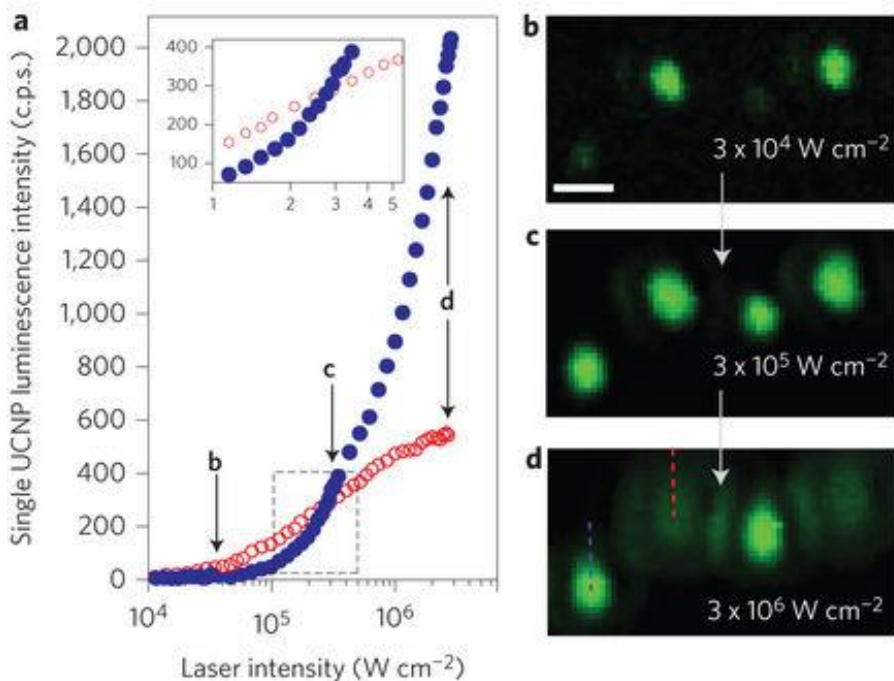


Figure 0.22 (a) Luminescence intensity of single 8 nm nanoparticles with 20% (blue) and 2% (red) Er^{3+} , each with 20% Yb^{3+} , plotted as a function of excitation intensity. Inset: zoom-in regions. (b-d) Confocal luminescence images taken at points shown in (a) of single nanoparticles of 20% (blue) and 2% (red) Er^{3+} .⁹⁴

Even if the surface quenching and concentration quenching effect is excluded, the luminescence in lanthanide-doped nanoparticles is still an extremely inefficient process because it is parity-forbidden. This results in very weak luminescence intensity and significantly limits the use of lanthanide-doped nanoparticles for practical applications although there are plentiful unique useful features for these nanoparticles. Different strategies have been devised to enhance the luminescence intensity and a natural thought process is to enhance the emission by designing the nanoparticles that can absorb more incident light. In 2009, Capobianco et al. proposed a strategy called “active-core/active-shell” to enhance the luminescence intensity of the lanthanide-doped

nanoparticles where they doped certain amount of extra sensitizers (Yb^{3+}) in the shell of core-shell nanoparticles, adding extra absorption of incident light to the $\text{Yb}^{3+}/\text{Er}^{3+}$ co-doped core nanoparticles (Figure 0.23).⁹⁵ This work stimulates many relevant research because it showed that different lanthanide dopants can be separately positioned into different layers of multilayer nanoparticles and contribute to the optical transitions.

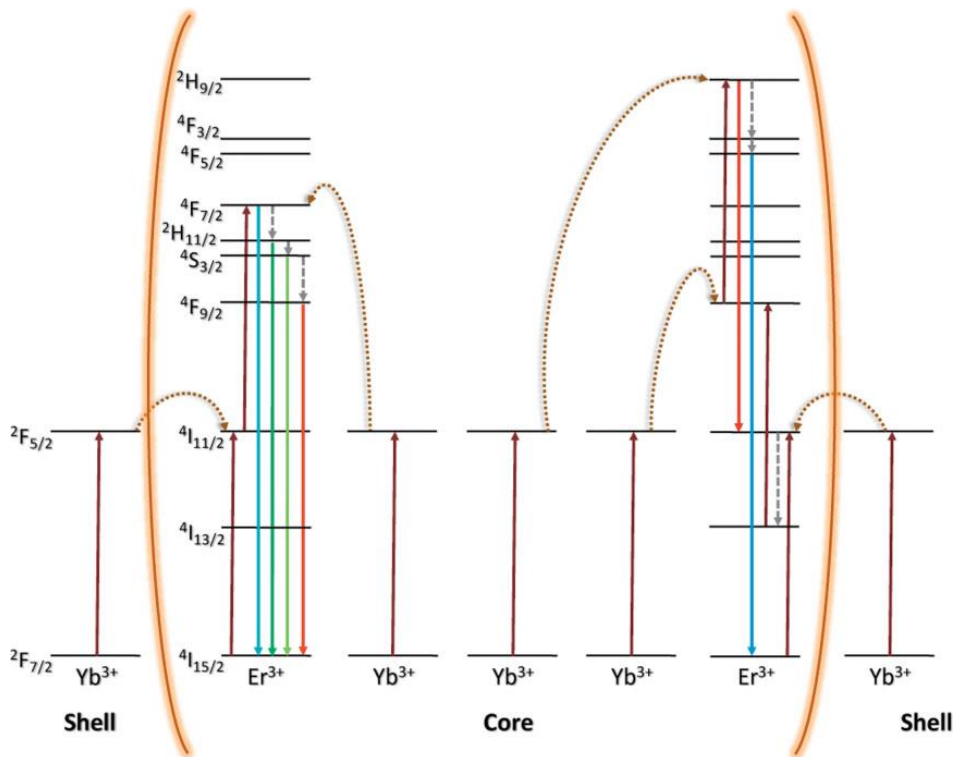


Figure 0.23 Schematic illustrations of the simplified energy levels in the active-core/active-shell approach where more incident photons are absorbed through the sensitizers in the shell.⁹⁵

With more control over the core-shell nanoparticle design, dopants rather than the routinely used Yb^{3+} have also been incorporated into the shell layer of the core-shell structures to tailor the optical properties. Nd^{3+} is one of the mostly studied dopants in the shell in recent years rather than Yb^{3+} because of two interesting features. First, Nd^{3+} has a high absorption peak centered at 808 nm, and 808 nm is a better candidate than the commonly used 980 nm for biological applications because 808 nm is attenuated much less than 980 nm by water. Second, the absorption cross-

section of Nd^{3+} at 808 nm is about ten times higher than that of Yb^{3+} at 980 nm possibly leading to brighter luminescence. Yan et al. studied doping of 10% Nd^{3+} in the shell and showed that the core-shell nanoparticles can be facily excited at 808 nm with much less heating induced by the laser irradiation (Figure 0.24).⁹⁶ This makes lanthanide-doped nanoparticles more relevant for biological/biomedical applications.⁹⁷⁻⁹⁹

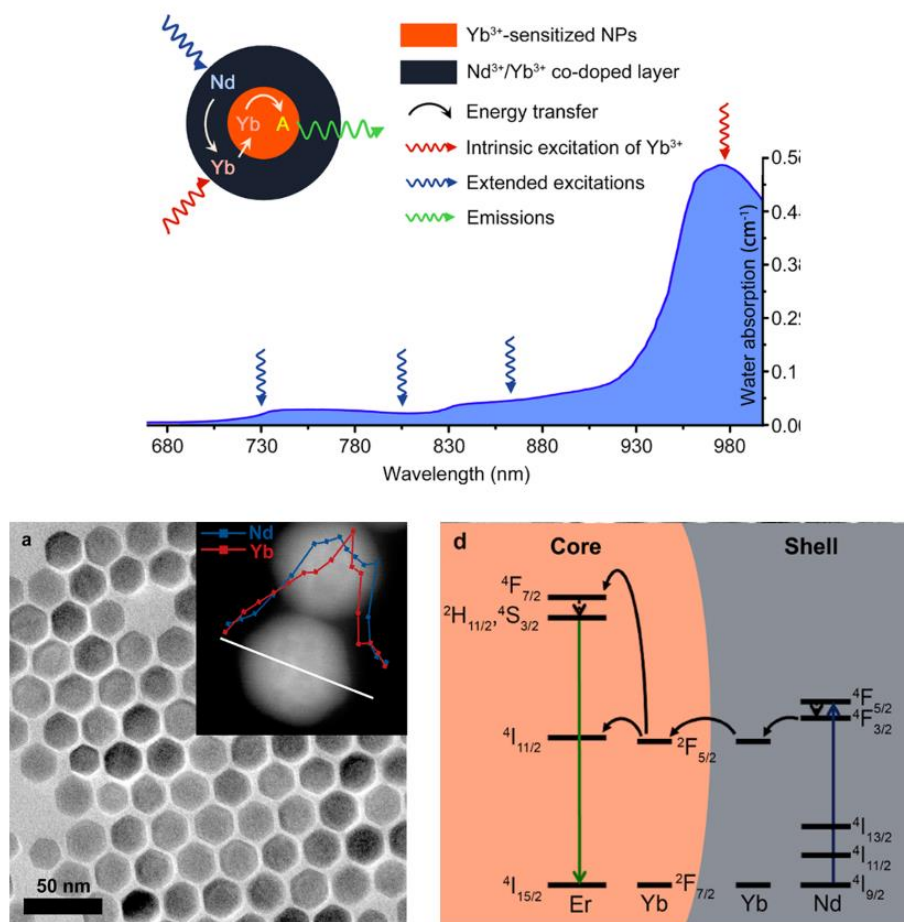


Figure 0.24 Comparison of water absorption at 980 nm and 808 nm. TEM image and the simplified energy level diagrams of the Nd^{3+} -doped nanoparticles.⁹⁶

0.5.5 Applications of Colloidal Lanthanide Nanoparticles

Because of the versatile yet easily tunable optical properties, lanthanide-doped nanoparticles have been attractive for many optics-related studies and applications where photons

need to be properly “managed”.^{67, 91, 100} For example, photon management is critical to biomedical applications such as photoluminescence imaging and photodynamic therapy while central to solar light harvesting in energy applications. Some of these applications can be completed with lanthanide bulk materials but could be improved with the nanoscale counterpart, while some of them can only be done with the judiciously designed colloidal lanthanide nanoparticles.

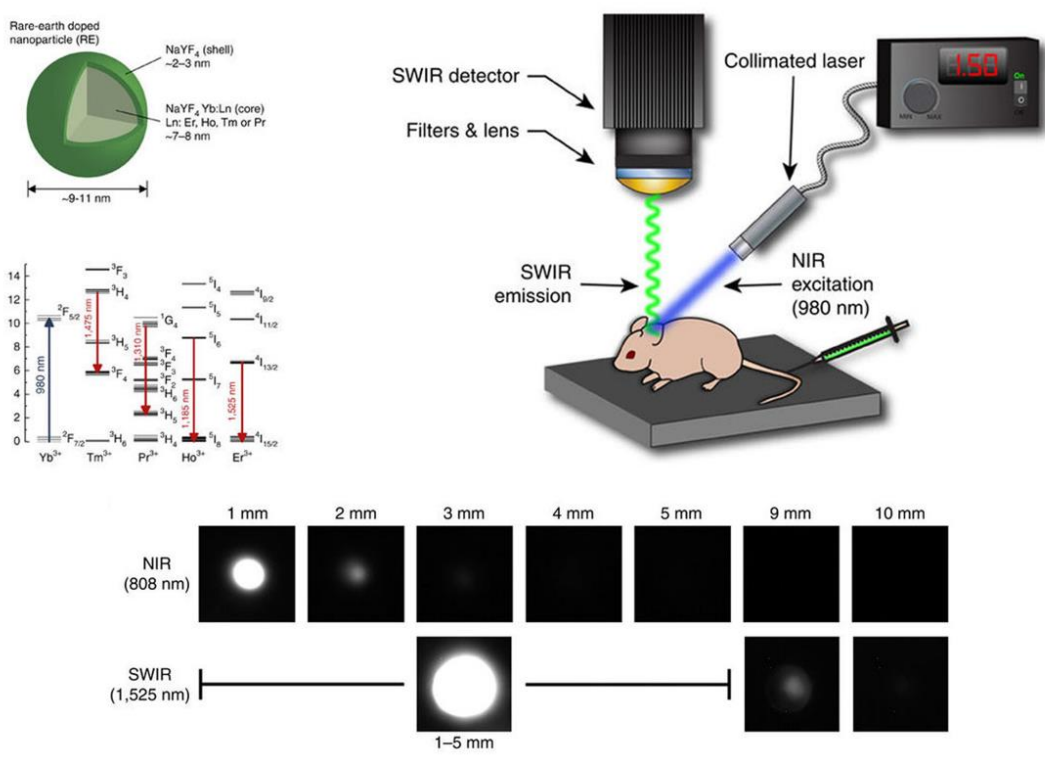


Figure 0.25 Schematic illustration of the lanthanide-doped nanoparticles and their energy levels emphasizing the emission > 1000 nm, falling into the biological imaging window (upper left). Setup for imaging of living mice using lanthanide-doped nanoparticles as the optical probe (upper right). Comparison of attenuation of different wavelength through the phantom tissues with different thickness (lower panel).¹⁰¹

Scattering and attenuation of light through tissue is a major challenge in bioimaging towards obtaining high-resolution and high contrast biomedical images carrying precise information. This issue can be mitigated by using light with longer wavelength, mainly wavelengths longer than 800 nm, and it is referred as NIR biological window for bioimaging.¹⁰²⁻

¹¹² However, it is not easy to design materials that can be excited and emit in the biological window. Lanthanides-doped nanoparticles, with the ladder-like energy levels, provide possibility for putting both the excitation and emission wavelength in the biological imaging window.¹¹⁰ Particularly, Yb³⁺/Er³⁺ co-doped nanoparticles can be excited at 980 nm and emit at 1525 nm, and they were used as biological imaging probes to generate images in vivo with high contrast and high resolution (Figure 0.25).^{101, 113-115} The images obtained from this longer wavelength had much better quality than those from the shorter 808 nm emission, and it also enabled the imaging through several millimeters of phantom tissue.

Another typical example showing the potential of photon management using lanthanide-doped nanoparticles is photodynamic therapy (PDT). PDT is a powerful platform to treat various diseases (especially multidrug resistant diseases) using the highly oxidative singlet oxygen generated from photosensitizers via light irradiation.¹¹⁶⁻¹¹⁷ Photosensitizers are usually excited by visible light and the visible excitation light has very limited penetration depth through tissues, making PDT incompetent in treating diseases deep beneath the skin. Lanthanide-doped nanoparticles converts NIR light with deep tissue penetration depth to visible light and makes the photosensitizers indirectly activatable by NIR light, making it possible using PDT to treat diseases deep beneath the skin.¹¹⁸⁻¹²² Zhang et al. developed a NIR-light-activated PDT system using mesoporous silica coated Yb³⁺/Er³⁺ co-doped nanoparticles and incorporated photosensitizers zinc phthalocyanine (ZnPc) into the silica (Figure 0.26).¹²¹ In their system, the nanoparticles/silica/ZnPc composites can be excited by 980 nm NIR light and generate singlet oxygen in vivo to kill the cancer cells in living mice.

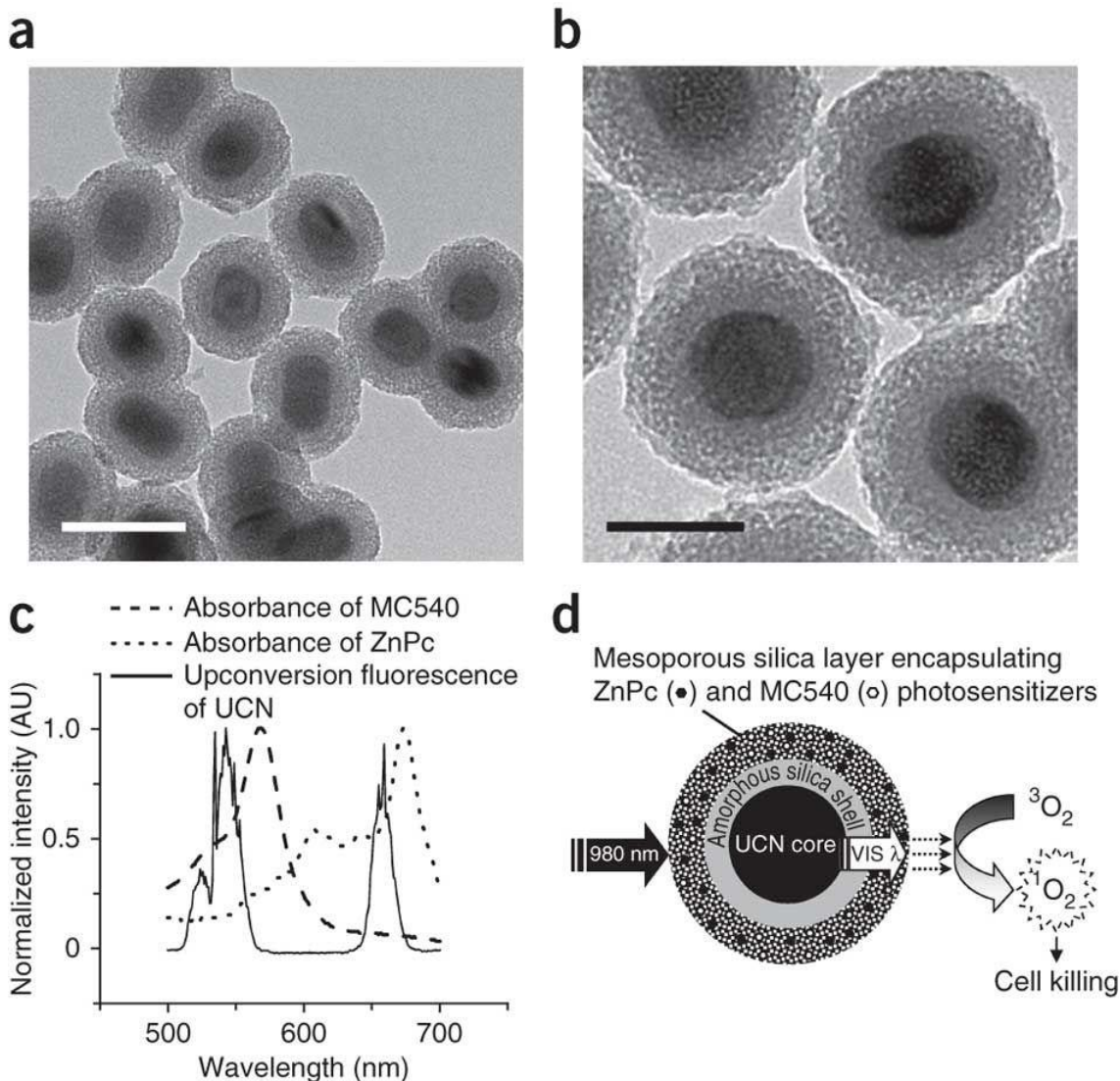


Figure 0.26 (a,b). TEM images of the mesoporous silica-coated lanthanide-doped nanoparticles. (c). Luminescence spectra of nanoparticles under 980 nm excitation and the absorption spectra of ZnPc. (d). Schematic illustration of mesoporous-silica-coated, ZnPc-incorporated system generating singlet oxygen under 980 nm excitation.¹²¹

The solar cell is another research area where photon management is the central topic. Solar cells with a band gap can only collect photons with energy higher than the band gap and convert the photons to electric energy that can be stored.¹²³⁻¹²⁹ One of most studied solar cell system is based on crystalline silicon and it has a band gap of 1.12 eV (~1107 nm).¹³⁰ Therefore, photons with wavelengths longer than 1107 nm cannot be absorbed by the solar cell and do not contribute

to the photocurrent generation. However, there is a significant portion of photons in the solar spectrum that are beyond the 1.12 eV limit, and it is believed that the efficiency for the solar cells can be dramatically improved if these photons can be harvested. Lanthanide-doped nanoparticles absorb multiple low energy photons and emit high energy photons, and it can contribute to sub-band-gap photon harvesting when the upconverted emission is above the bandgap of the crystalline silicon solar cells.^{64, 131-140}

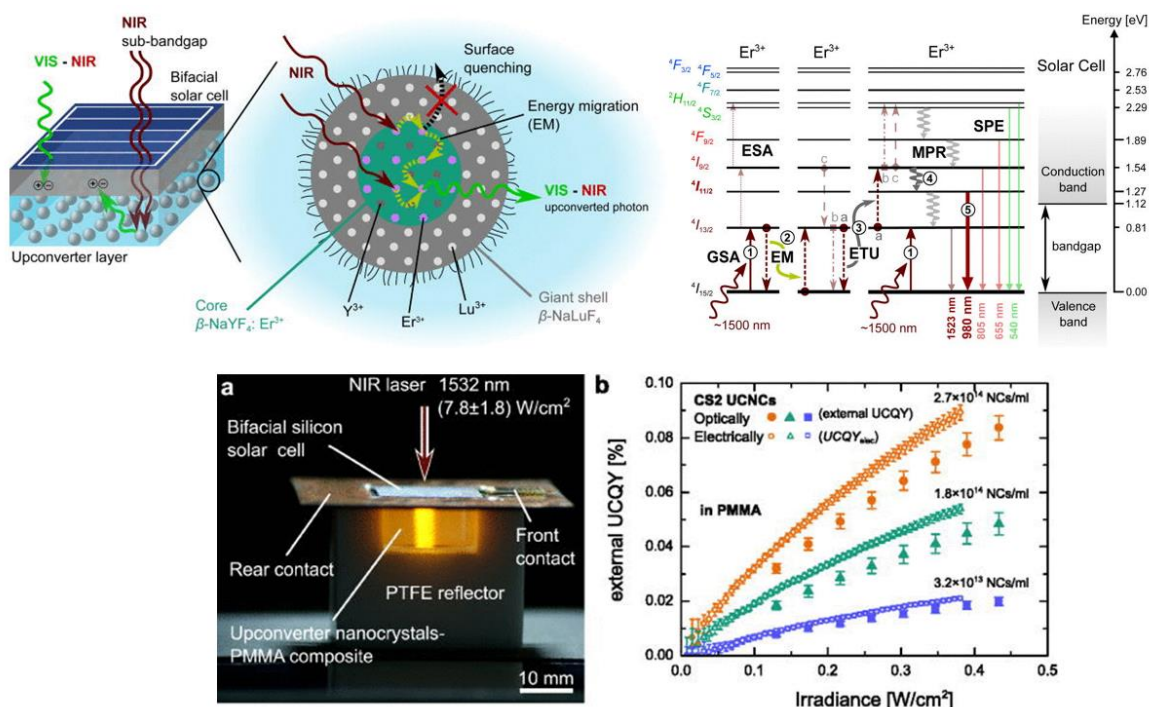


Figure 0.27 Schematic illustration of the improved bifacial solar cells with the upconverting contributions from the Er^{3+} -doped lanthanides. The Er^{3+} ions absorb the ~ 1500 nm photons in the solar spectrum that cannot be utilized in conventional solar cells and upconvert them into 980 nm photons that are above the 1.12 eV band gap.¹⁴¹

Fischer et al. designed Er^{3+} -doped core-shell nanoparticles and incorporated them with the conventional bifacial solar cells to improve the optical response of the whole system (Figure 0.27).¹⁴¹ In the core-shell nanoparticle, Er^{3+} dopants absorb two ~ 1500 nm photons (below the

band gap) and upconvert them into one 980 nm photon (above the band gap) that can be taken by the silicon solar cells.

0.6 Major Challenges in the Field

With all the synthesis, characterization, and applications shown above for lanthanide-doped nanoparticles, the major challenges still lies in the precise control of the nanoparticles with well-defined structures in the colloidal synthesis and understanding of the photophysical processes taking place between different dopants. Several representative challenges are listed as follows:

(1). Uniform, concentric, and quasi-isotropic lanthanide-doped core-shell nanoparticles. Uniform epitaxial shells on top of the core nanoparticles are important in tuning the optical properties of core-shell nanoparticles and irregular shell structures increase the complexity and unpredictability of the system. The well-confined excitation energy could be drained easily to surface quenchers through the thinner part in the irregular shell structures.

(2). Surface quenching. Surface quenching persists for all nanoparticles that emit light and is particularly relevant for lanthanide-doped nanoparticles because there are multiple metastable intermediate energy levels that are susceptible to surface quenching. Reducing surface quenching makes it dramatically easier putting lanthanide-doped nanoparticles in applications.

(4). Concentration quenching. Overcoming concentration quenching has been the Holy Grail in research about lanthanide-doped nanoparticles for long. Examples shown in the previous section described strategies to overcome this limitation, but it is heavily relied on pulsing laser with extremely high irradiation, which is unpractical for many scenarios. It is quietly demanding to develop certain approaches that make the heavily doped nanoparticles emit with low power excitation.

(3). Sensitization. Sensitization is often considered to be inevitable because lanthanide optical transitions are intrinsically weak. Sensitization limits the choice of excitation wavelengths and many more applications are expected if the lanthanide-doped nanoparticles can be excited with more available wavelengths.

0.7 Scope of this thesis

In this thesis, with the understanding of the state-of-the-art work and major challenges in the field, I will tailor the colloidal synthesis of lanthanide-doped nanoparticles, investigate how they grow in solution, and develop robust approaches to synthesize nanoparticles with uniform, concentric, and isotropic structures. With the synthesized nanoparticles, I study the optical tuning of various parameters including excitation, emission, sensitization, and relaxation, and understand how they collectively influence the optical output of the nanoparticles. With the controlled structures and optical properties, I showcase several examples how lanthanide-doped nanoparticles can be a powerful multifunctional platform in managing photons, benefiting a broad spectrum of applications.

Chapter 1 reveals the interdependence of surface and concentrating quenching dynamics in lanthanide-doped nanoparticles. We show that the major quenching mechanism for nanoparticles with high doping levels is the energy migration to surface defects, as opposed to the commonly accepted cross-relaxation between neighboring dopants. With an inert epitaxial shell growth onto the core nanoparticles, erbium (Er^{3+}) concentrations as high as 100 mol% in $\text{NaY}(\text{Er})\text{F}_4/\text{NaLuF}_4$ core/shell nanocrystals enhance the emission intensity of both upconversion and downshifted luminescence across different excitation wavelengths (980, 800, and 658 nm), with negligible concentration quenching effects.

Chapter 2 analyzes the critical effect of the doped epitaxial shells in enhancing the upconversion luminescence in one of the most widely studied system—Yb³⁺/Er³⁺ co-doped β -NaYF₄ nanoparticles. We show that doping (usually sensitizers) in the shell has two opposing effect—absorbing more incident light and draining more excitation energy to the surface sites, and the latter one overwhelms the former one. Therefore, the core nanoparticles coated with the inert epitaxial shell have the highest emission intensity and luminescence quantum yield, and the both emission intensity and quantum yield monotonously drops with the increasing doping level in the shell.

Chapter 3 develops a photocatalysis/photodynamic therapy platform by engineering the spectral feature of the upconversion nanoparticles. The nanoparticles can be excited by the biobeneign 808 nm laser at extremely low irradiance, and emit visible red light centered at 654 nm that further activates the highly efficient photosensitizers ZnPc. Two major challenges associated with the optical features in previous such platforms, excitation at 980 nm and emission at 540 nm are simultaneously addressed by using this new class of nanoparticles. We show that with our platform singlet oxygen can be effectively generated to rapidly kill cancer cells and dissociate solid cell spheroids.

Chapter 4 develops a class of multimodal imaging contrast agents that work for optical imaging, magnetic resonance imaging, and computed tomography with high performance. The contrast agents are composed of three distinct layers with three different functional lanthanide ions in a heteroepitaxial nanoparticle. Importantly, the optical emission, MRI relaxivity, and CT contrast are simultaneously enhanced by tuning the interfacial layer thickness in the heteroepitaxial structure, overcoming the conundrum that putting two imaging functions on the single entity often compromises the overall performance.

Chapter 5 introduces a surface-engineering strategy to enhance the MRI contrast remarkably approaching the known theoretical limit. Using monodispersed and ultrasmall NaGdF₄ nanoparticles and dual-solvent exchange-induced micellization, we demonstrate that the modified nanoparticles can be steadily dispersed in water, individually encapsulated, and does not coagulate. These features enhance the interaction between Gd³⁺ magnetic centers and the surrounding water protons and we obtain a MRI relaxivity as high as ~80 mM⁻¹s⁻¹.

Chapter of introduction, is unpublished work. Sha He and Adah Almutairi. The dissertation author was the primary investigator and author of this material.

0.8 References

1. Auzel, F., Upconversion and anti-stokes processes with f and d ions in solids. *Chem. Rev.* **2004**, *104*, 139-173.
2. Eliseeva, S. V.; Bunzli, J. C. G., Rare earths: jewels for functional materials of the future. *New J. Chem.* **2011**, *35*, 1165-1176.
3. Bunzli, J. C. G., Benefiting from the unique properties of lanthanide ions. *Accounts Chem. Res.* **2006**, *39*, 53-61.
4. de Sa, G. F.; Malta, O. L.; Donega, C. D.; Simas, A. M.; Longo, R. L.; Santa-Cruz, P. A.; da Silva, E. F., Spectroscopic properties and design of highly luminescent lanthanide coordination complexes. *Coord. Chem. Rev.* **2000**, *196*, 165-195.
5. Dorenbos, P., The 5d level positions of the trivalent lanthanides in inorganic compounds. *J. Lumines.* **2000**, *91*, 155-176.
6. Reid, M. F.; van Pieterse, L.; Wegh, R. T.; Meijerink, A., Spectroscopy and calculations for $4f(N) \rightarrow 4f(N-1)5d$ transitions of lanthanide ions in LiYF_4 . *Phys. Rev. B* **2000**, *62*, 14744-14749.
7. van Pieterse, L.; Reid, M. F.; Burdick, G. W.; Meijerink, A., $4f(n) \rightarrow 4f(n-1)5d$ transitions of the heavy lanthanides: Experiment and theory. *Phys. Rev. B* **2002**, *65*, 13.
8. Qin, X.; Liu, X. W.; Huang, W.; Bettinelli, M.; Liu, X. G., Lanthanide-Activated Phosphors Based on $4f-5d$ Optical Transitions: Theoretical and Experimental Aspects. *Chem. Rev.* **2017**, *117*, 4488-4527.
9. Ogasawara, K.; Watanabe, S.; Toyoshima, H.; Brik, M. G., First-Principles Calculations of $4f(n) \rightarrow 4f(n-1)5d$ Transition Spectra. In *Handbook on the Physics and Chemistry of Rare Earths, Vol 37: Optical Spectroscopy*, Gschneidner, K. A.; Bunzli, J. C. G.; Pecharsky, V. K., Eds. Elsevier Science Bv: Amsterdam, 2007; Vol. 37, pp 1-59.
10. Peijzel, P. S.; Meijerink, A.; Wegh, R. T.; Reid, M. F.; Burdick, G. W., A complete $4f(n)$ energy level diagram for all trivalent lanthanide ions. *J. Solid State Chem.* **2005**, *178*, 448-453.
11. Heine, J.; Muller-Buschbaum, K., Engineering metal-based luminescence in coordination polymers and metal-organic frameworks. *Chem. Soc. Rev.* **2013**, *42*, 9232-9242.
12. Haase, M.; Schafer, H., Upconverting Nanoparticles. *Angew. Chem.-Int. Edit.* **2011**, *50*, 5808-

5829.

13. Wu, J. W.; Zhang, H. B.; Du, S. W., Tunable luminescence and white light emission of mixed lanthanide-organic frameworks based on polycarboxylate ligands. *J. Mater. Chem. C* **2016**, *4*, 3364-3374.
14. Zaleski, C. M.; Depperman, E. C.; Kampf, J. W.; Kirk, M. L.; Pecoraro, V. L., Synthesis, structure, and magnetic properties of a large lanthanide-transition-metal single-molecule magnet. *Angew. Chem.-Int. Edit.* **2004**, *43*, 3912-3914.
15. Woodruff, D. N.; Winpenny, R. E. P.; Layfield, R. A., Lanthanide Single-Molecule Magnets. *Chem. Rev.* **2013**, *113*, 5110-5148.
16. Rinehart, J. D.; Long, J. R., Exploiting single-ion anisotropy in the design of f-element single-molecule magnets. *Chem. Sci.* **2011**, *2*, 2078-2085.
17. Sessoli, R.; Powell, A. K., Strategies towards single molecule magnets based on lanthanide ions. *Coord. Chem. Rev.* **2009**, *253*, 2328-2341.
18. AlDamen, M. A.; Clemente-Juan, J. M.; Coronado, E.; Marti-Gastaldo, C.; Gaita-Arino, A., Mononuclear lanthanide single-molecule magnets based on polyoxometalates. *J. Am. Chem. Soc.* **2008**, *130*, 8874-+.
19. Liu, X. W.; Deng, R. R.; Zhang, Y. H.; Wang, Y.; Chang, H. J.; Huang, L.; Liu, X. G., Probing the nature of upconversion nanocrystals: instrumentation matters. *Chem. Soc. Rev.* **2015**, *44*, 1479-1508.
20. Heffern, M. C.; Matosziuk, L. M.; Meade, T. J., Lanthanide Probes for Bioresponsive Imaging. *Chem. Rev.* **2014**, *114*, 4496-4539.
21. Mahmoudi, M.; Hosseinkhani, H.; Hosseinkhani, M.; Boutry, S.; Simchi, A.; Journeay, W. S.; Subramani, K.; Laurent, S., Magnetic Resonance Imaging Tracking of Stem Cells in Vivo Using Iron Oxide Nanoparticles as a Tool for the Advancement of Clinical Regenerative Medicine. *Chem. Rev.* **2011**, *111*, 253-280.
22. Terreno, E.; Delli Castelli, D.; Viale, A.; Aime, S., Challenges for Molecular Magnetic Resonance Imaging. *Chem. Rev.* **2010**, *110*, 3019-3042.
23. Villaraza, A. J. L.; Bumb, A.; Brechbiel, M. W., Macromolecules, Dendrimers, and Nanomaterials in Magnetic Resonance Imaging: The Interplay between Size, Function, and Pharmacokinetics. *Chem. Rev.* **2010**, *110*, 2921-2959.

24. Viswanathan, S.; Kovacs, Z.; Green, K. N.; Ratnakar, S. J.; Sherry, A. D., Alternatives to Gadolinium-Based Metal Chelates for Magnetic Resonance Imaging. *Chem. Rev.* **2010**, *110*, 2960-3018.
25. Aime, S.; Botta, M.; Fasano, M.; Terreno, E., Lanthanide(III) chelates for NMR biomedical applications. *Chem. Soc. Rev.* **1998**, *27*, 19-29.
26. Bottrill, M.; Nicholas, L. K.; Long, N. J., Lanthanides in magnetic resonance imaging. *Chem. Soc. Rev.* **2006**, *35*, 557-571.
27. Li, X. M.; Zhang, F.; Zhao, D. Y., Lab on upconversion nanoparticles: optical properties and applications engineering via designed nanostructure. *Chem. Soc. Rev.* **2015**, *44*, 1346-1378.
28. <http://www.sciencedirect.com/science/article/pii/S0168127316300216>.
29. <http://www.sciencedirect.com/science/article/pii/S016812731630023X>.
30. https://www.rp-photonics.com/rare_earth_doped_gain_media.html.
31. <http://www.physics-and-radio-electronics.com/physics/laser/ndyaglaser.html>.
32. Niemeyer, C. M., Nanoparticles, proteins, and nucleic acids: Biotechnology meets materials science. *Angew. Chem.-Int. Edit.* **2001**, *40*, 4128-4158.
33. Yin, Y.; Alivisatos, A. P., Colloidal nanocrystal synthesis and the organic-inorganic interface. *Nature* **2005**, *437*, 664-670.
34. Kamat, P. V., Photophysical, photochemical and photocatalytic aspects of metal nanoparticles. *J. Phys. Chem. B* **2002**, *106*, 7729-7744.
35. Kelly, K. L.; Coronado, E.; Zhao, L. L.; Schatz, G. C., The optical properties of metal nanoparticles: The influence of size, shape, and dielectric environment. *J. Phys. Chem. B* **2003**, *107*, 668-677.
36. Link, S.; El-Sayed, M. A., Spectral properties and relaxation dynamics of surface plasmon electronic oscillations in gold and silver nanodots and nanorods. *J. Phys. Chem. B* **1999**, *103*, 8410-8426.
37. Brigger, I.; Dubernet, C.; Couvreur, P., Nanoparticles in cancer therapy and diagnosis. *Adv. Drug Deliv. Rev.* **2002**, *54*, 631-651.

38. Sharma, V. K.; Yngard, R. A.; Lin, Y., Silver nanoparticles: Green synthesis and their antimicrobial activities. *Adv. Colloid Interface Sci.* **2009**, *145*, 83-96.
39. Astruc, D.; Lu, F.; Aranzaes, J. R., Nanoparticles as recyclable catalysts: The frontier between homogeneous and heterogeneous catalysis. *Angew. Chem.-Int. Edit.* **2005**, *44*, 7852-7872.
40. Boisselier, E.; Astruc, D., Gold nanoparticles in nanomedicine: preparations, imaging, diagnostics, therapies and toxicity. *Chem. Soc. Rev.* **2009**, *38*, 1759-1782.
41. Dreaden, E. C.; Alkilany, A. M.; Huang, X. H.; Murphy, C. J.; El-Sayed, M. A., The golden age: gold nanoparticles for biomedicine. *Chem. Soc. Rev.* **2012**, *41*, 2740-2779.
42. Klaine, S. J.; Alvarez, P. J. J.; Batley, G. E.; Fernandes, T. F.; Handy, R. D.; Lyon, D. Y.; Mahendra, S.; McLaughlin, M. J.; Lead, J. R., Nanomaterials in the environment: Behavior, fate, bioavailability, and effects. *Environ. Toxicol. Chem.* **2008**, *27*, 1825-1851.
43. Qian, X. M.; Peng, X. H.; Ansari, D. O.; Yin-Goen, Q.; Chen, G. Z.; Shin, D. M.; Yang, L.; Young, A. N.; Wang, M. D.; Nie, S. M., In vivo tumor targeting and spectroscopic detection with surface-enhanced Raman nanoparticle tags. *Nat. Biotechnol.* **2008**, *26*, 83-90.
44. Nel, A. E.; Madler, L.; Velegol, D.; Xia, T.; Hoek, E. M. V.; Somasundaran, P.; Klaessig, F.; Castranova, V.; Thompson, M., Understanding biophysicochemical interactions at the nano-bio interface. *Nat. Mater.* **2009**, *8*, 543-557.
45. Nie, S. M.; Emery, S. R., Probing single molecules and single nanoparticles by surface-enhanced Raman scattering. *Science* **1997**, *275*, 1102-1106.
46. Alivisatos, A. P., Semiconductor clusters, nanocrystals, and quantum dots. *Science* **1996**, *271*, 933-937.
47. Willets, K. A.; Van Duyne, R. P., Localized surface plasmon resonance spectroscopy and sensing. *Annu. Rev. Phys. Chem.* **2007**, *58*, 267-297.
48. Mayer, K. M.; Hafner, J. H., Localized Surface Plasmon Resonance Sensors. *Chem. Rev.* **2011**, *111*, 3828-3857.
49. Bruchez, M.; Moronne, M.; Gin, P.; Weiss, S.; Alivisatos, A. P., Semiconductor nanocrystals as fluorescent biological labels. *Science* **1998**, *281*, 2013-2016.
50. Chan, W. C. W.; Nie, S. M., Quantum dot bioconjugates for ultrasensitive nonisotopic detection. *Science* **1998**, *281*, 2016-2018.

51. Michalet, X.; Pinaud, F. F.; Bentolila, L. A.; Tsay, J. M.; Doose, S.; Li, J. J.; Sundaresan, G.; Wu, A. M.; Gambhir, S. S.; Weiss, S., Quantum dots for live cells, in vivo imaging, and diagnostics. *Science* **2005**, *307*, 538-544.
52. Dabbousi, B. O.; RodriguezViejo, J.; Mikulec, F. V.; Heine, J. R.; Mattoussi, H.; Ober, R.; Jensen, K. F.; Bawendi, M. G., (CdSe)ZnS core-shell quantum dots: Synthesis and characterization of a size series of highly luminescent nanocrystallites. *J. Phys. Chem. B* **1997**, *101*, 9463-9475.
53. Murray, C. B.; Norris, D. J.; Bawendi, M. G., Synthesis And Characterization of Nearly Monodisperse CdE (E = S, Se, Te) Semiconductor Nanocrystallites. *J. Am. Chem. Soc.* **1993**, *115*, 8706-8715.
54. Rycenga, M.; Cobley, C. M.; Zeng, J.; Li, W. Y.; Moran, C. H.; Zhang, Q.; Qin, D.; Xia, Y. N., Controlling the Synthesis and Assembly of Silver Nanostructures for Plasmonic Applications. *Chem. Rev.* **2011**, *111*, 3669-3712.
55. Rosi, N. L.; Mirkin, C. A., Nanostructures in biodiagnostics. *Chem. Rev.* **2005**, *105*, 1547-1562.
56. Saha, K.; Agasti, S. S.; Kim, C.; Li, X. N.; Rotello, V. M., Gold Nanoparticles in Chemical and Biological Sensing. *Chem. Rev.* **2012**, *112*, 2739-2779.
57. Huang, X. H.; El-Sayed, I. H.; Qian, W.; El-Sayed, M. A., Cancer cell imaging and photothermal therapy in the near-infrared region by using gold nanorods. *J. Am. Chem. Soc.* **2006**, *128*, 2115-2120.
58. Mirkin, C. A.; Letsinger, R. L.; Mucic, R. C.; Storhoff, J. J., A DNA-based method for rationally assembling nanoparticles into macroscopic materials. *Nature* **1996**, *382*, 607-609.
59. Hirsch, L. R.; Stafford, R. J.; Bankson, J. A.; Sershen, S. R.; Rivera, B.; Price, R. E.; Hazle, J. D.; Halas, N. J.; West, J. L., Nanoshell-mediated near-infrared thermal therapy of tumors under magnetic resonance guidance. *Proc. Natl. Acad. Sci. U. S. A.* **2003**, *100*, 13549-13554.
60. Cao, Y. W. C.; Jin, R. C.; Mirkin, C. A., Nanoparticles with Raman spectroscopic fingerprints for DNA and RNA detection. *Science* **2002**, *297*, 1536-1540.
61. Elghanian, R.; Storhoff, J. J.; Mucic, R. C.; Letsinger, R. L.; Mirkin, C. A., Selective colorimetric detection of polynucleotides based on the distance-dependent optical properties of gold nanoparticles. *Science* **1997**, *277*, 1078-1081.
62. Fu, Q.; Saltsburg, H.; Flytzani-Stephanopoulos, M., Active nonmetallic Au and Pt species on

- ceria-based water-gas shift catalysts. *Science* **2003**, *301*, 935-938.
63. Kamat, P. V., Quantum Dot Solar Cells. Semiconductor Nanocrystals as Light Harvesters. *Journal of Physical Chemistry C* **2008**, *112*, 18737-18753.
64. Huang, X. Y.; Han, S. Y.; Huang, W.; Liu, X. G., Enhancing solar cell efficiency: the search for luminescent materials as spectral converters. *Chem. Soc. Rev.* **2013**, *42*, 173-201.
65. Wang, F.; Liu, X. G., Recent advances in the chemistry of lanthanide-doped upconversion nanocrystals. *Chem. Soc. Rev.* **2009**, *38*, 976-989.
66. Chen, G. Y.; Qiu, H. L.; Prasad, P. N.; Chen, X. Y., Upconversion Nanoparticles: Design, Nanochemistry, and Applications in Theranostics. *Chem. Rev.* **2014**, *114*, 5161-5214.
67. Zhou, B.; Shi, B. Y.; Jin, D. Y.; Liu, X. G., Controlling upconversion nanocrystals for emerging applications. *Nat. Nanotechnol.* **2015**, *10*, 924-936.
68. Gu, Z. J.; Yan, L.; Tian, G.; Li, S. J.; Chai, Z. F.; Zhao, Y. L., Recent Advances in Design and Fabrication of Upconversion Nanoparticles and Their Safe Theranostic Applications. *Adv. Mater.* **2013**, *25*, 3758-3779.
69. Zhou, J.; Liu, Z.; Li, F. Y., Upconversion nanophosphors for small-animal imaging. *Chem. Soc. Rev.* **2012**, *41*, 1323-1349.
70. Dong, H.; Du, S. R.; Zheng, X. Y.; Lyu, G. M.; Sun, L. D.; Li, L. D.; Zhang, P. Z.; Zhang, C.; Yan, C. H., Lanthanide Nanoparticles: From Design toward Bioimaging and Therapy. *Chem. Rev.* **2015**, *115*, 10725-10815.
71. Yi, G. S.; Chow, G. M., Synthesis of hexagonal-phase NaYF₄ : Yb,Er and NaYF₄ : Yb,Tm nanocrystals with efficient up-conversion fluorescence. *Adv. Funct. Mater.* **2006**, *16*, 2324-2329.
72. Wang, F.; Han, Y.; Lim, C. S.; Lu, Y. H.; Wang, J.; Xu, J.; Chen, H. Y.; Zhang, C.; Hong, M. H.; Liu, X. G., Simultaneous phase and size control of upconversion nanocrystals through lanthanide doping. *Nature* **2010**, *463*, 1061-1065.
73. Johnson, N. J. J.; van Veggel, F., Sodium lanthanide fluoride core-shell nanocrystals: A general perspective on epitaxial shell growth. *Nano Res.* **2013**, *6*, 547-561.
74. Park, J.; An, K. J.; Hwang, Y. S.; Park, J. G.; Noh, H. J.; Kim, J. Y.; Park, J. H.; Hwang, N. M.; Hyeon, T., Ultra-large-scale syntheses of monodisperse nanocrystals. *Nat. Mater.* **2004**, *3*,

891-895.

75. Hyeon, T., Chemical synthesis of magnetic nanoparticles. *Chem. Commun.* **2003**, 927-934.
76. Kwon, S. G.; Hyeon, T., Colloidal Chemical Synthesis and Formation Kinetics of Uniformly Sized Nanocrystals of Metals, Oxides, and Chalcogenides. *Accounts Chem. Res.* **2008**, *41*, 1696-1709.
77. Lee, J. E.; Lee, N.; Kim, T.; Kim, J.; Hyeon, T., Multifunctional Mesoporous Silica Nanocomposite Nanoparticles for Theranostic Applications. *Accounts Chem. Res.* **2011**, *44*, 893-902.
78. Park, J.; Joo, J.; Kwon, S. G.; Jang, Y.; Hyeon, T., Synthesis of monodisperse spherical nanocrystals. *Angew. Chem.-Int. Edit.* **2007**, *46*, 4630-4660.
79. Lee, N.; Hyeon, T., Designed synthesis of uniformly sized iron oxide nanoparticles for efficient magnetic resonance imaging contrast agents. *Chem. Soc. Rev.* **2012**, *41*, 2575-2589.
80. Li, C. X.; Lin, J., Rare earth fluoride nano-/microcrystals: synthesis, surface modification and application. *J. Mater. Chem.* **2010**, *20*, 6831-6847.
81. Boyer, J. C.; Vetrone, F.; Cuccia, L. A.; Capobianco, J. A., Synthesis of colloidal upconverting NaYF₄ nanocrystals doped with Er³⁺, Yb³⁺ and Tm³⁺, Yb³⁺ via thermal decomposition of lanthanide trifluoroacetate precursors. *J. Am. Chem. Soc.* **2006**, *128*, 7444-7445.
82. Boyer, J. C.; Cuccia, L. A.; Capobianco, J. A., Synthesis of colloidal upconverting NaYF₄ : Er³⁺/Yb³⁺ and Tm³⁺/Yb³⁺ monodisperse nanocrystals. *Nano Lett.* **2007**, *7*, 847-852.
83. Mai, H. X.; Zhang, Y. W.; Si, R.; Yan, Z. G.; Sun, L. D.; You, L. P.; Yan, C. H., High-quality sodium rare-earth fluoride nanocrystals: Controlled synthesis and optical properties. *J. Am. Chem. Soc.* **2006**, *128*, 6426-6436.
84. Mai, H. X.; Zhang, Y. W.; Sun, L. D.; Yan, C. H., Highly efficient multicolor up-conversion emissions and their mechanisms of monodisperse NaYF₄ : Yb,Er core and core/shell-structured nanocrystals. *Journal of Physical Chemistry C* **2007**, *111*, 13721-13729.
85. Mai, H. X.; Zhang, Y. W.; Sun, L. D.; Yan, C. H., Size- and phase-controlled synthesis of monodisperse NaYF₄ : Yb,Er nanocrystals from a unique delayed nucleation pathway monitored with upconversion spectroscopy. *Journal of Physical Chemistry C* **2007**, *111*, 13730-13739.

86. Li, Z. Q.; Zhang, Y., An efficient and user-friendly method for the synthesis of hexagonal-phase NaYF₄: Yb, Er/Tm nanocrystals with controllable shape and upconversion fluorescence. *Nanotechnology* **2008**, *19*, 5.
87. Johnson, N. J. J.; Korinek, A.; Dong, C. H.; van Veggel, F., Self-Focusing by Ostwald Ripening: A Strategy for Layer-by-Layer Epitaxial Growth on Upconverting Nanocrystals. *J. Am. Chem. Soc.* **2012**, *134*, 11068-11071.
88. Peng, X. G.; Wickham, J.; Alivisatos, A. P., Kinetics of II-VI and III-V colloidal semiconductor nanocrystal growth: "Focusing" of size distributions. *J. Am. Chem. Soc.* **1998**, *120*, 5343-5344.
89. Talapin, D. V.; Rogach, A. L.; Haase, M.; Weller, H., Evolution of an ensemble of nanoparticles in a colloidal solution: Theoretical study. *J. Phys. Chem. B* **2001**, *105*, 12278-12285.
90. Wang, F.; Wang, J. A.; Liu, X. G., Direct Evidence of a Surface Quenching Effect on Size-Dependent Luminescence of Upconversion Nanoparticles. *Angew. Chem.-Int. Edit.* **2010**, *49*, 7456-7460.
91. Chen, G. Y.; Agren, H.; Ohulchansky, T. Y.; Prasad, P. N., Light upconverting core-shell nanostructures: nanophotonic control for emerging applications. *Chem. Soc. Rev.* **2015**, *44*, 1680-1713.
92. Zheng, W.; Huang, P.; Tu, D. T.; Ma, E.; Zhu, H. M.; Chen, X. Y., Lanthanide-doped upconversion nano-bioprobes: electronic structures, optical properties, and biodetection. *Chem. Soc. Rev.* **2015**, *44*, 1379-1415.
93. Zhao, J. B.; Jin, D. Y.; Schartner, E. P.; Lu, Y. Q.; Liu, Y. J.; Zvyagin, A. V.; Zhang, L. X.; Dawes, J. M.; Xi, P.; Piper, J. A.; Goldys, E. M.; Monro, T. M., Single-nanocrystal sensitivity achieved by enhanced upconversion luminescence. *Nat. Nanotechnol.* **2013**, *8*, 729-734.
94. Gargas, D. J.; Chan, E. M.; Ostrowski, A. D.; Aloni, S.; Altoe, M. V. P.; Barnard, E. S.; Sani, B.; Urban, J. J.; Milliron, D. J.; Cohen, B. E.; Schuck, P. J., Engineering bright sub-10-nm upconverting nanocrystals for single-molecule imaging. *Nat. Nanotechnol.* **2014**, *9*, 300-305.
95. Vetrone, F.; Naccache, R.; Mahalingam, V.; Morgan, C. G.; Capobianco, J. A., The Active-Core/Active-Shell Approach: A Strategy to Enhance the Upconversion Luminescence in Lanthanide-Doped Nanoparticles. *Adv. Funct. Mater.* **2009**, *19*, 2924-2929.
96. Wang, Y. F.; Liu, G. Y.; Sun, L. D.; Xiao, J. W.; Zhou, J. C.; Yan, C. H., Nd³⁺-Sensitized Upconversion Nanophosphors: Efficient In Vivo Bioimaging Probes with Minimized Heating

- Effect. *ACS Nano* **2013**, *7*, 7200-7206.
97. Zhong, Y. T.; Tian, G.; Gu, Z. J.; Yang, Y. J.; Gu, L.; Zhao, Y. L.; Ma, Y.; Yao, J. N., Elimination of Photon Quenching by a Transition Layer to Fabricate a Quenching-Shield Sandwich Structure for 800 nm Excited Upconversion Luminescence of Nd³⁺ Sensitized Nanoparticles. *Adv. Mater.* **2014**, *26*, 2831-2837.
98. Shen, J.; Chen, G. Y.; Vu, A. M.; Fan, W.; Bilsel, O. S.; Chang, C. C.; Han, G., Engineering the Upconversion Nanoparticle Excitation Wavelength: Cascade Sensitization of Tri-doped Upconversion Colloidal Nanoparticles at 800 nm. *Adv. Opt. Mater.* **2013**, *1*, 644-650.
99. Xie, X. J.; Gao, N. Y.; Deng, R. R.; Sun, Q.; Xu, Q. H.; Liu, X. G., Mechanistic Investigation of Photon Upconversion in Nd³⁺-Sensitized Core-Shell Nanoparticles. *J. Am. Chem. Soc.* **2013**, *135*, 12608-12611.
100. Chen, D. Q.; Wang, Y. S.; Hong, M. C., Lanthanide nanomaterials with photon management characteristics for photovoltaic application. *Nano Energy* **2012**, *1*, 73-90.
101. Naczynski, D. J.; Tan, M. C.; Zevon, M.; Wall, B.; Kohl, J.; Kulesa, A.; Chen, S.; Roth, C. M.; Riman, R. E.; Moghe, P. V., Rare-earth-doped biological composites as in vivo shortwave infrared reporters. *Nat. Commun.* **2013**, *4*, 10.
102. Weissleder, R., A clearer vision for in vivo imaging. *Nat. Biotechnol.* **2001**, *19*, 316-317.
103. Smith, A. M.; Mancini, M. C.; Nie, S. M., Bioimaging Second window for in vivo imaging. *Nat. Nanotechnol.* **2009**, *4*, 710-711.
104. Tao, Z. M.; Hong, G. S.; Shinji, C.; Chen, C. X.; Diao, S.; Antaris, A. L.; Zhang, B.; Zou, Y. P.; Dai, H. J., Biological Imaging Using Nanoparticles of Small Organic Molecules with Fluorescence Emission at Wavelengths Longer than 1000 nm. *Angew. Chem.-Int. Edit.* **2013**, *52*, 13002-13006.
105. Diao, S.; Hong, G. S.; Antaris, A. L.; Blackburn, J. L.; Cheng, K.; Cheng, Z.; Dai, H. J., Biological imaging without autofluorescence in the second near-infrared region. *Nano Res.* **2015**, *8*, 3027-3034.
106. Hong, G. S.; Diao, S. O.; Antaris, A. L.; Dai, H. J., Carbon Nanomaterials for Biological Imaging and Nanomedicinal Therapy. *Chem. Rev.* **2015**, *115*, 10816-10906.
107. Chen, J.; Kong, Y. F.; Wang, W.; Fang, H. W.; Wo, Y.; Zhou, D. J.; Wu, Z. Y.; Li, Y. X.; Chen, S. Y., Direct water-phase synthesis of lead sulfide quantum dots encapsulated by beta-lactoglobulin for in vivo second near infrared window imaging with reduced toxicity. *Chem.*

Commun. **2016**, *52*, 4025-4028.

108. Hemmer, E.; Benayas, A.; Legare, F.; Vetrone, F., Exploiting the biological windows: current perspectives on fluorescent bioprobes emitting above 1000 nm. *Nanoscale Horiz.* **2016**, *1*, 168-184.
109. Diao, S.; Blackburn, J. L.; Hong, G. S.; Antaris, A. L.; Chang, J. L.; Wu, J. Z.; Zhang, B.; Cheng, K.; Kuo, C. J.; Dai, H. J., Fluorescence Imaging In Vivo at Wavelengths beyond 1500 nm. *Angew. Chem.-Int. Edit.* **2015**, *54*, 14758-14762.
110. Liang, Y. J.; Liu, F.; Chen, Y. F.; Wang, X. J.; Sun, K. N.; Pan, Z. W., New function of the Yb³⁺ ion as an efficient emitter of persistent luminescence in the short-wave infrared. *Light-Sci. Appl.* **2016**, *5*, 6.
111. Hong, G. S.; Diao, S.; Chang, J. L.; Antaris, A. L.; Chen, C. X.; Zhang, B.; Zhao, S.; Atochin, D. N.; Huang, P. L.; Andreasson, K. I.; Kuo, C. J.; Dai, H. J., Through-skull fluorescence imaging of the brain in a new near-infrared window. *Nat. Photonics* **2014**, *8*, 723-730.
112. Hong, G. S.; Zou, Y. P.; Antaris, A. L.; Diao, S.; Wu, D.; Cheng, K.; Zhang, X. D.; Chen, C. X.; Liu, B.; He, Y. H.; Wu, J. Z.; Yuan, J.; Zhang, B.; Tao, Z. M.; Fukunaga, C.; Dai, H. J., Ultrafast fluorescence imaging in vivo with conjugated polymer fluorophores in the second near-infrared window. *Nat. Commun.* **2014**, *5*, 9.
113. Naczynski, D. J.; Sun, C.; Turkcan, S.; Jenkins, C.; Koh, A. L.; Ikeda, D.; Pratz, G.; Xing, L., X-ray-Induced Shortwave Infrared Biomedical Imaging Using RareEarth Nanoprobes. *Nano Lett.* **2015**, *15*, 96-102.
114. Shao, W.; Chen, G. Y.; Kuzmin, A.; Kutscher, H. L.; Pliss, A.; Ohulchanskyy, T. Y.; Prasad, P. N., Tunable Narrow Band Emissions from Dye-Sensitized Core/Shell/Shell Nanocrystals in the Second Near-Infrared Biological Window. *J. Am. Chem. Soc.* **2016**, *138*, 16192-16195.
115. Wang, R.; Li, X. M.; Zhou, L.; Zhang, F., Epitaxial Seeded Growth of Rare-Earth Nanocrystals with Efficient 800 nm Near-Infrared to 1525 nm Short-Wavelength Infrared Downconversion Photoluminescence for In Vivo Bioimaging. *Angew. Chem.-Int. Edit.* **2014**, *53*, 12086-12090.
116. Dougherty, T. J.; Gomer, C. J.; Henderson, B. W.; Jori, G.; Kessel, D.; Korbely, M.; Moan, J.; Peng, Q., Photodynamic therapy. *J. Natl. Cancer Inst.* **1998**, *90*, 889-905.
117. Dolmans, D.; Fukumura, D.; Jain, R. K., Photodynamic therapy for cancer. *Nat. Rev. Cancer* **2003**, *3*, 380-387.
118. Liu, K.; Liu, X. M.; Zeng, Q. H.; Zhang, Y. L.; Tu, L. P.; Liu, T.; Kong, X. G.; Wang, Y. H.;

- Cao, F.; Lambrechts, S. A. G.; Aalders, M. C. G.; Zhang, H., Covalently Assembled NIR Nanoplatform for Simultaneous Fluorescence Imaging and Photodynamic Therapy of Cancer Cells. *ACS Nano* **2012**, *6*, 4054-4062.
119. Wang, C.; Cheng, L.; Liu, Y. M.; Wang, X. J.; Ma, X. X.; Deng, Z. Y.; Li, Y. G.; Liu, Z., Imaging-Guided pH-Sensitive Photodynamic Therapy Using Charge Reversible Upconversion Nanoparticles under Near-Infrared Light. *Adv. Funct. Mater.* **2013**, *23*, 3077-3086.
120. Wang, C.; Tao, H. Q.; Cheng, L.; Liu, Z., Near-infrared light induced in vivo photodynamic therapy of cancer based on upconversion nanoparticles. *Biomaterials* **2011**, *32*, 6145-6154.
121. Idris, N. M.; Gnanasammandhan, M. K.; Zhang, J.; Ho, P. C.; Mahendran, R.; Zhang, Y., In vivo photodynamic therapy using upconversion nanoparticles as remote-controlled nanotransducers. *Nat. Med.* **2012**, *18*, 1580-U190.
122. Bechet, D.; Couleaud, P.; Frochot, C.; Viriot, M. L.; Guillemin, F.; Barberi-Heyob, M., Nanoparticles as vehicles for delivery of photodynamic therapy agents. *Trends Biotechnol.* **2008**, *26*, 612-621.
123. Gunes, S.; Neugebauer, H.; Sariciftci, N. S., Conjugated polymer-based organic solar cells. *Chem. Rev.* **2007**, *107*, 1324-1338.
124. Hagfeldt, A.; Boschloo, G.; Sun, L. C.; Kloo, L.; Pettersson, H., Dye-Sensitized Solar Cells. *Chem. Rev.* **2010**, *110*, 6595-6663.
125. Oregan, B.; Gratzel, M., A Low-Cost, High-Efficiency Solar-Cell Based on Dye-Sensitized Colloidal TiO₂ Films. *Nature* **1991**, *353*, 737-740.
126. Tian, B. Z.; Zheng, X. L.; Kempa, T. J.; Fang, Y.; Yu, N. F.; Yu, G. H.; Huang, J. L.; Lieber, C. M., Coaxial silicon nanowires as solar cells and nanoelectronic power sources. *Nature* **2007**, *449*, 885-U8.
127. Atwater, H. A.; Polman, A., Plasmonics for improved photovoltaic devices. *Nat. Mater.* **2010**, *9*, 205-213.
128. Law, M.; Greene, L. E.; Johnson, J. C.; Saykally, R.; Yang, P. D., Nanowire dye-sensitized solar cells. *Nat. Mater.* **2005**, *4*, 455-459.
129. Li, G.; Zhu, R.; Yang, Y., Polymer solar cells. *Nat. Photonics* **2012**, *6*, 153-161.

130. Saga, T., Advances in crystalline silicon solar cell technology for industrial mass production. *NPG Asia Mater.* **2010**, *2*, 96-102.
131. Goldschmidt, J. C.; Fischer, S., Upconversion for Photovoltaics - a Review of Materials, Devices and Concepts for Performance Enhancement. *Adv. Opt. Mater.* **2015**, *3*, 510-535.
132. Lian, H. Z.; Hou, Z. Y.; Shang, M. M.; Geng, D. L.; Zhang, Y.; Lin, J., Rare earth ions doped phosphors for improving efficiencies of solar cells. *Energy* **2013**, *57*, 270-283.
133. de Wild, J.; Meijerink, A.; Rath, J. K.; van Sark, W.; Schropp, R. E. I., Upconverter solar cells: materials and applications. *Energy Environ. Sci.* **2011**, *4*, 4835-4848.
134. Fischer, S.; Goldschmidt, J. C.; Loper, P.; Bauer, G. H.; Bruggemann, R.; Kramer, K.; Biner, D.; Hermle, M.; Glunz, S. W., Enhancement of silicon solar cell efficiency by upconversion: Optical and electrical characterization. *J. Appl. Phys.* **2010**, *108*, 11.
135. Yuan, C. Z.; Chen, G. Y.; Prasad, P. N.; Ohulchanskyy, T. Y.; Ning, Z. J.; Tian, H. N.; Sun, L. C.; Agren, H., Use of colloidal upconversion nanocrystals for energy relay solar cell light harvesting in the near-infrared region. *J. Mater. Chem.* **2012**, *22*, 16709-16713.
136. Bunzli, J. C. G.; Eliseeva, S. V., Lanthanide NIR luminescence for telecommunications, bioanalyses and solar energy conversion. *J. Rare Earths* **2010**, *28*, 824-842.
137. van der Ende, B. M.; Aarts, L.; Meijerink, A., Lanthanide ions as spectral converters for solar cells. *Phys. Chem. Chem. Phys.* **2009**, *11*, 11081-11095.
138. de Wild, J.; Rath, J. K.; Meijerink, A.; van Sark, W.; Schropp, R. E. I., Enhanced near-infrared response of a-Si:H solar cells with beta-NaYF₄:Yb³⁺ (18%), Er³⁺ (2%) upconversion phosphors. *Sol. Energy Mater. Sol. Cells* **2010**, *94*, 2395-2398.
139. Liu, M.; Lu, Y. L.; Xie, Z. B.; Chow, G. M., Enhancing near-infrared solar cell response using upconverting transparent ceramics. *Sol. Energy Mater. Sol. Cells* **2011**, *95*, 800-803.
140. Shalav, A.; Richards, B. S.; Green, M. A., Luminescent layers for enhanced silicon solar cell performance: Up-conversion. *Sol. Energy Mater. Sol. Cells* **2007**, *91*, 829-842.
141. Fischer, S.; Johnson, N. J. J.; Pichaandi, J.; Goldschmidt, J. C.; van Veggel, F., Upconverting core-shell nanocrystals with high quantum yield under low irradiance: On the role of isotropic and thick shells. *J. Appl. Phys.* **2015**, *118*, 12.

Chapter 1

Direct Evidence for Coupled Surface and Concentration Quenching Dynamics in Lanthanide-Doped Nanocrystals

1.1 Abstract

Luminescence quenching at high dopant concentrations generally limits the dopant concentration to less than 1-5 mol% in lanthanide-doped materials, and this remains a major obstacle in designing materials with enhanced efficiency/brightness. In this work, we provide direct evidence that the major quenching process at high dopant concentrations is the energy migration to the surface (i.e. surface quenching) as opposed to the common misconception of cross-relaxation between dopant ions. We show that after an inert epitaxial shell growth, erbium (Er^{3+}) concentrations as high as 100 mol% in $\text{NaY}(\text{Er})\text{F}_4/\text{NaLuF}_4$ core/shell nanocrystals enhance the emission intensity of both upconversion and downshifted luminescence across different excitation wavelengths (980, 800, and 658 nm), with negligible concentration quenching effects. Our results highlight the strong coupling of concentration and surface quenching effects in colloidal lanthanide-doped nanocrystals, and that inert epitaxial shell growth can overcome concentration quenching. These fundamental insights into the photophysical processes in highly-doped nanocrystals will give rise to enhanced properties not previously thought possible with compositions optimized in bulk.

1.2 Introduction

Lanthanide-doped nanocrystals have generated significant interest for broad range of applications from bioimaging, photovoltaics, to displays.¹⁻⁴ Using selective combinations

/compositions of lanthanide dopants, various photophysical processes such as quantum cutting, downshifting, and upconversion can be realized in this class of materials.⁵⁻¹⁰ A common limitation for realizing practical application is the limited brightness of lanthanide-doped nanocrystals and the challenges associated with enhancing luminescence efficiencies. One critical limitation of lanthanide-doped nanoparticles is that the concentration of emitters is generally restricted to low dopant (emitter ion) concentrations generally in the range of 1-5 mol%. Increasing the dopant concentration results in decrease of luminescence intensity, commonly referred to as “concentration quenching”. Despite the fact that the origins of concentration quenching in lanthanide-doped materials are still under debate,⁷ these guidelines and the optimized concentrations from bulk materials are commonly adopted in lanthanide-doped nanocrystals.^{11,12} Only recently, efforts to achieve high dopant concentrations are being addressed especially in lanthanide-doped upconversion nanocrystals. Zhao et al.^{13,14} and Gargas et al.¹⁵ independently demonstrated the use of high excitation irradiance ($\sim 10^6$ W cm⁻²) as a way to overcome concentration quenching at high dopant concentrations. Similarly, Liu and coworkers demonstrated the sub-lattice clustering of dopant ions as a pathway to achieve high dopant concentrations.¹⁶ More recently, Prasad and coworkers used organic dye sensitization as a route to alleviate concentration quenching.¹⁷ However, mechanistic investigations to understand the origins of concentration quenching and ways to overcome them especially with nanocrystalline materials are not fully addressed.

Two common explanations for concentration quenching are deleterious cross-relaxation between dopant ions in close proximity,¹¹ and/or enhanced energy migration via resonant energy transfer to the defects (i.e. the surface).¹² While the latter has only gained attention in the last decade with the development of colloidal nanocrystals, historically the cross-relaxation between

dopant ions is commonly regarded as the major cause of concentration quenching as observed in bulk materials. In this work, we address this fundamental question on the origins of concentration quenching in nanocrystalline materials, and demonstrate that the major quenching process at high dopant concentrations is predominantly due to energy migration to the surface and not cross-relaxation between dopant ions.

In colloidal nanocrystals, increasing the dopant ion concentration results in increased energy migration to the surface as the inter-ionic distance shortens.¹³ This suggests that the concentration quenching effects should be strongly coupled to the surface effects in nanocrystalline materials. In lanthanide-doped nanocrystals, the emission intensity decreases disproportionately with nanocrystal volume due to the fact that a significant fraction of the dopants lie within the characteristic distance for energy migration.¹⁴⁻¹⁶ Recent advances have established that the epitaxial growth of a shell spatially isolates the core, passivates surface defects, and reduces surface quenching.¹⁷⁻²⁰ In this context, we reasoned that the growth of thick (~10 nm) high-quality epitaxial shell should decouple both the surface and concentration quenching effects and allow for higher dopant concentrations within the core than those optimized in bulk compositions. Moreover, the ability to localize high dopant concentration in the core and confine the excitation energy with a high-quality shell should allow for novel mechanistic understanding of the photophysical processes that have not been previously possible with bulk materials or core only nanostructures.

1.3 Results and Discussion

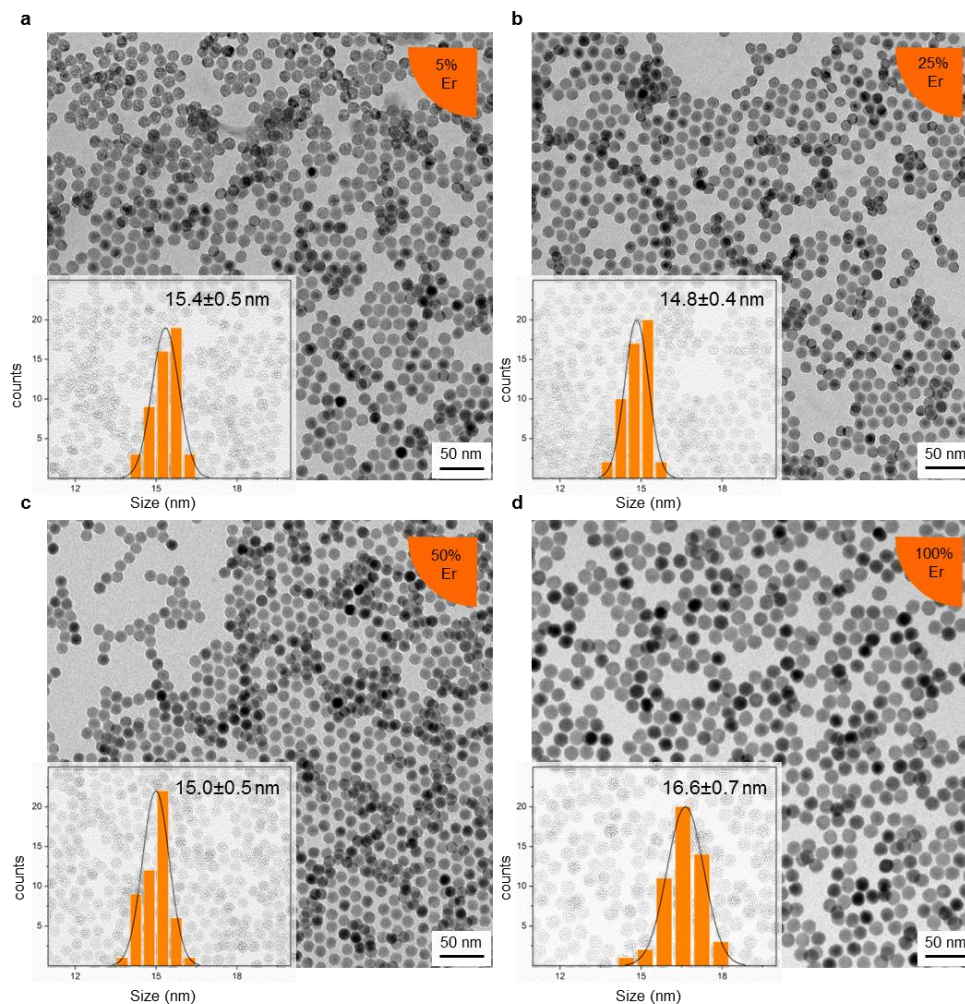


Figure 1.1 Transmission electron microscopy (TEM) images and size distribution of representative core nanocrystals (a) NaYF₄:5% Er³⁺, (b) NaYF₄:25% Er³⁺, (c) NaYF₄:50% Er³⁺, and (d) NaErF₄.

In this work, erbium (Er³⁺) is used as the active dopant ion for its rich energy level system that offers multiple excitation and emission pathways spanning the visible to the near-infrared (NIR) wavelengths. To systematically study and compare the effect of epitaxial shells on highly doped nanocrystals, we synthesized hexagonal phase (β) NaYF₄ core NCs with varying Er³⁺ dopant concentrations (5, 25, 50, and 100 mol%),²¹ followed by growing an inert thick (~10 nm) NaLuF₄ epitaxial shell (see experimental details for synthesis).^{19,22} All core NCs were similar in

size (~ 15 nm), and after shell growth the core-shell NCs were found to be about ~ 35 - 38 nm, with an average shell thickness of about 10 nm as shown in Figure 1.1 and 1.2, respectively.

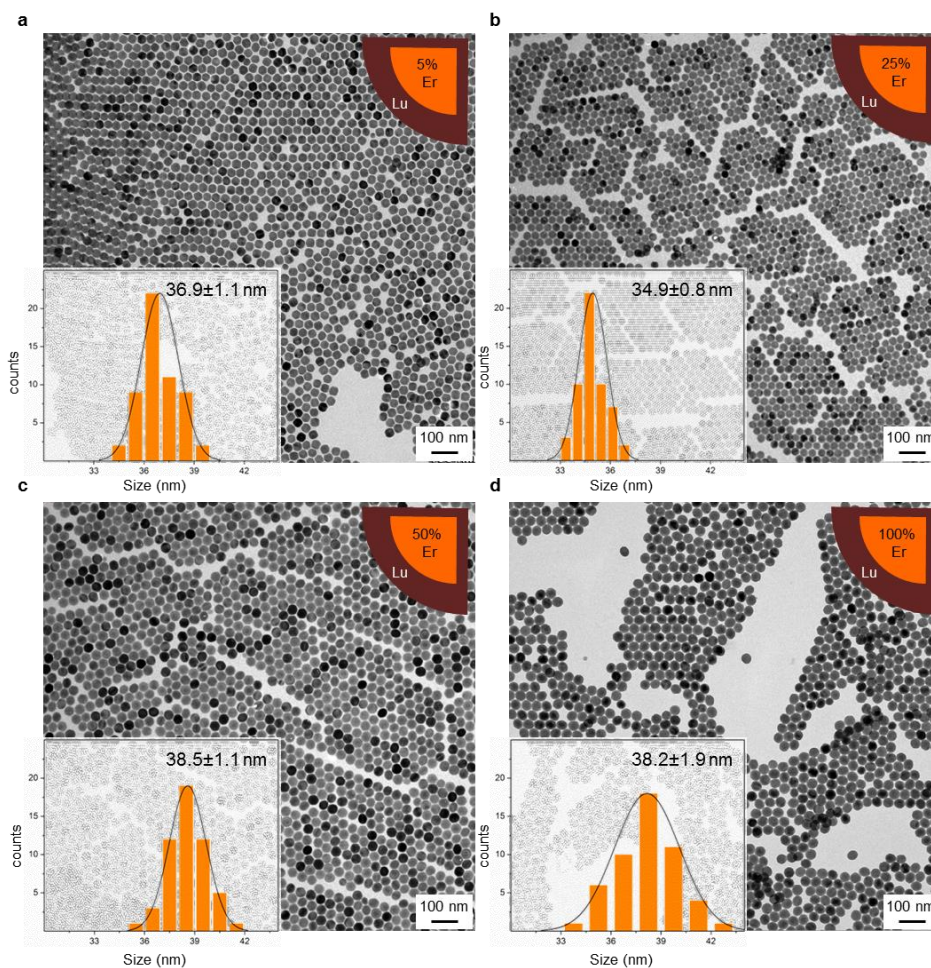


Figure 1.2 Transmission electron microscopy (TEM) images and size distribution of representative core-shell nanocrystals (a) $\text{NaYF}_4:5\% \text{Er}^{3+} / \text{NaLuF}_4$, (b) $\text{NaYF}_4:25\% \text{Er}^{3+} / \text{NaLuF}_4$, (c) $\text{NaYF}_4:50\% \text{Er}^{3+} / \text{NaLuF}_4$, and (d) $\text{NaErF}_4 / \text{NaLuF}_4$.

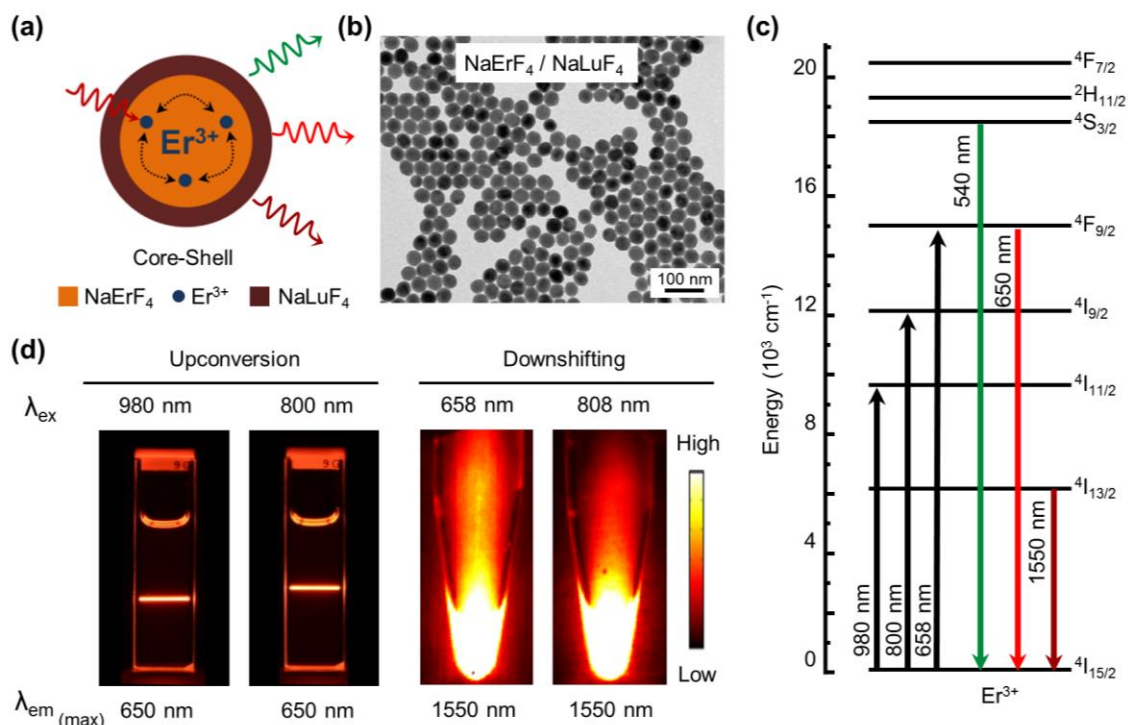


Figure 1.3. (a) Schematic illustration of the core-shell nanocrystals structural composition. (b) Representative transmission electron microscopy (TEM) image of the NaErF₄-NaLuF₄ core-shell nanocrystals. (c) Energy level diagram of erbium showing the multiple excitation pathways, and the multiple emission levels leading to upconverted or downshifted emission. (d) Upconversion and downshifted emission photographs of the colloidal dispersion of NaErF₄-NaLuF₄ core-shell nanocrystals at variable excitation wavelengths.

A schematic representation of the core-shell structure and transmission electron microscopy (TEM) image of 100 mol% Er-doped NaYF₄ core (i.e. NaErF₄) with a NaLuF₄ shell is shown in Figure 1.3 a and b respectively. Representative scanning electron microscopy (SEM), high resolution (HR)-TEM, and powder X-ray diffraction (XRD) analysis shown in Figure 1.4 and 1.5 further confirmed the high uniformity, crystallinity, and hexagonal phase of the synthesized core-shell nanocrystals. Upconversion and downshifted luminescence at various excitation fluxes for the erbium dopants as shown in the energy level diagram (Figure 1.3c) were systematically investigated for these doped core and core-shell nanostructures. Figure 1.3d shows the dispersion

photographs of the same dispersion of core-thick shell nanocrystals at variable excitation fluxes and emission pathways studied in this work.

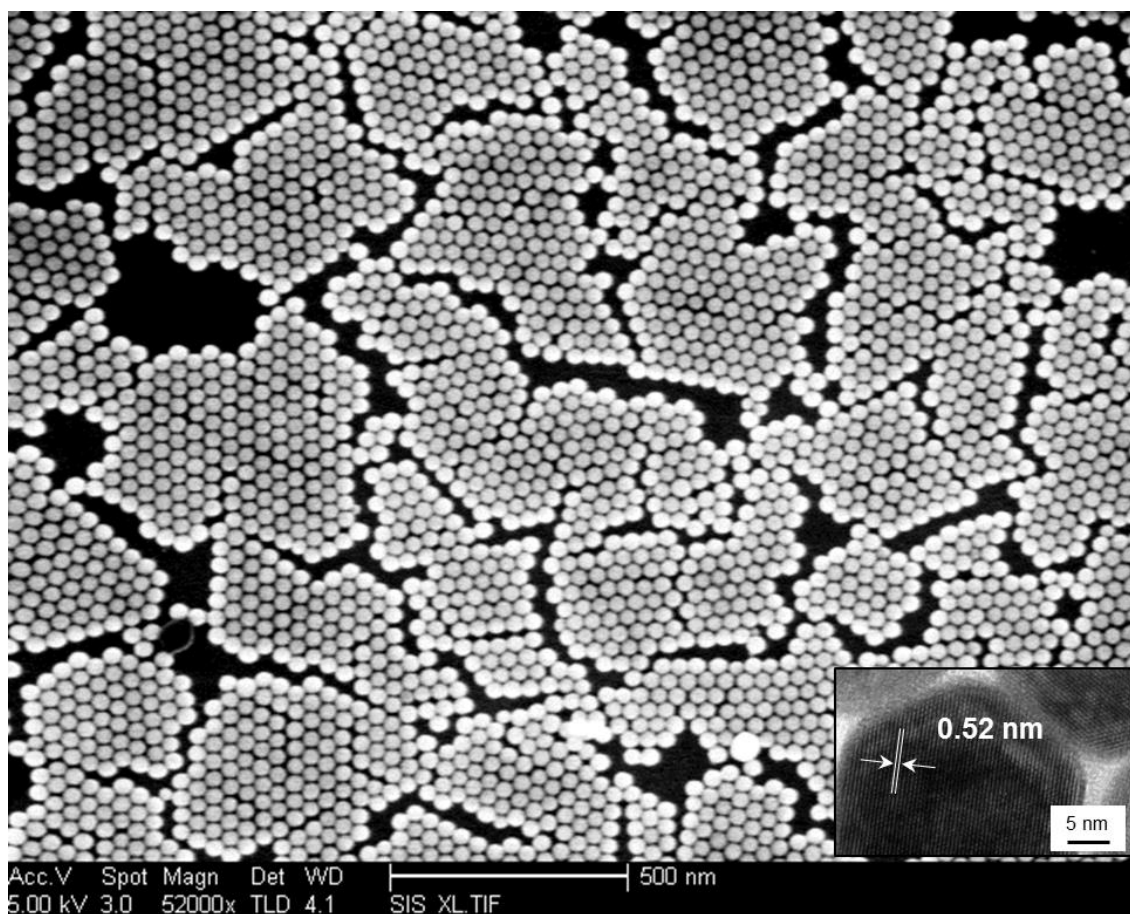


Figure 1.4 Scanning electron microscopy (SEM) image of NaErF₄/NaLuF₄ core-shell nanocrystals demonstrating high size uniformity. *Inset*: High resolution transmission electron microscopy (HR-TEM) image of a single core-shell nanocrystal confirming high crystallinity.

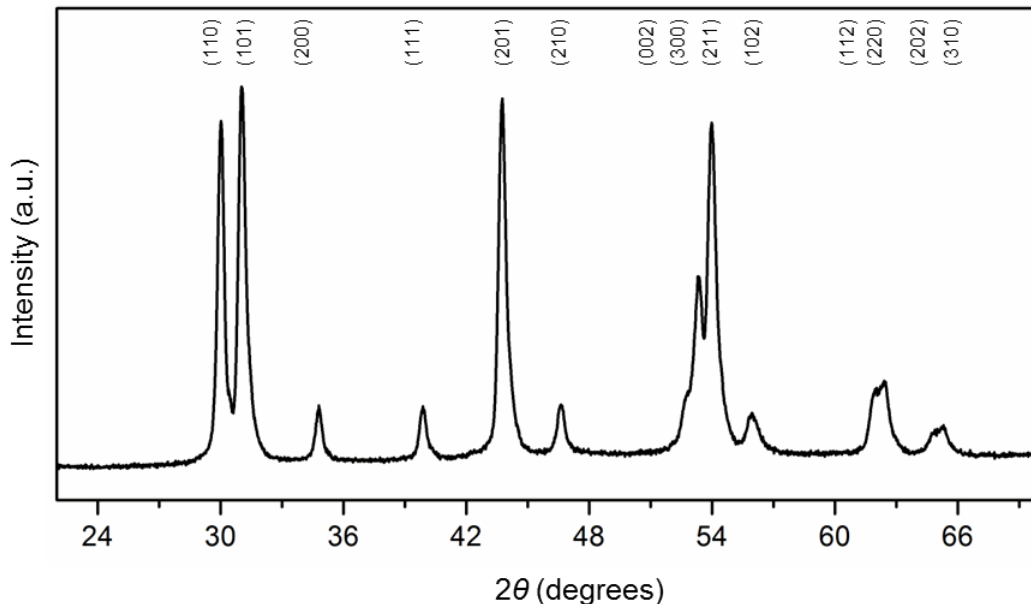


Figure 1.5 Representative powder X-ray Diffraction (XRD) pattern of the NaYF₄:25% Er³⁺/NaLuF₄ core/shell nanocrystals confirming the hexagonal phase, indexed to JCPDS file #28-1192.

We first investigated the upconversion emission properties of the core nanocrystals under 980 nm continuous-wave (CW) diode laser excitation. Consistent with concentration quenching the upconversion emission intensity decreases with increasing erbium concentration in the core nanocrystals (Figure 1.6). The visible green ($^2H_{11/2} \rightarrow ^4I_{15/2}$ and $^4S_{3/2} \rightarrow ^4I_{15/2}$), and red ($^4F_{9/2} \rightarrow ^4I_{15/2}$) emission bands are strongest for the 5 mol% Er³⁺-doped nanocrystals, and decrease with increasing erbium concentration, while being completely quenched in the heavily doped (100 mol% Er³⁺ or NaErF₄) nanocrystals.

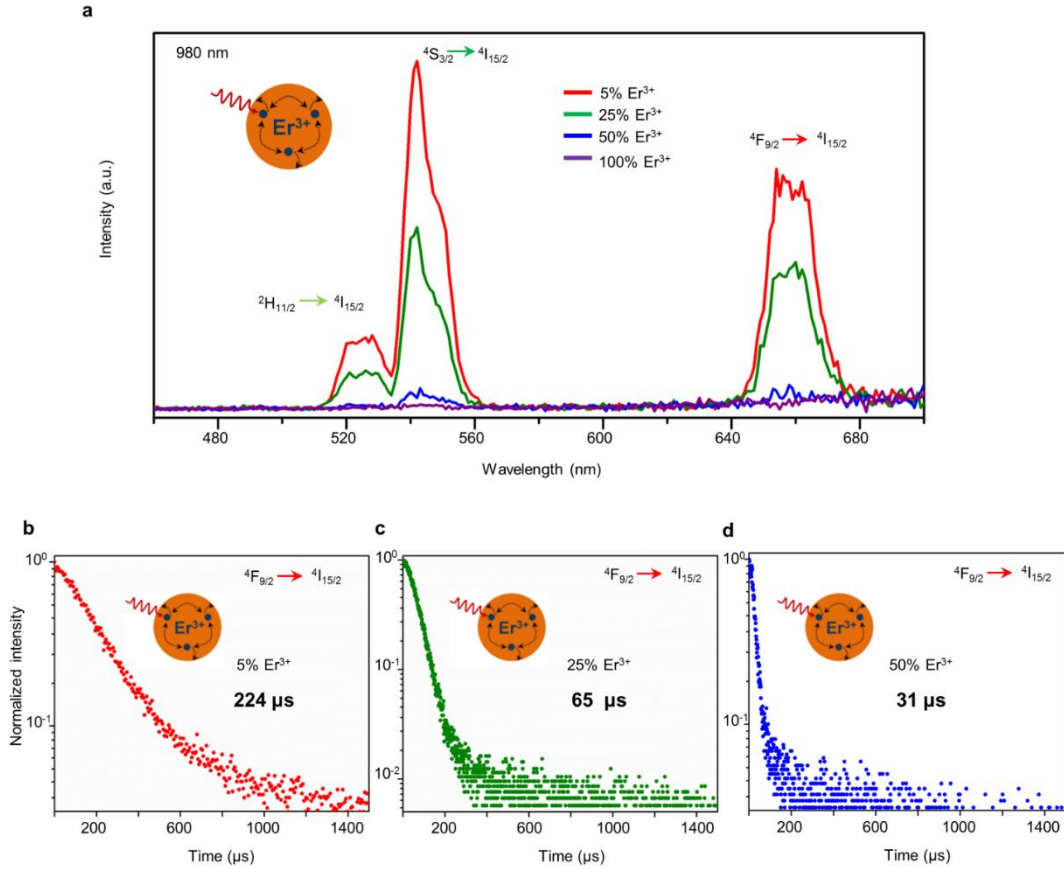


Figure 1.6 (a) Upconversion emission spectra of the core nanocrystals with variable Er^{3+} dopant concentrations under 980 nm CW laser diode excitation, (b-c) Luminescence decay of the ${}^4\text{F}_{9/2}$ level at 650 nm of the core nanocrystals with variable erbium dopant concentration and their corresponding lifetime values. Note that the 100% Er^{3+} core sample has no measurable luminescence and so the lifetimes could not be obtained as there was no measurable counts on the detector.

Surprisingly, after a thick (~ 10 nm) NaLuF_4 epitaxial shell growth on these nanocrystals we find that the upconversion emission increases monotonically with increasing erbium concentration, with the brightest being the heavily doped (100 mol% Er^{3+}) nanocrystals (Figure 1.7a). The enhanced upconverted emission with increase in dopant concentration is observed clearly in the digital photographs of the colloidal dispersion of the core-shell NCs (λ_{exc} : 980 nm) shown in Figure 1.7b. The enhanced luminescence from the 100 mol% Er^{3+} -doped (NaErF_4 - NaLuF_4) core-shell nanocrystals from a completely quenched core only structure (NaErF_4), establishes that surface quenching and concentration quenching are strongly coupled, and

highlights the role of epitaxial shell in decoupling these effects. Note that we do not provide an enhancement factor for the brightest core-shell structure, as the core is completely quenched with no observable/measurable emission.

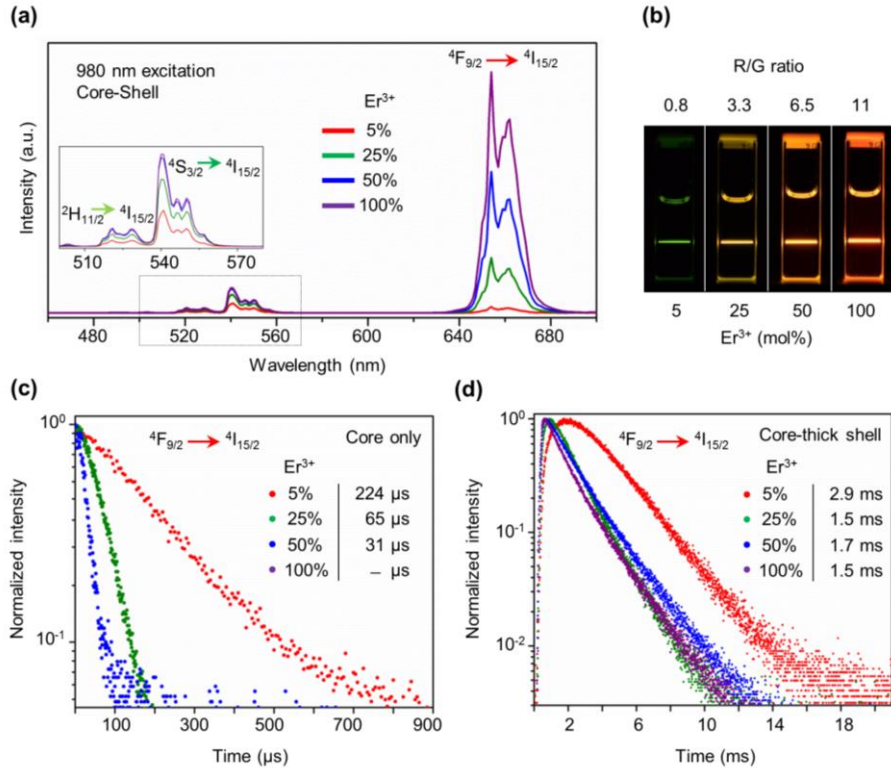


Figure 1.7 (a) Upconversion emission spectra of the core-shell nanocrystals with variable Er^{3+} dopant concentrations in the core ($\text{NaYF}_4\text{:X mol\% Er}^{3+}$, X: 5, 25, 50, and 100 mol%), Inset shows the green emission bands. (b) Upconversion emission photos of colloidal dispersion of core-shell nanocrystals (λ_{exc} : 980 nm), showing the enhanced emission with increase in dopant concentration. Luminescence decay of the ${}^4\text{F}_{9/2}$ level at 650 nm with variable erbium dopant concentration and their corresponding lifetime values of the (c) core nanocrystals, and (d) core-shell nanocrystals.

Since concentration and surface quenching would decrease the lifetime of emitting states, we examined the time-resolved population of the red emitting (${}^4\text{F}_{9/2}$) level under 980 nm excitation for the core and core-shell nanocrystals. For the core nanocrystals, the luminescence lifetime decreased from 225 to 31 μs as the dopant concentration increased from 5 to 50 mol% (Figure 1.7c, with full lifetime curves in Figure 1.8), and was completely quenched for the 100 mol% core nanocrystals. This concentration dependence in lifetime is consistent with the increased probability

of energy migrating to the surface as the dopant concentration increases and the inter-ionic distance shortens.¹²

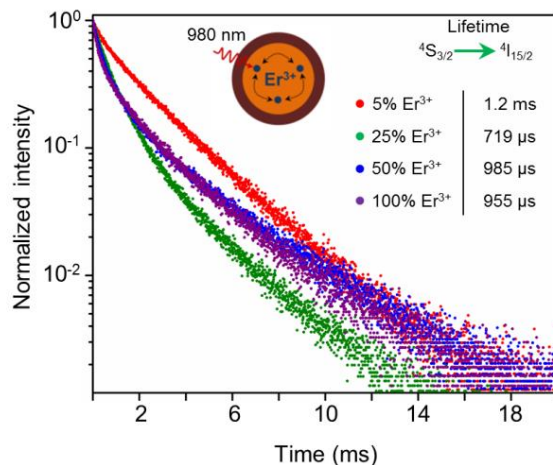


Figure 1.8 Luminescence decay of the $^4S_{3/2}$ level at 540 nm of the core-shell nanocrystals with variable erbium dopant concentration in the core and their corresponding lifetime values.

However, these measurements do not exclude cross-relaxation as a mechanism for concentration quenching, since cross-relaxation would also reduce the luminescence lifetimes at high emitter concentrations. To distinguish between the two mechanisms, we measured the lifetimes of the thick-shell nanoparticles, thereby eliminating energy migration to the surface. In contrast to the sharp concentration dependence and μs lifetimes of the cores, all of the core-shell nanocrystals exhibit long luminescence lifetimes greater than 1 ms with surprisingly little dependence on concentration (Figure 1.7d). While the lifetime increased from 224 μs to 2.9 ms for the 5 mol% Er^{3+} -doped nanocrystals after shell growth, the 100 mol% Er^{3+} -doped nanocrystals increased from a completely quenched (dark) state to 1.5 ms after shell growth. The similar decay time of ~ 1.5 ms for the 25, 50, and 100 mol% Er^{3+} -doped samples after shell growth, demonstrates that, even under high dopant concentrations that in principle favor rapid cross relaxation, no “concentration quenching” is observed in the lifetime or the emission of core-shell nanocrystals.

This suggests that cross-relaxation is not the dominant mechanism for concentration quenching. In contrast, when energy migration to the surface is suppressed by the growth of a thick shell, the heavy “concentration quenching” observed with the original cores is deactivated. These dual observations lead to the conclusion that energy migration to surface defects, not cross-relaxation is the major luminescence quenching pathway at high dopant concentrations.

Similar behavior is observed for the time-resolved population of the green emitting level ($^4S_{3/2} \rightarrow ^4I_{15/2}$) under 980 nm excitation (Figure 1.8). As expected the lifetime values of this level ($^4S_{3/2}$) were slightly shorter than the strongly red-emitting level ($^4F_{9/2}$).³⁴ Remarkably, for the brightest heavily doped (100 mol% Er^{3+}) core-shell nanocrystal, we determined the upconversion quantum yield under 980 nm excitation to be $5.2 \pm 0.3\%$ at only 10 W cm^{-2} irradiance (see *experimental section* for details). This further confirms the unique ability of epitaxial shell in overcoming concentration quenching, providing access to the benefits of high-dopant concentrations (i.e. more emission centers) without the disadvantages of quenching in high-surface-area nanocrystalline structures.

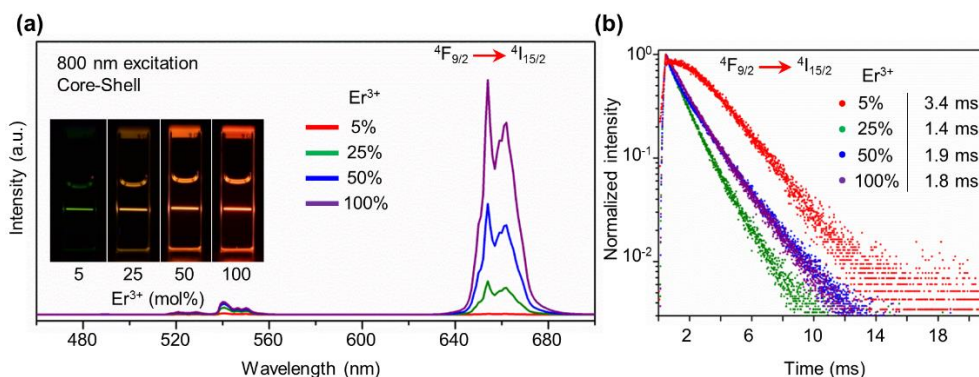


Figure 1.9 (a) Upconversion spectra of the core-shell nanocrystals with variable Er^{3+} dopant concentrations in the core ($\text{NaYF}_4\text{:X mol}\% \text{Er}^{3+}$, X: 5, 25, 50, and 100 mol%) excited at 800 nm, Inset shows the emission photos of colloidal dispersion of core-shell nanocrystals showing the amplified emission with increase in dopant concentration. (b) Luminescence decay of the $^4F_{9/2}$ level at 650 nm of the core-shell nanocrystals with variable erbium dopant concentration and their corresponding lifetime values.

To demonstrate the generality of this unique observation, we explored the upconversion emission properties of these core-shell nanocrystals under a second excitation wavelength. The transition from erbium ground state ($^4I_{15/2}$) to the $^4I_{9/2}$ manifold (Figure 1.3c) allows for direct excitation of the erbium at 800 nm, which lies in the NIR-I bioimaging window. Recent interest in excitation energy tuning in upconversion nanocrystals, especially using neodymium (Nd^{3+})-sensitization has focused on 800 nm excitation, for its biocompatibility, and minimal heating effects as compared to the conventional 980 nm excitation.²³⁻²⁴ Here, too, we observe a strong upconversion enhancement with increasing Er^{3+} -dopant concentration in the core-shell nanocrystals, with the brightest being the heavily doped (100 mol% Er^{3+}) core with a thick (~10 nm) NaLuF_4 shell (Figure 1.9a). Similar to the 980 nm excitation, the upconversion showed stronger monotonic enhancement of the red emission band with increasing dopant concentration (see inset Figure 1.3a for digital photographs of the upconversion emission). The luminescence decay curves of the red emitting level ($^4F_{9/2} \rightarrow ^4I_{15/2}$) upon 800 nm excitation shown in Figure 1.9b, once again exhibit long lifetimes that are independent of dopant concentration at high Er^{3+} -concentrations (25, 50, and 100 mol%), confirming the generality of our observations (Figure 1.9b). The enhanced upconverted emission observed at two separate excitation wavelengths from a core nanocrystal (100 mol% Er^{3+}) that is completely quenched, demonstrate the unique potential of the epitaxial shell in overcoming concentration quenching. Note that the epitaxial shells grown here are isotropic to the core, providing high-quality spatial confinement of the core from surface effects.

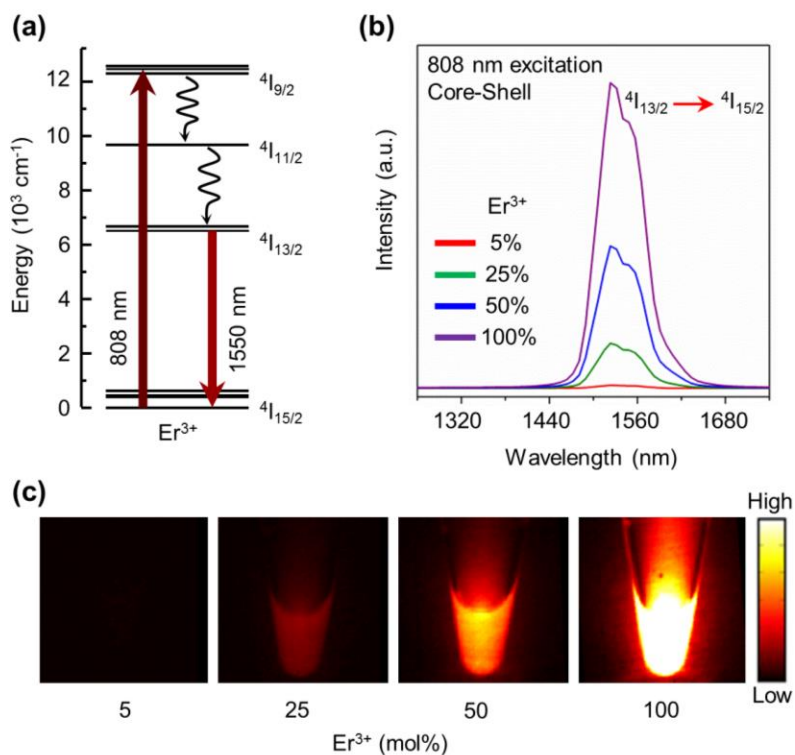


Figure 1.10 (a) Energy level diagram of Er^{3+} showing the excitation (808 nm) and the downshifted emission (1550 nm) levels. (b) Emission spectra of the core-shell nanocrystals with variable Er^{3+} dopant concentrations in the core showing downshifted infrared emission between 1450-1650 nm under 808 nm excitation. (c) Downshifted emission images from colloidal dispersion of core-shell nanocrystals (λ_{exc} : 808 nm) in the range of 0.9-1.7 μm , showing emission enhancement with increase in dopant concentration.

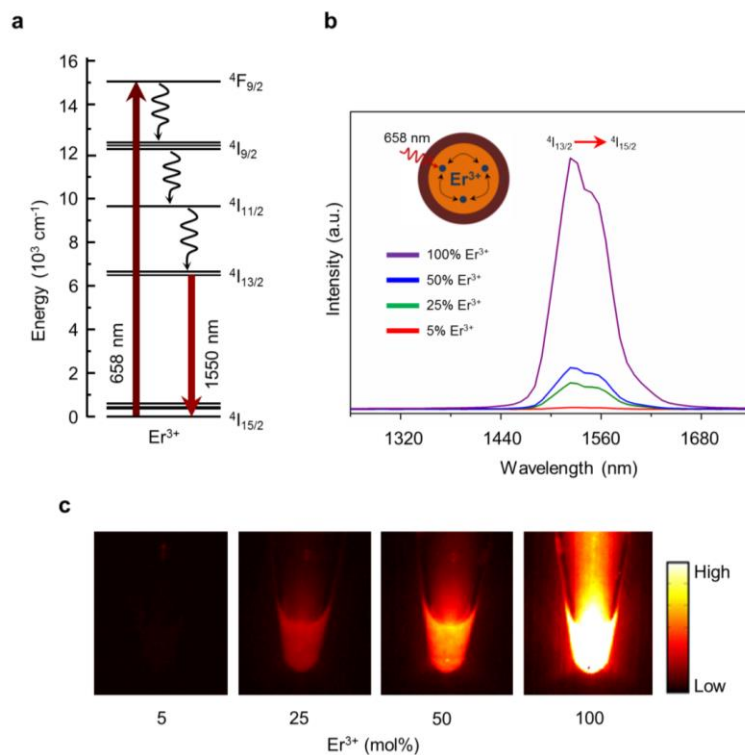


Figure 1.11 (a) Energy level diagram of Er^{3+} showing the excitation (658 nm) and the downshifted emission (1550 nm) levels. (b) Emission spectra of the core-shell nanocrystals with variable Er^{3+} -dopant concentrations in the core showing downshifted infrared emission between 1450-1650 nm under 658 nm excitation, and (c) Downshifted emission images from colloidal dispersion of core-shell nanocrystals (λ_{exc} : 658 nm) in the range of 0.9-1.7 μm , showing emission enhancement with increase in dopant concentration.

Next, we reasoned that suppression of both concentration and surface quenching in core-shell structures could also enhance the emission of Stokes, or downshifted emission in heavily-doped nanocrystals. Er^{3+} -doped nanocrystals emit NIR light centered at 1,550 nm via radiative relaxation from the first Er^{3+} excited state ($4I_{13/2}$) to the ground state ($4I_{15/2}$) (Figure 1.3c). This emission band lies within the NIR-II biological window (1,000-1,700 nm) that is currently being explored for bioimaging,²⁵ as it offers reduced tissue scattering and autofluorescence.²⁶⁻²⁷ Moreover, this emission band has critical importance for optical amplifiers as it overlaps with the minimal loss window (telecommunication window) in silica fibers.²⁸ However, due to concentration quenching, studies to date have been limited to erbium dopant concentrations below

2-5 mol%.^{12, 29} We first investigated the downshifted NIR emission (1,550 nm) from the core-shell nanocrystals excited at 808 nm ($^4I_{15/2} \rightarrow ^4I_{9/2}$) (see Figure 1.10a for energy level diagram).

The emission intensity at 1,550 nm exhibited a strong enhancement with increasing Er^{3+} -dopant concentration (Figure 1.10b), with the heavily doped (100 mol% Er^{3+}) core-shell nanocrystals as the brightest. The NIR emission images of the colloidal dispersion of core-shell nanocrystals (Figure 1.10c) excited at 808 nm clearly illustrate the enhanced emission at high dopant concentrations, demonstrating the ability of epitaxial shell to enhance the downshifted emission from heavily doped nanocrystals. Similar enhancement of downshifted NIR emission (1,550 nm) with increase in dopant concentration is also observed on excitation at 658 nm ($^4I_{15/2} \rightarrow ^4F_{9/2}$), and we again find the heavily-doped core-shell (100 mol% Er^{3+} in core) to be the brightest (Figure 1.11). These results provide direct evidence of achieving enhanced emission from a lanthanide-doped structure with a high active dopant concentration reaching 100 mol%, and establishes the unique role of inert epitaxial thick shell.

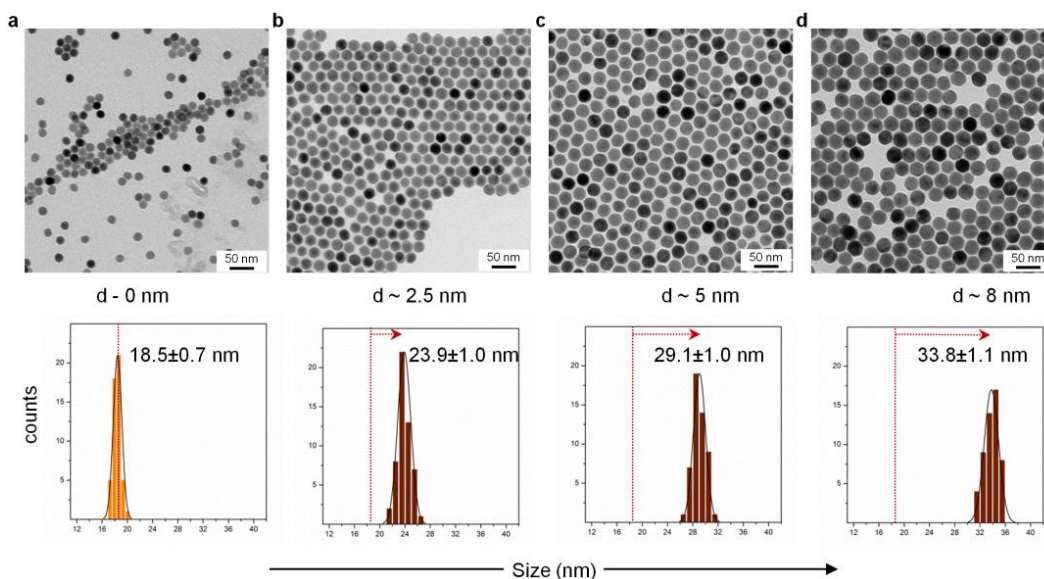


Figure 1.12 (a-d) TEM images of core ($NaErF_4$) and $NaErF_4/NaLuF_4$ core-shell nanocrystals with increasing shell thickness, and corresponding nanocrystal size distribution.

To validate the role of the inert/undoped shell in suppressing surface and concentration quenching, we attempted to reactivate energy migration pathways by modulating the shell thickness, and by introducing dopants into the shell using the 100 mol% Er^{3+} doped nanocrystals (NaErF_4) as core. First, core-shell nanocrystals with an undoped/inert NaLuF_4 shell having variable shell thickness ($d \sim 2.5, 5, \text{ and } 8 \text{ nm}$) were synthesized (see Figure 1.12, and Materials and Methods for synthesis details).

In 100 mol% Er^{3+} core nanocrystals, all of the erbium centers are effectively coupled to the surface, completely quenching the upconverted luminescence at 980 nm excitation (Figure 1.13a-b, $d: 0 \text{ nm}$). After shell growth, we observe a consistent increase in upconversion emission intensity with increasing shell thickness (Figure 1.13a-b), illustrating that the epitaxial shell decouples the erbium centers coupled to the surface (Figure 1.14 shows upconversion directly from the core-shell reaction flask). The strong coupling of surface and concentration quenching processes with increase in dopant concentration in the core is clearly evident on comparing the 5 mol% and 100 mol% Er^{3+} doped core-shell nanocrystals with different shell thickness (Figure 1.13c). The emission intensity of the 100 mol% Er^{3+} -doped nanocrystals with a thin 2.5 nm shell is already three times higher than the 5 mol% Er^{3+} -doped nanocrystals with a thick 10 nm shell, note that as a core, 5 mol% doped nanocrystals are the brightest and 100 mol% doped nanocrystals are completely quenched (dark). Taken together, our findings highlight the striking interdependence of surface and concentration effects, and demonstrate the role of epitaxial shell in decoupling these effects to achieve enhanced photophysical properties from heavily-doped nanostructures.

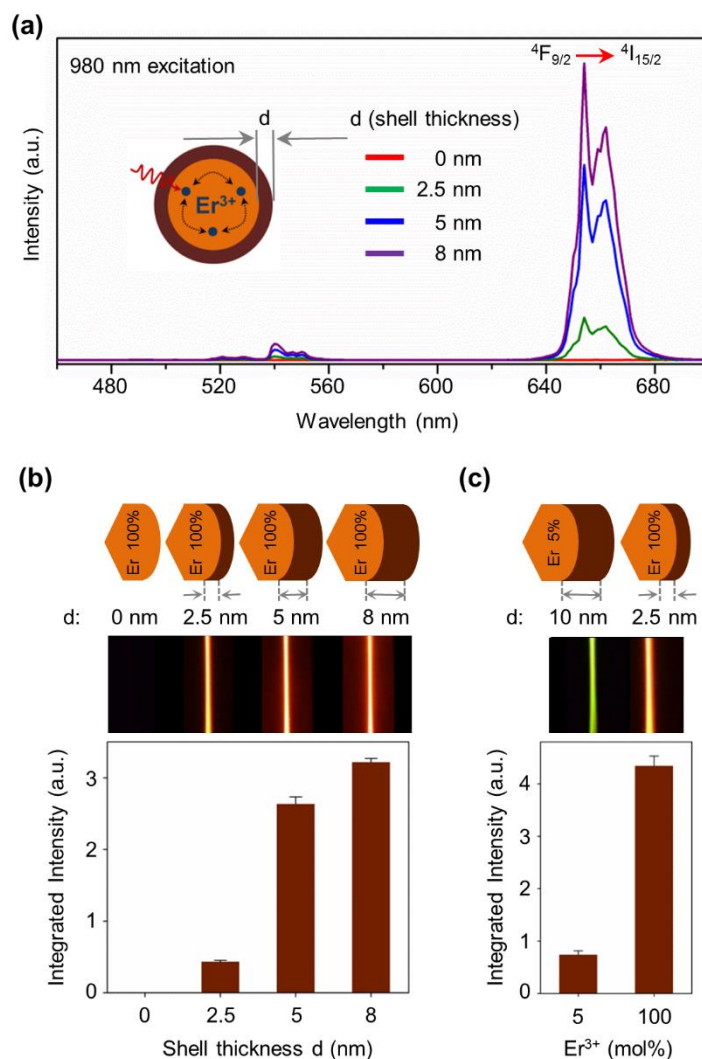


Figure 1.13 (a) Upconversion emission spectra of NaErF₄ core (d : 0 nm), and NaErF₄-NaLuF₄ core-shell nanocrystals with increasing shell thickness, λ_{exc} : 980 nm. (b) Integrated emission intensity as a function of shell thickness, and upconversion emission photos of colloidal dispersion of core-shell nanocrystals as a function of shell thickness. (c) Normalized integrated emission intensity of NaYF₄: Er³⁺(5 mol%)-NaLuF₄ core-shell nanocrystal with a shell thickness of d : 10 nm and NaErF₄-NaLuF₄ core-shell nanocrystal with a shell thickness of d : 2.5 nm, and the respective upconversion emission photos of the colloidal dispersion.

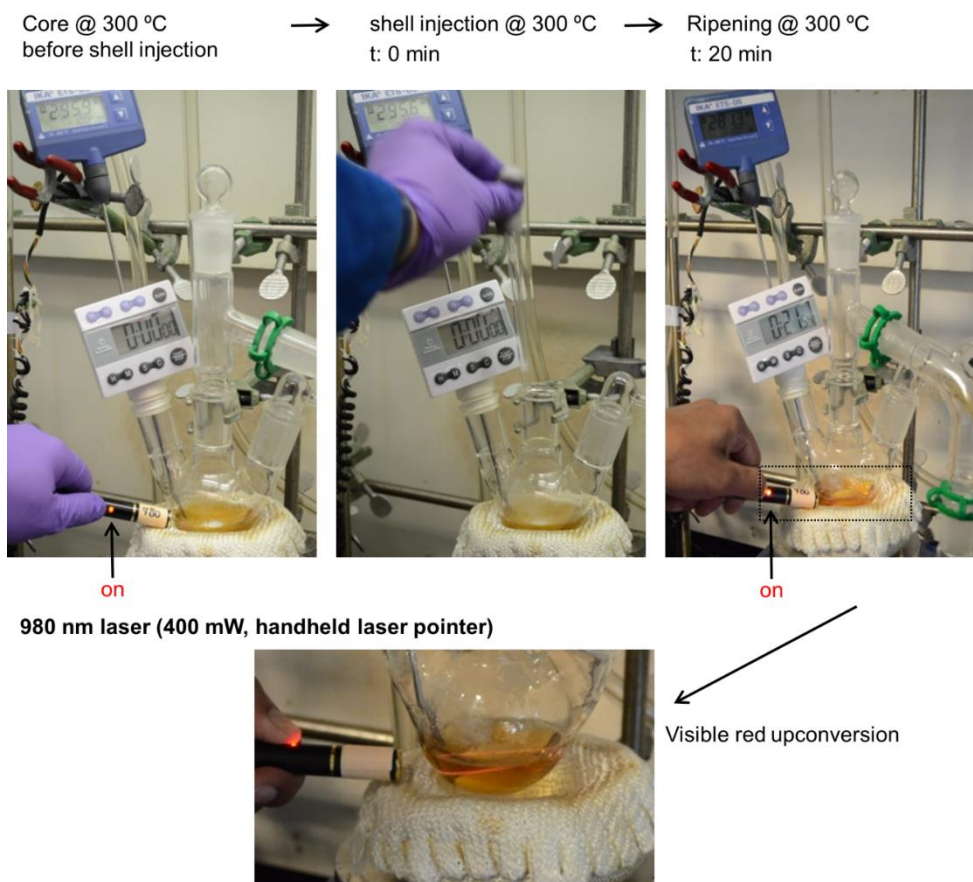


Figure 1.14 Digital photographs of the NaErF₄-NaLuF₄ core-shell reaction mixture at various stages of the reaction and the observed red upconversion using a handheld 980 nm laser (400 mW) pointer from the reaction mixture after 20 min ripening.

Finally, we hypothesized that if energy migration to the surface was the origin of concentration quenching, doping the epitaxial shell would reactivate quenching pathways and quench the emission. Core-shell nanocrystals with variable ytterbium (Yb³⁺) dopants concentrations (10, and 20 mol%) in the shell and 100 mol% Er³⁺ in the core, were used to study upconversion emission at 980 nm excitation (Figure 1.15). Doping ions in separate layers is a common strategy in conventional platforms to enhance the photophysical processes,⁴¹ and to avoid deleterious cross-relaxation between the active emitter and sensitizer ions.

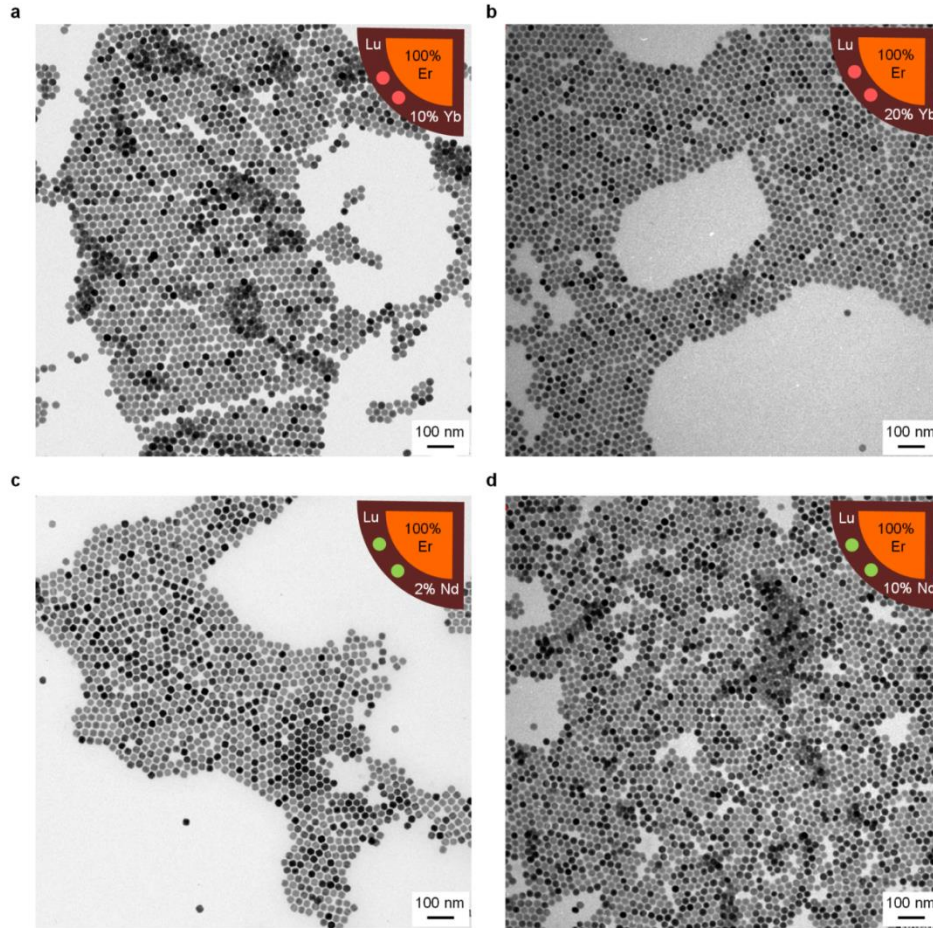


Figure 1.15 TEM images of core-shell nanocrystals with dopants in shell (a) $\text{NaErF}_4\text{-NaLuF}_4\text{:10\% Yb}^{3+}$, (b) $\text{NaErF}_4\text{-NaLuF}_4\text{:20\% Yb}^{3+}$, (c) $\text{NaErF}_4\text{-NaLuF}_4\text{:2\% Nd}^{3+}$, and (d) $\text{NaErF}_4\text{-NaLuF}_4\text{:10\% Nd}^{3+}$.

The overlap of ${}^2\text{F}_{5/2}$ level of Yb^{3+} with ${}^4\text{I}_{11/2}$ level of Er^{3+} (Figure 1.16a) allows for sensitizing upconversion at 980 nm excitation. Yb^{3+} doping in the shell resulted in luminescence quenching with increasing dopant concentration (Figure 1.16b), resulting from the coupling of the core Er^{3+} ions to the surface through the Yb^{3+} centers in the shell. Similarly, doping neodymium (Nd^{3+}) in the shell quenched the upconversion emission under 800 nm excitation, even at very low (2 mol%) dopant concentration in the shell (Figure 1.16c-d). The reactivation of concentration quenching by introducing dopants in the shell and also by modulating the shell thickness further

highlights the critical importance for an inert and thick epitaxial shell to overcome concentration quenching.

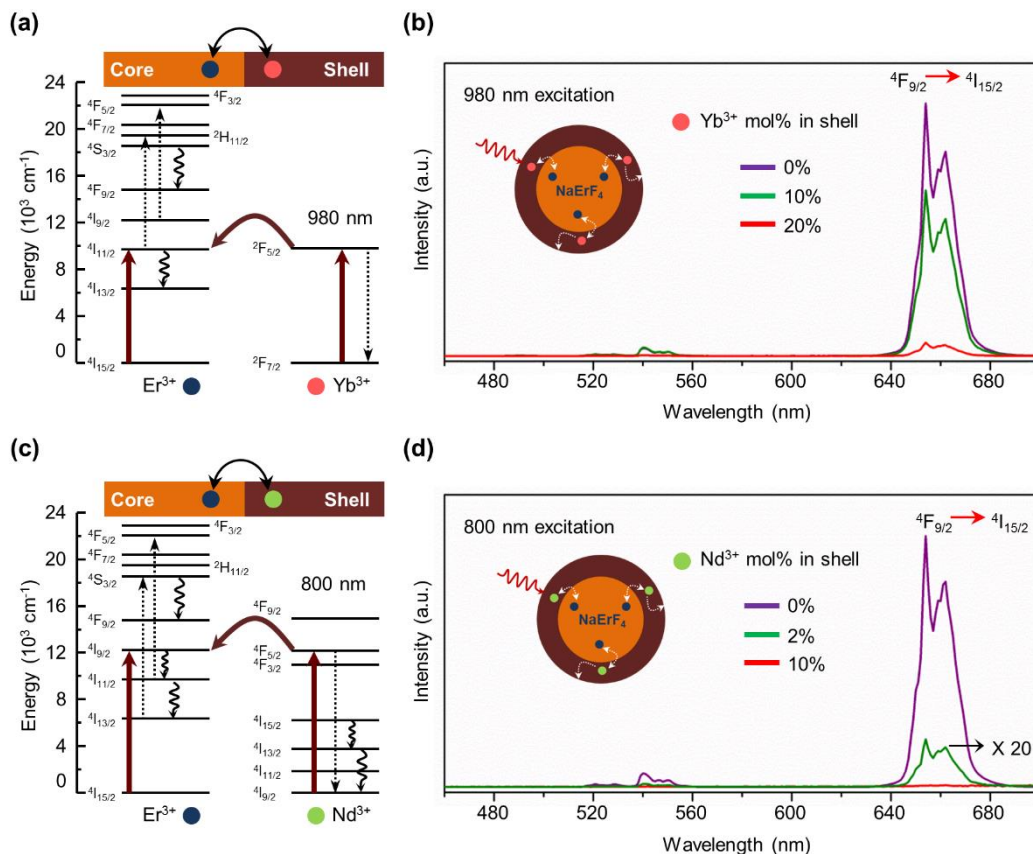


Figure 1.16 (a) Energy levels of core Er^{3+} and sensitizer Yb^{3+} in the shell showing possible energy transfer upon 980 nm excitation. (b) Upconversion emission spectra NaErF_4 - NaLuF_4 core-shell nanocrystals with variable Yb^{3+} doping in the shell. (c) Energy levels of core Er^{3+} and sensitizer Nd^{3+} in the shell showing possible energy transfer upon 800 nm excitation. (d) Upconversion emission spectra NaErF_4 - NaLuF_4 core-shell nanocrystals with variable Nd^{3+} doping in the shell.

We have thus provided here four independent results that together offer definitive evidence that “concentration quenching” is inexorably coupled to and a consequence of energy migration to surface defects. The four supporting evidences are: (1) the concentration dependent quenching of highly doped cores, (2) the strong enhancement of intensity with shell growth, (3) the lack of concentration dependence of the excited state lifetimes in core-shell nanocrystals, and (4) the reactivation of concentration quenching by doping the shells/reducing the shell thickness. Taken

together these results provide a new fundamental insight on the excited state energy dynamics that is unique to core-shell nanostructures, and provide a unique pathway to achieve high dopant concentrations with negligible quenching effects that are not achievable in bulk or core only structures.

1.4 Conclusions

In summary, our results provide new fundamental insights on energy migration, dopant concentration and surface effects in lanthanide-doped nanocrystals. First, the brightest core nanocrystals do not necessarily produce the brightest core-shell structures upon epitaxial growth, which is counter-intuitive. In fact, the brightest core-shell structure is completely “dark” or quenched as a core-only structure, highlighting the strong coupling of surface/concentration effects in nanocrystalline materials. Second, the luminescence decay curves of the heavily doped core-shell nanocrystals unequivocally demonstrate that the major deactivation pathway at high dopant concentrations is the energy migration to the surface as opposed to cross-relaxation between neighboring ions. Third, the enhancement of multiple photophysical processes from heavily doped (100 mol%) core-shell nanocrystals demonstrated here clearly establishes that concentration quenching can be overcome with inert epitaxial shell growth. This unexplored regime of spatially confined heavily doped nanostructures establishes a new paradigm in modulating/enhancing the photophysical processes in lanthanide-doped structures, and open new opportunities towards exploring unique nanoscale compositions that do not necessarily depend on compositions previously optimized in bulk.

1.5 Materials and Methods

Chemicals

Yttrium(III) acetate hydrate (99.9%), erbium(III) acetate hydrate (99.9%), neodymium(III) oxide (99.9%), ytterbium(III) oxide (99.9%), sodium trifluoroacetate (98%), oleic acid (90%), 1-octadecene (90%), Oleylamine (70%) were purchased from Sigma-Aldrich. Lutetium(III) oxide (99.9 %) from Alfa Aesar, sodium hydroxide from Fisher Scientific, ammonium fluoride from Spectrum. All chemicals were used as received.

Synthesis of core nanocrystals

Hexagonal phase (β) NaYF_4 (X mol% Er^{3+}) (X \rightarrow 5, 25, 50) doped nanocrystals were synthesized following previously reported procedure with slight modifications from calculated amounts of $\text{Y}(\text{CH}_3\text{CO}_2)_3 \cdot x\text{H}_2\text{O}$, and $\text{Er}(\text{CH}_3\text{CO}_2)_3 \cdot x\text{H}_2\text{O}$ to a total of 1.0 mmol.³² In a typical synthesis, acetate salts (1.0 mmol), oleic acid (6 mL), and 1-octadecene (17 mL) were taken in a 100 mL flask and heated to 120 °C under vacuum for 1 h and cooled to room temperature. To this solution at room temperature, methanol solution (10 mL) of ammonium fluoride (4 mmol) and sodium hydroxide (2.5 mmol) was added and stirred for 1 h. The reaction vessel was then heated to 70 °C to remove methanol and subsequently heated to 300 °C ($\sim 10^\circ\text{C}/\text{min}$) under argon and maintained for 60 min to obtain the erbium doped core NaYF_4 nanocrystals. (The shell growth was then performed directly on the core nanocrystals using sacrificial nanocrystals; *see section core-shell synthesis below*). Hexagonal phase (β) NaErF_4 nanocrystals were synthesized as described for the (β) NaYF_4 doped nanocrystals except that, $\text{Er}(\text{CH}_3\text{CO}_2)_3 \cdot x\text{H}_2\text{O}$ (1.0 mmol), oleic acid (4.5 mL), and 1-octadecene (15 mL) were used.

Synthesis of sacrificial nanocrystals as shell precursors

Cubic (α) NaLuF₄ nanocrystals were synthesized based on a previously reported procedure with slight modifications.³³ In a typical synthesis Lu₂O₃ (1 mmol) was mixed with 20 mL of 50 % aqueous trifluoroacetic acid and refluxed at 95 °C overnight to get a clear solution. The trifluoroacetate precursor (Lu(CF₃COO)₃) was then obtained as dry powder after removing excess trifluoroacetic acid and water at 65 °C. Sodium trifluoroacetate (2 mmol) was added to the lutetium trifluoroacetate precursor along with oleic acid (6 mL), oleylamine (6 mL), and 1-octadecene (12 mL) and heated to 120 °C under vacuum for 30 min to get a clear solution. The solution was subsequently heated to 300 °C (~20 °C/min) under argon and vigorously stirred until the reaction mixture turned turbid. Once turbid the reaction was left for another 5 min and then cooled to room temperature. The nanocrystals were precipitated by addition of ethanol, collected by centrifugation (1900 g, 5 min), washed with ethanol and dispersed in hexane. Cubic (α) NaLuF₄ (X mol% Nd³⁺) (X: 2, 10) doped nanocrystals were synthesized as described for the undoped cubic NaLuF₄, using Lu₂O₃ and Nd₂O₃ in respective molar ratios. Cubic (α) NaLuF₄ (X mol% Yb³⁺) (X: 10, 20) doped nanocrystals were synthesized as described for the undoped cubic NaLuF₄, using Lu₂O₃ and Yb₂O₃ in respective molar ratios.

Synthesis of core-shell nanocrystals

Hexagonal phase (β) NaYF₄ (X mol% Er³⁺) (X→5, 25, 50, 100) core / NaLuF₄ shell nanocrystals were synthesized following a previously reported method based on self-focusing by ripening.²⁴ To the core nanocrystals synthesized as described above, after 1 h at 300 °C, sacrificial nanocrystals (0.5 mmol, α -NaLuF₄) in 1-octadecene (1 mL) was injected and ripened for 12 min, followed by five more sacrificial nanoparticle injection (0.5 mmol each) and ripening cycle of 12

min each to yield core-shell NCs. After the final injection and ripening cycle (total ~3 mmol) the solution was cooled down to room temperature and the core-shell nanocrystals were precipitated by addition of ethanol, collected by centrifugation (1900 g, 5 min), and washed with ethanol before dispersing them in chloroform (10 mL).

Hexagonal phase (β) NaErF₄ core / NaLuF₄ (X mol% Nd³⁺) (X: 2, 10) doped shell nanocrystals were synthesized as described above using sacrificial (α -NaLuF₄:X mol% Nd³⁺ doped/ X: 2, 10) nanocrystals were used as shell precursors. Hexagonal phase (β) NaErF₄ core / NaLuF₄ (X mol% Yb³⁺) (X: 10, 20) doped shell nanocrystals were synthesized as described above except that, sacrificial (α -NaLuF₄:X mol% Yb³⁺ doped/X: 10, 20) nanocrystals were used as shell precursors.

Hexagonal phase (β) NaErF₄ core / NaLuF₄ shell nanocrystals with variable shell thickness were synthesized as described above for NaErF₄ core / NaLuF₄ shell nanocrystals. To the core nanocrystals synthesized as described above, after 1 h at 300 °C aliquot of the reaction mixture (1 mL) was retrieved as core nanocrystals and, sacrificial (0.5 mmol, α -NaLuF₄) in 1-octadecene (1 mL) was injected and ripened for 12 min, followed by five more sacrificial nanoparticle injection (0.5 mmol each) and ripening cycle of 12 min each to yield core-shell NCs. Core-shell nanocrystals with variable shell thickness was obtained by removing reaction mixture (1 mL) after every two injection and ripening cycle, totaling an injection of ~ 1 mmol shell sacrificial nanocrystals for every shell thickness. After the final injection and ripening cycle (total ~3 mmol) the solution was cooled down to room temperature and the core-shell nanocrystals were precipitated by addition of ethanol, collected by centrifugation (1900 g, 5 min), and washed with ethanol before dispersing them in chloroform (10 mL). The obtained reaction aliquots with core and core-shell nanocrystals with variable shell thickness were purified as described above and dispersed in chloroform (1 mL).

Characterization

Hexane dispersions of the nanocrystals were drop cast on a carbon-coated (400 mesh Cu) grid and air-dried before imaging. Size and size distribution analysis from the TEM images were obtained by measuring approximately 50 crystals. High resolution transmission electron microscopy (HR-TEM) images were obtained from a FEI Sphera microscope operating at 120 kV. Scanning electron microscopy (SEM) images were obtained from a FEI SFEG-UHR (Ultra high resolution) microscope. Hexane dispersions of the nanocrystals were drop cast on a silicon wafer and dried under vacuum before imaging. Powder X-ray diffraction (XRD) patterns were collected using a Bruker D8 Advance equipped with a 1-D Lynxeye silicon strip detector and Cu radiation ($K\alpha$ radiation, $\lambda=1.54178 \text{ \AA}$) using a step size of 0.02° and scan rate of 0.25 s per step . The sample was spun during collection to limit preferred orientation peaks. Upconversion emission spectra were obtained using a Fluorolog modular spectrofluorometer (Horiba) coupled with a 980 or 800 nm CW diode laser (Thorlabs) at an irradiance of $50\text{-}60 \text{ W cm}^{-2}$. Absolute upconversion quantum yield was obtained using a Horiba Jobin Yvon Fluorolog-3 spectrometer and a calibrated integrating sphere using a 980 nm CW diode laser operating at 10 W cm^{-2} . A neutral density filter on the excitation side (Thorlabs, NDUV10A, OD:1.0) was used, along with a short-pass filter on the emission end (Semrock, FF01-750/SP-25). The colloidal nanocrystal dispersion in toluene and solvent alone as blank were taken in a cylindrical quartz cuvette and used for determining the upconversion quantum yield. Emission spectra of the nanocrystal dispersion and the blank solvent were collected at 10 W cm^{-2} between 500-750 nm, along with the spectra of the scattered excitation light (970-990 nm) and corrected for detector sensitivity. The absolute quantum yield (QY) of the sample was determined from the integrated intensity of the emission (em) and scattering (Ex) spectrum, and calculated from $QY = (I_{em,NCs} - I_{em,blank}) / (I_{ex,blank} - I_{ex,NCs})$. Average QY was obtained

from five successive measurements, where one measurement refers to the sample emission spectra, and then collecting the sample scattered excitation light spectra, this is followed by replacing the sample with the solvent blank reference and collecting the excitation light spectra scattered by the solvent followed by emission spectra of the blank. The absolute QY for these each measurement was determined as described above and averaged. Lifetime measurements were obtained from Edinburgh FLS980 spectrometer with single monochromators and multichannel scaling (MCS) mode. The maximum pulse duration was 360 μ s. The excitation laser for 800 nm was a CNI laser (MLL-H-800-2.5W), and for 980 nm was a CNI laser (MLL-III-980-2W). On the emission end, a short-pass filter was used (Semrock, FF01-750/SP-25), and an excitation single-band bandpass filter for the 800 nm laser (FF01-794/32-25). Average excited state lifetimes were determined from bi-exponential fits and calculated using $\tau_{\text{avg}} = (A_1\tau_1^2 + A_2\tau_2^2)/(A_1\tau_1 + A_2\tau_2)$. Emission spectra of the downshifted emission in the NIR spectral region was collected with an Acton SP2300i spectrometer equipped with an InGaAs linear array detector (Princeton OMA-V) and using an 808 or 658 nm laser excitation. NIR fluorescence images of the downshifted emission were obtained using 2D InGaAs array (Princeton Instruments) with 350*256 pixel using 808 or 658 nm laser excitation at 1 or 5 ms exposure respectively.

Chapter 1, in full, is a reprint of the material as it appears in *J. Am. Chem. Soc.* 2017. Noah J. J. Johnson, Sha He, Shuo Diao, Emory M. Chan, Hongjie Dai, Adah Almutairi, American Chemical Society Press, 2017. The dissertation author was the primary investigator and author of this paper.

1.6 References

1. Wang, F.; Han, Y.; Lim, C. S.; Lu, Y.; Wang, J.; Xu, J.; Chen, H.; Zhang, C.; Hong, M.; Liu, X., Simultaneous phase and size control of upconversion nanocrystals through lanthanide doping. *Nature* **2010**, *463*, 1061-1065.
2. Wu, S.; Han, G.; Milliron, D. J.; Aloni, S.; Altoe, V.; Talapin, D. V.; Cohen, B. E.; Schuck, P. J., Non-blinking and photostable upconverted luminescence from single lanthanide-doped nanocrystals. *Proc. Natl. Acad. Sci. USA* **2009**, *106*, 10917-10921.
3. Su, L. T.; Karuturi, S. K.; Luo, J.; Liu, L.; Liu, X.; Guo, J.; Sum, T. C.; Deng, R.; Fan, H. J.; Liu, X.; Tok, A. I. Y., Photon upconversion in hetero-nanostructured photoanodes for enhanced near-infrared light harvesting. *Adv Mater* **2013**, *25*, 1603-1607.
4. Goldschmidt, J. C.; Fischer, S., Upconversion for photovoltaics – a review of materials, devices and concepts for performance enhancement. *Adv Opt Mater* **2015**, *3*, 510-535.
5. Haase, M.; Schäfer, H., Upconverting nanoparticles. *Angew Chem Int Ed Engl* **2011**, *50*, 5808-5829.
6. Wegh, R. T.; Donker, H.; Oskam, K. D.; Meijerink, A., Visible quantum cutting in LiGdF₄ : Eu³⁺ through downconversion. *Science* **1999**, *283*, 663-666.
7. Auzel, F., Upconversion and anti-stokes processes with f and d ions in solids. *Chem. Rev.* **2004**, *104*, 139-173.
8. Dong, H.; Sun, L.-D.; Yan, C.-H., Energy transfer in lanthanide upconversion studies for extended optical applications. *Chem Soc Rev* **2015**, *44*, 1608-1634.
9. Huang, X.; Han, S.; Huang, W.; Liu, X., Enhancing solar cell efficiency: The search for luminescent materials as spectral converters. *Chem Soc Rev* **2013**, *42*, 173-201.
10. Ye, X.; Collins, J. E.; Kang, Y.; Chen, J.; Chen, D. T. N.; Yodh, A. G.; Murray, C. B., Morphologically controlled synthesis of colloidal upconversion nanophosphors and their shape-directed self-assembly. *Proc Natl Acad Sci USA* **2010**, *107*, 22430-22435.
11. Zhang, Y.; Liu, X., Nanocrystals: Shining a light on upconversion. *Nat. Nanotechnol.* **2013**, *8*, 702-703.
12. Stouwdam, J. W.; van Veggel, F. C. J. M., Near-infrared emission of redispersible Er³⁺, Nd³⁺, and Ho³⁺ doped LaF₃ nanoparticles. *Nano Lett.* **2002**, *2*, 733-737.

13. Tu, L.; Liu, X.; Wu, F.; Zhang, H., Excitation energy migration dynamics in upconversion nanomaterials. *Chem Soc Rev* **2015**, *44*, 1331-1345.
14. Zheng, W.; Huang, P.; Tu, D. T.; Ma, E.; Zhu, H. M.; Chen, X. Y., Lanthanide-doped upconversion nano-bioprobes: electronic structures, optical properties, and biodetection. *Chem. Soc. Rev.* **2015**, *44*, 1379-1415.
15. Johnson, N. J. J.; van Veggel, F. C. J. M., Sodium lanthanide fluoride core-shell nanocrystals: A general perspective on epitaxial shell growth. *Nano Res.* **2013**, *6*, 547-561.
16. Chen, G.; Agren, H.; Ohulchanskyy, T. Y.; Prasad, P. N., Light upconverting core-shell nanostructures: nanophotonic control for emerging applications. *Chem Soc Rev* **2015**, *44*, 1680-1713.
17. Wang, F.; Wang, J. A.; Liu, X. G., Direct evidence of a surface quenching effect on size-dependent luminescence of upconversion nanoparticles. *Angew Chem Int Ed Engl* **2010**, *49*, 7456-7460.
18. Zhang, F.; Che, R. C.; Li, X. M.; Yao, C.; Yang, J. P.; Shen, D. K.; Hu, P.; Li, W.; Zhao, D. Y., Direct imaging the upconversion nanocrystal core/shell structure at the subnanometer level: Shell thickness dependence in upconverting optical properties. *Nano Lett* **2012**, *12*, 2852-2858.
19. Johnson, N. J. J.; Korinek, A.; Dong, C.; van Veggel, F. C. J. M., Self-focusing by Ostwald ripening: A strategy for layer-by-layer epitaxial growth on upconverting nanocrystals. *J Am Chem Soc* **2012**, *134*, 11068-11071.
20. Su, Q.; Han, S.; Xie, X.; Zhu, H.; Chen, H.; Chen, C.-K.; Liu, R.-S.; Chen, X.; Wang, F.; Liu, X., The effect of surface coating on energy migration-mediated upconversion. *J Am Chem Soc* **2012**, *134*, 20849-20857.
21. Li, Z. Q.; Zhang, Y.; Jiang, S., Multicolor core/shell-structured upconversion fluorescent nanoparticles. *Adv Mater* **2008**, *20*, 4765-4769.
22. Johnson, N. J. J.; van Veggel, F. C. J. M., Lanthanide-based heteroepitaxial core-shell nanostructures: Compressive versus tensile strain asymmetry. *ACS Nano* **2014**, *8*, 10517-10527.
23. Wang, Y. F.; Liu, G. Y.; Sun, L. D.; Xiao, J. W.; Zhou, J. C.; Yan, C. H., Nd³⁺-Sensitized Upconversion Nanophosphors: Efficient In Vivo Bioimaging Probes with Minimized Heating Effect. *ACS Nano* **2013**, *7*, 7200-7206.
24. Xie, X. J.; Gao, N. Y.; Deng, R. R.; Sun, Q.; Xu, Q. H.; Liu, X. G., Mechanistic investigation

- of photon upconversion in Nd³⁺-sensitized core-shell nanoparticles. *J Am Chem Soc* **2013**, *135*, 12608-12611.
25. Naczynski, D. J.; Tan, M. C.; Zevon, M.; Wall, B.; Kohl, J.; Kulesa, A.; Chen, S.; Roth, C. M.; Riman, R. E.; Moghe, P. V., Rare-earth-doped biological composites as in vivo shortwave infrared reporters. *Nat Commun* **2013**, *4*, 2199.
 26. Hong, G.; Diao, S.; Chang, J.; Antaris, A. L.; Chen, C.; Zhang, B.; Zhao, S.; Atochin, D. N.; Huang, P. L.; Andreasson, K. I.; Kuo, C. J.; Dai, H., Through-skull fluorescence imaging of the brain in a new near-infrared window. *Nat Photonics* **2014**, *8*, 723-730.
 27. Hong, G.; Zou, Y.; Antaris, A. L.; Diao, S.; Wu, D.; Cheng, K.; Zhang, X.; Chen, C.; Liu, B.; He, Y.; Wu, J. Z.; Yuan, J.; Zhang, B.; Tao, Z.; Fukunaga, C.; Dai, H., Ultrafast fluorescence imaging in vivo with conjugated polymer fluorophores in the second near-infrared window. *Nat Commun* **2014**, *5*, 4206.
 28. Polman, A., Erbium implanted thin film photonic materials. *J Appl Phys* **1997**, *82*, 1-39.
 29. Miritello, M.; Cardile, P.; Lo Savio, R.; Priolo, F., Energy transfer and enhanced 1.54 μm emission in erbium-ytterbium disilicate thin films. *Opt Express* **2011**, *19*, 20761-20772.

Chapter 2

On the Critical Role of Optically Inert Epitaxial Shell in Enhancing Upconversion Luminescence of Core-Shell Nanoparticles

2.1 Abstract

Lanthanide-doped upconversion nanoparticles (UCNPs) suffer from the intrinsically weak optical transitions, and various strategies have been developed to enhance the optical emission. Designing core-shell UCNPs featuring “active shell”, i.e. doping sensitizers in the shell has been one of the most prevalent strategies because it increases the absorption of excitation light. However, how the active shell affects the overall upconversion processes besides increasing absorption is poorly characterized and investigated. Herein, by tuning the doping level (0 – 100 mol%) of sensitizers (Yb^{3+}) in the shell of core-shell UCNPs, we systematically characterized how active shells affect the overall upconversion emission efficiency. We show that sensitizers (Yb^{3+}) doped in the shell enable significant migration/bridging of excitation energy to the surface while absorbing more excitation light. The former factor overwhelms the latter one, and the overall upconversion luminescence intensity monotonically decreases with the increased doping level of sensitizers in the shell, which is contradictory to the commonly accepted concept of using active shell to enhance upconversion luminescence. The UCNPs coated with inert shell (NaLuF_4), even with the least absorbance of excitation light, have the brightest upconversion emission because the surface quenching pathways are effectively cut off. Our results highlight the critical role of optically inert shells in dramatically enhancing upconversion emission where active shell with higher absorbance cannot achieve. The findings give rise to the fundamental understanding of the

photophysical process in the core–shell UCNPs and should provide guidance in designing highly luminescent core–shell NPs for various applications.

2.2 Introduction

Lanthanide-doped colloidal nanoparticles (NPs) have been attracting increasing research interest in myriad research fields because of their versatile yet tunable optical properties.¹⁻² With the unique 4f manifold in lanthanide trivalent cations, NPs co-doped with various lanthanide ions can be excited and emit at a broad spectrum of wavelengths ranging from ultraviolet (UV) to near infrared (NIR) regime.³⁻⁴ One of the most attractive features of the lanthanide-doped NPs is upconversion (UC), i.e. anti-stokes shift photoluminescence.⁵ With the ladder-like energy levels and relatively long lifetime on the intermediate energy levels, lanthanide-doped NPs absorb multiple low-energy photons, usually near-infrared (NIR) photons under low irradiance, and convert them into high-energy photons, mostly as visible or ultraviolet (UV) emission. This unique property brings numerous advantages to the existing optics research platforms.⁶⁻⁸ For example, upconversion nanoparticles (UCNPs) with NIR light excitation brings much less background interference and penetrates deeper into tissue for bioimaging, overcoming the limitations of conventional bioimaging nanoprobe.⁹⁻¹³ UCNPs can also enhance the performance of conventional solar cells by harvesting sub-bandgap photons from solar spectrum to supra-bandgap photons for enhanced photocurrent generation with the same irradiation.^{12, 14-16} Together with sharp emission bands, long luminescence decay lifetime, and excellent photostability, lanthanide-doped UCNPs have found a broad range of optics-related applications including lasing, lightning, and photon management.¹⁷⁻¹⁸

Despite these prospects, UC is intrinsically an inefficient process, and the upconverted luminescence is usually extremely weak, which greatly limits its application in practical settings. Various strategies have been explored to enhance the upconverted luminescence intensity of UCNPs either by increasing the absorbance or by mitigating the quenching of emission. Increasing the doping concentration of optically active lanthanide ions, usually sensitizers (Yb^{3+} , Nd^{3+}) in the UCNPs¹⁹⁻²⁰ enhances the absorption of excitation light, but it also raises the possibility of energy-migration-induced luminescence quenching. Coating epitaxial shell on the core NPs is another dominant strategy to enhance the photoluminescence because it reduces the possible migration of excitation energy to the surface sites and defects. The combination of these two strategies, known as the active-shell approach,²¹ features coating epitaxial shell doped with sensitizers on the luminescent core NPs to enhance the optical emission. For example, it has been demonstrated that the $\text{NaYF}_4:\text{Yb}/\text{Er}@\text{NaGdF}_4:\text{Yb}/\text{Nd}$ core-shell UCNPs have brighter UC luminescence than $\text{NaYF}_4:\text{Yb}/\text{Er}$ core NPs upon excitation at various wavelengths (980 nm, 808 nm).²² This approach has gained a lot of research attention because of its simplicity and effectiveness in harvesting more incident light and contributing to the enhanced emission intensity.²³⁻²⁸

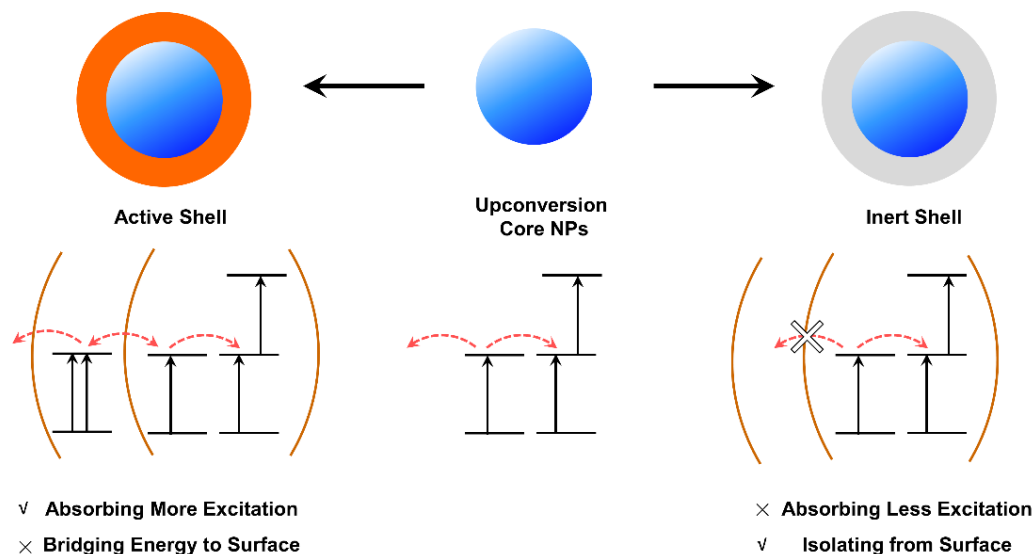
However, for photoluminescent colloidal NPs such as semiconducting quantum dots, gold nanoclusters, and lanthanide-doped UCNPs, etc., a large fraction of atoms/ions are on the NP surface and lie within the characteristic distance of energy migration.²⁹⁻³⁰ The energy at the excited states upon absorption of incident photons is susceptible to surface quenching, which significantly decreases the luminescence intensity. It has been established that proper shielding of excitation energy in the core NPs from surface quenching using epitaxial shells effectively reduces surface quenching and enhances the emission intensity.³¹⁻³² Doping extra optically active ions in the epitaxial shell has been proved to reintroduce the quenching pathways to the excited energy in the

core NPs.³³⁻³⁵ In the case of lanthanide-doped UCNPs with active shell, the possibility of bridging excitation energy to the surface sites *via* sensitizers doped in the shell, or the negative effect of active shells, is usually not considered and well characterized besides the known contribution of increasing absorption of incident light.²¹ We reasoned that the overall contribution of active shell to the luminescence of UCNPs could be more complicated, and both of the positive and negative factors of active shells need to be systematically characterized to evaluate how doping in the shell determines the luminescence intensity of UCNPs and to obtain insight in designing highly emissive core-shell UCNPs.

2.3 Results and Discussion

Herein, using hexagonal phase (β)-NaYF₄:Gd/Yb/Er as core NPs and NaLuF₄:Yb (x mol%) ($0 < x < 100$) as the epitaxial shells with tunable doping concentrations, we systematically investigated how doping sensitizers in the shell (resulting in active shell *versus* inert shell) affects the UC luminescence of core-shell UCNPs by considering both absorption of excitation light and energy migration to the surfaces (Scheme 2.1). We show that sensitizers (Yb³⁺) doped in the shell enable significant migration/bridging of excitation energy in the core to the surface while absorbing more incident light. The former factor is more dominant than the latter one, and the overall UC luminescence intensity monotonically decreases with the increased doping level of sensitizers in the shell. This, however, is contradictory to the commonly accepted conception that active shell design enhances UC luminescence intensity. The core-shell UCNPs with active shell coating (NaYbF₄) have the lowest emission intensity although with the highest absorbance to incident light (980 nm). On the contrary, the UCNPs with inert shell coating (NaLuF₄), although with the least absorbance to 980 nm excitation, have the brightest UC luminescence due to the

effective cutoff of the quenching pathways from the core NPs to the surfaces sites. To highlight, we emphasize the critical role of inert epitaxial shells in enhancing UC luminescence of core-shell UCNPs.



Scheme 2.1 Lanthanide-doped core and core-shell UCNPs. In the center, core UCNPs are susceptible to surface quenching and thus have weak luminescence. On the left, an epitaxial coating of the active shell (NaYbF_4) onto the core enhance the absorbance of excitation light to the NPs but also bridge more excited energy to the surface quenchers, therefore not greatly enhancing the UC luminescence. On the right, an epitaxial coating of the inert shell onto the core isolates the excited energy in the core from surface quenchers and therefore enhance the UC luminescence, although not promoting the absorbance of the NPs.

We took a well-established protocol³⁶ to synthesize core-shell UCNPs with the same compositions $\beta\text{-NaYF}_4\text{:Gd(10\%/Yb(18\%/Er(2\%))$ in the core, but different compositions $\beta\text{-NaLuF}_4\text{:Yb}$ (x mol%, $0 < x < 100$) in the shell (See Materials and Methods for details). $\beta\text{-NaYF}_4$ NPs co-doped with the sensitizers Yb^{3+} and the activators Er^{3+} are one of the most efficient UC system known to date and have been commonly used as the model system for mechanistic investigations of various UC processes.³⁷ Gd^{3+} is doped into the NP crystal lattice to facilitate the formation of hexagonal phase and to control the size of the NPs.³⁸ The β -

NaYF₄:Gd(10%)/Yb(18%)/Er(2%) core NPs had diameters around 16 nm (Figure 2.1a), which is in perfect agreement with previously reported results.

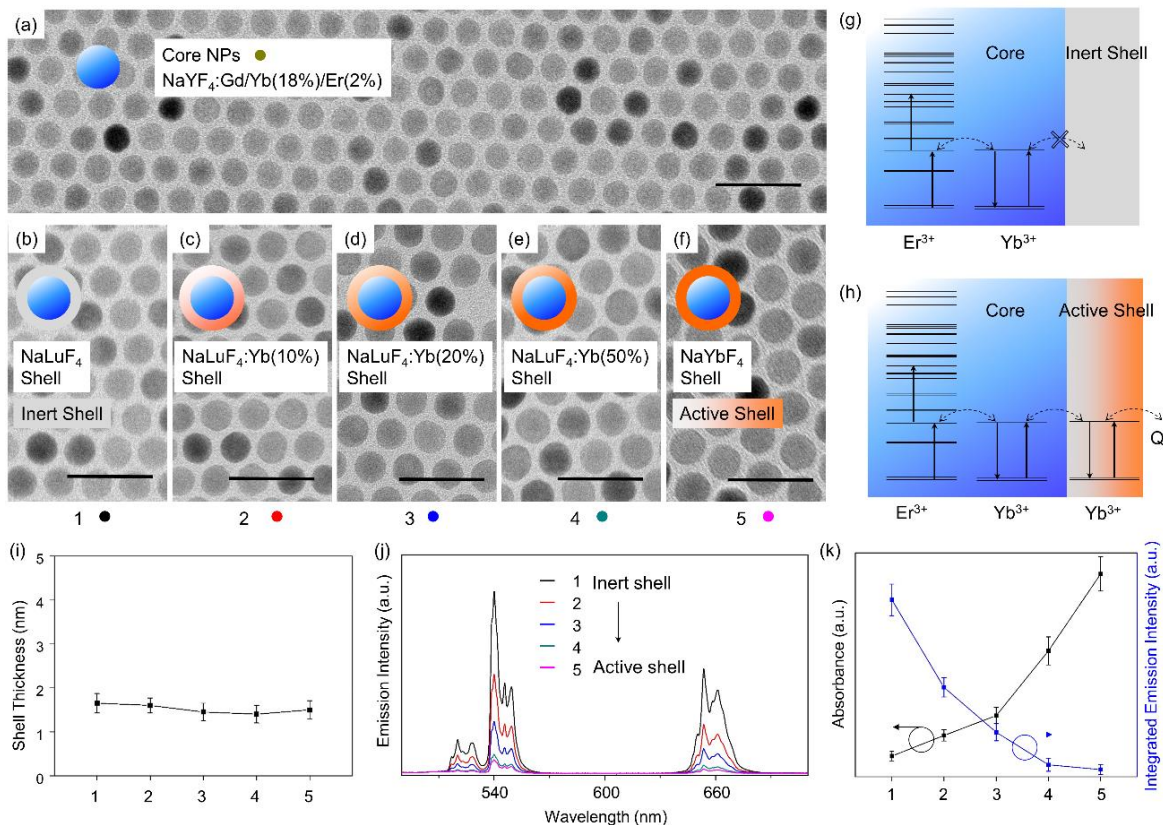


Figure 2.1 TEM images of the (a) NaYF₄:Gd/Yb/Er core UCNPs, (b) core@NaLuF₄, denoted as “1”, black dot, (c) core@NaLuF₄:Yb(10%), denoted as “2”, red dot, (d) core@NaLuF₄:Yb(20%), denoted as “3”, blue dot, (e) core@NaLuF₄:Yb(50%), denoted as “4”, green dot, and (f) core@NaYbF₄, denoted as “5”, magenta dot, core–shell UCNPs. Simplified energy levels of the (g) core/inert shell UCNPs and (h) core/active shell UCNPs. (i) Shell thickness of the each core–shell UCNPs. (j) UC luminescence spectra in the visible light range of each core–shell UCNPs when excited at 980 nm. (k) Comparison of the absorbance (black) and integrated emission intensity (blue) of each core–shell UCNPs.

We chose NaLuF₄:Yb (x mol%, $0 < x < 100$) as the shell epitaxially grown on core NPs because both NaLuF₄ and NaYbF₄ have smaller crystal lattices than the core, and therefore they can grow uniformly and concentrically on the core NPs.³⁹ Uniform core–shell architectures are critical to accurate optical characterization in this study because they rule out the possibility of structural deformation-induced luminescence changes.

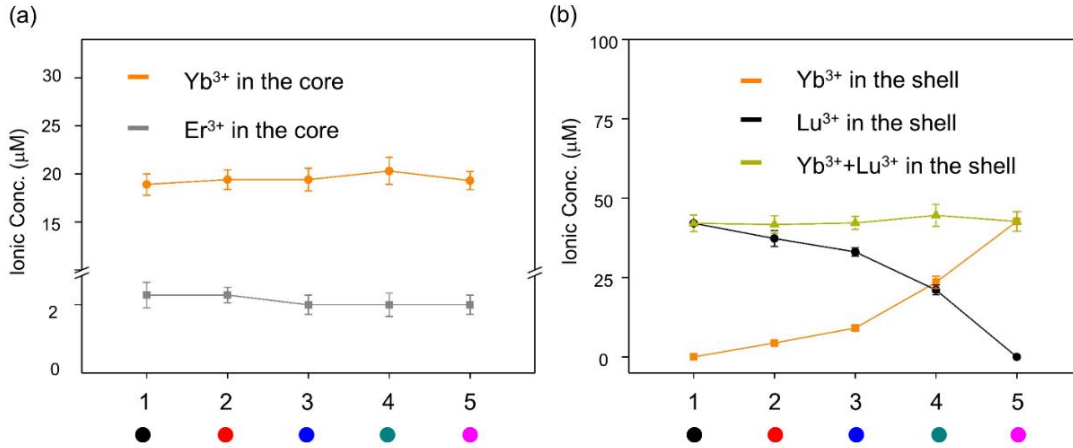


Figure 2.2 Ionic concentration of the dopants in the (a) core and (b) shells of the core-shell UCNPs shown in Figure 2.1.

Also, the fact that the sensitizers (Yb^{3+}) in the core and shell lattice are the same allows us to study the energy transfer between core and shell, and possibly provides more insight in how the doping in the shell can affect the excitation energy in the cores. We elevated the doping concentration of Yb^{3+} in the shell from 0% to 10%, 20%, 50%, and finally to 100% while compensating them with optically inert Lu^{3+} ions (Figure 2.1 b–f). The elemental concentration of different dopants in each sample were confirmed with inductively coupled plasma atomic emission spectroscopy (ICP-AES) (Figure 2.2). The core-shell architectures are all uniform, and the shell thicknesses of all five samples are found between 1.7 nm and 1.9 nm regardless of the shell compositions (Figure 2.1i), indicating that this class of core-shell UCNPs are suitable for investigating how the doping levels as the only factor can affect the UC luminescence.

First, we characterized the steady-state emission of five core-shell UCNPs respectively by exciting them with a 980 nm NIR diode laser (corresponding to the transition ${}^2\text{F}_{7/2} \rightarrow {}^2\text{F}_{5/2}$ in Yb^{3+}) and recording their upconverting luminescence spectra in the visible range from 480 nm to 720 nm. All five samples have two major emission peaks centered at 540 nm and 654 nm (Figure 2.1j), corresponding to the transitions ${}^4\text{S}_{3/2} \rightarrow {}^4\text{I}_{15/2}$ and ${}^4\text{F}_{9/2} \rightarrow {}^4\text{I}_{15/2}$ of Er^{3+} (Figure 2.1g, h), respectively.

This suggests that the doping level of sensitizers in the shell does not affect the position of emission peaks from the activators in the core, again demonstrating the suitability of this system in investigating the change of luminescence intensity. However, different from the previously reported findings that core-shell NPs with 10% – 20% doping of Yb^{3+} in the shell (i.e. active shells) have the highest emission intensity,²¹ we observed a monotonic decrease of the UC emission intensity with the increasing doping level of the active ions (Yb^{3+}) in the shell (Figure 2.1j). The $\beta\text{-NaYF}_4\text{:Gd(10\%/Yb(18\%/Er(2\%))@NaLuF}_4$ core-shell NPs (inert shell) have the highest emission intensity and the intensity drastically dropped by half with only 10% Yb^{3+} doping introduced in the NaLuF_4 shell ($\beta\text{-NaYF}_4\text{:Gd(10\%/Yb(18\%/Er(2\%))@NaLuF}_4\text{:Yb(10\%)}$) (Figure 2.1k). When the doping concentration of Yb^{3+} is increased to 100% to form completely optically active shell (NaYbF_4) on the core with maximized absorbance, the overall emission intensity is only one-tenth of that for the core NPs with completely inert shells (NaLuF_4). Notably, even the UC emission intensity monotonically decreased, the absorbance of the core-shell NPs increased by almost 10 times from inert shell (NaLuF_4) to active shell (NaYbF_4) samples (Figure 2.1k), which reflects the increasing doping level of Yb^{3+} in the shell (Figure 2.2). This striking negative correlation between the absorbance and emission in core-shell UCNPs clearly demonstrated that doping sensitizers to construct active shells on the core NPs is not the appropriate approach to elevating emission brightness of core-shell UCNPs.

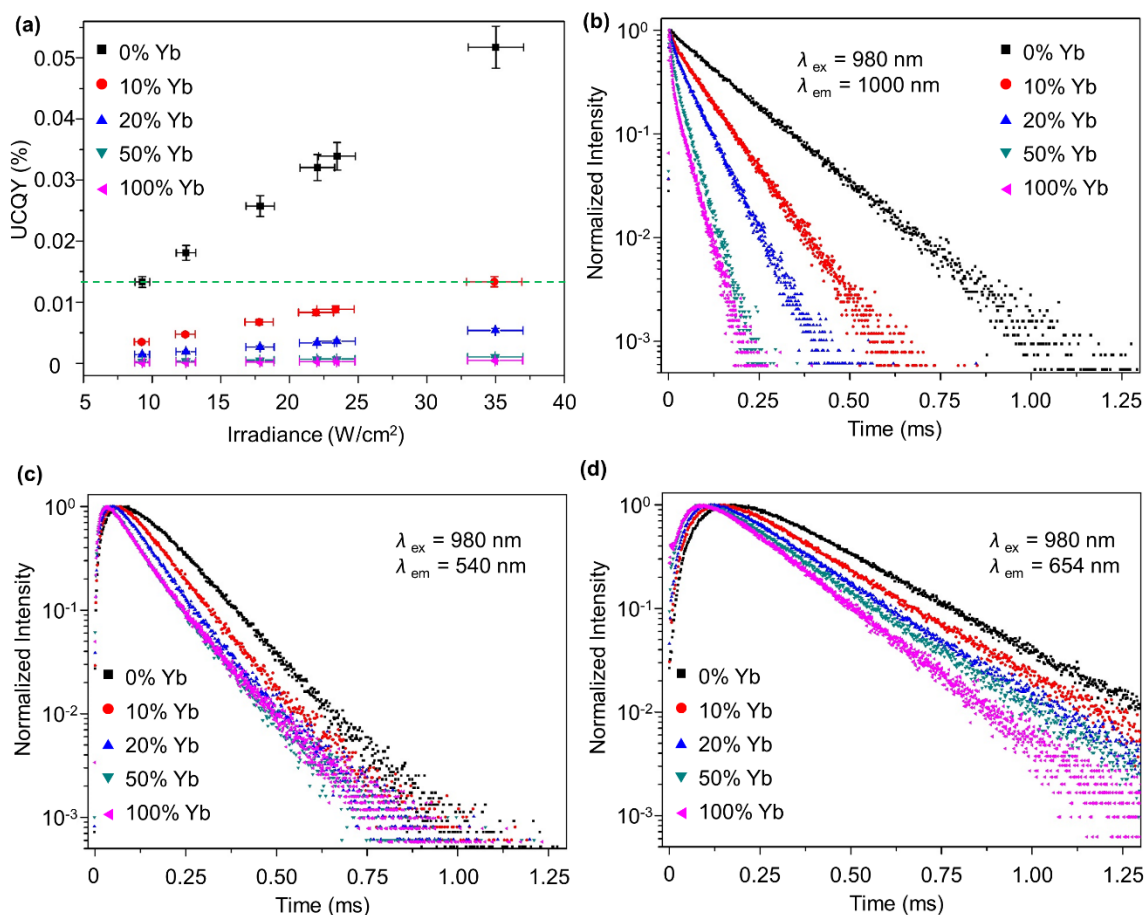


Figure 2.3 (a) Internal UCQY of the core-shell UCNPs with 980 nm excitation at different power densities. Luminescence decay lifetime of (b) $^2F_{5/2}$ energy level in the Yb^{3+} (excited at 980 nm, emitting at 1000 nm), (c) $^4S_{3/2}$ energy level in the Er^{3+} (excited at 520 nm, emitting at 540 nm), (d) $^4F_{9/2}$ energy level in the Er^{3+} (excited at 620 nm, emitting at 654 nm), of the core-shell UCNPs.

We next characterized the internal quantum yield (QY) of UC luminescence for all five samples to gain more insight into the correlation between absorbance and emission in core-shell UCNPs (See Materials and Methods for details). Internal UC QY is the number of emitted higher energy photons *versus* the absorbed lower energy photons, and it is used to assess the upconverting efficiency of different systems by correlating the absorbance and emission of UCNPs.^{12, 15-16} We tuned the power density of excitation laser (980 nm) from 9 W/cm² to 35 W/cm² and found that all five samples have increasing QY with elevating excitation flux (Figure 2.3a), which confirms

the nonlinear nature of UC emission processes.³³ The core–shell NPs with inert shells (NaLuF₄) have the highest internal QY across the whole tuned range of excitation power density (0.014% at 9 W/cm² excitation and 0.05% at 35 W/cm² excitation). With only 10% Yb³⁺ doping in the shell to make it “optically active” and absorb more 980 nm excitation light, the QY of the β -NaYF₄:Gd(10%)/Yb(18%)/Er(2%)@NaLuF₄:Yb(10%) core–shell NPs at the highest excitation flux (35 W/cm²) irradiance drastically dropped by 72% from 0.05% to 0.014%, almost identical to the QY of the inert shell (NaLuF₄) sample at the lowest excitation irradiance (9 W/cm²) (Figure 2.3a, green dotted line). This is direct evidence for the assertion that doping in the shell is detrimental to the UC efficiency. The decreasing QY with increasing doping levels corroborates the changes of the steady-state emission intensity we observed above and clearly demonstrated that the inert shell of core–shell UCNPs is critical in enhancing the UC luminescence intensity.

Moreover, when we normalized the all the QY values within the group of same excitation power density and examined how the doping in the shell affects the QY at the same excitation power density, we found that the QY for the inert-shell UCNPs (core@NaLuF₄) is almost 100 times higher than that of the active shell UCNPs (core@NaYbF₄), regardless of the excitation power density (tuning from 9 – 35 W/cm², Figure 2.4a). This enhancement factor around 100 matches well with the decrease of absorbance by 10 times (inert shell *versus* active shell) and increase of emission by 10 times (Figure 1k), and further suggests that the inert shell (NaLuF₄) is critical in achieving high QY of the luminescence.

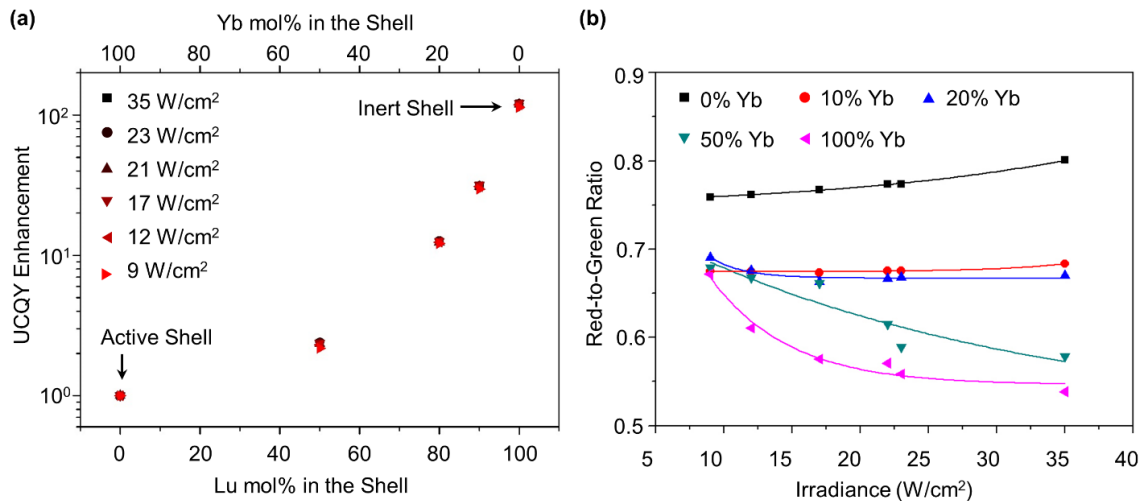


Figure 2.4 (a) Internal UCQY enhancement by normalizing the QY of core@NaYbF₄ to 1. (b) red-to-green ratio of all five core-shell UCNPs.

Besides the intensity of the UC emission peaks, the ratio between different emission peaks is also an interesting feature to investigate. Particularly for the β -NaYF₄ NPs co-doped with Yb³⁺ and Er³⁺, the red-to-green ratio, i.e. the peak intensity integrated from the red region (600 – 700 nm) *versus* the green region (500 – 600 nm) is an important factor in demonstrating the efficiency of UC emission. The typical emission peaks in the red regions ($^4F_{9/2} \rightarrow ^4I_{15/2}$) are three-photon UC and are less likely to occur than the two-photon UC processes in the visible green regions ($^4S_{3/2} \rightarrow ^4I_{15/2}$).⁴⁰⁻⁴¹ In general, the red-to-green ratio increases when the laser excitation power density increases and introduces more incident photons for UC. Therefore, the increase of red-to-green ratio is usually a sign of improved UC emission efficiency. We observed that the increase of green-to-red ratio upon elevating the laser excitation power density (9 – 35 W/cm²) only occurs when the core UCNPs are coated with the optically inert shells (NaLuF₄) (Figure 2.4b). When the Yb³⁺ are doped in the shell to make them “optically active”, the red-to-green ratio drops significantly, indicating the three-photon red UC emission is not as favored as compared to the two-photon green emission. The decrease of red emission compared to the green emission with the doping of

sensitizers in the shell can be explained by the resonance energy transfer between the Er^{3+} and the Yb^{3+} in the shell. With more Yb^{3+} doped in the shell to form active shells, the excitation energy at the excited states of Er^{3+} are more susceptible to the surface quenching, leaving emission from that state much less favored.

To further understand how the varied doping concentration of Yb^{3+} sensitizers in the shell affects the UC emission intensity, we characterized the luminescence decay lifetime at the first excited states of Yb^{3+} ($^2\text{F}_{5/2}$) and the two typical emissive states ($^4\text{S}_{3/2}$, $^4\text{F}_{9/2}$) of all five core-shell UCNPs. Luminescence decay lifetime is known to be sensitive to surface quenching and indicates the fate of excited energy at different energy levels in the lanthanide-doped UCNPs.⁴²⁻⁴³ We first examined the lifetime of the $^2\text{F}_{5/2}$ level in Yb^{3+} (excited at 980 nm, emitting at 1000 nm) which indicates how the energy dissipates after being excited from ground state $^2\text{F}_{7/2}$ level in Yb^{3+} . With the increase of Yb^{3+} doping level in the shell, more “leaking” sites were built in the shell for the excited energy confined in the core NPs migrating to the surface quenchers and the lifetime value was significantly shortened (Figure 2.3b), in perfect agreement with the monotonous decrease in the UC steady-state emission intensity (Figure 2.1j) and internal QY (Figure 2.2a) we showed above. In comparison, the decay lifetime for the energy levels $^4\text{S}_{3/2}$, $^4\text{F}_{9/2}$ in Er^{3+} (corresponding to emission wavelengths at 540 nm and 654 nm) also show a similar decreasing trend, but the trend was much less significant than that of 1000 nm emission level in the Yb^{3+} . These data unambiguously demonstrated that the UC emission intensity is largely dependent on the shielding of first excitation state ($^2\text{F}_{5/2}$ of Yb^{3+}) and shielding the first excitation state is critical to improving the emission intensity. Doping Yb^{3+} in the shell to construct active shell in core-shell NPs inevitably exposed the first excitation state to surface quenching and therefore significantly jeopardize the emission intensity.

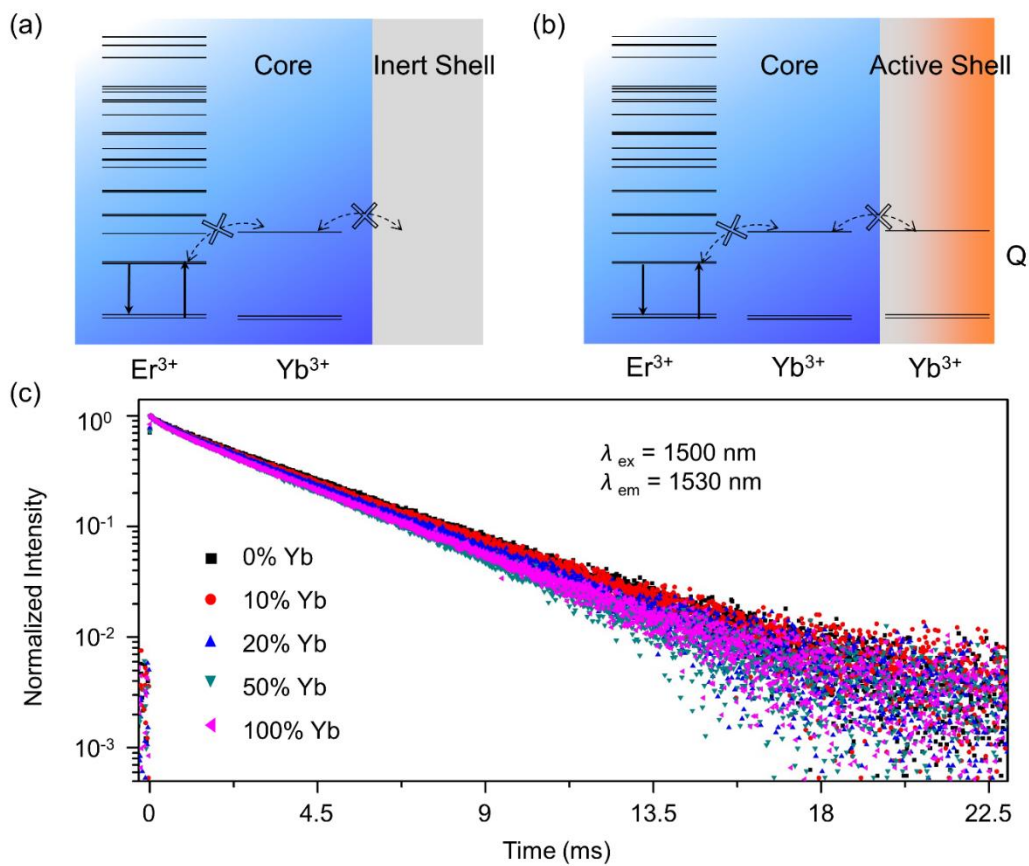


Figure 2.5 Downshifting luminescence. (a-b) energy levels of the dopants in the core and shells and their energy transfer pathway. (c) Luminescence decay lifetime of 1530 nm emission upon excitation at 1500 nm.

Next, we reasoned that the downshifting luminescence in the Er³⁺ ($^4I_{13/2} \rightarrow ^4I_{15/2}$, emission at 1530 nm) could also be affected by the shell composition because the optical transition in Yb³⁺ we investigated above ($^2F_{5/2} \rightarrow ^2F_{7/2}$, excitation at 980 nm and emission at 1000 nm) is also, in fact, downshifting luminescence. The change of downshifting luminescence should also give us insight on how the excitation energy migrates between the dopants in the core-shell structures. The downshifting luminescence at 1530 nm from Er³⁺ lies within second-infrared bioimaging window⁴⁴ and the telecommunication window⁴⁵ and has been recently explored on core-shell NPs.³⁵ We expected the lifetime at $^4I_{13/2}$ exhibits a similar profile, that is significant decrease with the increased doping of sensitizers in the shell, as the lifetime at the $^2F_{5/2}$ of Yb³⁺ shows in Figure

2.3b. However, in contrary to what we predicted, the lifetime at $^4I_{13/2}$ remained unchanged with the increased doping level of sensitizers in the shell, indicating that the transition of $^4I_{13/2} \rightarrow ^4I_{15/2}$ is independent of the shell composition change (Figure 2.5c). As we compared the energy levels in Er^{3+} and in Yb^{3+} , we found that the transition (excitation at 1500 nm and emission at 1530 nm) in Er^{3+} is lower than the energy gap between the $^2F_{5/2}$ and $^2F_{7/2}$ in Yb^{3+} (1000 nm), therefore, the $NaYbF_4$ is actually “optically inert shells” to this optical transition. This once again attests that shielding the first excitation state is critical in maintaining the long lifetime of the excited state and enhanced luminescence intensity.

However, when the same 1530 nm emission ($^4I_{13/2} \rightarrow ^4I_{15/2}$) was generated by the 980 nm excitation, the emission behavior is different from what has been investigated above. There is a significant decrease in the lifetime at the $^4I_{13/2}$ level (1530 nm emission) when it was indirectly excited from the $^4I_{11/2}$ level (980 nm) (Figure 2.6c). The excitation energy at the $^4I_{11/2}$ level in Er^{3+} in the core NPs can be easily transferred to the $^2F_{5/2}$ level in the Yb^{3+} through resonance energy transfer and subsequently transferred to surface quenchers in the surroundings. The emission behavior at the same energy level is different depending on where it is excited, demonstrating the critical role of optically inert shell without doping in enhancing luminescence in core-shell NPs.

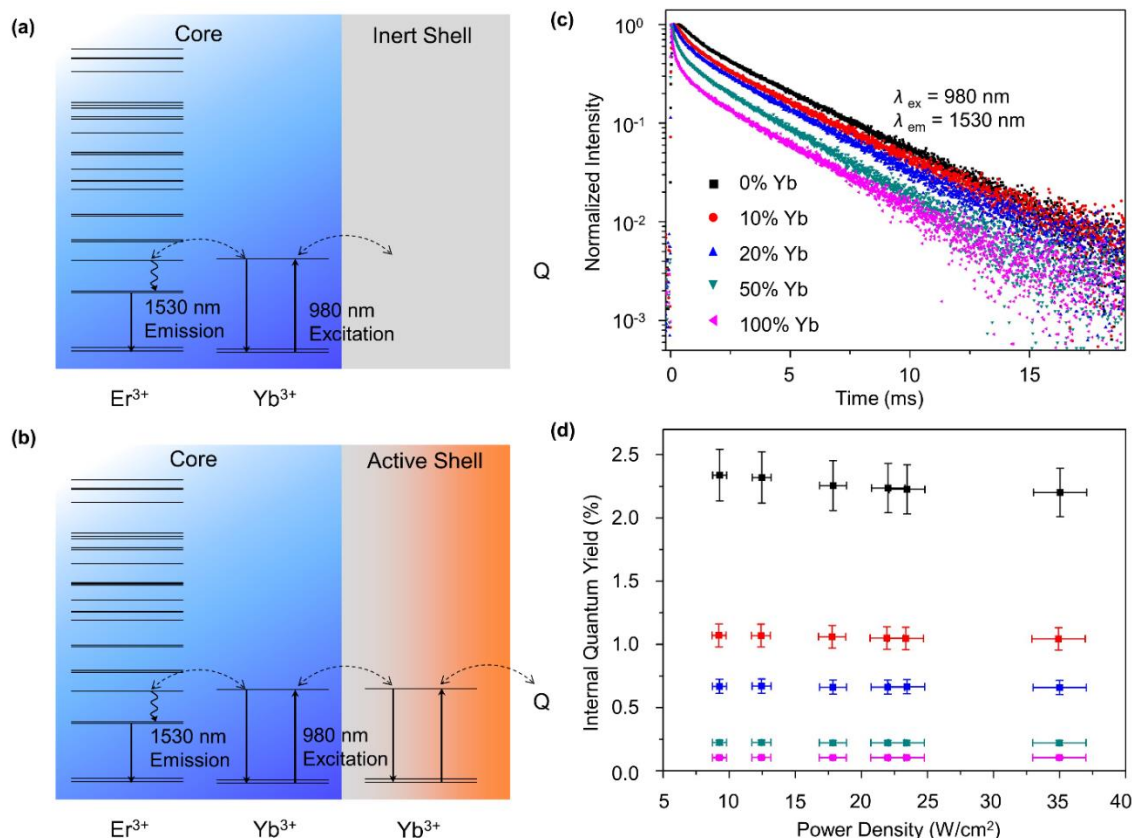


Figure 2.6 Downshifting luminescence. (a-b) energy levels of the dopants in the core and shells and their energy transfer pathway. (c) Luminescence decay lifetime of 1530 nm emission upon excitation at 980 nm. (d) Luminescence QY of the 1530 nm emission.

To further demonstrate that shielding the excitation energy level with the inert epitaxial shell is crucial to enhance the UC emission intensity, we grew an extra layer of inert shell (NaLuF_4) on top of the core@active shell UCNPs to form core@active shell@inert shell ($\beta\text{-NaYF}_4\text{:Gd(10\%)/Yb(18\%)/Er(2\%)}@\text{NaYbF}_4@\text{NaLuF}_4$, or core@Yb@Lu core-shell-shell) UCNPs and examined their optical properties (Figure 2.7a). Because the shell in this core-shell-shell sample has a mixed composition (inert shell on top of the active shell), we expected that the steady-state emission intensity, internal QY, and the luminescence decay lifetime of this particular type of UCNPs should all lie within the range of the brightest (core@ NaLuF_4) and dimmest (core@ NaYbF_4) samples.

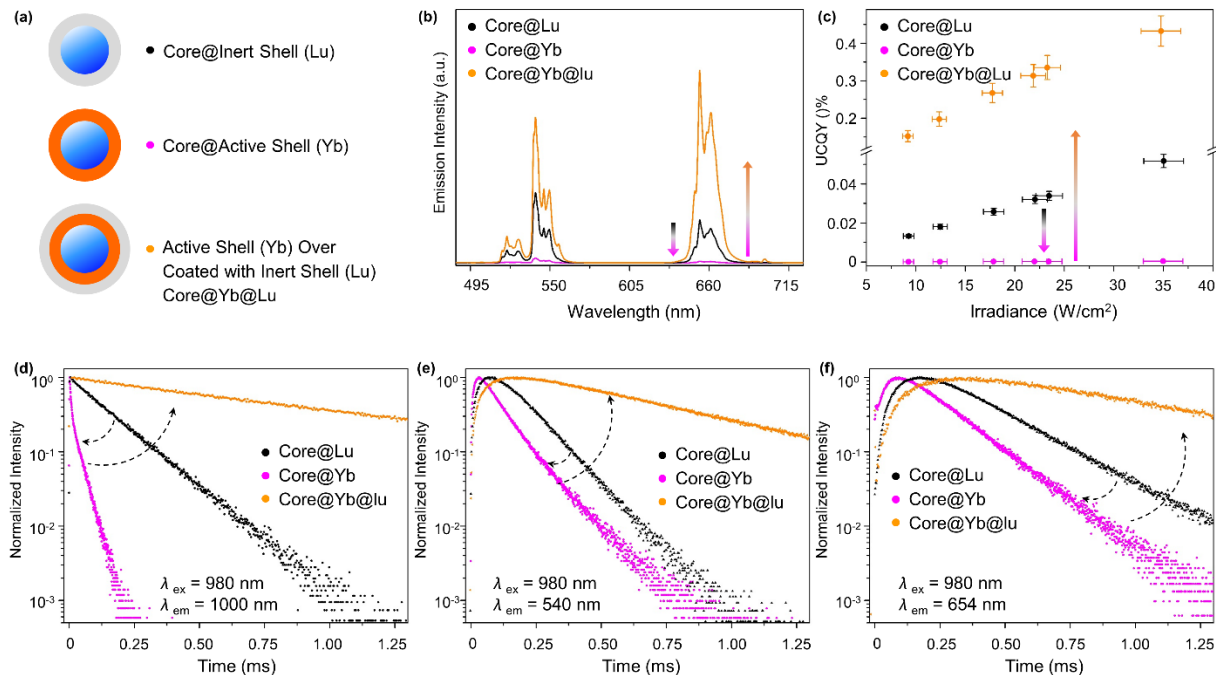


Figure 2.7 (a) Schematic illustration of the core/inert shell, core/active shell, and core/active shell/inert shell UCNPs. (b) UC luminescence spectra of the three samples excited by 980 nm. (c) Internal UCQY of the three samples excited at 980 nm with various excitation power densities. (d-f) Luminescence decay lifetime of $^2F_{5/2}$ energy level in the Yb^{3+} (excited at 980 nm, emitting at 1000 nm), $^4S_{3/2}$ energy level in the Er^{3+} (excited at 980 nm, emitting at 540 nm), $^4F_{9/2}$ energy level in the Er^{3+} (excited at 980 nm, emitting at 654 nm).

However, surprisingly, the core-shell-shell UCNPs has much higher emission intensity than either the core/active shell or the core/inert shell UCNPs (Figure 2.7b). Particularly, the red visible UC emission of the core-shell-shell UCNPs is enhanced by 110 times than that of the core@NaYbF₄ sample, and by 25 times than the core@NaLuF₄ sample. We also characterized the internal UCQY of three samples and found that the QY of the core-shell-shell UCNPs (2.0% at 35 W/cm²) is 4600 times higher than that of the core@NaYbF₄ UCNPs (4×10⁻⁴%) (Figure 2.7c) given that they have the same absorbance provided by the NaYbF₄ shell layer. Comparing the core-shell-shell sample with the core@NaLuF₄ sample, the former one has both higher absorbance and high luminescence QY, which is different from the negative correlation between absorbance and

emission intensity we observe above (Figure 2.1k). Higher doping concentration of sensitizers only brings higher emission intensity when all the sensitizers are properly shielded from the surfaces. This again demonstrates that for core/multishell UCNPs, the utmost shell should be kept optically inert (without dopants) to maximize the emission efficiency.

Luminescence decay lifetime of the core-shell-shell UCNPs at different emitting levels ($^2F_{5/2}$ level in the Yb^{3+} , $^4S_{3/2}$ level in the Er^{3+} , $^4F_{9/2}$ level in the Er^{3+}) also attests the critical contribution from the utmost undoped $NaLuF_4$ shell (Figure 2.7 d—f). With the coating of $NaLuF_4$ shell on top of the $core@NaYbF_4$ core-shell NPs, all lifetime profiles changed to very slow rising and slow decay, indicating that the excitation energy retain at the excited states and have higher probability of converting to higher energy photons instead of being transferred to surface quenchers. Taken together, the steady-state emission profile, internal QY, and lifetime analysis conclusively proved that the epitaxially inert shell is of critical importance to the UC emission intensity from NPs.

Knowing that both Yb^{3+} and Lu^{3+} in the shell have smaller ionic radii than most of the dopants in the core of UCNPs and make growing the uniform shells easy, we also compared the contribution from structural uniformity resulting from Yb^{3+} and Lu^{3+} to the UC emission intensity. To proceed this, we deliberately prepared core-shell UCNPs with irregular shells first (Figure 2.8a) and used either Yb^{3+} (Figure 2.8b) or Lu^{3+} (Figure 2.8c) to transform the irregular shells to regular shells. As we discussed above, Gd^{3+} has a larger ionic radius than Y^{3+} and exert compressive strain on the core-shell interface resulting in non-concentric shells on the core NPs (Figure 2.8a). The $core@NaGdF_4$ UCNPs had a wide, bi-mode size distribution (10.6 ± 2.9 nm, 18.5 ± 4.1 nm, Figure 2.8d) but nevertheless decent UC emission intensity in the visible range upon 980 nm excitation as shown in the cuvette photo (Figure 2.8g). Both Yb^{3+} and Lu^{3+} have smaller ionic radii than that

of Gd^{3+} , and doping Yb^{3+} and Lu^{3+} can exert tensile strain on the core-shell interfaces leading to uniform and concentric shells (Figure 2.8e and 2.f). Upon transforming the irregular shells to regular shells on the core NPs, it is generally expected to enhance the UC emission intensity because of the improved shielding of luminescence centers from surface quenching. TEM images confirmed that both $core@NaGdF_4:Yb(50\%)$ (Figure 2.8b and 2.8e) and $core@NaGdF_4:Lu(50\%)$ (Figure 2.8c and 2.8f) UCNPs had uniform, quasi-spherical morphologies and similarly narrow, single-mode size distribution (18.9 ± 1.2 nm, 19.0 ± 1.4 nm). However, the emission intensity of the $core@NaGdF_4:Yb(50\%)$ is much weaker than that of $core@NaGdF_4$ NPs (Figure 2.8h), highlighting the detrimental effect of introducing extra sensitizers into the shell on UC emission, although with more uniform shells to better “wrap” the luminescent centers in the cores. In comparison, the $core@NaGdF_4:Lu(50\%)$ NPs has significantly improved emission over the $core@NaGdF_4$ and $core@NaGdF_4:Yb(50\%)$ NPs (Figure 2.8i), demonstrating the inert shell, upon being grown properly to form uniform, concentric shells, can remarkably enhance the UC emission where the active shell cannot although forming similar concentric shells.

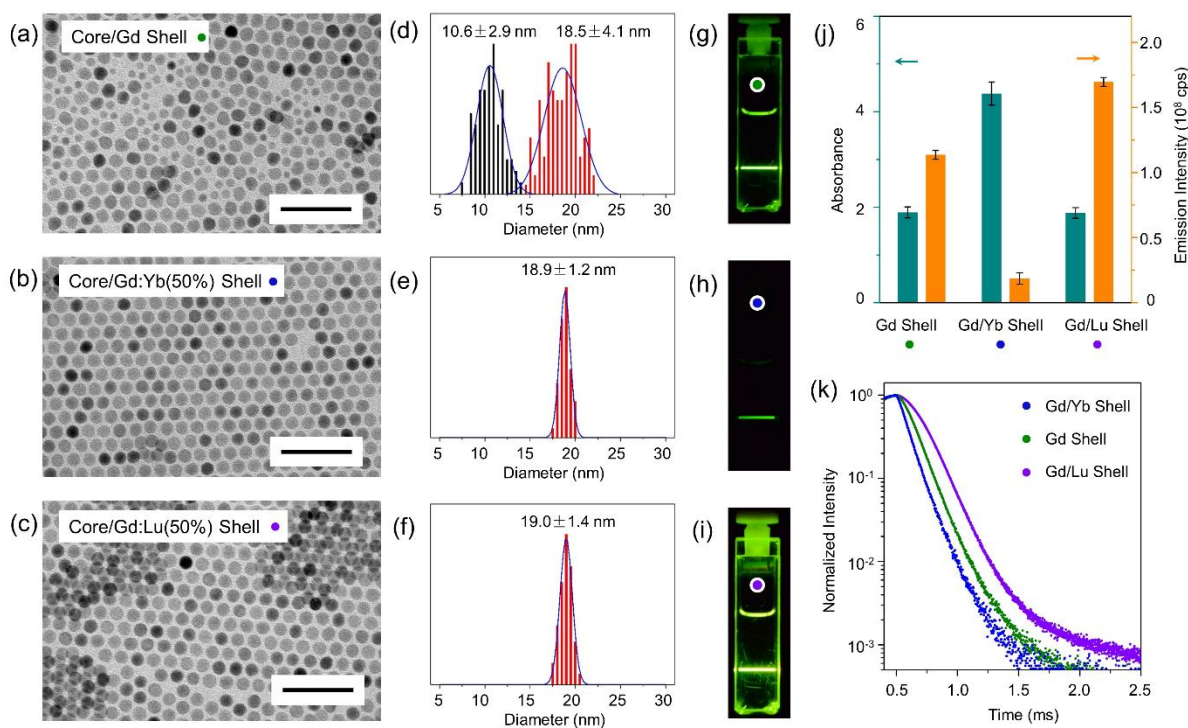


Figure 2.8 TEM images of the (a) $\text{NaYF}_4:\text{Gd}/\text{Yb}/\text{Er}@\text{NaGdF}_4$ core@ NaGdF_4 , (b) core@ $\text{NaGdF}_4:\text{Yb}(50\%)$, and (c) core@ $\text{NaGdF}_4:\text{Lu}(50\%)$ core-shell UCNPs. Size distribution of the (d) core@ NaGdF_4 , (e) core@ $\text{NaGdF}_4:\text{Yb}(50\%)$, and (f) core@ $\text{NaGdF}_4:\text{Lu}(50\%)$ core-shell UCNPs. Cuvette images of the (g) $\text{NaYF}_4:\text{Gd}/\text{Yb}/\text{Er}@\text{NaGdF}_4$ core@ NaGdF_4 , (h) core@ $\text{NaGdF}_4:\text{Yb}(50\%)$, and (i) core@ $\text{NaGdF}_4:\text{Lu}(50\%)$ core-shell UCNPs. (j) Comparison of absorbance and emission intensity of the three different samples. (k) Luminescence lifetime of the three different samples.

Importantly, we also note here that the significant increment in luminescence emission intensity from core@ NaGdF_4 NPs to core@ $\text{NaGdF}_4:\text{Lu}(50\%)$ NPs (Figure 8j) is not caused by increased absorption of excitation because either Gd or Lu does not absorb at 980 nm. This can be confirmed by the quantification of absorbance for both UCNPs at 980 nm. In contrast, the core@ $\text{NaGdF}_4:\text{Yb}(50\%)$ UCNPs have significantly improved absorbance at 980 nm because of Yb^{3+} doping but decreased emission, highlighting again that doping extra sensitizers in the shell, even though it assists forming uniform and concentric shell, is not the proper way to enhance the UC luminescence. The discrepancy resulting from doping Yb^{3+} or Lu^{3+} , which can also be confirmed by the luminescence lifetime (Figure 2.8k), shed light on the fact that Lu^{3+} enhances the

luminescence better than Yb^{3+} not because of the smaller ionic radius, but because it does not have any energy levels, or its optical “inertness”.

2.4 Conclusions

In summary, we have conclusively demonstrated that the doping in the shell is critical to enhancing the UC luminescence intensity in lanthanide-doped core-shell UCNPs. The NPs with the inert shell coating have the highest emission intensity, and it decreases proportionally with the increase of doping concentrations of Yb^{3+} sensitizers in the shell. Steady-state emission spectra, luminescence QY, and luminescence decay lifetime together unambiguously proved this striking negative correlation between absorbance and emission. The dim luminescence of core-active-shell UCNPs can be easily enhanced by overcoating another layer of inert epitaxial shell. Our results highlight the critical role of inert epitaxial shell in enhancing the UC luminescence of core-shell UCNPs and that shielding the luminescent centers from surface quenching is more crucial than increasing the absorbance of incident light.

2.5 Materials and Methods

Chemicals

Yttrium acetate hydrate (99.9%), gadolinium acetate hydrate (99.9%), ytterbium acetate hydrate (99.9%), erbium acetate hydrate (99.9%), ytterbium oxide, gadolinium oxide, trifluoroacetic acid (TFA), 1-octadecene (>90%), oleic acid (>90%), oleylamine (>70%), sodium trifluoroacetate, sodium hydroxide, methanol, chloroform, ethanol, and toluene were all purchased from Sigma. Ammonium fluoride was purchased from Spectrum. Lutetium oxide

(anhydrous, 99.9%) was purchased from Alfa Aesar. All chemicals were used as received without further purification unless specified.

Synthesis of β -NaYF₄:Gd(10%)/Yb(18%)/Er(2%) core nanoparticles

β -NaYF₄:Gd(10%)/Yb(18%)/Er(2%) core nanoparticles were synthesized according to a previously published procedure with slight modifications. In a typical synthesis, yttrium acetate hydrate (0.7 mmol), gadolinium acetate hydrate (0.1 mmol), ytterbium acetate hydrate (0.18 mmol), erbium acetate hydrate (0.02 mmol) were mixed with 1-octadecene (15 mL) and oleic acid (6 mL), followed by being heated at 120 °C under vacuum for 45 min. After it was cooled to room temperature, a methanol solution (10 mL) with ammonium fluoride (4 mmol) and sodium hydroxide (2.5 mmol) was added and stirred for another 45 min. The mixture was quickly brought to 300 °C and kept for 60 min with gentle argon flow protection. After the solution was cooled to room temperature, the core nanoparticles were obtained by adding excess ethanol, washing, and finally dispersed in 5 mL chloroform for further use.

Synthesis of α -NaLuF₄:Yb (x mol%) ($x = 0, 10, 20, 50, 100$) sacrificial shell nanoparticles

Shell nanoparticles were synthesized according to our previously published procedure. Briefly, in total 1 mmol of lutetium oxide and ytterbium oxide with different ratio were dissolved with aqueous TFA solution (50%) overnight at 95 °C oil bath to obtain a clear solution, and dried at 70 °C to yield white powders as lutetium/ytterbium trifluoroacetate. The white powders were mixed with 1-octadecene (12 mL), oleylamine (6 mL) and oleic acid (6 mL), heated to 120 °C, kept for 30 min, then to 300 °C, kept for 25 min to obtain the shell nanoparticles. The shell

nanoparticles were rinsed, dispersed in 10 mL hexane, and stored at 37 °C incubation chamber for further use.

Synthesis of β -NaYF₄:Gd/Yb/Er@NaLuF₄:Yb (x mol%) core-shell nanoparticles ($x = 0, 10, 20, 50, 100$)

Core-shell nanoparticles were synthesized accordingly our previously published procedure. In a typical synthesis, 3 mL hexane dispersion of the α -NaLuF₄:Yb (x mol%) ($x = 0, 10, 20, 50, 100$) shell nanoparticles were mixed with 1 mL 1-octadecene, the hexane was removed by gentle argon flow, the shell nanoparticle dispersion was injected into the β -NaYF₄:Gd/Yb/Er core nanoparticle solution after it has been heated at 300 °C for 60 min. After 10-12 min ripening, the solution was cooled to room temperature and washed to obtain core-shell nanoparticles with the same composition in the core but different compositions in the shell.

Synthesis of β -NaYF₄:Gd/Yb/Er@NaYbF₄@NaLuF₄ core/active shell/inert shell hetero-epitaxial nanoparticles

Core/active shell/inert shell nanoparticles were synthesized following procedure described above. The α -NaYbF₄ and α -NaLuF₄ nanoparticles were subsequently injected into the core solution and ripened.

Characterization

The photoluminescence spectra was recorded on. The luminescence decay lifetime was examined at. The quantum yield was measured .The elemental concentration of nanoparticles were

determined by ICP-AES. We followed one of our previously published protocol for the measurement of luminescence quantum yield (QY).⁴¹

Chapter 2, is unpublished work by Sha He and Adah Almutairi. The dissertation author was the primary investigator and author of this material.

2.6 References

1. Eliseeva, S. V.; Bunzli, J. C. G., Rare earths: jewels for functional materials of the future. *New J. Chem.* **2011**, *35*, 1165-1176.
2. Wang, F.; Liu, X. G., Recent advances in the chemistry of lanthanide-doped upconversion nanocrystals. *Chem. Soc. Rev.* **2009**, *38*, 976-989.
3. Zhang, C.; Yang, L.; Zhao, J.; Liu, B.; Han, M.-Y.; Zhang, Z., White-Light Emission from an Integrated Upconversion Nanostructure: Toward Multicolor Displays Modulated by Laser Power. *Angew. Chem.-Int. Edit.* **2015**, *54*, 11531-11535.
4. Wang, F.; Liu, X. G., Upconversion multicolor fine-tuning: Visible to near-infrared emission from lanthanide-doped NaYF₄ nanoparticles. *J. Am. Chem. Soc.* **2008**, *130*, 5642-+.
5. Zhou, B.; Shi, B. Y.; Jin, D. Y.; Liu, X. G., Controlling upconversion nanocrystals for emerging applications. *Nat. Nanotechnol.* **2015**, *10*, 924-936.
6. Yang, W.; Li, X.; Chi, D.; Zhang, H.; Liu, X., Lanthanide-doped upconversion materials: emerging applications for photovoltaics and photocatalysis. *Nanotechnology* **2014**, *25*.
7. Huang, X. Y.; Han, S. Y.; Huang, W.; Liu, X. G., Enhancing solar cell efficiency: the search for luminescent materials as spectral converters. *Chem. Soc. Rev.* **2013**, *42*, 173-201.
8. Chen, G. Y.; Qju, H. L.; Prasad, P. N.; Chen, X. Y., Upconversion Nanoparticles: Design, Nanochemistry, and Applications in Theranostics. *Chem. Rev.* **2014**, *114*, 5161-5214.
9. Ju, Q.; Chen, X.; Ai, F.; Peng, D.; Lin, X.; Kong, W.; Shi, P.; Zhu, G.; Wang, F., An upconversion nanoprobe operating in the first biological window. *Journal of Materials Chemistry B* **2015**, *3*, 3548-3555.
10. Atre, A. C.; Dionne, J. A., Realistic upconverter-enhanced solar cells with non-ideal absorption and recombination efficiencies. *J. Appl. Phys.* **2011**, *110*, 9.
11. Boriskina, S. V.; Green, M. A.; Catchpole, K.; Yablonovitch, E.; Beard, M. C.; Okada, Y.; Lany, S.; Gershon, T.; Zakutayev, A.; Tahersima, M. H.; Sorger, V. J.; Naughton, M. J.; Kempa, K.; Dagenais, M.; Yao, Y.; Xu, L.; Sheng, X.; Bronstein, N. D.; Rogers, J. A.; Alivisatos, A. P.; Nuzzo, R. G.; Gordon, J. M.; Wu, D. M.; Wisser, M. D.; Salleo, A.; Dionne, J.; Bermel, P.; Greffet, J. J.; Celanovic, I.; Soljacic, M.; Manor, A.; Rotschild, C.; Raman, A.; Zhu, L. X.; Fan, S. H.; Chen, G., Roadmap on optical energy conversion. *J. Opt.* **2016**, *18*, 48.

12. Goldschmidt, J. C.; Fischer, S., Upconversion for Photovoltaics - a Review of Materials, Devices and Concepts for Performance Enhancement. *Adv. Opt. Mater.* **2015**, *3*, 510-535.
13. Naczynski, D. J.; Tan, M. C.; Zevon, M.; Wall, B.; Kohl, J.; Kulesa, A.; Chen, S.; Roth, C. M.; Riman, R. E.; Moghe, P. V., Rare-earth-doped biological composites as in vivo shortwave infrared reporters. *Nature Communications* **2013**, *4*.
14. Fischer, S.; Ivaturi, A.; Frohlich, B.; Rudiger, M.; Richter, A.; Kramer, K. W.; Richards, B. S.; Goldschmidt, J. C., Upconverter Silicon Solar Cell Devices for Efficient Utilization of Sub-Band-Gap Photons Under Concentrated Solar Radiation. *IEEE J. Photovolt.* **2014**, *4*, 183-189.
15. Fischer, S.; Goldschmidt, J. C.; Loper, P.; Bauer, G. H.; Bruggemann, R.; Kramer, K.; Biner, D.; Hermle, M.; Glunz, S. W., Enhancement of silicon solar cell efficiency by upconversion: Optical and electrical characterization. *J. Appl. Phys.* **2010**, *108*, 11.
16. Fischer, S.; Johnson, N. J. J.; Pichaandi, J.; Goldschmidt, J. C.; van Veggel, F., Upconverting core-shell nanocrystals with high quantum yield under low irradiance: On the role of isotropic and thick shells. *J. Appl. Phys.* **2015**, *118*, 12.
17. Chen, X.; Jin, L.; Kong, W.; Sun, T.; Zhang, W.; Liu, X.; Fan, J.; Yu, S. F.; Wang, F., Confining energy migration in upconversion nanoparticles towards deep ultraviolet lasing. *Nature Communications* **2016**, *7*.
18. Deng, R. R.; Qin, F.; Chen, R. F.; Huang, W.; Hong, M. H.; Liu, X. G., Temporal full-colour tuning through non-steady-state upconversion. *Nat. Nanotechnol.* **2015**, *10*, 237-242.
19. Punjabi, A.; Wu, X.; Tokatli-Apollon, A.; El-Rifai, M.; Lee, H.; Zhang, Y. W.; Wang, C.; Liu, Z.; Chan, E. M.; Duan, C. Y.; Han, G., Amplifying the Red-Emission of Upconverting Nanoparticles for Biocompatible Clinically Used Prodrug-Induced Photodynamic Therapy. *ACS Nano* **2014**, *8*, 10621-10630.
20. Shen, J.; Chen, G. Y.; Ohulchanskyy, T. Y.; Kesseli, S. J.; Buchholz, S.; Li, Z. P.; Prasad, P. N.; Han, G., Tunable Near Infrared to Ultraviolet Upconversion Luminescence Enhancement in (α -NaYF₄:Yb,Tm)/CaF₂ Core/Shell Nanoparticles for In situ Real-time Recorded Biocompatible Photoactivation. *Small* **2013**, *9*, 3213-3217.
21. Vetrone, F.; Naccache, R.; Mahalingam, V.; Morgan, C. G.; Capobianco, J. A., The Active-Core/Active-Shell Approach: A Strategy to Enhance the Upconversion Luminescence in Lanthanide-Doped Nanoparticles. *Adv. Funct. Mater.* **2009**, *19*, 2924-2929.
22. Xie, X. J.; Gao, N. Y.; Deng, R. R.; Sun, Q.; Xu, Q. H.; Liu, X. G., Mechanistic Investigation of Photon Upconversion in Nd³⁺-Sensitized Core-Shell Nanoparticles. *J. Am. Chem. Soc.*

2013, 135, 12608-12611.

23. Wu, X.; Zhang, Y. W.; Takle, K.; Bilsel, O.; Li, Z. J.; Lee, H.; Zhang, Z. J.; Li, D. S.; Fan, W.; Duan, C. Y.; Chan, E. M.; Lois, C.; Xiang, Y.; Han, G., Dye-Sensitized Core/Active Shell Upconversion Nanoparticles for Optogenetics and Bioimaging Applications. *ACS Nano* **2016**, *10*, 1060-1066.
24. Chen, D. Q.; Yu, Y. L.; Huang, F.; Lin, H.; Huang, P.; Yang, A. P.; Wang, Z. X.; Wang, Y. S., Lanthanide dopant-induced formation of uniform sub-10 nm active-core/active-shell nanocrystals with near-infrared to near-infrared dual-modal luminescence. *J. Mater. Chem.* **2012**, *22*, 2632-2640.
25. Yang, D. M.; Li, C. X.; Li, G. G.; Shang, M. M.; Kang, X. J.; Lin, J., Colloidal synthesis and remarkable enhancement of the upconversion luminescence of BaGdF₅:Yb³⁺/Er³⁺ nanoparticles by active-shell modification. *J. Mater. Chem.* **2011**, *21*, 5923-5927.
26. Huang, S. Q.; Gu, L.; Miao, C.; Lou, Z. Y.; Zhu, N. W.; Yuan, H. P.; Shan, A. D., Near-infrared photocatalyst of Er³⁺/Yb³⁺ codoped (CaF₂@TiO₂) nanoparticles with active-core/active-shell structure. *J. Mater. Chem. A* **2013**, *1*, 7874-7879.
27. Ding, M. Y.; Chen, D. Q.; Ma, D. Y.; Dai, J. B.; Li, Y. T.; Ji, Z. G., Highly enhanced upconversion luminescence in lanthanide-doped active-core/luminescent-shell/active-shell nanoarchitectures. *J. Mater. Chem. C* **2016**, *4*, 2432-2437.
28. Huang, X. Y.; Lin, J., Active-core/active-shell nanostructured design: an effective strategy to enhance Nd³⁺/Yb³⁺ cascade sensitized upconversion luminescence in lanthanide-doped nanoparticles. *J. Mater. Chem. C* **2015**, *3*, 7652-7657.
29. Chen, X.; Peng, D. F.; Ju, Q.; Wang, F., Photon upconversion in core-shell nanoparticles. *Chem. Soc. Rev.* **2015**, *44*, 1318-1330.
30. Johnson, N. J. J.; van Veggel, F., Sodium lanthanide fluoride core-shell nanocrystals: A general perspective on epitaxial shell growth. *Nano Res.* **2013**, *6*, 547-561.
31. Chen, G.; Agren, H.; Ohulchanskyy, T. Y.; Prasad, P. N., Light upconverting core-shell nanostructures: nanophotonic control for emerging applications. *Chemical Society Reviews* **2015**, *44*, 1680-1713.
32. Wang, M. Y.; Tian, Y.; Zhao, F. Y.; Li, R. F.; You, W. W.; Fang, Z. L.; Chen, X. Y.; Huang, W.; Ju, Q., Alleviating the emitter concentration effect on upconversion nanoparticles via an inert shell. *J. Mater. Chem. C* **2017**, *5*, 1537-1543.

33. Wang, Y.; Deng, R. R.; Xie, X. J.; Huang, L.; Liu, X. G., Nonlinear spectral and lifetime management in upconversion nanoparticles by controlling energy distribution. *Nanoscale* **2016**, *8*, 6666-6673.
34. Wang, F.; Wang, J. A.; Liu, X. G., Direct Evidence of a Surface Quenching Effect on Size-Dependent Luminescence of Upconversion Nanoparticles. *Angew. Chem.-Int. Edit.* **2010**, *49*, 7456-7460.
35. Johnson, N. J. J.; He, S.; Diao, S.; Chan, E. M.; Dai, H. J.; Almutairi, A., Direct Evidence for Coupled Surface and Concentration Quenching Dynamics in Lanthanide-Doped Nanocrystals. *J. Am. Chem. Soc.* **2017**, *139*, 3275-3282.
36. Johnson, N. J. J.; Korinek, A.; Dong, C. H.; van Veggel, F., Self-Focusing by Ostwald Ripening: A Strategy for Layer-by-Layer Epitaxial Growth on Upconverting Nanocrystals. *J. Am. Chem. Soc.* **2012**, *134*, 11068-11071.
37. Chan, E. M.; Levy, E. S.; Cohen, B. E., Rationally Designed Energy Transfer in Upconverting Nanoparticles. *Advanced Materials* **2015**, *27*, 5753-5761.
38. Wang, F.; Han, Y.; Lim, C. S.; Lu, Y. H.; Wang, J.; Xu, J.; Chen, H. Y.; Zhang, C.; Hong, M. H.; Liu, X. G., Simultaneous phase and size control of upconversion nanocrystals through lanthanide doping. *Nature* **2010**, *463*, 1061-1065.
39. Johnson, N. J. J.; van Veggel, F., Lanthanide-Based Heteroepitaxial Core-Shell Nanostructures: Compressive versus Tensile Strain Asymmetry. *ACS Nano* **2014**, *8*, 10517-10527.
40. Capobianco, J. A.; Vetrone, F.; Boyer, J. C.; Speghini, A.; Bettinelli, M., Enhancement of red emission (F-4(9/2)-> I-4(15/2)) via upconversion in bulk and nanocrystalline cubic Y2O3 : Er3+. *Journal of Physical Chemistry B* **2002**, *106*, 1181-1187.
41. Fischer, S.; Bronstein, N. D.; Swabeck, J. K.; Chan, E. M.; Alivisatos, A. P., Precise Tuning of Surface Quenching for Luminescence Enhancement in Core-Shell Lanthanide-Doped Nanocrystals. *Nano Letters* **2016**, *16*, 7241-7247.
42. Liu, Y. J.; Lu, Y. Q.; Yang, X. S.; Zheng, X. L.; Wen, S. H.; Wang, F.; Vidal, X.; Zhao, J. B.; Liu, D. M.; Zhou, Z. G.; Ma, C. S.; Zhou, J. J.; Piper, J. A.; Xi, P.; Jin, D. Y., Amplified stimulated emission in upconversion nanoparticles for super-resolution nanoscopy. *Nature* **2017**, *543*, 229-+.
43. Lu, Y.; Zhao, J.; Zhang, R.; Liu, Y.; Liu, D.; Goldys, E. M.; Yang, X.; Xi, P.; Sunna, A.; Lu, J.; Shi, Y.; Leif, R. C.; Huo, Y.; Shen, J.; Piper, J. A.; Robinson, J. P.; Jin, D., Tunable lifetime multiplexing using luminescent nanocrystals. *Nature Photonics* **2014**, *8*, 33-37.

44. Hong, G.; Diao, S.; Chang, J.; Antaris, A. L.; Chen, C.; Zhang, B.; Zhao, S.; Atochin, D. N.; Huang, P. L.; Andreasson, K. I.; Kuo, C. J.; Dai, H., Through-skull fluorescence imaging of the brain in a new near-infrared window. *Nature Photonics* **2014**, *8*, 723-730.
45. Polman, A., Erbium implanted thin film photonic materials. *Journal of Applied Physics* **1997**, *82*, 1-39.

Chapter 3

Leveraging Spectral Matching between Photosensitizers and Upconversion Nanoparticles for 808 nm-Activated Photodynamic Therapy

3.1 Abstract

Upconversion nanoparticles (UCNPs) are promising platforms to enhance the performance of photodynamic therapy (PDT) of cancer. When coupled with UCNPs, the photosensitizers in PDT are indirectly activated by near-infrared (NIR) excitation that allows for deeper tissue penetration and reduced attenuation. To achieve maximum performance, the upconverted emission peak of the UCNPs and absorption band of the photosensitizers need to overlap significantly. However, the spectral mismatch between the upconverted emission maximum of UCNPs (predominantly in the green) and absorption maximum of most available photosensitizers (in the red) greatly limits the therapeutic efficacy of the current UCNP-PDT platforms. Here we report a UCNP-PDT platform that offers strong spectral overlap between the UCNP emission under bio-benign 808 nm NIR excitation and photosensitizers (zinc phthalocyanine, ZnPc) absorption. The spectrally matched UCNP red emission is 40 times stronger than the green, and is independent of laser power density across a wide range ($0.6 - 3.4 \text{ W/cm}^2$) that is suitable for biological systems. The spectrally matched UCNP-PDT platform enables rapid generation (5 min) of cytotoxic singlet oxygen *via* NIR excitation at extremely low laser power density (0.6 W/cm^2). Using this platform, we show that the actively growing HeLa cancer cell spheroids can be suppressed by PDT, demonstrating the suitability and effectiveness of the spectrally matched platforms for cancer therapeutics.

3.2 Introduction

Photodynamic therapy (PDT) is a promising strategy for cancer treatment over traditional approaches because it is more selective, less invasive, and overcomes multidrug resistance.¹⁻⁶ The strategy involves activating photosensitizers with light irradiation, usually visible light, to generate cytotoxic singlet oxygen ($^1\text{O}_2$) that kills cancer cells.¹ Despite the advantages of PDT, commonly used photosensitizers have extremely low water solubility resulting in poor accumulation at tumor sites.⁷ More importantly, the visible activating light in PDT has limited tissue penetration and significant attenuation by biological medium leading to poor therapeutic efficacy.⁸ Nanoparticles (NPs) such as quantum dot,⁹ gold,¹⁰ and silica¹¹⁻¹² load the photosensitizers as cargos and enhance their accumulation at tumor sites by taking advantage of their large surface-to-volume ratio, tunable surface chemistry, and targeting capability.^{7, 9-15} However, they do not address the fundamental limitation of attenuation and poor penetration of visible activating light, making it still challenging for clinical viability of these platforms.⁸

Lanthanide (Ln)-doped upconversion nanoparticles (UCNPs) are a class of NPs that emit ultraviolet (UV) or visible light under near-infrared (NIR) light excitation.¹⁶⁻¹⁷ NaYF_4 -based UCNPs co-doped with $\text{Yb}^{3+}/\text{Er}^{3+}$ are one of the most efficient upconverting systems known to date and have been investigated widely to improve the performance of conventional PDT.¹⁸ $\text{Yb}^{3+}/\text{Er}^{3+}$ co-doped UCNPs convert NIR excitation (980 nm) that has deeper tissue penetration into visible emission, and this locally emitted light subsequently activates the photosensitizers coated on the UCNPs.¹⁹⁻²⁴ However, the use of 980 nm excitation has recently raised concerns as it overlaps with the strong 980-nm-centered absorption band of water.²⁵⁻²⁶ Water is abundant in most biological samples across different scales from cells, cultured tissues to small animals and the human body. Thus, the 980 nm laser excitation is significantly attenuated through the biological medium and

the laser alone without any photothermal agents can induce unselective local heating effect that causes localized tissue damage.²⁵ This overlap greatly limits the adaptation of 980 nm excited UCNP-PDT application, and there is an increasing effort to find suitable UCNP-PDT platforms that are biologically relevant to fully leverage the immense potential of NIR light for cancer therapeutics.

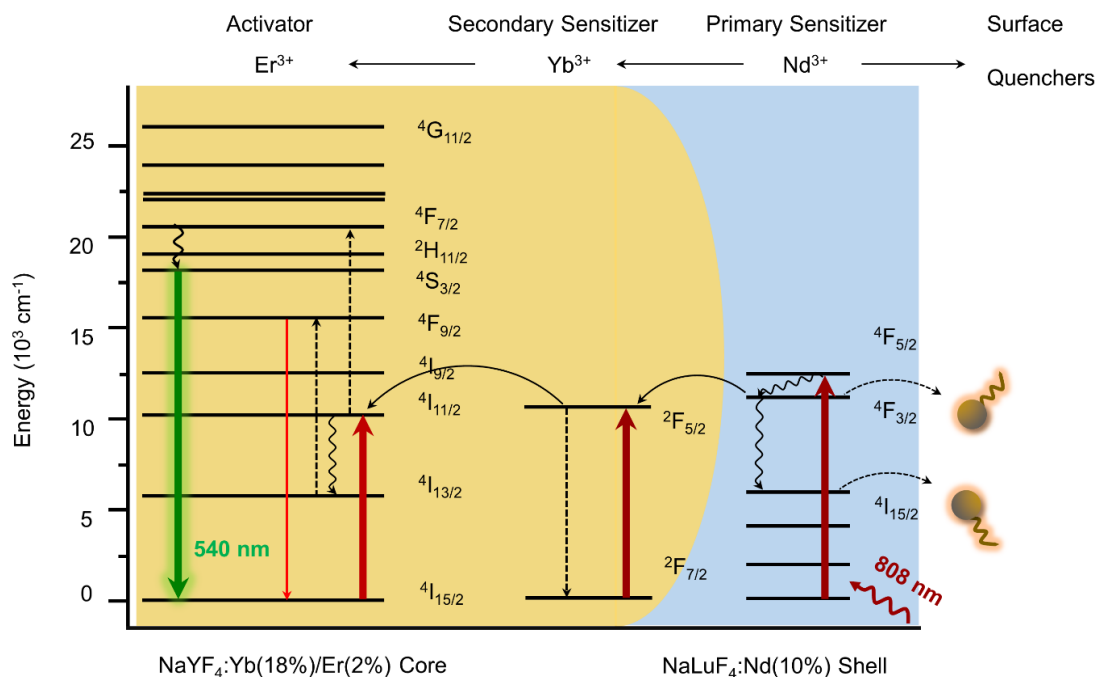
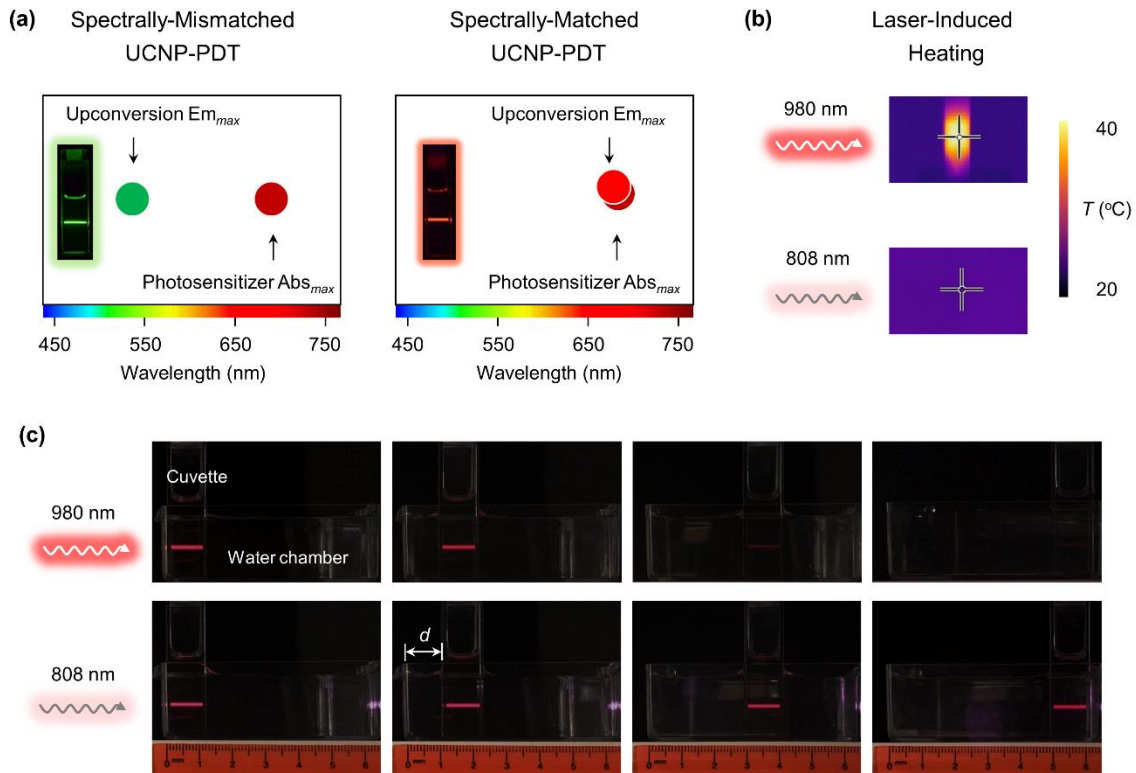


Figure 3.1 Energy level diagram of the conventional Nd^{3+} -doped NPs. They absorb the 808 nm excitation *via* Nd^{3+} in the shell, transfer the excitation energy to Yb^{3+} , and to activators (Er^{3+}) for dominant green upconversion emission (540 nm) that does not match the absorption maximum of photosensitizer ZnPc. The excitation energy is susceptible to surface quenching due to the doping in the shell.

Recent efforts in improving UCNP-PDT have focused on Nd^{3+} co-doped $\text{Yb}^{3+}/\text{Er}^{3+}$ UCNPs that allow for excitation at bio-benign 808 nm and dramatically reduce the laser induced heating effect.²⁷⁻³⁶ However, these novel UCNP-PDT platforms excitable with 808 nm do not address two major challenges that are critical towards realizing their clinical utilization. First, Nd^{3+} ions are usually doped in the shell of the UCNPs and bridge the excitation energy in the core to the surface

sites.³⁵⁻³⁶ Excitation at 808 nm is absorbed by Nd^{3+} in the shell and transferred to $\text{Yb}^{3+}/\text{Er}^{3+}$ in the core for upconversion *via* a cascading process (Figure 3.1). Both cases lead to unfavorable quenching pathway for the upconversion emission.³⁷ Thus, the upconversion emission for the Nd^{3+} -doped UCNPs is usually weaker than the pristine $\text{Yb}^{3+}/\text{Er}^{3+}$ co-doped UCNPs.³⁵⁻³⁶ Excitation at 808 nm with higher power density/flux is required to achieve the same therapeutic outcome, which also inevitably reintroduces the laser-induced heating effects due to the high laser power.

Second, and more importantly, all reported UCNP-PDT platforms with 808 nm excitation regardless of the excitation power density have a strong green emission (540 nm, $^4\text{S}_{3/2} \rightarrow ^4\text{I}_{15/2}$ of Er^{3+}), and very minimal/negligible red emission (654 nm, $^4\text{F}_{9/2} \rightarrow ^4\text{I}_{15/2}$ of Er^{3+})³¹⁻³⁶ where most of the photosensitizers absorb (Scheme 3.1a). Most of the red emission in these designs is quenched by energy migration to surface sites.³⁸⁻⁴² To highlight, most of the highly efficient photosensitizers, such as zinc phthalocyanine (ZnPc), chlorin e6 (Ce6), and methylene blue (MB) have major absorption band in the red spectral region (600 to 700 nm) (Scheme 3.1a) and therefore require strong visible upconverted red emission to activate them effectively.¹³⁻¹⁴ Punjabi *et al.* attempted to address the mismatch by increasing the doping level of Yb^{3+} in the UCNPs to amplify the red emission. The upconverted red emission band matched with the absorption of the photosensitizer protoporphyrin IX, but it was still limited to 980 nm excitation.⁴² To date, UCNP-PDT platforms have not been tailored to simultaneously have excitation with 808 nm at biologically relevant low power ($\sim 0.6 \text{ W/cm}^2$), and a strong red upconverting emission spectrally matching the absorption of photosensitizers.



Scheme 3.1 The characteristics of the UCNP-PDT platforms. (a) Comparison between spectrally-mismatched platforms featuring green upconversion and spectrally-matched platforms featuring red upconversion emission. The red upconversion emission matches the absorption maximum of photosensitizers. Inset: digital photographs of cuvettes with UCNP samples. Conventional green-emitting UCNPs (left) and red-emitting UCNPs in this study (right) with 808 nm excitation. (b) Comparison of temperature increase in the gel phantoms irradiated by 980 nm laser and 808 nm laser at the same power density for 10 min. (c) Comparison of upconversion emission change from the red-emitting UCNPs upon 980 nm and 808 nm excitation in this study immersed in water at variable excitation distance ($d = 0, 1, 3, 5$ cm from left to right).

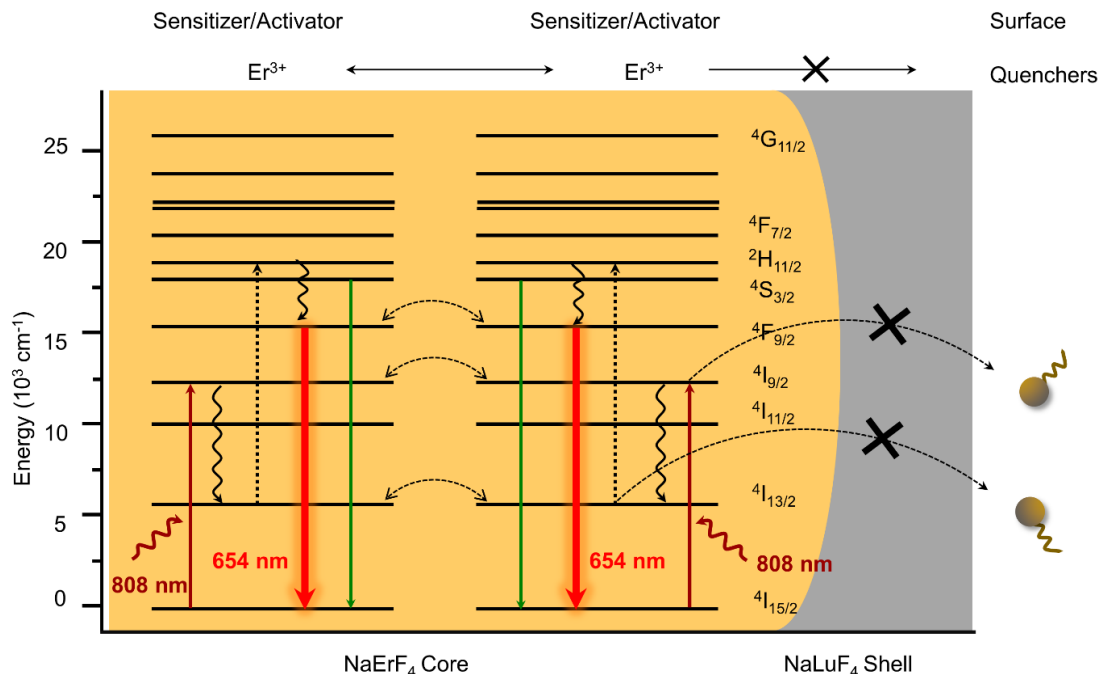


Figure 3.2 Energy level diagram of the β -NaErF₄@NaLuF₄ CS-NPs in this study. They absorb the 808 nm excitation and emit dominant red upconversion (654 nm) at Er³⁺. The red emission matches with the absorption maximum of photosensitizer ZnPc. The excitation energy is not susceptible to surface quenching due to the undoped shell.

Herein we report a β -NaErF₄@NaLuF₄ core-shell (CS) UCNP/ZnPc-based PDT platform to simultaneously address the limitations mentioned above. This UCNP-PDT platform has completely matched spectral profile between the UCNP and photosensitizer in the visible red band (Scheme 3.1a), has no overheating effects (Scheme 3.1b), and the UCNP emission under 808 nm remains largely unaffected even after passing through a \sim 5 cm block of water as compared to the 980 nm excitation (Scheme 3.1c), highlighting their relevance to biological setting. In this platform, the CS-NPs are directly excited at 808 nm through the ground-state-absorption ($^4I_{15/2} \rightarrow ^4I_{9/2}$) and excited-state-absorption ($^4I_{9/2} \rightarrow ^4G_{11/2}$, $^4I_{13/2} \rightarrow ^4S_{3/2}$) of activators (Er³⁺) in the core⁴³⁻⁴⁴ without any previously used sensitizers (Yb³⁺, Nd³⁺).³⁵⁻³⁶ The undoped thick epitaxial shell (NaLuF₄) confines the excitation energy within the core and away from surface quenchers. Both features assist to achieve strong upconverted emission (Figure 3.2). Moreover, the independence of

upconversion emission to concentration quenching in CS-NPs as we have shown in our previous work,⁴⁴ allows Er³⁺ luminescent centers at high doping concentration (100% molar ratio in this study compared to 0.5%-2% in conventional designs^{18, 35-36}) that is beneficial for localized photosensitizer ZnPc activation.

3.3 Results and Discussion

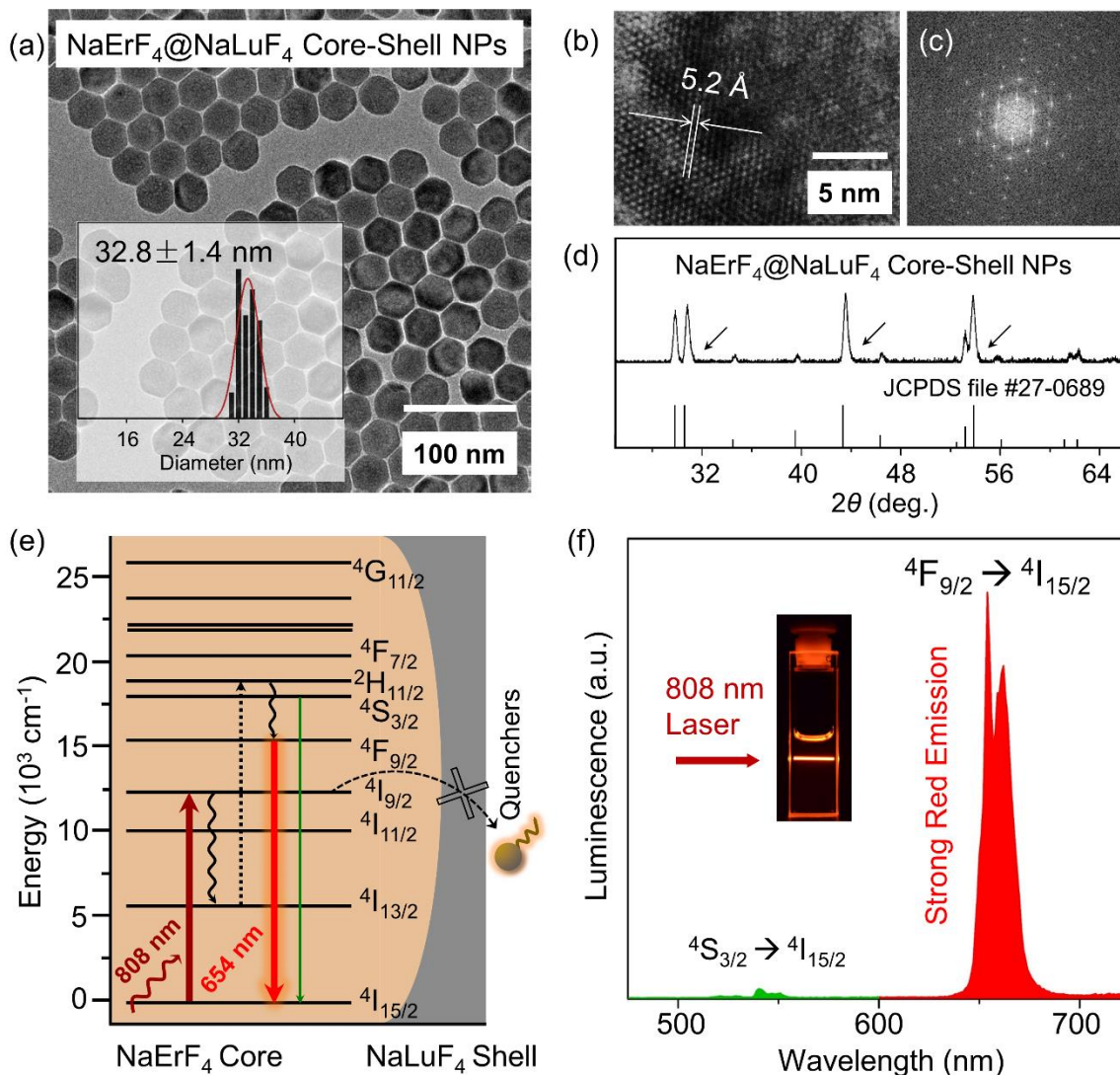


Figure 3.3 Characterization β - NaErF_4 @ NaLuF_4 CS-NPs. (a) TEM image and size distribution (inset) of the CS-NPs. (b) High-resolution TEM image of single CS-NP confirming its high crystallinity. The size of lattice fringe is 5.2 Å. (c) FFT diffractogram and (d) powder XRD pattern of the CS-NPs confirming the hexagonal phase by indexing to JCPDS file # 27-0689. The black arrow in (d) indicates the shift of peaks towards the high angle. (e) Energy level diagram of the Er^{3+} in the CS-NPs. (f) Upconversion emission spectra of CS-NPs in the visible region (475 nm – 725 nm) with 808 nm laser excitation. Inset: digital photograph of the cuvette containing CS-NPs with laser excitation.

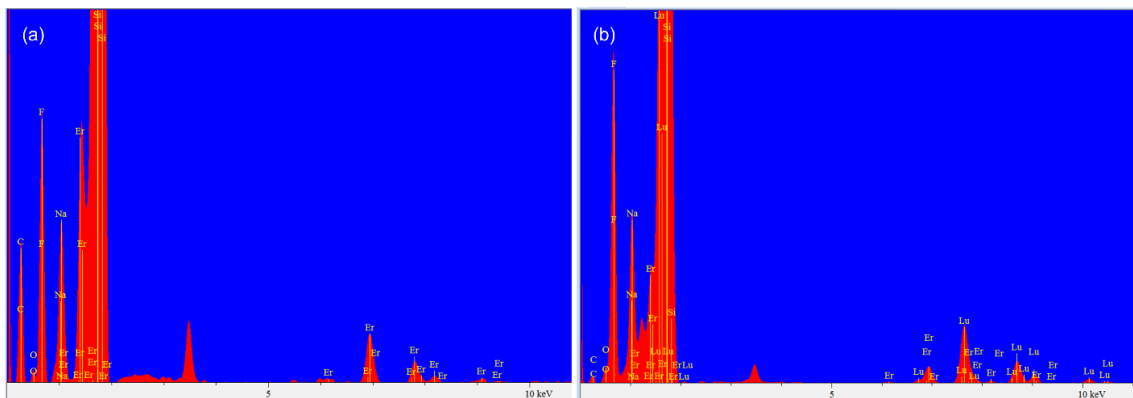


Figure 3.4 EDX spectra of (a) NaErF₄ core and (b) NaErF₄@NaLuF₄ CS-NPs showing only Er in the core while both Er and Lu in the CS-NPs.

We synthesized highly crystalline and uniform β -NaErF₄@NaLuF₄ CS-NPs (Figure 3.3 a-b) by following previous reports on self-focusing *via* ripening.⁴⁴⁻⁴⁶ Kinetically-stable α -NaLuF₄ NPs were prepared and used as sacrificial precursors for the overgrowth of the epitaxial NaLuF₄ shell. After β -NaErF₄ core NPs have formed in the high-temperature solution, α -NaLuF₄ NPs were rapidly injected into the solution and β -NaErF₄@NaLuF₄ CS-NPs formed *via* Ostwald ripening (see Materials and Methods for experimental details).

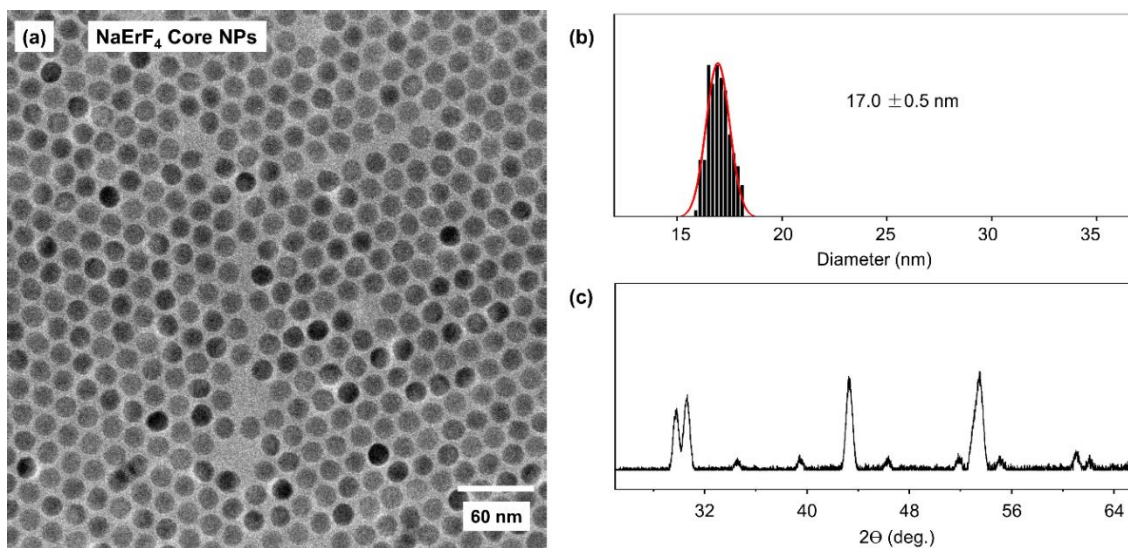


Figure 3.5 (a) TEM images, (b) size distribution, and (c) XRD pattern of NaErF₄ core NPs.

Energy Dispersive Spectroscopy (EDS) confirmed the element composition of the core and CS nanostructures (Figure 3.4). Transmission electron microscopy (TEM) images revealed that both the core and CS-NPs are highly monodispersed and hexagonal with average sizes of 17.0 nm (Figure 3.5) and 32.8 nm (Figure 3.6 and 3.7), respectively. The corresponding fast Fourier transform (FFT) diffractogram of the CS-NPs indicated their hexagonal phase (Figure 3.3c). Powder X-Ray diffraction (XRD) pattern confirmed that the NaLuF₄ shells adapt the crystal lattice of NaErF₄ cores and uniformly grow around them (Figure 3.3d), which is critical to enhancing the upconversion emission under low power excitation.⁴⁷

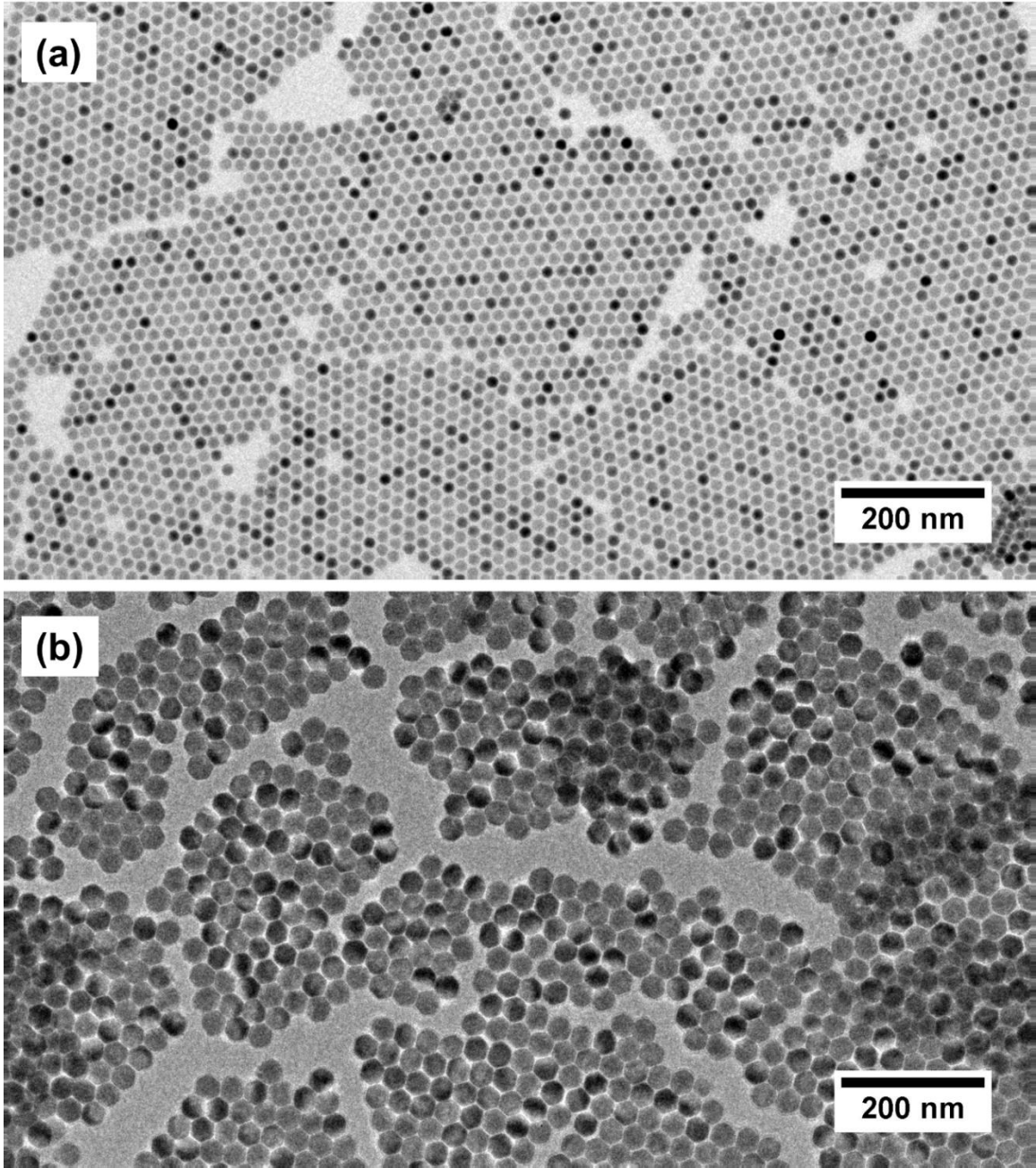


Figure 3.6 Low-magnification TEM images of (a) NaErF_4 core and (b) $\text{NaErF}_4@ \text{NaLuF}_4$ CS-NPs showing their excellent uniformity and monodispersity.

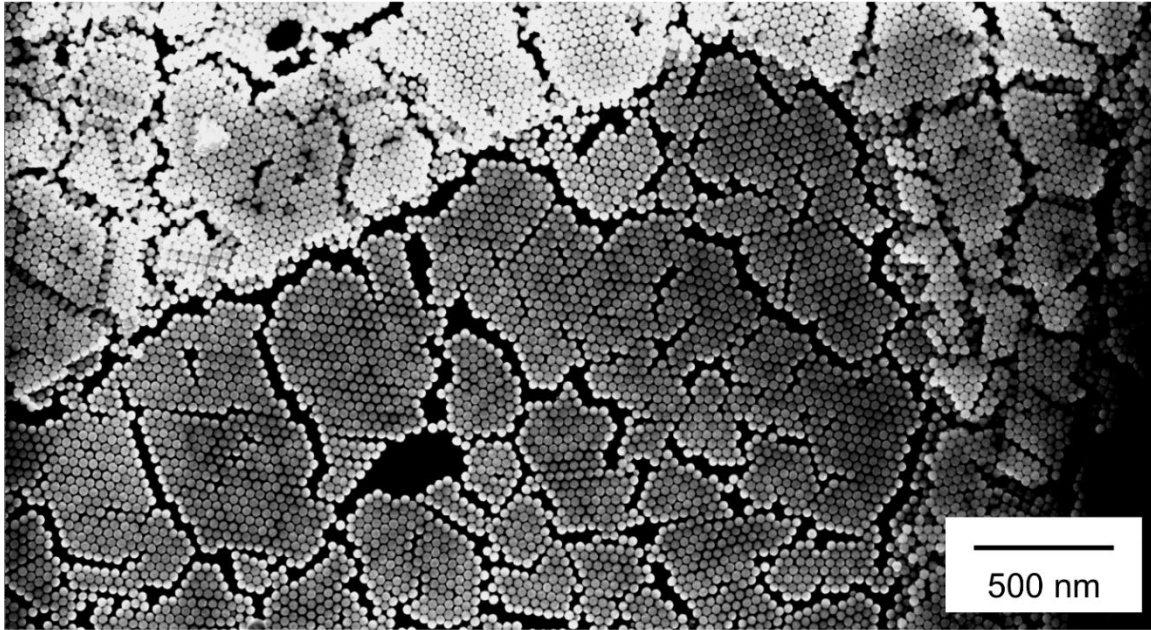


Figure 3.7 Low-magnification SEM image of NaErF₄@NaLuF₄ CS-NPs.

Upconversion emission properties of the as-synthesized β -NaErF₄ core NPs and β -NaErF₄@NaLuF₄ CS-NPs were obtained by exciting them with an 808 nm continuous wave diode laser (3 W/cm²) (see Materials and Methods for details). The β -NaErF₄ core NPs do not have any observable/measurable emission due to the dominant surface quenching at high dopant concentration (100 mol% Er³⁺).⁴⁴ β -NaErF₄@NaLuF₄ CS-NPs have two major emission peaks centered at 540 nm and 654 nm corresponding to transitions $^4S_{3/2} \rightarrow ^4I_{15/2}$ and $^4F_{9/2} \rightarrow ^4I_{15/2}$ of Er³⁺ respectively (Figure 3.3e, f). Thick, uniformly grown epitaxial NaLuF₄ shell effectively suppressed the surface quenching and enhanced the upconversion emission of both peaks compared to the cores. The integrated emission intensity at 654 nm (red) is approximately 40 times stronger than that of 540 nm (green), giving a discernible red emission from the CS-NP colloidal dispersion (Figure 3.3f, inset). The 654 nm emission intensity *versus* excitation power density reveals a double logarithmic increment, indicating that the transition $^4F_{9/2} \rightarrow ^4I_{15/2}$ originated from a two-photon upconversion process of the 808 nm excitation (Figure 3.8).

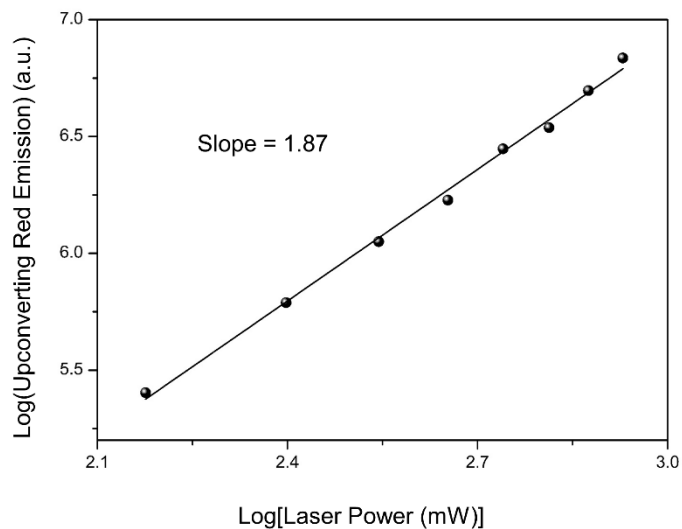


Figure 3.8 The log-to-log plot of red upconversion emission peak intensity (integrated through 600 – 700 nm) to the 808 nm laser excitation power.

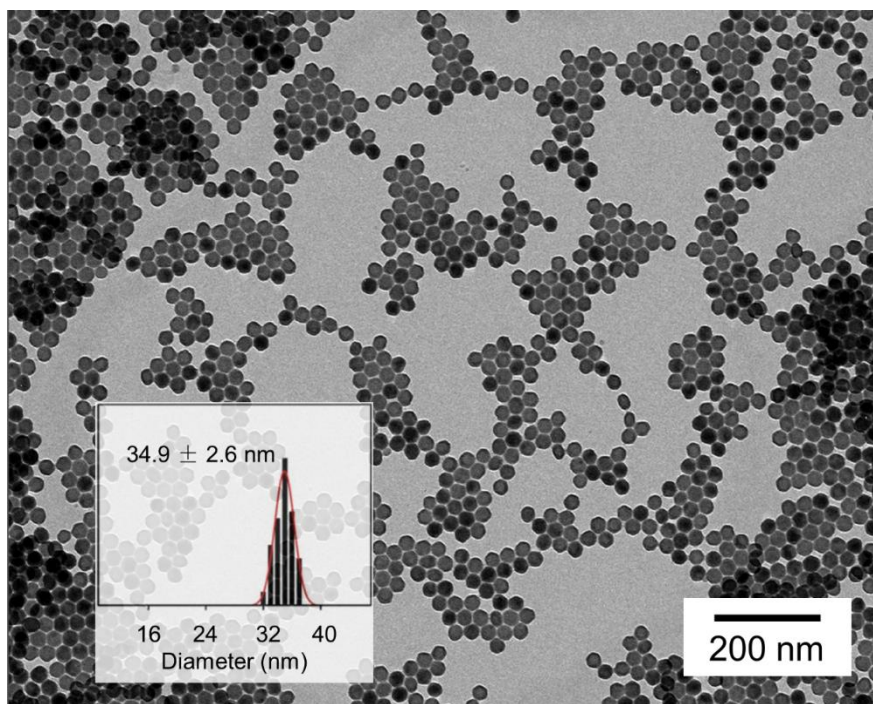


Figure 3.9 TEM image of β -NaYF₄:Yb(18%)/Er(2%)@NaLuF₄:Nd(10%) NPs.

To compare our spectrally-matched platform with previously reported 808 nm-excited yet spectrally-mismatched UCNP-PDT systems, we synthesized β -NaYF₄:Yb/Er@NaLuF₄:Nd NPs

(Nd³⁺-doped NPs) commonly used in other studies³⁵⁻³⁶ and investigated their upconversion emission properties. Nd³⁺-doped NPs have similar sizes to our CS-NPs (Figure 3.9) and are excited with 808 nm laser as well through the cascade energy transfer pathway (Figure 3.1). As shown in Figure 3.10a, upon 808 nm laser excitation, Nd³⁺-doped NPs have two major emission peaks also centered at 540 nm and 654 nm respectively, but the emission intensity of 654 nm peak is only one-eighth of the 540 nm peak. The emission maximum in the green regime is not matched with the absorption maximum of the photosensitizer ZnPc (Figure 3.10a), clearly highlighting the limitation of such spectral mismatched systems. In comparison, our CS-NP platform features a 654 nm peak 40 times stronger than 540 nm peak and spectrally matches the absorption maximum of the ZnPc (Figure 3.10b). This enormous red-to-green ratio (I_{red}/I_{green}) show negligible change with the variable excitation power density (3.4 W/cm² to 0.6 W/cm²), highlighting that spectral matching with dominant red upconverting emission works at a range of laser excitation power density (Figure 3.11). This is particularly important in correlating UCNP-PDT systems with biologically-relevant excitation power densities and to potentially realize clinical translation because tissue attenuation and scattering will vary the excitation laser intensity at different penetration depths.

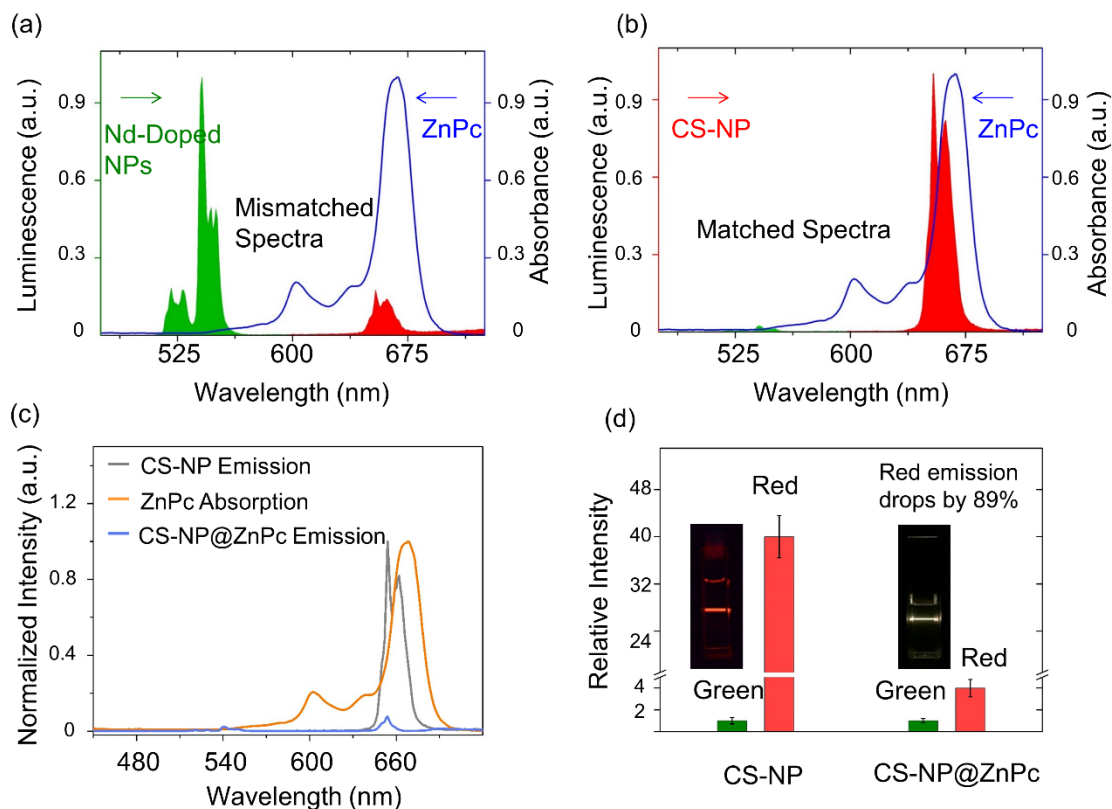


Figure 3.10 Spectral matching between the UCNP emission and the photosensitizers ZnPc. (a) Absorption spectra of ZnPc and upconversion green emission spectra of Nd^{3+} -doped NPs with minimal overlap. (b) Absorption spectra of ZnPc and upconversion emission spectra of $\beta\text{-NaErF}_4\text{@NaLuF}_4$ CS-NPs with maximal overlap between them. (c) Comparison of UC emission spectra between CS-NPs alone and CS-NPs coated with ZnPc. (d) Intensity change of upconverted green emission and red emission from the CS-NPs. Inset: digital photographs of CS-NPs (red) and CS-NP@ZnPc (yellow).

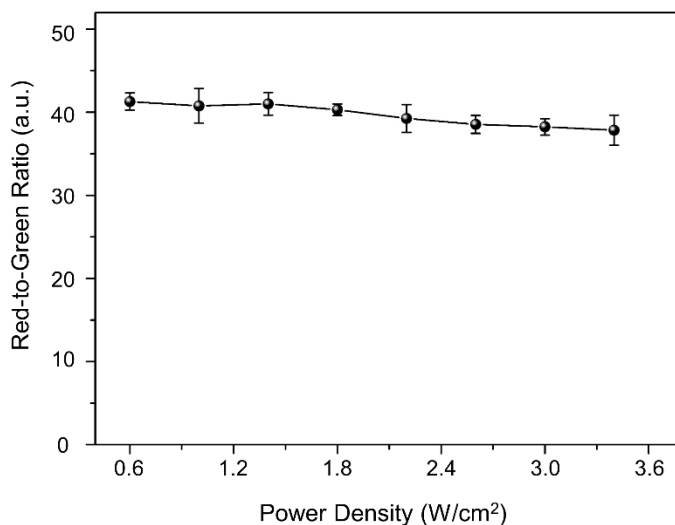


Figure 3.11 The red-to-green ratio *versus* the 808 nm laser excitation at different pump power density. The upconversion emission intensity in the red region was integrated through 600 – 700 nm while the green was integrated through 500 – 600 nm.

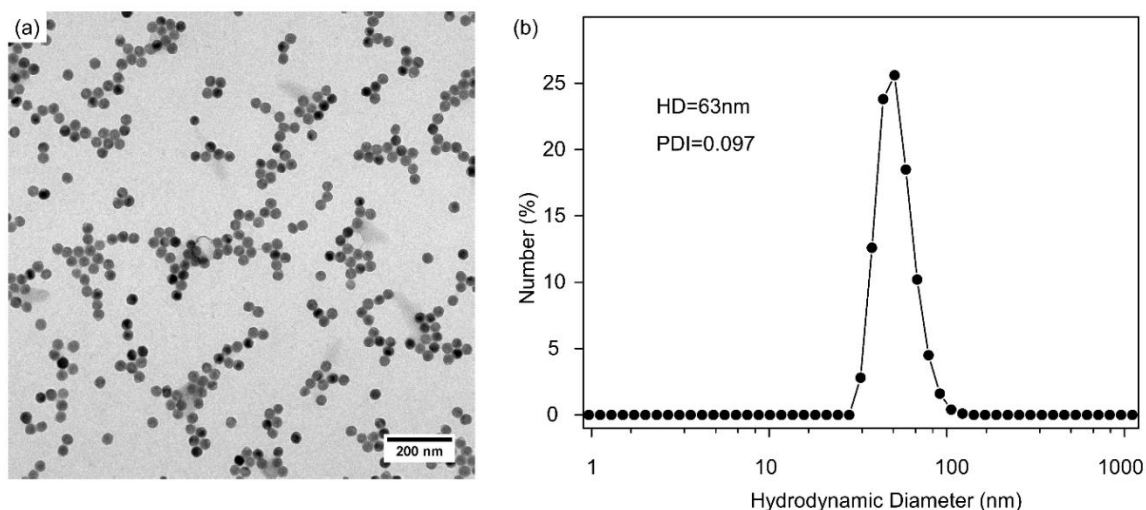


Figure 3.12 Phase transfer of NaErF₄@NaLuF₄ CS-NPs into water with ZnPc and DSPE-PEG 2000 surface coating. (a) TEM image showing that CS-NP@ZnPc@PEG are not aggregated after phase transfer. (d) DLS of the CS-NP@ZnPc@PEG showing their low PDI.

To demonstrate the utility of this UNCP-PDT platform, we coated ZnPc onto the CS-NPs and investigated their optical properties. Using PEGylated phospholipids (DSPE-PEG 2000) as surfactants, we transferred the CS-NPs from chloroform to water through micellization,⁴⁸⁻⁴⁹ generating water-dispersible NPs with biocompatible PEGylated surfaces (see Materials and

Methods for details). The hydrophobic ZnPc was encapsulated and stabilized between the DSPE-PEG 2000 and the oleate intercalated layer on the surface of CS-NPs. Dynamic Laser Scattering (DLS) measurements and TEM images confirmed that the ZnPc-coated PEGylated CS-NPs (CS-NP@ZnPc@PEG) were well-dispersed in water without any aggregation (Figure 3.12). The small hydrodynamic diameter of CS-NP@ZnPc@PEG (63 nm) indicated that all the coated ZnPc firmly attached with the CS-NP, thereby the photosensitization of ZnPc *via* the upconverted red emission is more efficient due to the reduced distance between the UCNP and ZnPc dye. The loading density of ZnPc on CS-NPs was about 400 molecules per particle (see Materials and Methods for details), much more than the previously reported encapsulation⁵⁰ due to the large CS-NP surface area (32.8 nm in diameter and 3400 nm² in surface area). We measured the upconversion emission spectra of CS-NP@ZnPc@PEG with 808 nm excitation and found that the intensity of red emission ($^4F_{9/2} \rightarrow ^4I_{15/2}$) decreased by 89% while the green emission ($^4S_{3/2} \rightarrow ^4I_{15/2}$) remained unchanged (Figure 3.10c, d). Therefore, the red-to-green ratio (I_{red}/I_{green}) of the CS-NP@ZnPc@PEG drastically dropped from 40 to 4 giving an overall yellow emission of the solution, in stark contrast with the original red emission of CS-NPs alone (Figure 3.10d, inset). This clearly demonstrates the effective re-absorption of the red emission by the ZnPc coated on the NP surfaces.

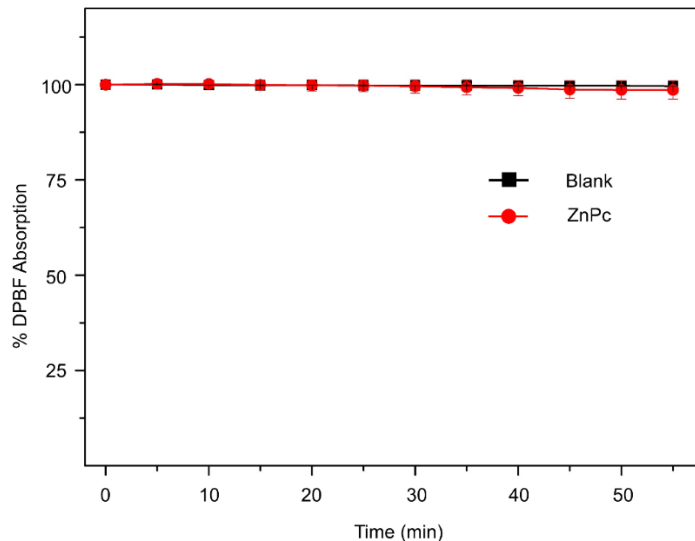


Figure 3.13 Determination of singlet oxygen generation of ZnPc@PEG in the dark confirming that ZnPc does not generate singlet oxygen without light activation.

We next examined the generation of cytotoxic singlet oxygen from the photosensitizer ZnPc upon 808 nm laser excitation. 1,3-Diphenylisobenzofuran (DPBF) was used as a singlet oxygen indicator as it reacts irreversibly with singlet oxygen and causes a decrease in its absorbance centered at 430 nm, which can be monitored by UV-Vis spectroscopy.⁵¹ We first confirmed that ZnPc alone without light exposure (either ambient light or laser light) does not generate singlet oxygen in solution using DPBF over time (~ 1 h) (Figure 3.13). Then, DPBF was added into freshly prepared CS-NP@ZnPc@PEG, CS-NP@PEG, and ZnPc@PEG aqueous solution respectively. All three groups were irradiated with 808 nm continuous wave laser (0.6 W/cm²) in the dark for the same time, and the absorbance of DPBF was recorded every 5 min. Immediately after laser irradiation for 5 min, we observed a decrease of absorbance in the CS-NP@ZnPc@PEG group, indicating generation of singlet oxygen by photo-activated ZnPc in the solution (Figure 3.14a). The absorbance of DPBF decreased from 100% to 36% over time (~1 h), evidently suggesting that our platform generates singlet oxygen continuously under low power 808

nm laser excitation. In contrast, no change in absorbance was recorded in either CS-NP@PEG or ZnPc@PEG group over the same duration, further confirming that the singlet oxygen is induced by the activation of ZnPc *via* upconverted red emission from the CS-NPs.

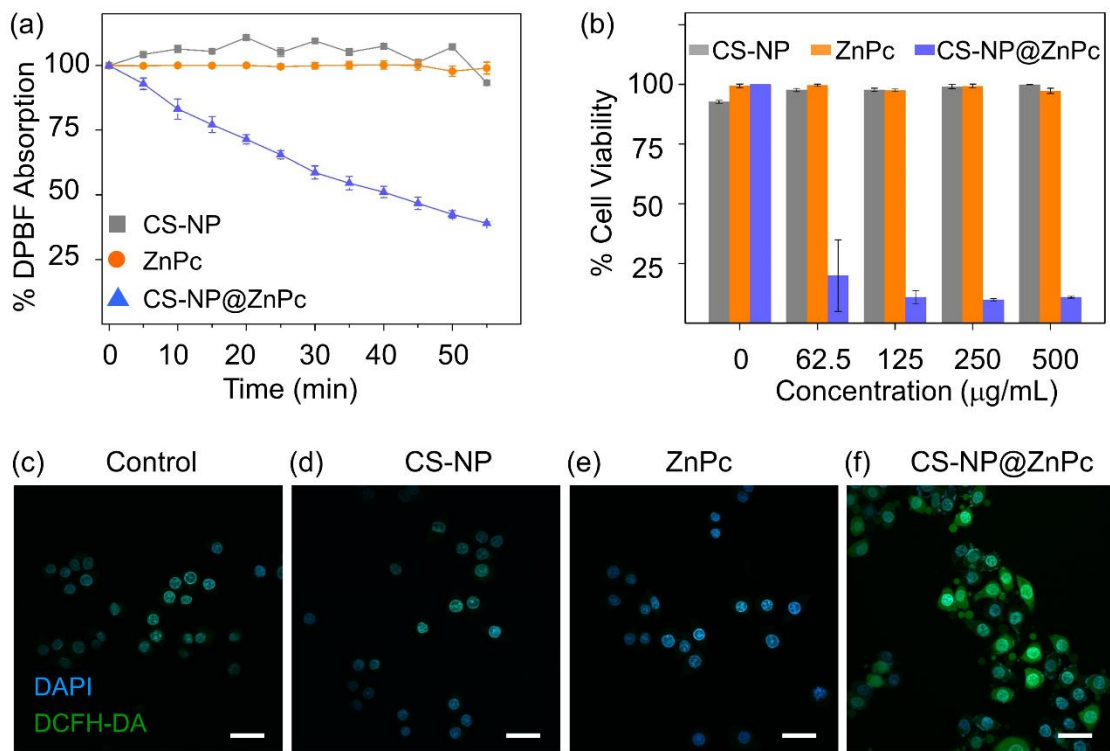


Figure 3.14 *in vitro* PDT on HeLa cells. (a) Quantification of $^1\text{O}_2$ generation in solution with 808 nm excitation using DPBF as the indicator. (b) The viability of HeLa cells after incubation with different groups and exposure to 808 nm laser irradiation for 20 min. (c – f) Intracellular visualization of singlet oxygen using DCFH-DA as the green fluorescent indicator (Scale bar 40 μm).

Next, we performed *in vitro* PDT on HeLa cells with CS-NP@ZnPc@PEG upon 808 nm continuous wave laser irradiation. Intracellular uptake of photosensitizers is critical to PDT as singlet oxygen generated inside the cells exerts highest oxidative stress to the pivotal organelles in the cytoplasm.⁵² Therefore, we first incubated the HeLa cells with CS-NP@ZnPc@PEG and confirmed that cells internalize them efficiently (see Materials and Methods for details). Both TEM (Figure 3.15) and confocal microscopy images (Figure 3.16) clearly showed that the CS-

NP@ZnPc@PEG were internalized in the cytoplasm of HeLa cells after 3 h incubation, and with an increase of accumulation with prolonged incubation time (Figure 3.15).

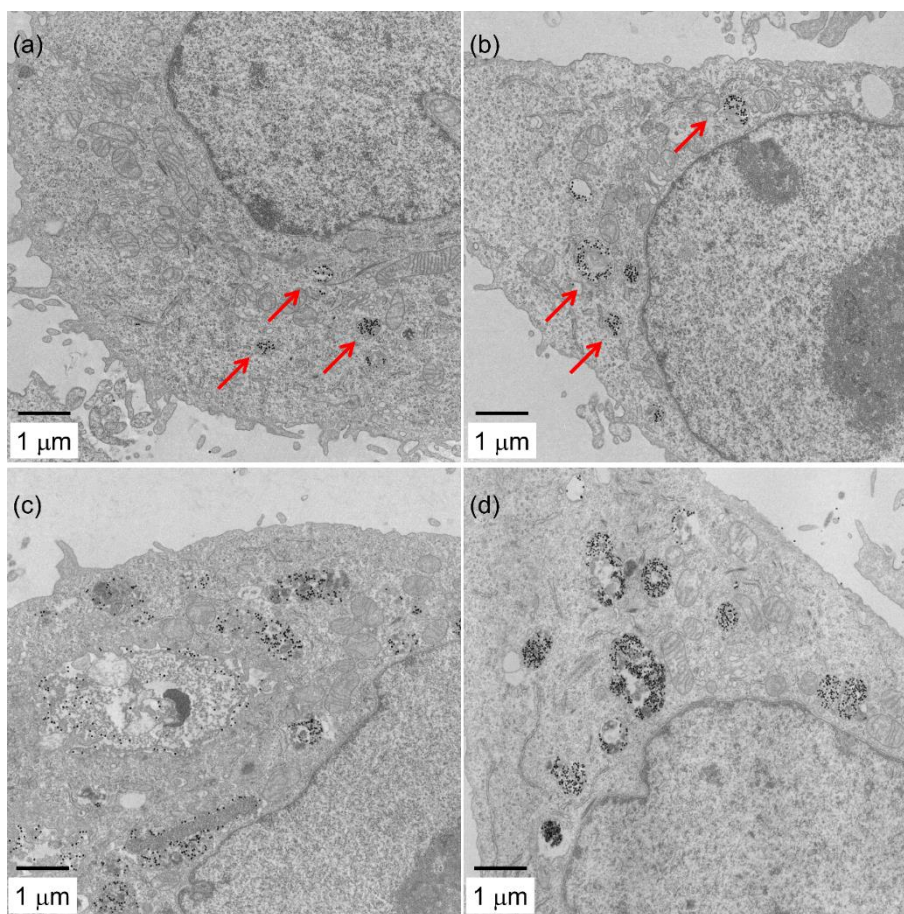


Figure 3.15 TEM of HeLa cells with the intracellular uptake of the CS-NP@ZnPc@PEG with incubation time of (a) 3 h, (b) 6 h, (c) 12 h, and (d) 24 h. With prolonged incubation time, there was an increased intracellular accumulation of CS-NP@ZnPc@PEG but all the organelles stayed intact, demonstrating the biocompatibility of CS-NP@ZnPc@PEG before singlet oxygen was generated.

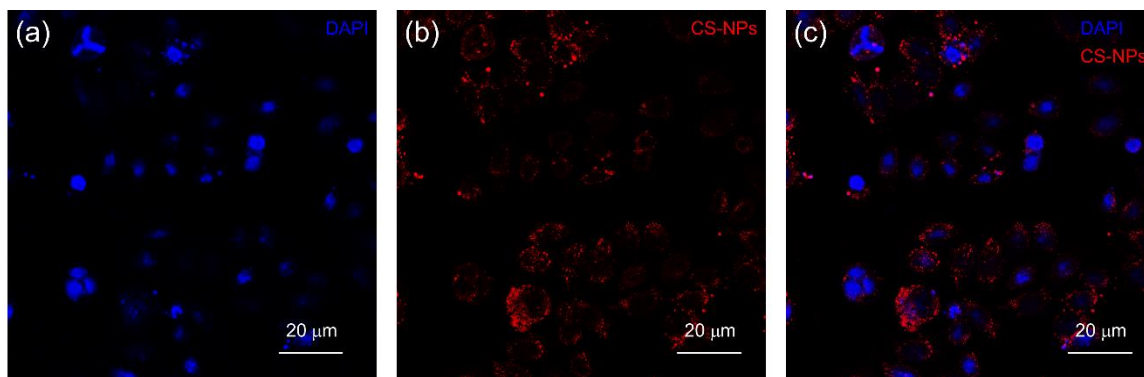


Figure 3.16 Confocal microscopy images of HeLa cells with the intracellular uptake of the CS-NP@ZnPc@PEG.

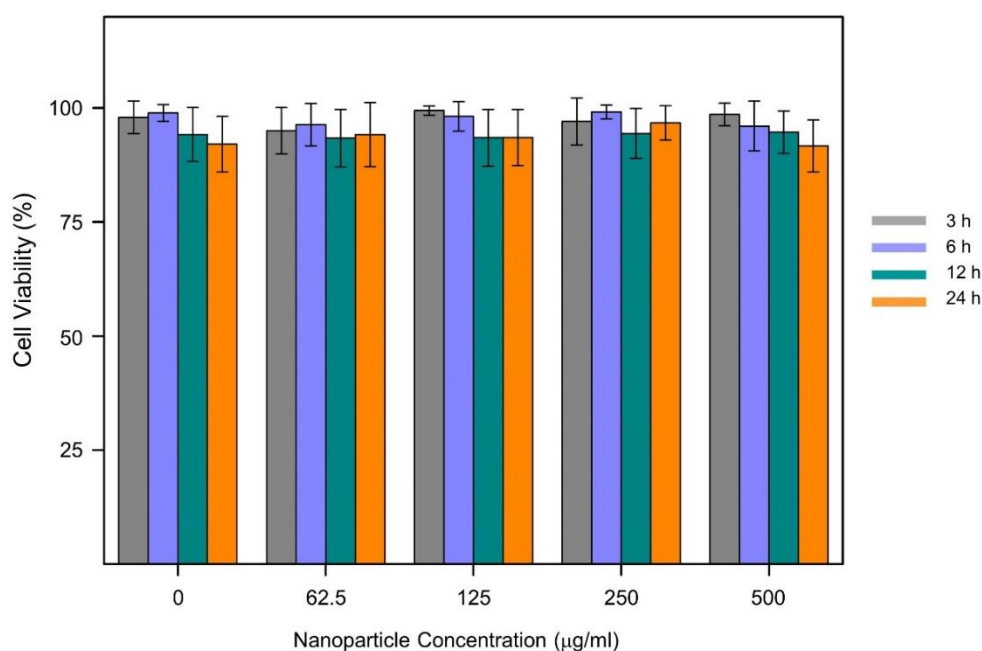


Figure 3.17 Toxicity of CS-NP@ZnPc@PEG to HeLa cells in the dark with different NP concentration and different incubation time.

We then evaluated the cytotoxicity of CS-NP@ZnPc@PEG by incubating HeLa cancer cells and RAW 264.7 cells (used as a representative normal cell line for control) with different NP concentrations in the dark for variable time. Without laser irradiation or any other light exposure, we found that the CS-NP@ZnPc@PEG were not toxic to HeLa cells (Figure 3.17) or RAW 264.7 cells (Figure 3.18) even after incubation with the NP concentration of 0.5 mg/mL for 24 h. This is because CS-NP@ZnPc@PEG did not generate singlet oxygen in the absence of light. These data

further validate the biocompatibility provided by the PEGylated NP surfaces as shown above. Also, when HeLa cells without the incubation of CS-NP@ZnPc@PEG were subjected to 808 nm laser irradiation, they were still viable even at laser power density as high as 1.3 W/cm^2 (Figure 3.19). These results again attest the biological relevance of 808 nm excitation compared with 980 nm.

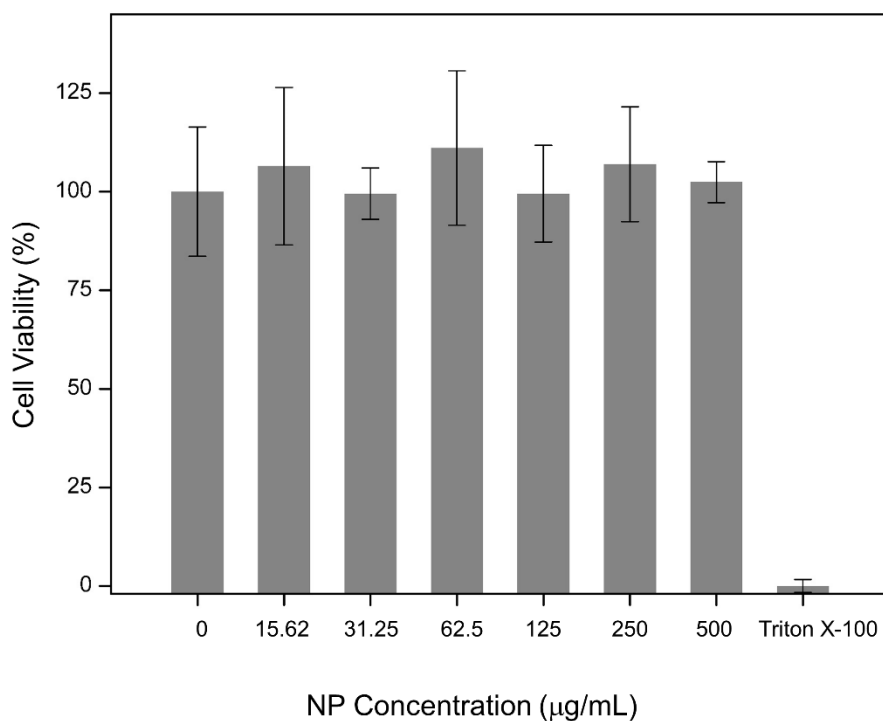


Figure 3.18 *in vitro* cell viability of RAW264.7 cells incubated with CS-NP@ZnPc@PEG at different concentrations for 24 h. Triton X-100 was used as negative control.

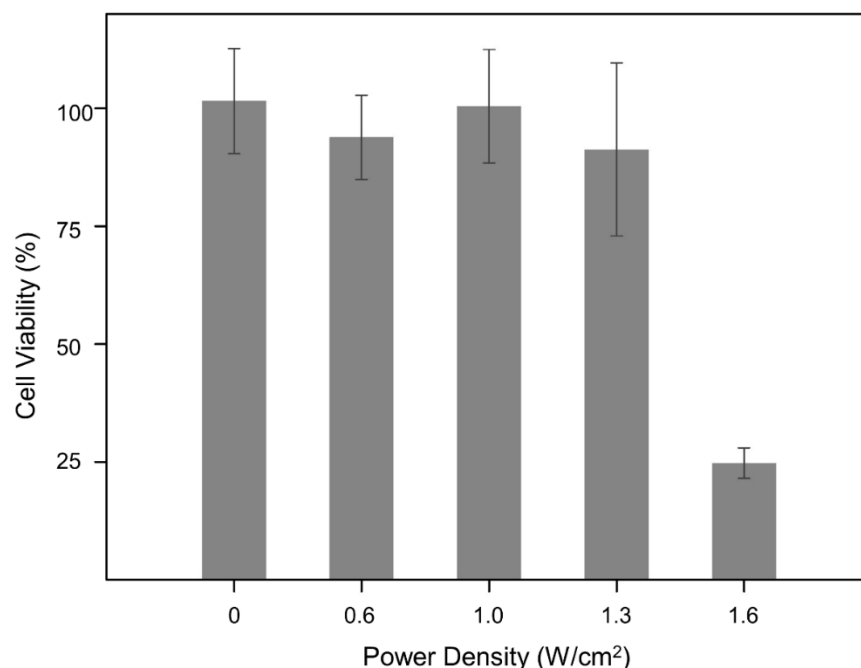


Figure 3.19 Cell viability under 808 nm laser irradiation with different power density to determine the safe threshold for laser working in the PDT experiments.

However, when we exposed the HeLa cells incubated with CS-NP@ZnPc@PEG to 808 nm laser irradiation, they were effectively killed. As shown in Figure 3.14b, even at low NP concentration (0.0625 mg/mL), ~25% of the HeLa cells lost their viability in the CS-NP@ZnPc@PEG group after 808 nm laser irradiation at 0.6 W/cm². In comparison, the groups incubated with CS-NP@PEG or ZnPc@PEG did not show any significant cell death after laser irradiation. This difference in cell viability confirms that 808 nm laser irradiation or ZnPc alone were not responsible for the loss of viability. In other words, PDT in this platform was only triggered by the concurrent presence of 808 nm laser, CS-NPs, and ZnPc. Taken together, these results demonstrate that spectrally-matched UCNP-ZnPc platform allows effective killing of the cancer cells by PDT at low power 808 nm excitation.

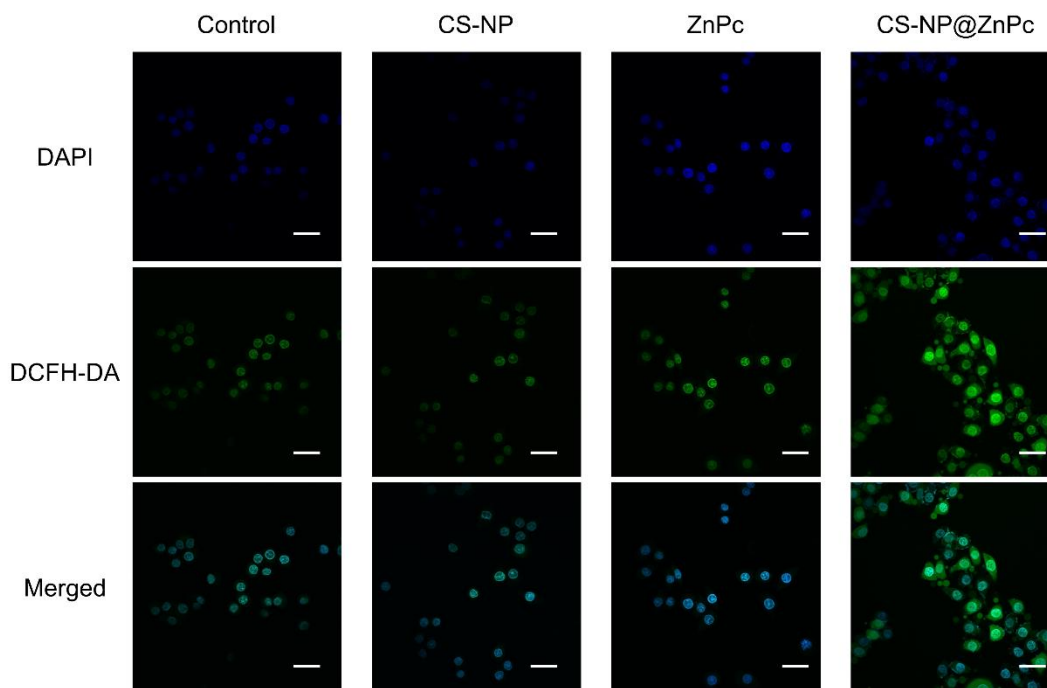


Figure 3.20 Confocal microscopy images of HeLa cells showing intracellular visualization of singlet oxygen in split and merged imaging channels (Scale bar 40 μm).

To gain more insight into the *in vitro* PDT process and validate that intracellular generation of singlet oxygen is the primary cause of the death of cancer cells, we used 2', 7'-dichlorofluorescein diacetate (DCFH-DA) to visualize the intracellular presence of singlet oxygen after CS-NP@ZnPc@PEG incubation and laser irradiation. DCFH-DA is a highly sensitive fluorescent sensor for singlet oxygen and emits green fluorescence after being oxidized by singlet oxygen, allowing *in situ* confirmation of singlet oxygen.⁵³ After incubating HeLa cells with CS-NP@ZnPc@PEG, CS-NP@PEG, or ZnPc@PEG and exposing them to laser irradiation for 20 min, we added DCFH-DA into the cell culture media and characterized their emission by confocal microscopy. As shown in Figure 3.14 c-f and Figure 3.20, we observed distinct green fluorescence in the cytoplasm of HeLa cells only in the CS-NP@ZnPc@PEG group, confirming the intracellular abundance of singlet oxygen after laser irradiation. In contrast, the cells incubated with CS-

NP@PEG or ZnPc@PEG did not show characteristic green emission in the cytoplasm. Therefore, the presence of intracellular singlet oxygen is consistent with the decrease in cell viability that we determined above (Figure 3.14b). These studies evidently correlate the generation of singlet oxygen and the killing of cancer cells using spectrally matched UCNP-ZnPc platform.

Finally, to demonstrate the potential of this platform for cancer therapy, we cultured three-dimensional (3D) HeLa cell spheroids and examined the PDT effect of spectrally matched UCNP-ZnPc platform on the cancer spheroids (Figure 3.21a). An actively growing cancer cell spheroid is an advanced model to simulate the *in vivo* tumor site regarding cellular communication and development of extracellular matrices.⁵⁴ We cultured HeLa cell spheroids up to an average size of 3 mm (Figure 3.21b) on top of the meniscus of agarose hydrogel and then incubated the spheroids with CS-NP@ZnPc@PEG in the dark for 24 h (see Materials and Methods for details).

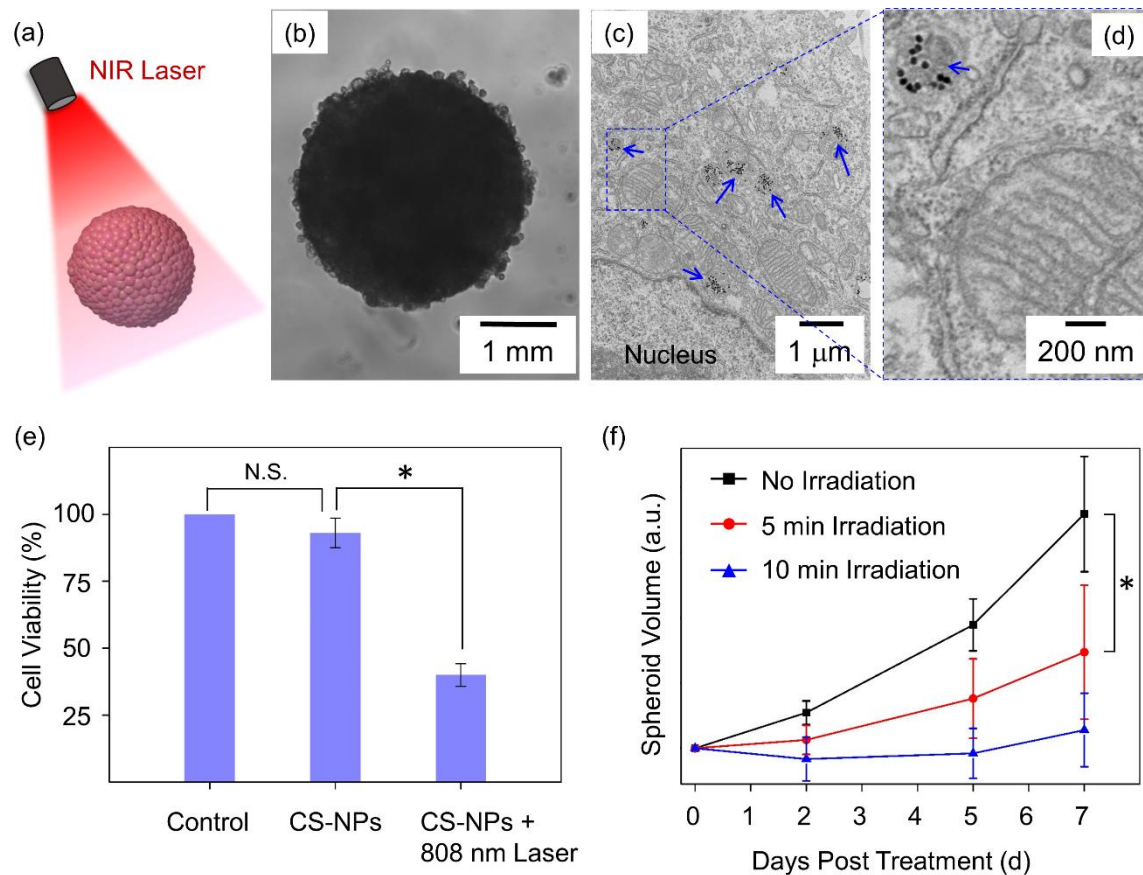


Figure 3.21 PDT on cancer cell spheroids. (a) The schematic illustration of the PDT on HeLa cancer cell spheroids. (b) Optical microscope image of a typical cell spheroids with a size of ca. 3 mm. (c) TEM image of HeLa cells within the spheroids with internalized CS-NPs@ZnPc@PEG (blue arrow). (d) Enlarged image of figure (c) showing the presence of NPs and an intact mitochondria. (e) Cell viability in the cell spheroids incubated with CS-NPs@ZnPc@PEG only, with both CS-NPs@ZnPc@PEG and 808 nm laser irradiation. The control group was with neither incubation nor irradiation. * $p < 0.05$. (f) Cell spheroid volume change after CS-NPs@ZnPc@PEG incubation for the same time but laser irradiation for the different time. * $p < 0.05$.

TEM images of sliced HeLa cell spheroids again confirmed that the CS-NP@ZnPc@PEG were internalized by the HeLa cells in the spheroids (Figure 3.21c, d). We found that the most of the cell organelles stayed intact and organized, indicating that the cells within the spheroids were viable with the NP incubation in the dark. This was further confirmed by the non-significantly

different viability between the cell spheroids incubated with CS-NP@ZnPc@PEG and the blank control group (Figure 3.21e).

However, after irradiated the cell spheroids at 0.6 W/cm^2 for 10 min after they internalized with CS-NP@ZnPc@PEG, we found that the overall cell viability dropped to 35 % of their initial value, significantly lower than either the blank control or those with NP incubation but no laser exposure (Figure 3.21e). This is clear indication of the effective PDT by CS-NP@ZnPc@PEG under laser activation in the three-dimensional (3D) cell environment. Furthermore, we monitored the volume changes of the cell spheroids after one-time laser exposure (0.6 W/cm^2) for different time. The growth of HeLa cell spheroids was significantly slowed after only 5min laser exposure (Figure 3.21f), indicating that the cytotoxic singlet oxygen stayed within the cancer cells and subsequently disabled the cellular functions. When the laser exposure time increased to 10 min, the spheroid volume did not increase significantly even after seven days (Figure 3.21f), consistent with the loss of cell viability we showed above (Figure 3.21e). This clearly demonstrates that our UCNP-PDT platform with the spectral matching feature can effectively treat tumors in different biological settings with extremely low power 808 nm excitation.

3.4 Conclusions

In conclusion, we have presented an 808 nm-activated PDT platform by leveraging the spectral match between red-emitting $\beta\text{-NaErF}_4\text{@NaLuF}_4$ UCNPs and red-absorbing photosensitizers ZnPc. The UCNP/ZnPc PDT platform generates 40 times stronger red emission than green emission under bio-benign 808 nm excitation at extremely low yet biologically relevant laser power density than other UCNP-PDT platforms reported to date (Table 1). High local concentration of Er^{3+} activators (100 mol%) in the CS-NPs convert 808 nm to 654 nm, activates

the photosensitizers ZnPc on the NP surfaces, and generates cytotoxic singlet oxygen because of the spectral matching. Using 3D grown HeLa cell spheroids we show that tumor cells with a “single” short irradiation (5 min) of low power laser (0.6 W/cm²) can be effectively treated using the spectrally-matched UCNP-PDT platform. The strategy demonstrated in this study can be widely explored further where UCNP-coated molecular photosensitizers can be potentially applied to other diseases including macular degeneration, psoriasis, and atherosclerosis.⁵⁵ Moreover, coupling this platform with light-degradable polymers⁵⁶⁻⁵⁷ or activatable polymers that respond to inflammation,⁵⁸ we highlight that low power bio-benign laser-activated therapeutic platforms will become clinically viable to address a broad spectrum of medical challenges.

Table 3.1 Spectral features of the UCNPs and photosensitizers used in this work and other various studies.

UCNP Excitation	UCNP Em _{max}	I _{red} /I _{green}	Photosensitizer Abs _{max}	Reference
808 nm	540 nm	< 1	667 nm	34
980 nm	540 nm	< 1	660 nm	40
980 nm	654 nm	~ 2	667 nm	41
980 nm	654 nm	~ 2	640 nm	42
808 nm	654 nm	~ 40	667 nm	This work

3.5 Materials and Methods

Chemicals

Yttrium acetate hydrate (99.9%), erbium acetate hydrate (99.9%), ytterbium acetate hydrate (99.9%), neodymium oxide (99.9%), trifluoroacetic acid, 1-octadecene (>90%), oleic acid

(>90%), oleylamine (>70%), sodium trifluoroacetate, sodium hydroxide, zinc phthalocyanine (ZnPc), 1,3-Diphenylisobenzofuran (DPBF) (97%), 2,7-Dichlorofluorescein diacetate (DCFH-DA) (97%), methanol, chloroform, ethanol, toluene were all purchased from Sigma. Ammonium fluoride was purchased from Spectrum. Lutetium oxide (99.9%) was purchased from Alfa Aesar. 1,2-distearoyl-sn-glycero-3-phosphoethanolamine-N-[(polyethylene glycol)-2000] (DSPE-PEG-2000) was purchased from Avanti Lipids. All chemicals were used as received without further purification unless specified.

Synthesis of hexagonal (β)-NaErF₄ core NPs

Briefly, 1 mmol of erbium acetate hydrate was dissolved in 1-octadecene (15 mL) and oleic acid (4.5 mL) in a 100mL three-neck flask. The slurry was quickly heated to 120 °C under vacuum and kept for 45 min to obtain a clear, pinkish-orange solution. The clear solution was cooled down to room temperature, and a methanol solution (10mL) of ammonium fluoride (4 mmol) and sodium hydroxide (2.5 mmol) was added into the flask. The mixture was stirred at room temperature for 45 min and subsequently heated to 70 °C to remove methanol. During the heating process, the slurry became progressively transparent and more yellow. The solution was then quickly heated to 300 °C (~ 15 °C/min) under a gentle argon flow and maintained at this temperature for 1 h. Finally, the reaction mixture was cooled to room temperature naturally. The NPs were precipitated by adding ethanol, and collected by centrifugation (1900 g, 5 min) and washed several times with ethanol. The resulting pellet was then dispersed in chloroform for further studies.

Synthesis of cubic (α)-NaLuF₄ NPs (Sacrificial shell NPs)

In a typical synthesis, Lu₂O₃ (1 mmol) was dissolved in 50% trifluoroacetic acid aqueous solution (20 mL), and the slurry was refluxed overnight at 95 °C to obtain a clear solution. The clear solution was then put at 70 °C to remove the solvent, remaining ~2 mmol lutetium trifluoroacetate (Lu (CF₃COO)₃) as dry powder. To the dry powder, sodium trifluoroacetate (2 mmol) was added along with 1-octadecene (12 mL), oleic acid (6 mL), and oleylamine (6 mL). The slurry was quickly heated to 120 °C under vacuum and maintained for 30 min to obtain a clear yellow solution. The clear solution was subsequently heated to 300 °C rapidly (~15°C/min) under a gentle argon flow and vigorously stirred until the solution became cloudy. The cloudy solution was kept 300 °C for 15 min to obtain kinetically-stable α -NaLuF₄ NPs. The synthesized NPs were likewise cleaned, dispersed in hexane (10 mL) and stored at 37 °C for characterization and subsequent synthesis.

Synthesis of α -NaLuF₄:Nd(10%) NPs

α -NaLuF₄:Nd(10%) were synthesized with the same protocol described above except that Lu₂O₃ (0.9 mmol) and Nd₂O₃ (0.1 mmol) were used.

Synthesis of β -NaErF₄@NaLuF₄ CS-NPs

As synthesized cubic phase NPs (α -NaLuF₄ ~1.0 mmol) in hexane were mixed with 1mL 1-octadecene and hexane was removed under a gentle flow of argon. After the β -NaErF₄ core NPs have been heated at 300 °C for 1 h, 1-octadecene dispersion of sacrificial shell NPs (α -NaLuF₄) was subsequently injected into the solution and allowed to ripen (12-15 min) to yield CS NPs. Seven injection-and-ripening cycles were performed while carefully maintaining the reaction

mixture at 300 °C to generate the thick shell (7.9 nm) in this study. Finally, the CS-NPs were cleaned as described above.

Synthesis of β -NaYF₄:Yb(18%)/Er(2%)@NaLuF₄:Nd(10%) NPs (Nd³⁺-doped NPs)

Synthesis of Nd³⁺-doped NPs were synthesized following the same protocol of synthesis of β -NaErF₄@NaLuF₄ CS-NPs described above except that starting with yttrium acetate (0.8 mmol), ytterbium acetate (0.18 mmol), erbium acetate (0.02 mmol), 1-octadecene (15mL) and oleic acid (6mL). After the solution has been heated at 300 °C for 1 h, α -NaLuF₄:Nd(10%) with the same mole amount of α -NaLuF₄ in β -NaErF₄@NaLuF₄ synthesis was injected into the solution to obtain Nd³⁺-doped NPs.

Phase transfer of CS-NPs into water (CS-NP@PEG)

5 mg as synthesized β -NaErF₄@NaLuF₄ CS-NPs in chloroform was mixed with 20 mg DSPE-PEG 2000 in a 20 mL screw-neck glass vial. The vial was left open overnight in a fume hood at room temperature to slowly evaporate chloroform and leave an oily layer at the bottom. The vial was mounted on a rotary evaporator (Buchi R-205) at 60 °C for 1 h to remove excess chloroform completely. Distilled water (10 mL) was added to the vial, and the vial was sonicated for 5 min to transfer the NPs into water. The solution was filtered twice through 0.22 μ m sterile polyethersulfone (PES) syringe filter (30 mm diameter, Low Hold-up volume, Olympus Plastics), and subsequently centrifuged using a Optima L-80 XP from Beckman Coulter with 50.2 Ti rotor ultracentrifuge operating at 45000 rpm (~184,000 g) at 4 °C for 1 h. The supernatant with excess empty micelles was carefully removed, and the pellet was re-dispersed into 5 mL distilled water and stored at 4 °C for further studies. We denote the obtained aqueous solution as CS-NP@PEG.

When a higher concentration of the NPs in the solution is needed, the as-prepared aqueous solution was concentrated by centrifugation (3000 g, 30 min) using a Vivaspin® 20 centrifugal concentrator (100K MWCO, PES) using a Allegra® X-15R Benchtop centrifuge (Beckman, with a swing-out bucket).

Loading photosensitizers onto the CS-NPs (CS-NP@ZnPc@PEG)

Along with 5 mg NPs and 20 mg DSPE-PEG 2000, 0.46 mg ZnPc were together added into the chloroform solution in the vial and dried overnight. The rest of the procedures were the same with that for the phase transfer of NPs protocols and we denote the aqueous solution as CS-NP@ZnPc@PEG.

Transferring photosensitizers into water without CS-NPs (ZnPc@PEG)

0.46 mg ZnPc was mixed with 20 mg DSPE-PEG 2000 in the vial and the rest of the procedures were the same as described above. We denote the aqueous solution as ZnPc@PEG and this was used as control group.

Quantification of ZnPc loading

2 mg ZnPc was dissolved in 40 mL CHCl₃ as stock solution (0.05 mg/mL). 500 µL stock solution was mixed with 25 mg DSPE-PEG 2000 and transferred to water following the same procedure described above, resulting in an aqueous solution of ZnPc with a final concentration of 0.005 mg/mL. The absorption spectra of the ZnPc aqueous solution was recorded with UV-Vis spectrometer (500 – 800 nm) at a series of dilution, and the absorbance at 670 nm was plotted

against its concentration as the standard curve. The absorbance of CS-NP@ZnPc@PEG at 670 nm was also measured, and the concentration of ZnPc was calculated accordingly.

Determination of singlet oxygen

ZnPc is extremely sensitive to light and experiments were done with extreme care in a dark room. 2.7 mg DPBF was dissolved in 10 mL EtOH and aliquoted as the stock solution (~1 mM). 10 μ L DPBF solution was added into 1 mL H₂O, solution of CS-NP@PEG, ZnPc@PEG, and CS-NP@ZnPc@PEG in a glass vial, respectively. All solutions were gently stirred for 5 min before being transferred to a quartz cuvette for UV-Vis spectrometry measurement. The solution was continuously irradiated with an 808 nm continuous wave (CW) diode IR laser system (Dragon Lasers) coupled with fiber optic (M35L01, Thorlabs) in a dark room. The absorbance of DPBF in solution (between 350 nm and 600 nm) was measured every 5 min using a UV-Vis-NIR spectrometer (Shimazu UV-3600).

Dark cytotoxicity of CS-NP@ZnPc@PEG

HeLa/Raw264.7 cells were seeded onto a 96 well plate with a population of 10^4 cells/well. The cells were cultured under 5% CO₂ atmosphere at 37 °C with phosphate-free DMEM (Thermo Fisher), supplemented with 10% Fetal Bovine Serum (FBS) (Omega Scientific), 1% sodium pyruvate (Thermo Fisher), 1% Penicillin-streptomycin (Thermo Fisher). Cells were incubated 24 h to allow residing onto the plate. CS-NP@ZnPc@PEG with various concentrations were added to the cells and incubated in the dark for different time (3 h – 24 h). After the incubation, the cells were washed three times using phosphate-free DMEM and finally 100 μ L phosphate-free DMEM with 10% CCK-8 (Dojindo Molecular Tech) was added to each well for incubation of 3 h. Cell

viability was determined by reading the absorbance at 450 nm using a plate reader (SpectraMax M5, Molecular Devices).

Tolerance of HeLa cells to laser irradiance

HeLa cells were seeded onto 96 well plate with a population of 10^4 cell/well. The cells were cultured under 5% CO₂ atmosphere at 37 °C with phosphate-free DMEM (10% FBS, 1% sodium pyruvate, 1% Penicillin-streptomycin). Cells were incubated 24 h to allow firm adherence onto the plate. After that, the cells were exposed to 808 nm laser irradiation for 20 min at different power density. After irradiation, the cells were incubated for another 24 h and the cell viability was determined by the same method described above.

***In vitro* PDT**

HeLa cells were seeded onto 96 well plate with a population of 10^4 cells/well. The cells were cultured under 5% CO₂ atmosphere at 37 °C with phosphate-free DMEM (10% FBS, 1% sodium pyruvate, 1% Penicillin-streptomycin). Cells were incubated 24 h to allow firm adherence onto the plate. Different concentration of CS-NP@PEG, CS-NP@ZnPc@PEG, ZnPc@PEG were added to the cells and incubated for 24 h. Cells were then washed three times with phosphate-free DMEM to remove excess NPs and incubated with 100 µL media. Each group was exposed to an 808 nm continuous laser irradiation for 20 min at a power density of 0.6 W/cm². Control groups were protected from light by sanitized black aluminum foil. After irradiation, the cell viability was determined by the same method described above.

Confocal laser scanning microscope imaging

Glass coverslip was put into 24 well plate, and 500 μL poly-L-lysine was added into the well to immerse the cover slide. After 30 min incubation at 37 $^{\circ}\text{C}$, the slide was rinsed twice with cell culture media. HeLa cells were seeded into the well with a population of 50,000 cells/well. After 24 h incubation, 500 $\mu\text{g}/\text{mL}$ CS-NP@ZnPc@PEG was added into the well. After another 24 h incubation, cells were fixed with PFA (4%) at 37 $^{\circ}\text{C}$ for 15 min. The coverslip with fixed cells was rinsed twice with PBS. A droplet of mounting media was cast onto a glass slide, and the coverslip with fixed cells was flipped over and attached to the mounting media. Confocal microscopy images were taken with a Leica SP5 confocal microscope.

Visualization of intracellular singlet oxygen

HeLa cells were seeded into a 2.5cm cell culture dish with a population of 10^5 cells and incubated for 24 h before experiments. Different samples were added into the cell culture media and incubated for another 6 h. After washing with media for three times, DCFH-DA was added into the dish to a final concentration of 10^{-5} M and the cells were incubated for 20 min. After irradiation with 808 nm laser for 20 min, the dish was taken to microscopy characterization immediately. Images were taken with a confocal microscope (Olympus FV-1000) with a 488 nm argon laser for excitation and emission at 510-540 nm.

Cell TEM

HeLa cells were seeded into a 5 cm cell culture dish with a population of 10^6 cells and incubated 24 h before experiments. UCNP@ZnPc@PEG was added into the dish with a final concentration of 500 $\mu\text{g}/\text{mL}$. After different incubation times, cells were fixed with 0.1 M sodium

cacodylate (SC) buffer (pH 7.4) with 2% glutaraldehyde (v/v) to obtain a cell pellet. The cell pellets were washed in 0.1 M SC buffer three times on ice, fixed with 1% osmium tetroxide in SC buffer for 1h on ice, washed in 0.1 M SC buffer three times, washed with DI water. The pellet was dehydrated with 50%, 70%, 90%, 2 × 100% ETOH, and finally dry acetone at room temperature. Each of the dehydration steps took around 5-8 min. Finally, the cell pellet was embedded in Durcupan and incubated in an oven at 60 °C for 48 h. The plastic slab was sectioned with a Leica Reichert-Jung ultramicrotomes, and the thin slice was imaged with JEOL 1200 EX II TEM operating at 80 KV equipped with a 35 mm port digital camera.

PDT on tumor spheroids

HeLa tumor spheroids were cultured using liquid-overlay culture. Briefly, a 96-well tissue culture plate was coated with autoclaved agarose (1% w/v, 40 μL/well). HeLa cells were seeded (100 cells/well) in phosphate-free DMEM medium (Life Technologies) supplemented with 10% FBS (Omega Scientific), 1 mM Sodium Pyruvate (Life Technologies), and 10 μg/mL Ciprofloxacin HCl (Santa Cruz Biotech). Spheroids were grown for 14 days, with media being changed every 2-3 days throughout the period. On day 14, spheroids were double washed with 100 μL media and incubated with 100 μg/mL of CS-NP@ZnPc@PEG, or fresh cell growth media as control, for 24 h in the dark. Following the incubation, the spheroids were again double washed with media and irradiated for 0, 5, 10 min of 808 nm laser light (Dragon Lasers, 0.6 W/cm²). The spheroid size was measured by light microscopy (Nikon FV100) over the course of 7 days. To quantify the live cells in the wells, we dissociated the spheroids 24 h after laser treatment by using 25% Trypsin-EDTA (Life Technologies), stained with Trypan Blue (Life Technologies), and counted on an automated cell counter (TC20, Bio-Rad).

TEM on tumor spheroids

The HeLa tumor spheroids were processed following the same procedure described above to visualize the cellular uptake of CS-NPs@ZnPc@PEG in HeLa cells in the spheroids.

Characterization

The size and uniformity of the β -NaErF₄ core and β -NaErF₄@NaLuF₄ CS NPs were confirmed using transmission electron microscopy (TEM) (FEI, Technai G2 Sphera, operating at 120 kV). One droplet of the NP stock solution was diluted with 1 mL of hexane, and drop cast onto a Pelco[®] carbon-coated 400 square mesh copper grid (Ted Pella, Inc.) and air dried for 1 hour before imaging. Scanning electron microscopy (SEM) images and energy-dispersive X-ray spectroscopy (EDX) analysis were performed on FEI SFEG UHR scanning electron microscope (operating at 5 kV). The statistical analysis of the size was taken with measurement of at least 100 NPs on TEM images and presented as a mean \pm standard deviation. The crystal phase of NPs was determined by powder X-ray diffraction (XRD) using Siemens KFL Cu 2K diffractometer with a resolution of 0.02° and a scanning speed of 1°/min. Upconversion emission spectra of the β -NaErF₄ core and β -NaErF₄@NaLuF₄ CS NPs were collected with a Fluorolog modular spectrofluorometer (Horiba) coupled with an 808 nm (L808P1WJ, Thorlabs) or 980 nm (L975P1WJ, Thorlabs) continuous wave (CW) laser diode mounted on a temperature controlled laser diode mount (TCLDM9, Thorlabs) operating at 200 mW (power density 3 W/cm²). The slit for the collection of the spectra was set to 1 nm and the integration time was set to 0.5 s. Upconverted emission was collected perpendicular to the direction of excitation light. Dynamic light scattering (DLS) experiments were performed using a Zetasizer Nano ZS (Malvern Instruments) at room

temperature. Elemental concentration was determined by digesting the NPs in 70% HNO₃ for at least two days and analyzed using a Perkin Elmer Optima 3000 DV inductively coupled plasma atomic emission spectrometer (ICP-AES).

Chapter 3, is unpublished work. Sha He, and Adah Almutairi. The dissertation author was the primary investigator and author of this material.

3.6 References

1. Dolmans, D.; Fukumura, D.; Jain, R. K., Photodynamic Therapy for Cancer. *Nat. Rev. Cancer* **2003**, *3*, 380-387.
2. Celli, J. P.; Spring, B. Q.; Rizvi, I.; Evans, C. L.; Samkoe, K. S.; Verma, S.; Pogue, B. W.; Hasan, T., Imaging and Photodynamic Therapy: Mechanisms, Monitoring, and Optimization. *Chem. Rev.* **2010**, *110*, 2795-2838.
3. Tong, R.; Kohane, D. S., Shedding Light on Nanomedicine. *Wiley Interdiscip. Rev.-Nanomed. Nanobiotechnol.* **2012**, *4*, 638-662.
4. Ma, P.; Xiao, H.; Yu, C.; Liu, J.; Cheng, Z.; Song, H.; Zhang, X.; Li, C.; Wang, J.; Gu, Z.; Lin, J., Enhanced Cisplatin Chemotherapy by Iron Oxide Nanocarrier-Mediated Generation of Highly Toxic Reactive Oxygen Species. *Nano Lett.* **2017**, *17*, 928-937.
5. Huang, Y. R.; He, S.; Cao, W. P.; Cai, K. Y.; Liang, X. J., Biomedical Nanomaterials for Imaging-guided Cancer Therapy. *Nanoscale* **2012**, *4*, 6135-6149.
6. Spring, B. Q.; Rizvi, I.; Xu, N.; Hasan, T., The Role of Photodynamic Therapy in Overcoming Cancer Drug Resistance. *Photochem. Photobiol. Sci.* **2015**, *14*, 1476-1491.
7. Lucky, S. S.; Soo, K. C.; Zhang, Y., Nanoparticles in Photodynamic Therapy. *Chem. Rev.* **2015**, *115*, 1990-2042.
8. Fan, W. P.; Huang, P.; Chen, X. Y., Overcoming the Achilles' heel of photodynamic therapy. *Chem. Soc. Rev.* **2016**, *45*, 6488-6519.
9. Samia, A. C. S.; Chen, X. B.; Burda, C., Semiconductor Quantum Dots for Photodynamic Therapy. *J. Am. Chem. Soc.* **2003**, *125*, 15736-15737.
10. Lin, J.; Wang, S. J.; Huang, P.; Wang, Z.; Chen, S. H.; Niu, G.; Li, W. W.; He, J.; Cui, D. X.; Lu, G. M.; Chen, X. Y.; Nie, Z. H., Photosensitizer-Loaded Gold Vesicles with Strong Plasmonic Coupling Effect for Imaging-Guided Photothermal/Photodynamic Therapy. *ACS Nano* **2013**, *7*, 5320-5329.
11. Kim, S.; Ohulchanskyy, T. Y.; Pudavar, H. E.; Pandey, R. K.; Prasad, P. N., Organically Modified Silica Nanoparticles Co-encapsulating Photosensitizing Drug and Aggregation-Enhanced Two-Photon Absorbing Fluorescent Dye Aggregates for Two-Photon Photodynamic Therapy. *J. Am. Chem. Soc.* **2007**, *129*, 2669-2675.

12. Hulchanskyy, T. Y.; Roy, I.; Goswami, L. N.; Chen, Y.; Bergey, E. J.; Pandey, R. K.; Oseroff, A. R.; Prasad, P. N., Organically Modified Silica Nanoparticles with Covalently Incorporated Photosensitizer for Photodynamic Therapy of Cancer. *Nano Lett.* **2007**, *7*, 2835-2842.
13. Chatterjee, D. K.; Fong, L. S.; Zhang, Y., Nanoparticles in Photodynamic Therapy: An Emerging Paradigm. *Adv. Drug Del. Rev.* **2008**, *60*, 1627-1637.
14. Bechet, D.; Couleaud, P.; Frochot, C.; Viriot, M.-L.; Guillemin, F.; Barberi-Heyob, M., Nanoparticles as Vehicles for Delivery of Photodynamic Therapy Agents. *Trends Biotechnol.* **2008**, *26*, 612-621.
15. Zhuang, X. X.; Ma, X. W.; Xue, X. D.; Jiang, Q.; Song, L. L.; Dai, L. R.; Zhang, C. Q.; Jin, S. B.; Yang, K. N.; Ding, B. Q.; Wang, P. C.; Liang, X. J., A Photosensitizer-Loaded DNA Origami Nanosystem for Photodynamic Therapy. *ACS Nano* **2016**, *10*, 3486-3495.
16. Chen, G.; Qiu, H.; Prasad, P. N.; Chen, X., Upconversion Nanoparticles: Design, Nanochemistry, and Applications in Theranostics. *Chem. Rev.* **2014**, *114*, 5161-5214.
17. Dong, H.; Du, S.-R.; Zheng, X.-Y.; Lyu, G.-M.; Sun, L.-D.; Li, L.-D.; Zhang, P.-Z.; Zhang, C.; Yan, C.-H., Lanthanide Nanoparticles: From Design toward Bioimaging and Therapy. *Chem. Rev.* **2015**, *115*, 10725-10815.
18. Wang, C.; Cheng, L.; Liu, Z., Upconversion Nanoparticles for Photodynamic Therapy and Other Cancer Therapeutics. *Theranostics* **2013**, *3*, 317-330.
19. Wang, C.; Tao, H.; Cheng, L.; Liu, Z., Near-Infrared Light Induced In Vivo Photodynamic Therapy of Cancer Based on Upconversion Nanoparticles. *Biomaterials* **2011**, *32*, 6145-6154.
20. Idris, N. M.; Gnanasammandhan, M. K.; Zhang, J.; Ho, P. C.; Mahendran, R.; Zhang, Y., In vivo Photodynamic Therapy Using Upconversion Nanoparticles as Remote-Controlled Nanotransducers. *Nat. Med.* **2012**, *18*, 1580-U190.
21. Wang, C.; Cheng, L.; Liu, Y. M.; Wang, X. J.; Ma, X. X.; Deng, Z. Y.; Li, Y. G.; Liu, Z., Imaging-Guided pH-Sensitive Photodynamic Therapy Using Charge Reversible Upconversion Nanoparticles under Near-Infrared Light. *Adv. Funct. Mater.* **2013**, *23*, 3077-3086.
22. Cui, S. S.; Yin, D. Y.; Chen, Y. Q.; Di, Y. F.; Chen, H. Y.; Ma, Y. X.; Achilefu, S.; Gu, Y. Q., In Vivo Targeted Deep-Tissue Photodynamic Therapy Based on Near-Infrared Light Triggered Upconversion Nanoconstruct. *ACS Nano* **2013**, *7*, 676-688.

23. Liu, Y. Y.; Liu, Y.; Bu, W. B.; Cheng, C.; Zuo, C. J.; Xiao, Q. F.; Sun, Y.; Ni, D. L.; Zhang, C.; Liu, J. A.; Shi, J. L., Hypoxia Induced by Upconversion-Based Photodynamic Therapy: Towards Highly Effective Synergistic Bioreductive Therapy in Tumors. *Angew. Chem. Int. Ed.* **2015**, *54*, 8105-8109.
24. Raj, J. G. J.; Quintanilla, M.; Vetrone, F., Near-Infrared Triggered Generation of Reactive Oxygen Species from Upconverting Nanoparticles Decorated with an Organoiridium Complex. *J. Mat. Chem. B* **2016**, *4*, 3113-3120.
25. Dong, J.; Zink, J. I., Light or Heat? The Origin of Cargo Release from Nanoimpeller Particles Containing Upconversion Nanocrystals under IR Irradiation. *Small* **2015**, *11*, 4165-4172.
26. Zhan, Q.; Qian, J.; Liang, H.; Somesfalean, G.; Wang, D.; He, S.; Zhang, Z.; Andersson-Engels, S., Using 915 nm Laser Excited Tm³⁺/Er³⁺/Ho³⁺-Doped NaYbF₄ Upconversion Nanoparticles for in Vitro and Deeper in Vivo Bioimaging without Overheating Irradiation. *ACS Nano* **2011**, *5*, 3744-3757.
27. Wang, Y.-F.; Liu, G.-Y.; Sun, L.-D.; Xiao, J.-W.; Zhou, J.-C.; Yan, C.-H., Nd³⁺-Sensitized Upconversion Nanophosphors: Efficient In Vivo Bioimaging Probes with Minimized Heating Effect. *ACS Nano* **2013**, *7*, 7200-7206.
28. Shen, J.; Chen, G.; Vu, A.-M.; Fan, W.; Bilsel, O. S.; Chang, C.-C.; Han, G., Engineering the Upconversion Nanoparticle Excitation Wavelength: Cascade Sensitization of Tri-doped Upconversion Colloidal Nanoparticles at 800 nm. *Adv. Opt. Mater.* **2013**, *1*, 644-650.
29. Xie, X.; Gao, N.; Deng, R.; Sun, Q.; Xu, Q.-H.; Liu, X., Mechanistic Investigation of Photon Upconversion in Nd³⁺-Sensitized Core-Shell Nanoparticles. *J. Am. Chem. Soc.* **2013**, *135*, 12608-12611.
30. Zhong, Y.; Tian, G.; Gu, Z.; Yang, Y.; Gu, L.; Zhao, Y.; Ma, Y.; Yao, J., Elimination of Photon Quenching by a Transition Layer to Fabricate a Quenching-Shield Sandwich Structure for 800 nm Excited Upconversion Luminescence of Nd³⁺ Sensitized Nanoparticles. *Adv. Mater.* **2014**, *26*, 2831-2837.
31. Feng, L. L.; He, F.; Liu, B.; Yang, G. X.; Gai, S. L.; Yang, P. P.; Li, C. X.; Dai, Y. L.; Lv, R. C.; Lin, J., g-C₃N₄ Coated Upconversion Nanoparticles for 808 nm Near-Infrared Light Triggered Phototherapy and Multiple Imaging. *Chem. Mater.* **2016**, *28*, 7935-7946.
32. Lv, R. C.; Yang, D.; Yang, P. P.; Xu, J. T.; He, F.; Gai, S. L.; Li, C. X.; Dai, Y. L.; Yang, G. X.; Lin, J., Integration of Upconversion Nanoparticles and Ultrathin Black Phosphorus for Efficient Photodynamic Theranostics under 808 nm Near-Infrared Light Irradiation. *Chem. Mater.* **2016**, *28*, 4724-4734.

33. Wang, D.; Xue, B.; Kong, X.; Tu, L.; Liu, X.; Zhang, Y.; Chang, Y.; Luo, Y.; Zhao, H.; Zhang, H., 808 nm Driven Nd³⁺-Sensitized Upconversion Nanostructures for Photodynamic Therapy and Simultaneous Fluorescence Imaging. *Nanoscale* **2015**, *7*, 190-197.
34. Zeng, L. Y.; Pan, Y. W.; Zou, R. F.; Zhang, J. C.; Tian, Y.; Teng, Z. G.; Wang, S. J.; Ren, W. Z.; Xiao, X. S.; Zhang, J. C.; Zhang, L. L.; Li, A. G.; Lu, G. M.; Wu, A. G., 808 nm-excited Upconversion Nanoprobes with Low Heating Effect for Targeted Magnetic Resonance Imaging and High-Efficacy Photodynamic Therapy in HER2-Overexpressed Breast Cancer. *Biomaterials* **2016**, *103*, 116-127.
35. Liu, B.; Li, C.; Yang, P.; Hou, Z.; Lin, J., 808-nm-Light-Excited Lanthanide-Doped Nanoparticles: Rational Design, Luminescence Control and Theranostic Applications. *Adv. Mater.* **2017**, *29*, 1605434.
36. Xie, X.; Li, Z.; Zhang, Y.; Guo, S.; Pendharkar, A. I.; Lu, M.; Huang, L.; Huang, W.; Han, G., Emerging \approx 800 nm Excited Lanthanide-Doped Upconversion Nanoparticles. *Small* **2017**, *13*, 1602843.
37. Wang, F.; Wang, J. A.; Liu, X. G., Direct Evidence of a Surface Quenching Effect on Size-Dependent Luminescence of Upconversion Nanoparticles. *Angew. Chem. Int. Ed.* **2010**, *49*, 7456-7460.
38. Ai, F.; Ju, Q.; Zhang, X.; Chen, X.; Wang, F.; Zhu, G., A Core-Shell-Shell Nanoplatfrom Upconverting Near-infrared Light at 808 nm for Luminescence Imaging and Photodynamic Therapy of Cancer. *Sci. Rep.* **2015**, *5*, 10785.
39. Tian, G.; Ren, W.; Yan, L.; Jian, S.; Gu, Z.; Zhou, L.; Jin, S.; Yin, W.; Li, S.; Zhao, Y., Red-Emitting Upconverting Nanoparticles for Photodynamic Therapy in Cancer Cells Under Near-Infrared Excitation. *Small* **2013**, *9*, 1929-1938.
40. Chen, F.; Zhang, S.; Bu, W.; Chen, Y.; Xiao, Q.; Liu, J.; Xing, H.; Zhou, L.; Peng, W.; Shi, J., A Uniform Sub-50 nm-Sized Magnetic/Upconversion Fluorescent Bimodal Imaging Agent Capable of Generating Singlet Oxygen by Using a 980 nm Laser. *Chem. Eur. J.* **2012**, *18*, 7082-7090.
41. Park, Y. I.; Kim, H. M.; Kim, J. H.; Moon, K. C.; Yoo, B.; Lee, K. T.; Lee, N.; Choi, Y.; Park, W.; Ling, D.; Na, K.; Moon, W. K.; Choi, S. H.; Park, H. S.; Yoon, S.-Y.; Suh, Y. D.; Lee, S. H.; Hyeon, T., Theranostic Probe Based on Lanthanide-Doped Nanoparticles for Simultaneous In Vivo Dual-Modal Imaging and Photodynamic Therapy. *Adv. Mater.* **2012**, *24*, 5755-5761.

42. Punjabi, A.; Wu, X.; Tokatli-Apollon, A.; El-Rifai, M.; Lee, H.; Zhang, Y.; Wang, C.; Liu, Z.; Chan, E. M.; Duan, C.; Han, G., Amplifying the Red-Emission of Upconverting Nanoparticles for Biocompatible Clinically Used Prodrug-Induced Photodynamic Therapy. *ACS Nano* **2014**, *8*, 10621-10630.
43. Capobianco, J. A.; Vetrone, F.; Boyer, J. C.; Speghini, A.; Bettinelli, M., Enhancement of Red Emission (F-4(9/2)-> I-4(15/2)) via Upconversion in Bulk and Nanocrystalline Cubic Y₂O₃ : Er³⁺. *J. Phys. Chem. B* **2002**, *106*, 1181-1187.
44. Johnson, N. J. J.; He, S.; Diao, S.; Chan, E. M.; Dai, H. J.; Almutairi, A., Direct Evidence for Coupled Surface and Concentration Quenching Dynamics in Lanthanide-doped Nanocrystals. *J. Am. Chem. Soc.* **2017**, *139*, 3275-3282.
45. Johnson, N. J. J.; Korinek, A.; Dong, C.; van Veggel, F. C. J. M., Self-Focusing by Ostwald Ripening: A Strategy for Layer-by-Layer Epitaxial Growth on Upconverting Nanocrystals. *J. Am. Chem. Soc.* **2012**, *134*, 11068-11071.
46. Johnson, N. J. J.; van Veggel, F. C. J. M., Lanthanide-Based Heteroepitaxial Core-Shell Nanostructures: Compressive versus Tensile Strain Asymmetry. *ACS Nano* **2014**, *8*, 10517-10527.
47. Fischer, S.; Johnson, N. J. J.; Pichaandi, J.; Goldschmidt, J. C.; van Veggel, F., Upconverting Core-Shell Nanocrystals with High Quantum Yield under Low Irradiance: On the Role of Isotropic and Thick Shells. *J. Appl. Phys.* **2015**, *118*, 193105.
48. Li, L. L.; Zhang, R. B.; Yin, L. L.; Zheng, K. Z.; Qin, W. P.; Selvin, P. R.; Lu, Y., Biomimetic Surface Engineering of Lanthanide-Doped Upconversion Nanoparticles as Versatile Bioprobes. *Angew. Chem. Int. Ed.* **2012**, *51*, 6121-6125.
49. Johnson, N. J. J.; He, S.; Hun, V. A. N.; Almutairi, A., Compact Micellization: A Strategy for Ultrahigh T-1 Magnetic Resonance Contrast with Gadolinium-Based Nanocrystals. *ACS Nano* **2016**, *10*, 8299-8307.
50. Wu, T. Q.; Wilson, D.; Branda, N. R., Fluorescent Quenching of Lanthanide-Doped Upconverting Nanoparticles by Photoresponsive Polymer Shells. *Chem. Mater.* **2014**, *26*, 4313-4320.
51. Farmilo, A.; Wilkinson, F., On The Mechanism of Quenching of Singlet Oxygen in Solution. *Photochem. Photobiol.* **1973**, *18*, 447-450.
52. Ryter, S. W.; Kim, H. P.; Hoetzel, A.; Park, J. W.; Nakahira, K.; Wang, X.; Choi, A. M. K., Mechanisms of Cell Death in Oxidative Stress. *Antioxid. Redox Signal.* **2007**, *9*, 49-89.

53. Han, K.; Lei, Q.; Wang, S. B.; Hu, J. J.; Qiu, W. X.; Zhu, J. Y.; Yin, W. N.; Luo, X.; Zhang, X. Z., Dual-Stage-Light-Guided Tumor Inhibition by Mitochondria-Targeted Photodynamic Therapy. *Adv. Funct. Mater.* **2015**, *25*, 2961-2971.
54. Sutherland, R. M., Cell and Environment Interactions in Tumor Microregions - The Multicell Spheroid Model. *Science* **1988**, *240*, 177-184.
55. Huang, Z., A Review of Progress in Clinical Photodynamic Therapy. *Technol. Cancer Res. Treat.* **2005**, *4*, 283-293.
56. Viger, M. L.; Grossman, M.; Fomina, N.; Almutairi, A., Low Power Upconverted Near-IR Light for Efficient Polymeric Nanoparticle Degradation and Cargo Release. *Adv. Mater.* **2013**, *25*, 3733-3738.
57. Carling, C. J.; Olejniczak, J.; Foucault-Collet, A.; Collet, G.; Viger, M. L.; Huu, V. A. N.; Duggan, B. M.; Almutairi, A., Efficient Red Light Photo-uncaging of Active Molecules in Water upon Assembly into Nanoparticles. *Chem. Sci.* **2016**, *7*, 2392-2398.
58. Lux, C. D.; Joshi-Barr, S.; Nguyen, T.; Mahmoud, E.; Schopf, E.; Fomina, N.; Almutairi, A., Biocompatible Polymeric Nanoparticles Degrade and Release Cargo in Response to Biologically Relevant Levels of Hydrogen Peroxide. *J. Am. Chem. Soc.* **2012**, *134*, 15758-15764.

Chapter 4

Simultaneous Enhancement of Photoluminescence, MRI Relaxivity, and CT Contrast by Tuning the Interfacial Layer of Lanthanide Heteroepitaxial Nanoparticles

4.1 Abstract

Nanoparticle (NP)-based exogenous contrast agents assist biomedical imaging by enhancing the target visibility against the background. However, it is challenging to design a single type of contrast agents that are simultaneously suitable for various imaging modalities. Simple integration of different components into a single NP contrast agent does not guarantee the optimized properties of each individual components. Herein, we describe lanthanide-based core-shell-shell (CSS) NPs as triple-modal contrast agents that have concurrently enhanced performance compared to their individual components in photoluminescence (PL) imaging, magnetic resonance imaging (MRI), and computed tomography (CT). The key to simultaneous enhancement of PL intensity, MRI r_1 relaxivity, and X-ray attenuation capability in CT is tuning the interfacial layer in the CSS NP architecture. By increasing the thickness of the interfacial layer, we show that (i) PL intensity is enhanced from completely quenched/dark state to brightly emissive state of both upconversion and downshifting luminescence at different excitation wavelengths (980 and 808 nm), (ii) MRI r_1 relaxivity is enhanced by fivefold from $11.4 \text{ mM}^{-1}\text{s}^{-1}$ to $52.9 \text{ mM}^{-1}\text{s}^{-1}$ (per Gd^{3+}) at clinically-relevant field strength 1.5 T, and (iii) the CT Hounsfield Unit gain is 70% higher than the conventional iodine-based agents at the same mass concentration. Our results demonstrate that judiciously designed contrast agents for multimodal imaging can achieve simultaneously enhanced performance compared to their individual stand-alone structures, and highlight that multimodality can be achieved without compromising on individual modality performance.

4.2 Introduction

Multimodal imaging is the next frontier in precise medical diagnosis of various diseases because it integrates the advantages of different imaging modalities while offsetting their individual limitations.¹⁻⁶ In particular, photoluminescence (PL) imaging offers high detection sensitivity and multiplexing but suffers from limited penetration depth of light into tissues.¹ Both magnetic resonance imaging (MRI) and computed tomography (CT) have unlimited detection depth and render three-dimensional images, but suffer from moderate detection sensitivity and lack of multiplexing.³ MRI and CT are complementary because MRI lends high resolution on soft tissues while CT excels at hard tissues. Therefore, the combination of PL, MRI, and CT gives rise to medical images with high resolution, high sensitivity, and more information for medical diagnosis without limit in detection depth of the target site.⁷⁻¹¹

Contrast agents (CAs) are commonly used in these imaging modalities to enhance the visibility of the target site against the background.^{3, 6, 12-19} They can be engineered to accumulate specifically at the disease site, delineate the contour of it with imaging signals, and provide more accurate diagnostic information.²⁰ In multimodal imaging, a multifunctional CA that works for different modes is preferred over the combination of singly functional ones because separate administration of different types of CAs for various modalities increases the risk of toxicity and other side effects. Despite the potential advantages of such concepts, it remains challenging to design multimodal CAs that simultaneously facilitate PL imaging, MRI, and CT with high performance.²¹⁻²²

Lanthanide (Ln)-doped nanoparticles (NPs) have shown potential as multimodal imaging CAs because of their diverse yet tunable optical and magnetic properties.²³⁻²⁵ With the unique *4f*

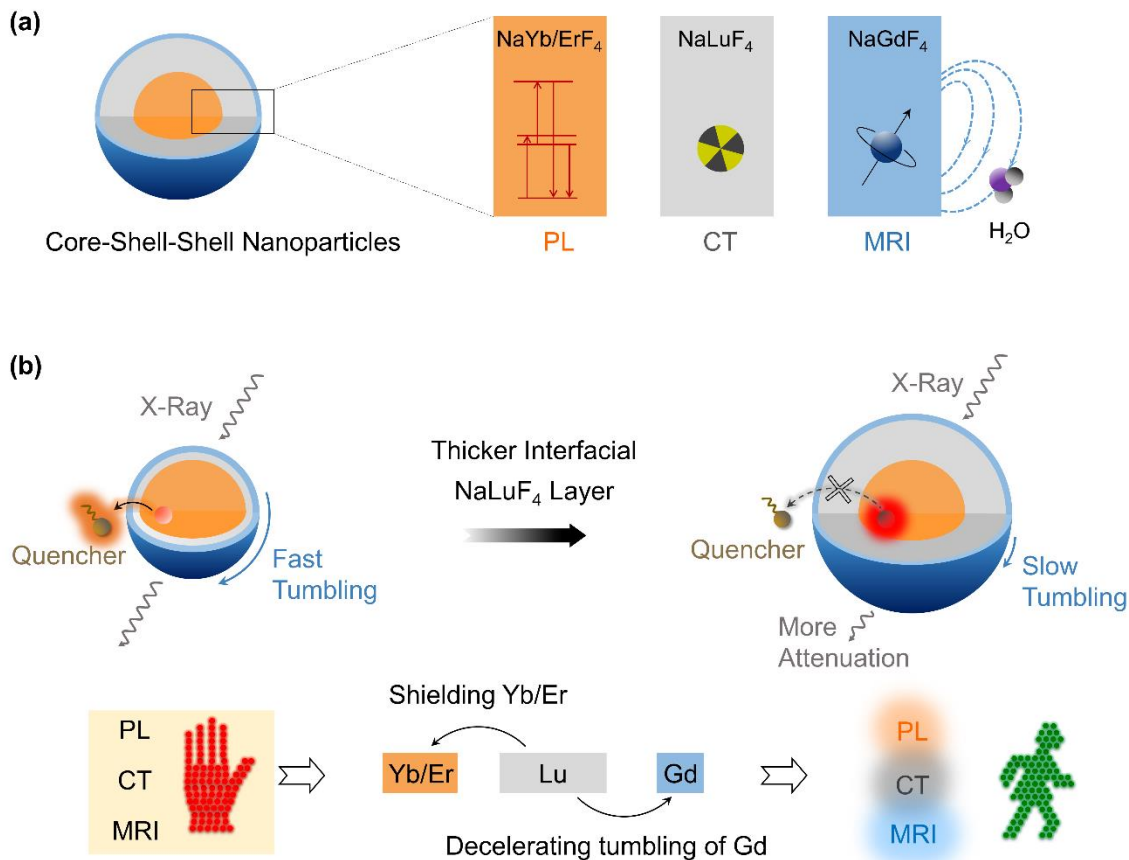
manifold of Ln trivalent cations (Ln^{3+}), Ln-doped NPs upon excitation emit luminescence at different wavelengths ranging from ultraviolet (UV) to near-infrared (NIR) regime.²⁶⁻²⁸ Along with large anti-Stokes shift, low background interference, and excellent photostability, Ln-doped NPs are superior CAs for PL imaging.²⁹⁻³¹ Ln^{3+} such as Gd^{3+} , Dy^{3+} , and Ho^{3+} are potent agents to relax the water protons for MRI because they have either large number of unpaired electrons in the $4f$ orbitals and/or large magnetic moment.^{24,32} With atomic numbers ranging from 57 to 71, Ln-doped NPs attenuate X-ray more strongly than most commercially available X-ray CT CAs (iodine-based, atomic number 53).³³⁻³⁴ Although the physical properties are diverse and suitable for different imaging applications respectively, the chemical properties of all Ln ions are quite similar making it easy to incorporate several types of Ln ions into a single architecture for use as multimodal CAs.²⁴ This offers better stability and simpler synthesis than the post-synthetic modifications typical of other multimodal CAs, i.e., coating a PL NP with gadolinium chelates or decorating fluorescent dyes on iron oxide NPs.^{8-11, 23-24, 35-36} For these reasons, multimodal imaging platforms using Ln-doped NPs as CAs—especially for combined PL, MRI, and CT imaging—have received considerable research interest.²⁴

Despite the promise of Ln-doped NPs in multimodal imaging, it has been challenging to integrate these imaging functions rationally and optimize every modality concurrently.²² The overall performance of multimodal CAs in multimodal imaging does not equal to the simple addition of imaging functions from every single component. The Ln-based PL/CT/MRI triple-modal CAs could have weaker optical emission than the PL single-modal CAs and weaker magnetic resonance relaxivity than the MRI single-modal CAs.³⁷⁻⁴⁵ For example, the high-efficiency PL emission in Ln-doped NPs usually relies on the doping and sparse distribution (doping level < 20%) of relatively heavy ions (Yb^{3+} and Er^{3+} or Tm^{3+} or Ho^{3+}) in the host matrix

composed of relatively lighter ions (NaYF_4).⁴⁶⁻⁴⁷ Therefore, NPs optimized for strong PL emission would perform poorly in CT because CT requires heavier ions. In contrast, enhancing CT contrast with high concentrations of heavy Ln ions would inevitably quench the PL in most cases.

This dilemma persists in Ln-based core-shell (CS) NPs. For instance, luminescent Ln-doped core NPs are usually coated with NaGdF_4 epitaxial shell making the CS NPs function as PL-MRI dual-mode CAs.⁴⁸ High-efficiency PL requires thick epitaxial shells on the core NPs regardless of the core composition. When the thick shell is comprised of NaGdF_4 , many of the Gd^{3+} ions are not exposed to the NP surface and thus not all Gd^{3+} ions contribute to the relaxation of water protons limiting their MRI performance.⁴⁹⁻⁵⁰ In short, it is challenging to design Ln-NP-based multimodal CAs that have improved performance than their single mode performance, without compromising on one or more modalities.

4.3 Results and Discussion

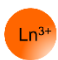
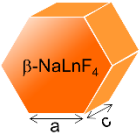


Scheme 4.1 (a) Schematic illustration for the β -Yb/Er@Lu@Gd hetero-epitaxial CSS NPs and their use as CAs for photoluminescence (PL) imaging, magnetic resonance imaging (MRI), and computed tomography (CT). (b) The overall performance for the CSS NPs is poor when the interfacial NaLuF₄ layer is thin because it allows surface quenching to PL, fast tumbling of the NP, and attenuating fewer X-rays. The performance in three modalities is simultaneously enhanced with a thick interfacial NaLuF₄ layer because it eliminates surface quenching to PL, decelerates tumbling of magnetic centers, and attenuates more X-rays.

Herein, we report the design and synthesis of β -NaYb_{0.2}/Er_{0.8}F₄@NaLuF₄@NaGdF₄ (Yb/Er@Lu@Gd) hetero-epitaxial triple-layer core-shell-shell (CSS) NPs as triple-modal imaging CAs (Scheme 4.1, upper panel) to address the limitations discussed above. The key to overcoming the conundrum of simultaneously optimizing and enhancing all three modalities is to modulate the interfacial NaLuF₄ layer thickness in the CSS-NP architecture (Scheme 4.1, lower

panel). While thicker interfacial NaLuF₄ layer allows heavy atoms (Lu³⁺) in the NP to attenuate more X-rays for enhanced CT contrast, it also acts as a thick epitaxial shell that shields all Yb³⁺/Er³⁺ luminescent centers in the core from surface quenching, therefore enhancing the PL. The thicker NaLuF₄ interfacial layer is also a larger substrate to decelerate the tumbling of all paramagnetic Gd³⁺ centers in the outermost NaGdF₄ thin layer, therefore enhancing the MRI.⁵¹⁻⁵⁴

Table 4.1 Ionic properties of all four Ln³⁺ ions incorporated in the CSS NPs in this study. The ionic radius of lutetium is smaller than that of either erbium or ytterbium, allowing Frank–van der Merwe growth mode of NaLuF₄ shell on NaYb/ErF₄ core towards thick yet highly uniform epitaxial NaLuF₄ shells on NaYb/ErF₄ cores. The ionic radius of gadolinium is larger than that of lutetium allowing Stranski–Krastanov growth mode for a uniform thin NaGdF₄ shell on NaLuF₄.

		Gadolinium (Gd)	Erbium (Er)	Ytterbium (Yb)	Lutetium (Lu)
	Ionic Radii (Å) ^{***}	1.193	1.144	1.125	1.117
	Unit Cell Volume (Å ³)	113.0	108.1	105.7	104.1
	Unit Cell Parameter a (Å)	6.020	5.959	5.929	5.901
	Unit Cell Parameter c (Å)	3.601	3.514	3.471	3.453

Importantly, we can enhance the PL further by growing thicker NaLuF₄ interfacial layer without tuning the thin shell of NaGdF₄. Therefore, all paramagnetic Gd³⁺ centers in the thin NaGdF₄ layer are always fully exposed to surrounding water protons to maximize MRI relaxivity. Also, these CSS-NP structures are possible because the crystal lattice size of the NaLuF₄ in the interfacial layer is smaller than that of NaYb/ErF₄ in the core (Table 4.1) allowing favorable tensile-strained shell growth.⁵⁵ Thus, thick (ca. 10 nm) and uniform (roundness close to 1) epitaxial shells can be successfully grown onto the cores, resulting in monodispersed NP architectures

without structural deformation. To highlight, we show below that the structural uniformity is a critical factor to realize simultaneous enhancement of the individual modalities within a composite trimodal structure.

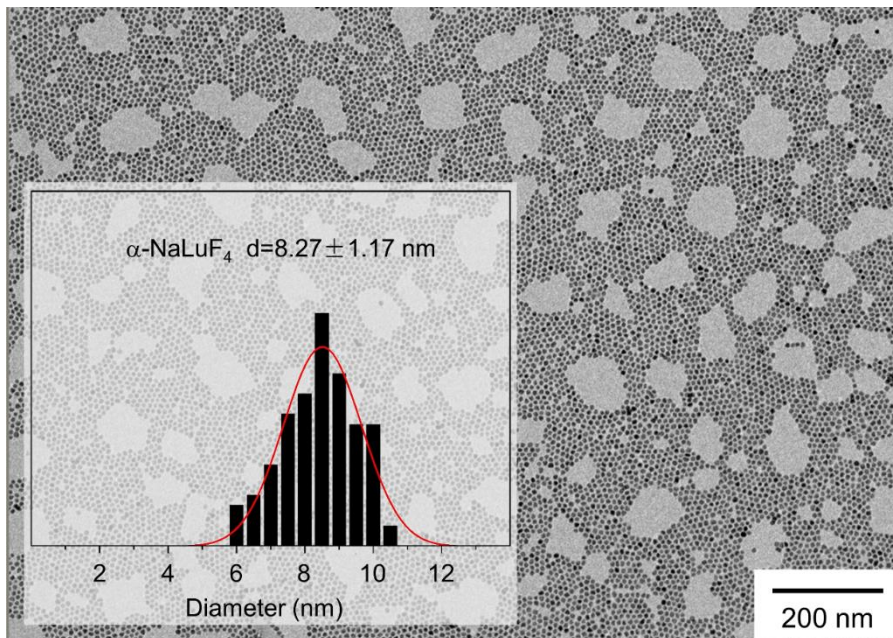


Figure 4.1 TEM image and size distribution of the α -NaLuF₄ NPs.

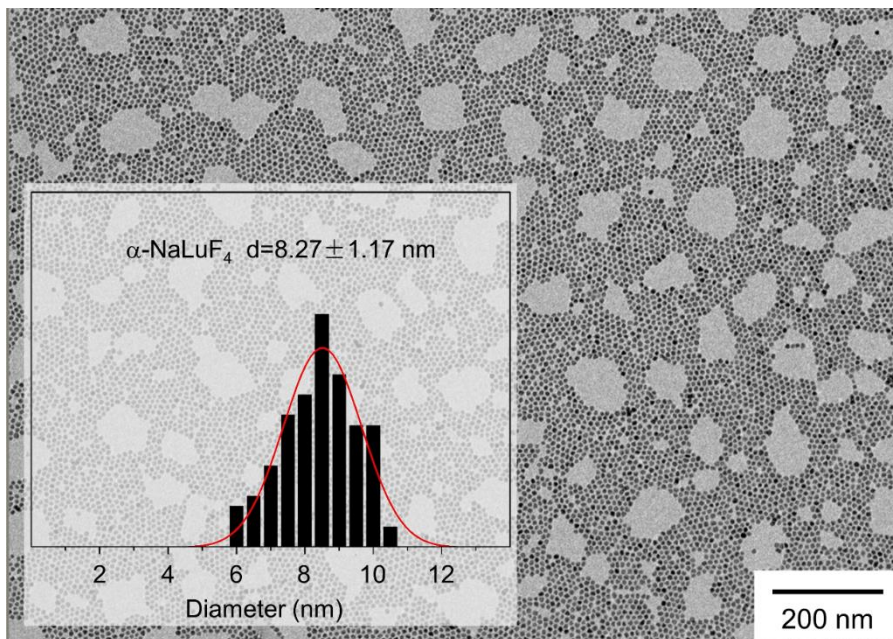


Figure 4.2 TEM image and size distribution of the α -NaGdF₄ NPs.

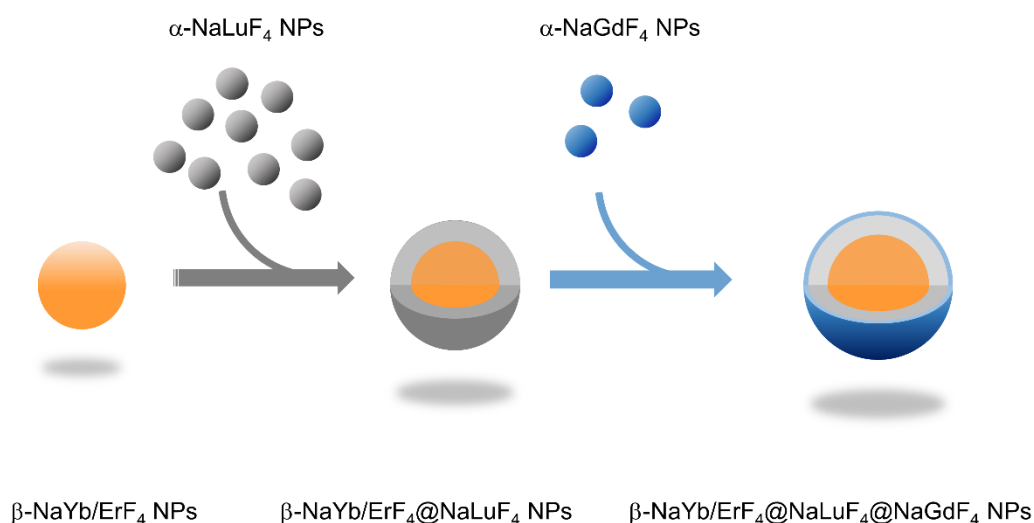


Figure 4.3 Schematic illustration for the synthesis procedure for β -NaYb/ErF₄@NaLuF₄@NaGdF₄ CSS NPs.

Table 4.2 Calculated molar equivalency of each Ln³⁺ for the synthesis of Yb/Er core, Yb/Er@Lu CS, and Yb/Er@Lu@Gd CSS NPs. On the synthesized Yb/Er core NPs with radii of 8.6 nm, we designed to achieve 10 nm thick NaLuF₄ shell and 0.6 nm NaGdF₄ shell on the cores. NaLuF₄ shell as thick as 10 nm effectively protects the excitation energy from surface quenching and concentration quenching at high doping level of Yb³⁺ and Er³⁺ in the core. NaGdF₄ shell as thin as 0.6 nm exposes all Gd³⁺ ions to the NP surfaces and maximizes the MRI relaxivity. To achieve this, 9.4 mmol of α -NaLuF₄ and 0.96 mmol α -NaGdF₄ sacrificial NPs need to be ripened and grown on the cores.

Samples	Designed radius (nm)	Designed layer thickness (nm)	Molar equivalency (mmol)
Yb/Er Core	8.6	8.6	1.0
Yb/Er@Lu CS	18.6	10.0	9.4
Yb/Er@Lu@Gd CSS	19.2	0.6	0.96

Highly uniform Yb/Er@Lu@Gd hetero-epitaxial CSS-NPs were synthesized following a previously reported self-focusing procedure.⁵⁶⁻⁵⁷ Kinetically stable α -NaLuF₄ and α -NaGdF₄ NPs

were synthesized and used as sacrificial NPs to grow shells on the β -NaYb/ErF₄ core NPs. The α -NaLuF₄ NPs had an average diameter of 8.27 nm (Figure 4.1) while α -NaGdF₄ NPs were 6.18 nm (Figure 4.2). After thermodynamically stable β -NaYb/ErF₄ core NPs were formed, α -NaLuF₄ and α -NaGdF₄ NPs were injected into the β -NaYb/ErF₄ core solution to form CSS-NPs (Figure 4.3) *via* Ostwald ripening (See Materials and Methods for details).

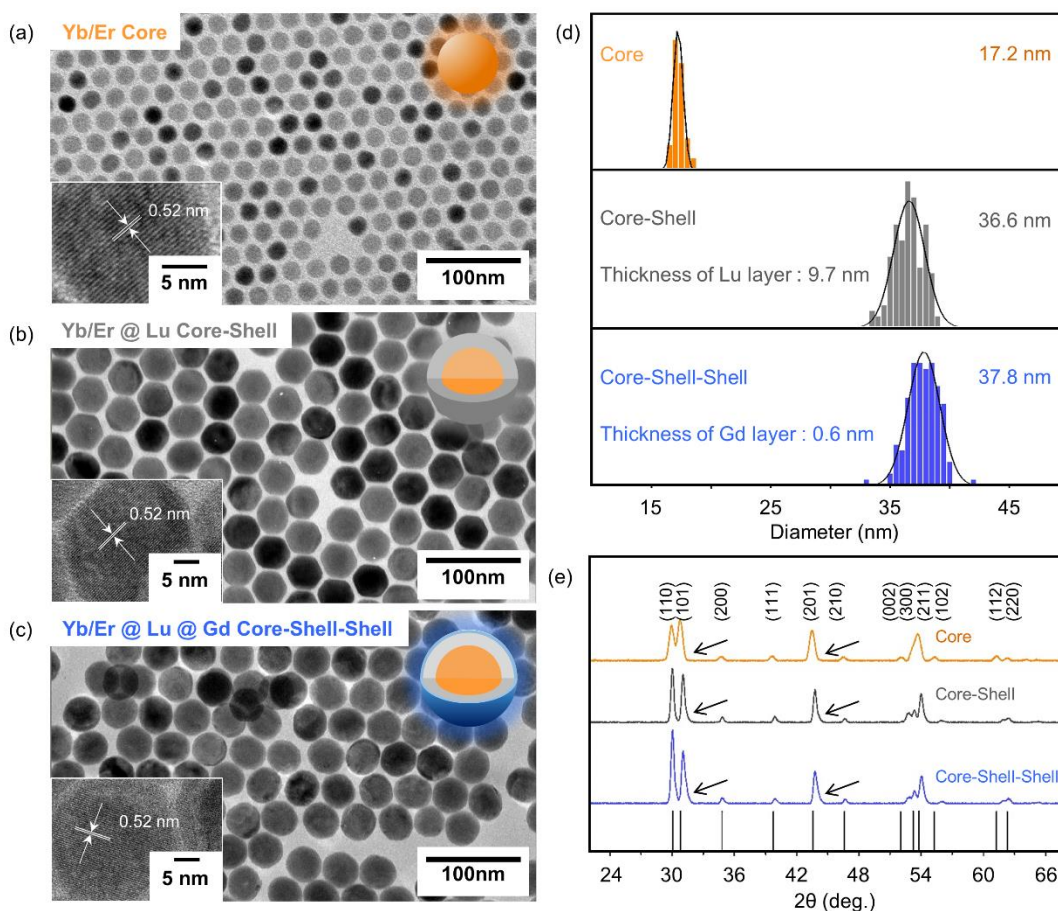


Figure 4.4 (a) to (c) TEM images of the synthesized β -NaYb/ErF₄ core, β -NaYb/ErF₄@NaLuF₄ CS and β -NaYb/ErF₄@NaLuF₄@NaGdF₄ CSS NPs. Inset: high-resolution TEM images showing their lattice fringes. (d) Size distribution of the three samples measured from TEM images respectively. (e) XRD pattern of the three samples respectively. The black arrows are showing the slight shift of the peaks in the CS and CSS NPs versus core NPs toward the high angle.

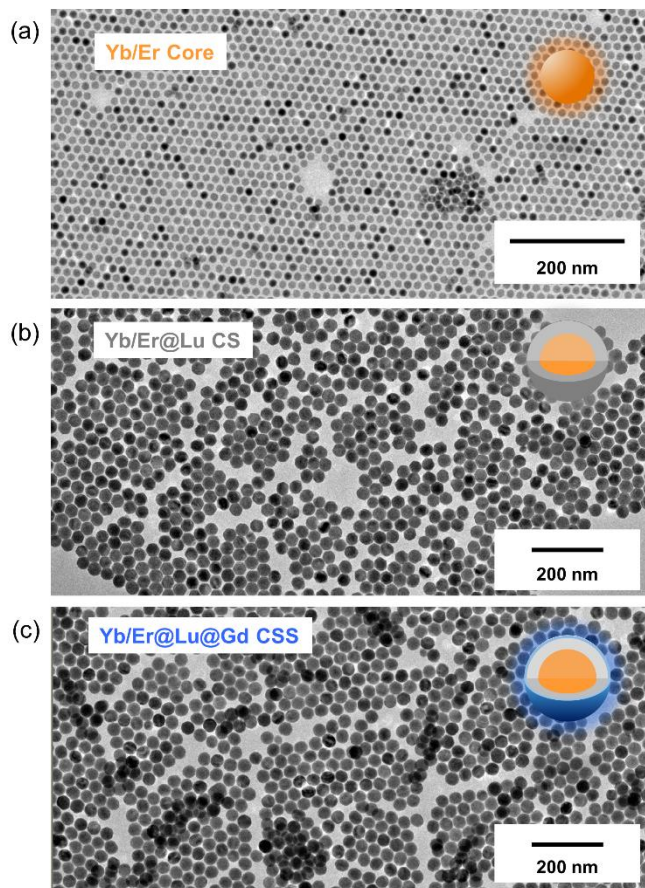


Figure 4.5 Low magnification TEM images of the core, CS and CSS NPs.

To obtain the CSS-NPs shown in Figure 4.4 a – c, ca. 9.4 mmol α -NaLuF₄ NPs and 0.96 mmol α -NaGdF₄ NPs were injected successively and ripened against 1 mmol β -NaYb/ErF₄ core NPs (See Table 4.2 for details). The size of the NPs grew from 17.2 nm (Yb/Er core) to 36.6 nm after NaLuF₄ shell growth (Yb/Er@Lu CS) and finally to 37.8 nm after of the NaGdF₄ shell growth (Yb/Er@Lu@Gd CSS) (Figure 4.4d), while perfectly retaining their quasi-spherical shapes (Figure 4.5 and 4.6). Measured sizes from representative transmission electron microscopy (TEM) images (Table 4.3) and element analyses from inductively coupled plasma atomic emission spectroscopy (ICP-AES) (Table 4.4) confirmed the molar ratio of each Ln³⁺ in the CSS-NPs. Energy-dispersive X-ray spectroscopy (EDS) confirmed the elemental composition of the core,

CS, and CSS structures (figure 7). The very minimal shift of the peaks of CS and CSS NPs in the X-ray Diffraction (XRD) pattern as compared to the core NPs confirmed that both shell layer perfectly adapted the crystal lattice of the core NPs (Figure 4.4e). Two critical morphological parameters—circularity and roundness—were calculated by characterizing the Feret diameters of the core, CS, and CSS-NPs, respectively. Neither circularity nor roundness changed significantly during NP growth from 17.2 nm to 37.8 nm further validating the shape uniformity across all three structures (Figure 4.8).

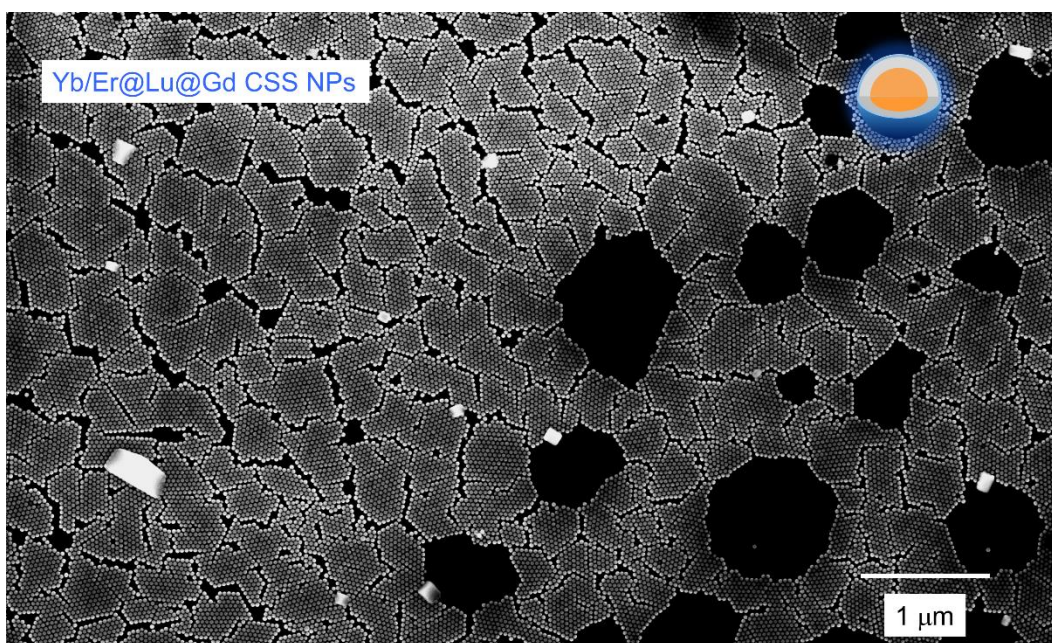


Figure 4.6 Low magnification SEM image of the β -NaYb/ErF₄@NaLuF₄@NaGdF₄ CSS NPs showing their excellent uniformity and monodispersity.

Table 4.3 Calculated molar equivalency of compositions in the Yb/Er@Lu@Gd CSS NPs by measuring the size of each sample on a representative TEM image. The molar ratio for (Yb+Er) / Lu / Gd is 1 / 9 / 0.93 and is consistent with the calculated amount in Table 4.2. We obtained 9 mmol out of the injected 9.4 mmol Lu and 0.93 mmol out of the injected 0.96 mmol Gd because of the minimal loss in the ripening process.

	Measured radius from TEM images (nm)	Compositions	Calculated molar equivalency (mmol)
Yb/Er Core	8.6	Yb + Er	1.0
Yb/Er@Lu CS	18.3	Lu	9.0
Yb/Er@Lu@Gd CSS	18.9	Gd	0.93

Table 4.4 Elemental concentrations of different Ln³⁺ in core, CS, and CSS NPs obtained from ICP-AES, which is consistent with both Table 4.2 and Table 4.3.

	Er ³⁺ (mM)	Yb ³⁺ (mM)	Lu ³⁺ (mM)	Gd ³⁺ (mM)
Yb/Er Core	2.41 ± 0.1	0.62 ± 0.1	/	/
Molar equivalency	(Er ³⁺ + Yb ³⁺) / Lu ³⁺ / Gd ³⁺ = 0.98 / 0 / 0			
Yb/Er@Lu CS	1.47 ± 0.1	0.38 ± 0.1	16.45 ± 0.3	/
Molar equivalency	(Er ³⁺ + Yb ³⁺) / Lu ³⁺ / Gd ³⁺ = 1 / 8.89 / 0			
Yb/Er@Lu@Gd CSS	2.07 ± 0.1	0.54 ± 0.1	23.29 ± 0.4	2.31 ± 0.1
Molar equivalency	(Er ³⁺ + Yb ³⁺) / Lu ³⁺ / Gd ³⁺ = 1 / 8.92 / 0.89			

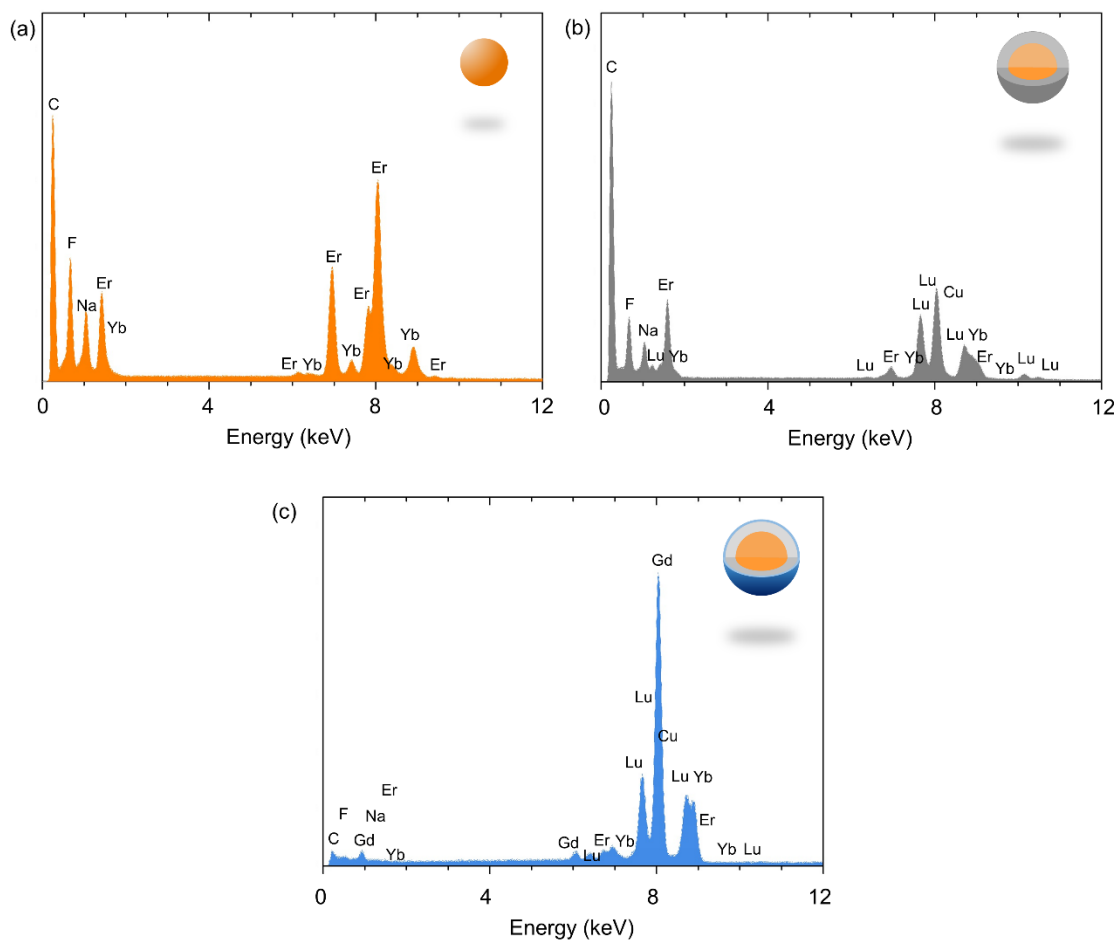


Figure 4.7 Energy dispersive X-ray spectroscopy (EDS) of (a) β -NaYb/ErF₄ core, (b) β -NaYb/ErF₄@NaLuF₄ CS, and (c) β -NaYb/ErF₄@NaLuF₄@NaGdF₄ CSS NPs showing the elemental composition of each structure. The peak of carbon and copper comes from the sample grid of TEM.

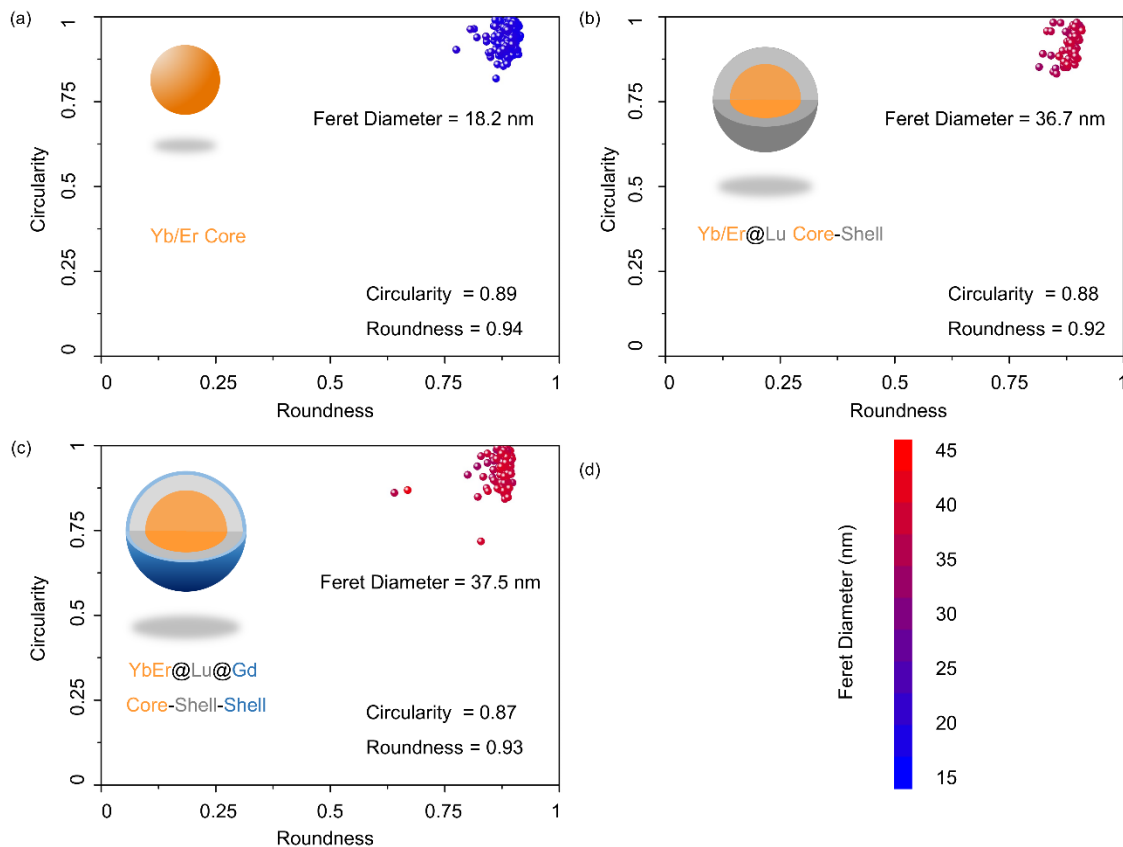


Figure 4.8 Morphological characterization of the (a) core, (b) CS, and (c) CSS NPs.

To assess the functional capabilities of these CSS-NP-based CAs, we first characterized the PL properties to validate that the epitaxial NaLuF_4 shell enhances the PL of the $\beta\text{-NaYb/ErF}_4$ core. For the $\beta\text{-NaYb/ErF}_4$ core NPs without the shell, the high concentration of both the sensitizer and activator ions (Yb^{3+} 20%, and Er^{3+} 80% respectively) enhances the excitation energy migration to the surface⁵⁷ and quenches all the possible emission pathways (Figure 4.9a). No detectable emission peaks for the core NPs were observed across either the visible (450 – 750 nm) or the NIR (750 – 900 nm) regime (Figure 4.9b) with excitation by a continuous wave diode laser at 980 nm. Our attempts to increase the excitation power density of laser from 2.5 W/cm^2 to 40 W/cm^2 did not result in any detectable emission from the core NPs either (Figure 4.10).

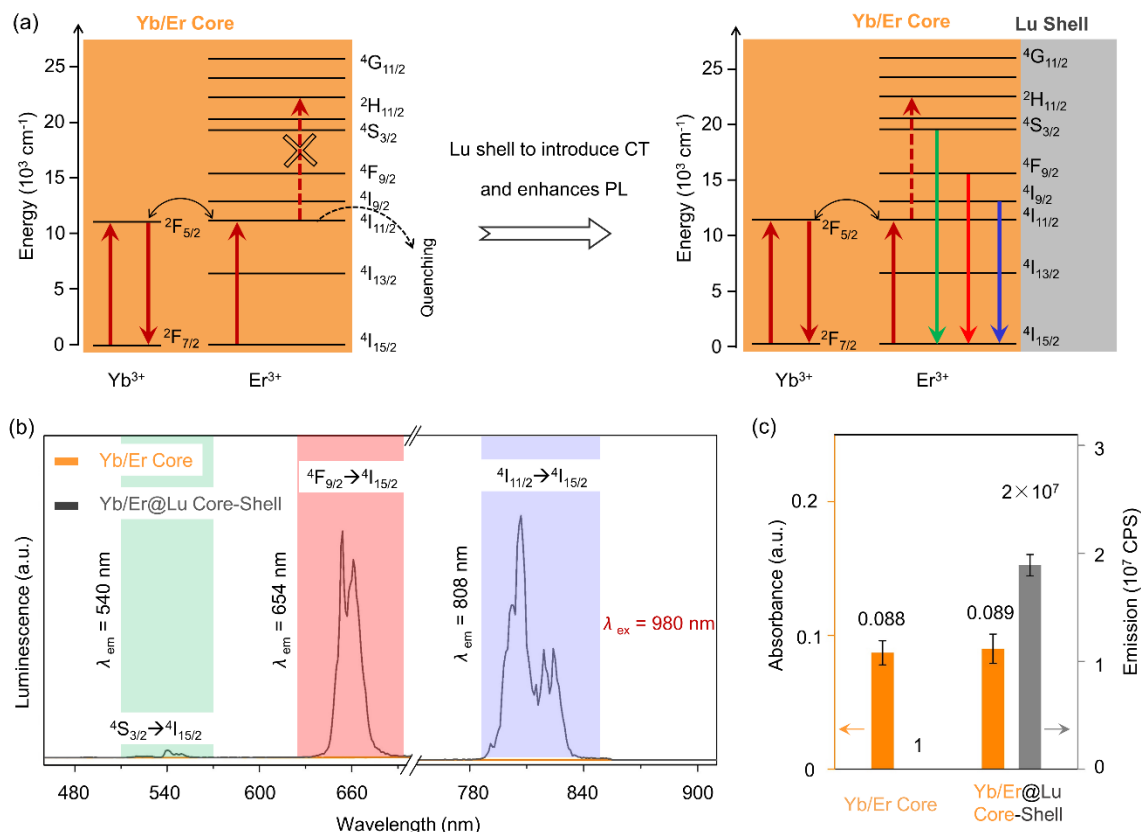


Figure 4.9 Photoluminescent properties of the β -NaYb/ErF₄@NaLuF₄ CS NPs. (a) The simplified energy level diagram of Yb³⁺/Er³⁺ showing multiple optical transitions migrate to the surface and are quenched. The upconversion PL emissions are recovered after epitaxial deposition of the NaLuF₄ shell. (b) The PL spectra across the visible and NIR range of the β -NaYb/ErF₄ core (orange) and β -NaYb/ErF₄@NaLuF₄ CS (gray) NPs, showing three major emission peaks at 540 nm, 654 nm, and 808 nm. (c) Comparison of absorbance (orange) at 980 nm and integrated emission intensity (gray) of β -NaYb/ErF₄ core and β -NaYb/ErF₄@NaLuF₄ CS NPs.

However, after NaLuF₄ epitaxial shells were grown onto the cores to form β -Yb/Er@Lu CS-NPs, the excitation energy in the cores was sequestered from surface quenching (Figure 4.9a), and all three major emission peaks, 540 nm ($4S_{3/2} \rightarrow 4I_{15/2}$), 654 nm ($4F_{9/2} \rightarrow 4I_{15/2}$), and 808 nm ($4I_{9/2} \rightarrow 4I_{15/2}$) were immediately recovered (Figure 4.9b). Unlike the Yb/Er core NPs, the PL of the CS-NPs increased two orders of magnitude when the 980 nm laser excitation power density was elevated from 2.5 W/cm² to 40 W/cm² (Figure 4.10). While we denoted the emission intensity

of the completely quenched cores at 2.5 W/cm² excitation as 1, the integrated emission intensity of the CS-NPs at the same excitation power density demonstrated an enhancement factor of PL as high as 2×10^7 (Figure 4.9c).

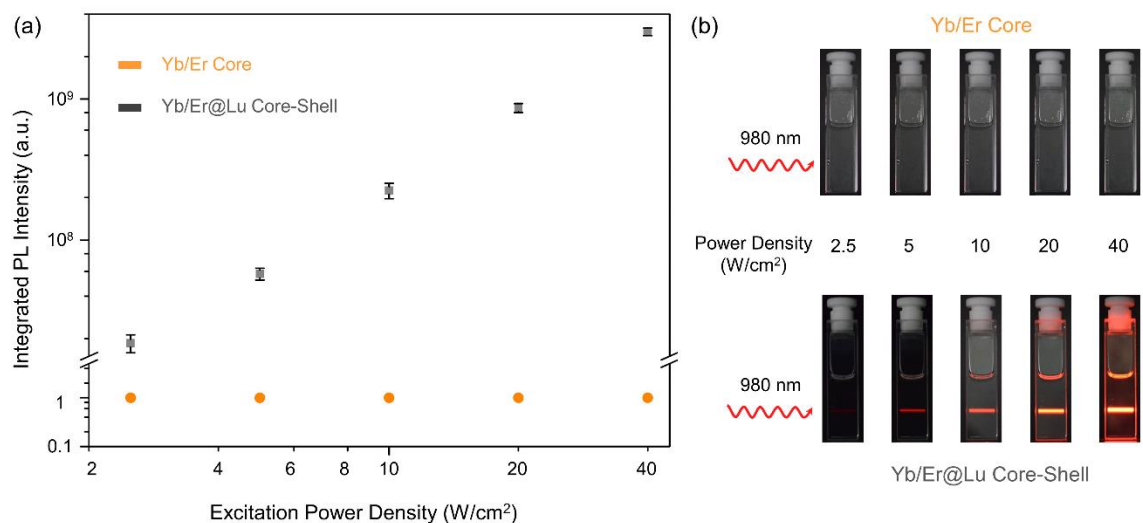


Figure 4.10 (a) Power density-dependent PL intensity of Yb/Er core and Yb/Er@Lu CS NPs. There is no emission peaks for the Yb/Er cores and we denoted the emission intensity as 1. (b) Photographs of samples excited at 980 nm with variable laser power density.

The absorbance at 980 nm of both β -NaYb/ErF₄ core and β -NaYb/ErF₄@NaLuF₄ CS NPs remains the almost the same (0.088 for core and 0.089 for CS) (Figure 4.9c), highlighting the critical contribution of the optically inert NaLuF₄ shell in enhancing the PL by shielding the luminescent centers (both sensitizers Yb³⁺ and activators Er³⁺) in the core from surface quenching.

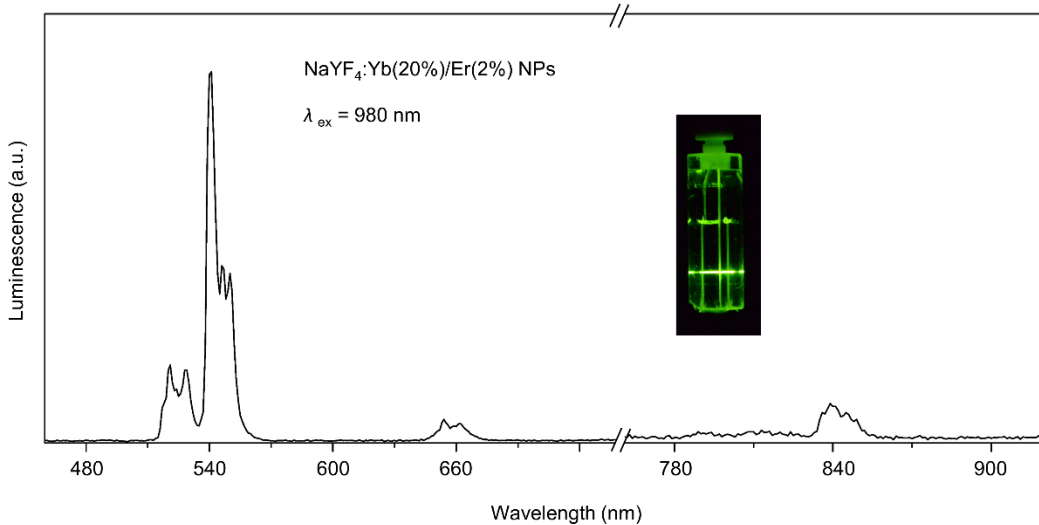


Figure 4.11 PL spectra of NaYF₄:Yb(20%)/Er(2%) NPs excited at 980 nm, showing major emission in the visible green regime instead of visible red and NIR regime.

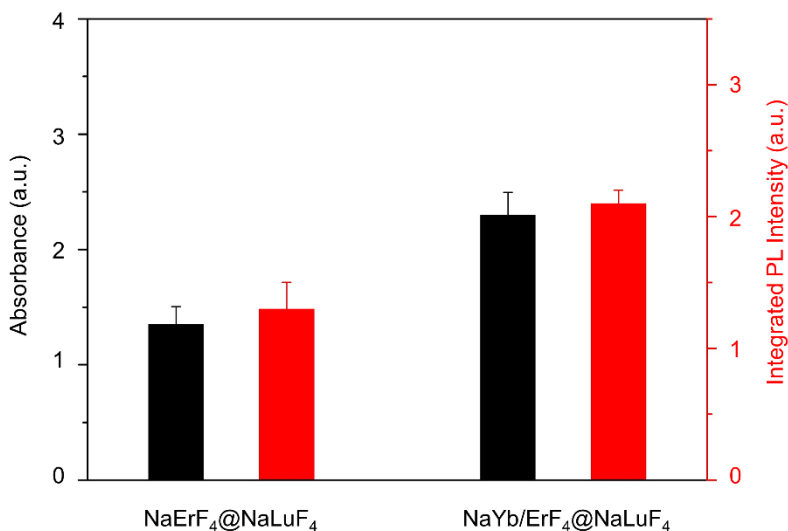


Figure 4.12 Absorbance at 980 nm and integrated PL intensity of Er@Lu CS NPs and Yb/Er@Lu CS NPs.

There are several other advantages in the β -NaYb/ErF₄@NaLuF₄ CS structures over other PL CAs. With the NaLuF₄ shells, the major emission peaks are at 654 nm and 808 nm when excited at 980 nm. Both emission peaks are within the biological imaging window,^{26, 58} and they function

better than the dominant green emission at 540 nm seen in Yb^{3+} (18%)/ Er^{3+} (2%) co-doped NaYF_4 NPs (Figure 4.11). Compared to the singly doped $\text{NaErF}_4@NaLuF_4$,⁵⁷ the $\text{NaYb/ErF}_4@NaLuF_4$ CS NPs here have enhanced absorbance of 980 nm excitation owing to larger absorption cross-section of the sensitizer Yb^{3+} — this results in brighter PL emission (Figure 4.12).

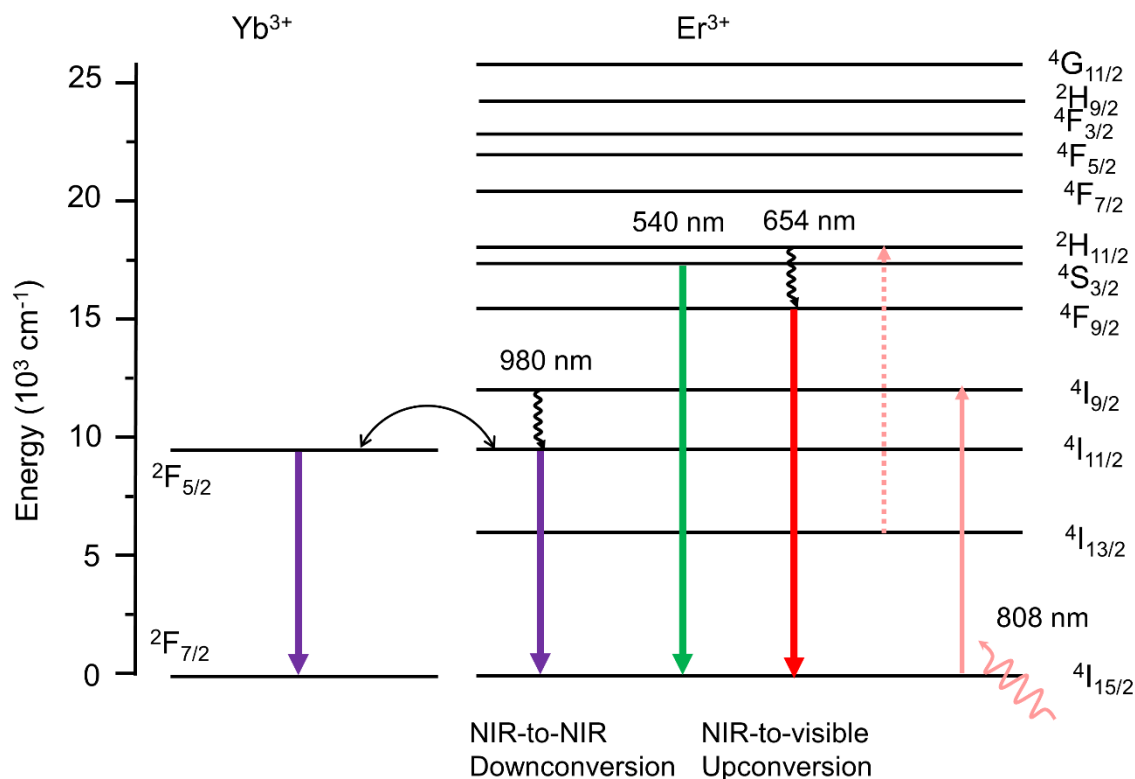


Figure 4.13 Simplified energy level diagram of $\text{Yb}^{3+}/\text{Er}^{3+}$ luminescent pair showing excitation at 808 nm.

With the high doping concentration of Er^{3+} (80%) in the core, the Yb/Er@Lu CS-NPs can also be excited at 808 nm (Figure 4.13), another bio-benign wavelength in the biological imaging window. Upon 808 nm excitation, they emit at visible regime (654 nm) *via* upconversion and at the NIR regime (980 nm) *via* downshifting simultaneously (Figure 4.14) which cannot be easily realized in conventional systems. In short, the NaLuF_4 epitaxial shell enhances the PL of the NaYb/ErF_4 cores at various excitation and emission wavelengths.

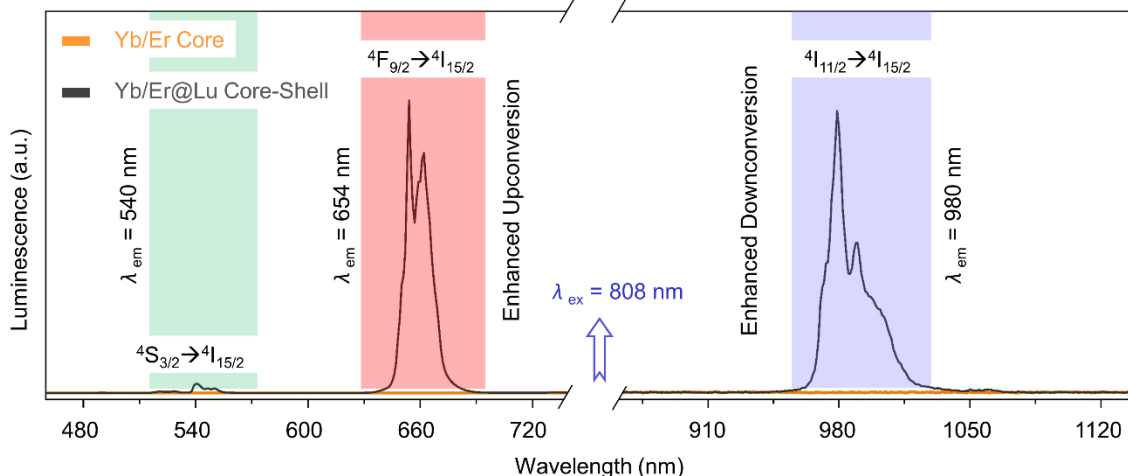


Figure 4.14 PL spectra across the visible and NIR regime of the Yb/Er core NPs and Yb/Er@Lu CS NPs with 808 nm excitation.

Next, we explored whether MRI modality is enhanced when incorporated into the same NP structure without affecting the enhanced PL properties (Figure 4.15a). On depositing NaGdF₄ shell the size of the NP grew from 36.6 nm (Yb/Er@Lu CS) to 37.8 nm (Yb/Er@Lu@Gd CSS) while the MRI r_1 relaxivity increased from 0.1 mM⁻¹s⁻¹ (Figure 4.15a) to 52.9 mM⁻¹s⁻¹ (per Gd³⁺) (Figure 15b) at 1.5 Tesla (T). This is the highest MRI contrast at clinical field reported to date for multimodal imaging CAs that includes an MRI modality.³² Comparing the high relaxivity reported here for the CSS NP, we emphasize that only an ultras-small Gd³⁺ NP with controlled surface coating has reported higher relaxivity.⁵⁹ For Yb/Er@Lu CS-NPs, an r_1 value of 0.1 mM⁻¹s⁻¹ is well within the detection limit confirming that the Yb/Er@Lu CS with strong PL is silent in MRI. This is because Lu³⁺ does not have any unpaired electrons in the $4f$ orbitals but has extremely short electron spin relaxation time (10⁻¹³ s). In contrast, Gd³⁺ ions have seven unpaired electrons and a 10⁵-fold longer electron spin relaxation time (10⁻⁸ s) than Lu³⁺ (Table 4.5)—both of these factors contribute to the high MRI relaxivity of Yb/Er@Lu@Gd CSS NPs compared to Yb/Er@Lu CS NPs.⁶⁰

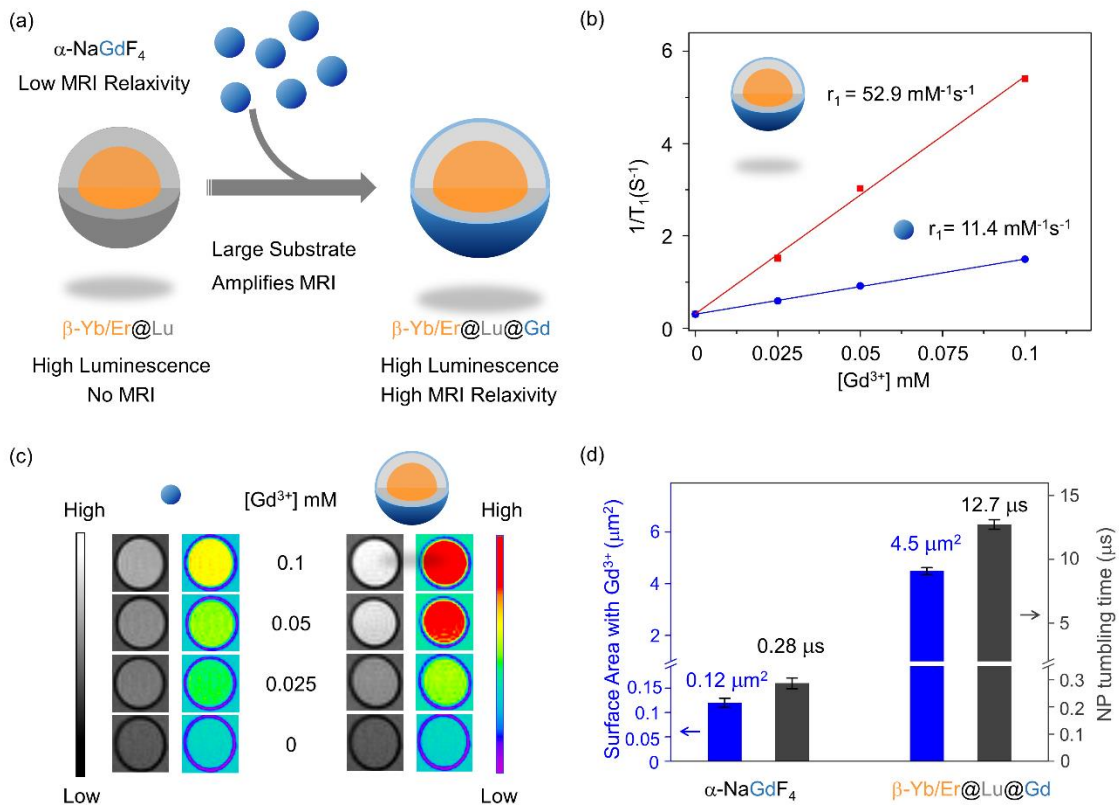


Figure 4.15 MRI relaxivity of the β -NaYb/ErF₄@NaLuF₄@NaGdF₄ CSS NPs. (a) Schematic illustration showing that the MRI-silent β -NaYb/ErF₄@NaLuF₄ CS NPs gain MRI relaxivity upon deposition of a thin layer of NaGdF₄. (b) Relaxivity plot of α -NaGdF₄ and β -NaYb/ErF₄@NaLuF₄@NaGdF₄ CSS NPs against Gd³⁺ concentration at 1.5 T. (c) Concentration-dependent phantom images of α -NaGdF₄ and β -NaYb/ErF₄@NaLuF₄@NaGdF₄ CSS NPs. (d) Comparison of NP surface areas with Gd³⁺ and NP tumbling time.

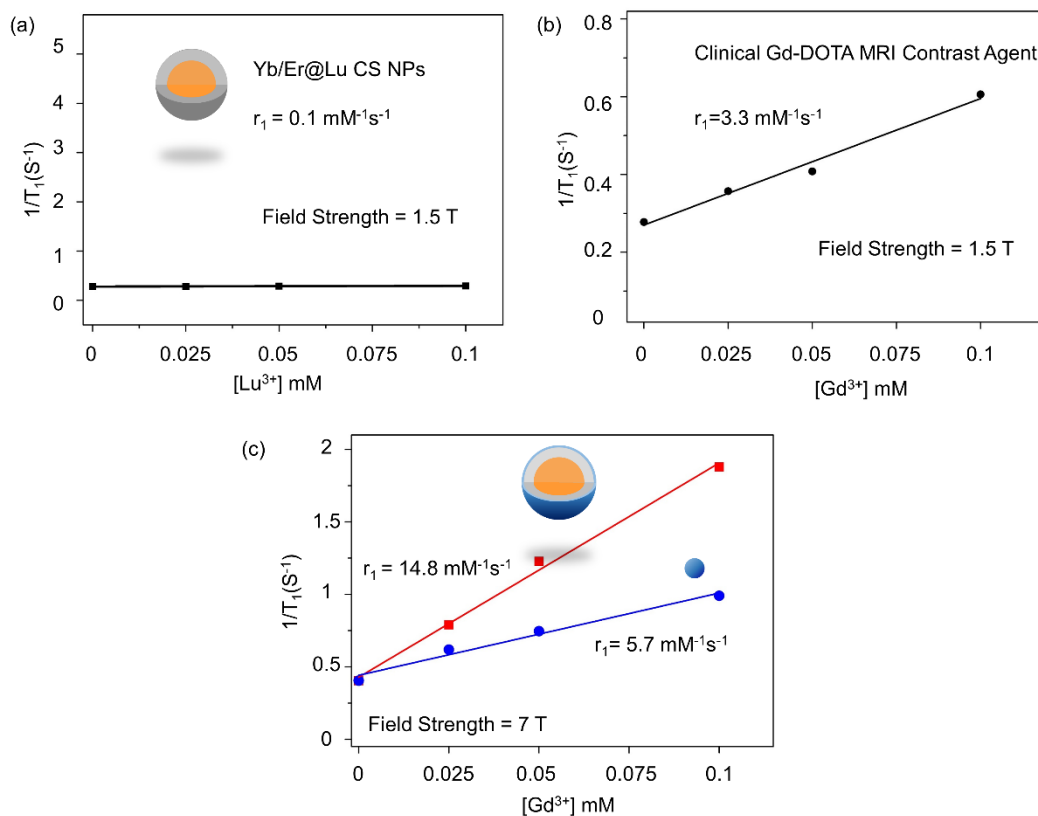


Figure 4.16 (a) r_1 relaxivity of the Yb/Er@Lu CS NPs at the magnetic field strength of 1.5T. (b) r_1 relaxivity of the clinical Gd-DOTA MRI contrast agents at the magnetic field strength of 1.5 T. (c) r_1 relaxivity of the CSS NPs and α -NaGdF₄ NPs at the magnetic field strength of 7.0 T.

Table 4.5 Paramagnetic properties of all four Ln³⁺ ions incorporated in the CSS NPs in this study.

	Gadolinium (Gd)	Erbium (Er)	Ytterbium (Yb)	Lutetium (Lu)
4f orbital	Half Filled	Partially Filled	Partially Filled	Filled
Unpaired electrons	7	3	1	0
Environment of the Unpaired Electrons	Isotropic	Anisotropic	Anisotropic	/
Electron Spin Relaxation Time (s)	10 ⁻⁸	10 ⁻¹³	10 ⁻¹³	10 ⁻¹³

To study the advantage of the CSS structure in enhancing the MRI contrast, we compared the relaxivity of the sacrificial α -NaGdF₄ NPs that were used to grow the NaGdF₄ shell and the final CSS structures (Figure 4.15b). The relaxivity of the α -NaGdF₄ NPs was lower than the CSS NPs at about 11.4 mM⁻¹s⁻¹ (per Gd³⁺), while still being higher than the commercially available MRI CAs, Gd-DOTA (3.3 mM⁻¹s⁻¹ per Gd³⁺, Figure 4.16b). Concentration-dependent MRI phantom images confirmed that the final Yb/Er@Lu@Gd CSS structures with a thin NaGdF₄ shell had a fivefold enhancement of MRI relaxivity (52.9 mM⁻¹s⁻¹) than the sacrificial α -NaGdF₄ NPs (Figure 4.15c). When normalized to the same Gd³⁺ ionic concentration (0.1 mM), the β -Yb/Er@Lu@Gd CSS-NPs with r_1 of 52.9 mM⁻¹s⁻¹ provided much shorter spin-lattice relaxation time (180 ms) for water protons in the vicinity and much higher contrast against the background than α -NaGdF₄ NPs (670 ms). The enhanced MRI relaxivity allows a much lower dosage of the CAs in clinical scans. We also tested these materials in high field MRI (> 3 T) as it offers improved signal-to-noise ratio compared to the clinical field (1.5 T).^{54, 61} The CSS NP CAs exhibited an r_1 value of 14.8 mM⁻¹s⁻¹ at 7.0 T—the highest MRI relaxivity reported to date for contrast agents integrating multiple modalities (Figure 4.16c).

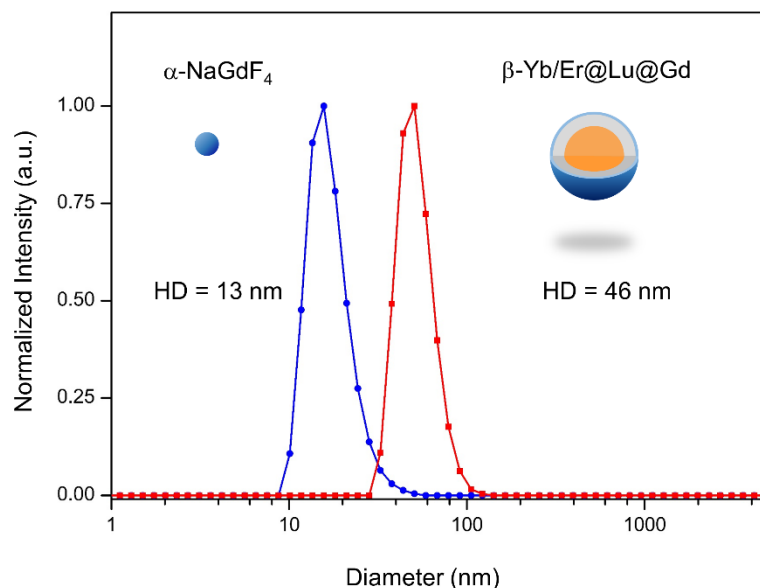


Figure 4.17 Hydrodynamic diameters (HD) of the α -NaGdF₄ and β -Yb/Er@Lu@Gd CSS NPs.

The relaxivity enhancement of the CSS NPs highlights three important advantages of the CSS structure for MRI as compared to the α -NaGdF₄ NPs. First, for the α -NaGdF₄ NPs at ~ 6 nm in diameter, approximately 80% of the Gd³⁺ ions are anchored inside the α -NaGdF₄ crystal lattice⁶²⁻⁶³ without access to the surrounding water protons (water exclusion)—this effectively exclude them from contributing to the MRI relaxivity. However, with a thickness of only 0.6 nm (Figure 4.1d), the NaGdF₄ thin shell in a CSS-NP is likely a monolayer because the lattice size of the β -NaGdF₄ is almost exactly 0.6 nm (Table 4.1). This suggests that all of the Gd³⁺ ions in the CSS NPs are directly exposed to the surrounding water molecules and contribute to water proton relaxation. Second, the surface area increased from 0.12 μm^2 to 4.5 μm^2 per particle for the CSS-NP relative to the smaller α -NaGdF₄ NPs (Figure 4.15d). This facilitates one single NP CA to influence more water protons simultaneously.⁴⁹⁻⁵⁰ Third, it has been well established that slow

tumbling CAs relax water protons more effectively as opposed to faster tumbling CAs.⁵¹⁻⁵⁴ Comparing α -NaGdF₄ NPs to the CSS NPs, the hydrodynamic size increased from 13 nm to 46 nm (Figure 4.17). This significantly increased the tumbling time from 0.28 μ s to 12.7 μ s (Figure 4.15d) and enhanced the MRI relaxivity.⁶⁴ Thus the CSS structure enables water access to all paramagnetic Gd³⁺ centers while simultaneously acting as a slower tumbling substrate to achieve larger relaxivity enhancement than that achievable with a stand-alone NaGdF₄-based MRI CA.

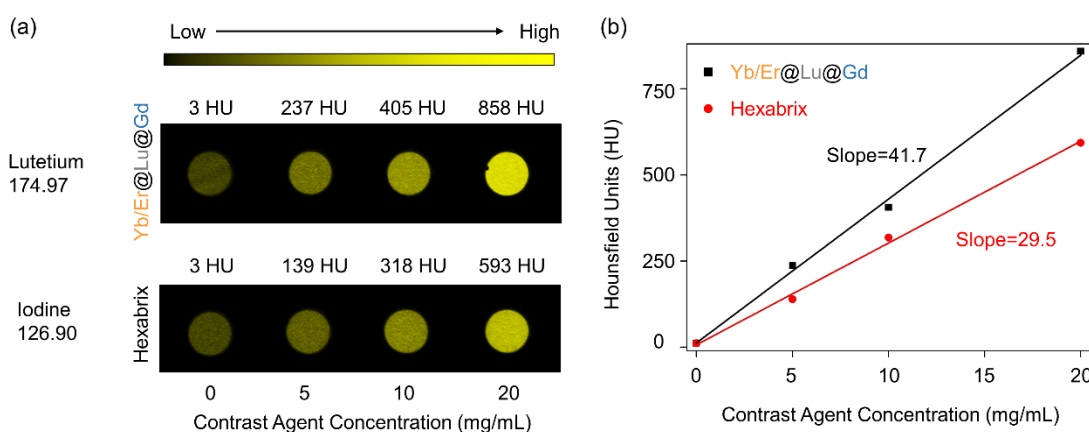


Figure 4.18 Comparison of image contrast between β - NaYb/ErF₄@NaLuF₄@NaGdF₄ CSS NPs and Hexabrix in the same CT construct. (a) The concentration-dependent phantom images and (b) HU values against the concentration of the two types of CT contrast agents.

Next, we studied whether the CSS structure with both strong PL and high MRI also generates high CT contrast. We expected the β -Yb/Er@Lu@Gd CSS-NP to have better X-ray attenuation capabilities than other CT CAs commonly based on iodine because of the higher atomic number of the Ln³⁺ ions.³⁴ While the interfacial NaLuF₄ layer in the hetero-epitaxial CSS structures enhances PL emission for the NaYb/ErF₄ core and MRI relaxivity for the NaGdF₄ outer layer, it accounts for approximately 80% of the total mass of a single β -Yb/Er@Lu@Gd CSS-NP. We prepared CSS-NPs in serial dilutions and compared their Hounsfield Unit (HU) values to the commercially available iodine-based CT CAs (Hexabrix) at the same mass concentration (Figure

4.18a). The contrast of water was measured to be 3 HU, close to the defined 0 HU in most studies.³³ Hexabrix (5 mg/mL) increased the contrast to 139 HU, while CSS-NPs at the same mass concentration achieved a contrast of 237 HU—a gain of nearly 70% more than Hexabrix. When the HU values of the CAs were normalized to the mass concentration of CAs (per mg/mL), the β -Yb/Er@Lu@Gd CSS-NP had a contrast of 41.7 HU/(mg/mL). In comparison, the mass concentration-normalized signal from Hexabrix was only 29.5 HU/(mg/mL) (Figure 4.18b). This again suggests that the same image contrast can be achieved with much lower concentrations of CAs.

To verify that the interfacial NaLuF₄ layer of the β -Yb/Er@Lu@Gd CSS-NP is critical in achieving simultaneously enhanced PL emission, MRI relaxivity, and CT contrast, we synthesized β -Yb/Er@Lu@Gd CSS-NPs with varying interfacial NaLuF₄ layer thickness (Figure 4.19a, b, c). By depositing different amount of sacrificial α -NaLuF₄ NPs onto the β -NaYb/ErF₄ core NPs (Table 7), we obtained CSS-NPs with the interfacial NaLuF₄ layer of thicknesses at 1.0 nm, 4.9 nm and 10.1 nm (Figure 4.19d, e, f). All three samples as confirmed from TEM (Figure 4.20) are uniform, monodispersed and quasi-spherical (Figure 4.21).

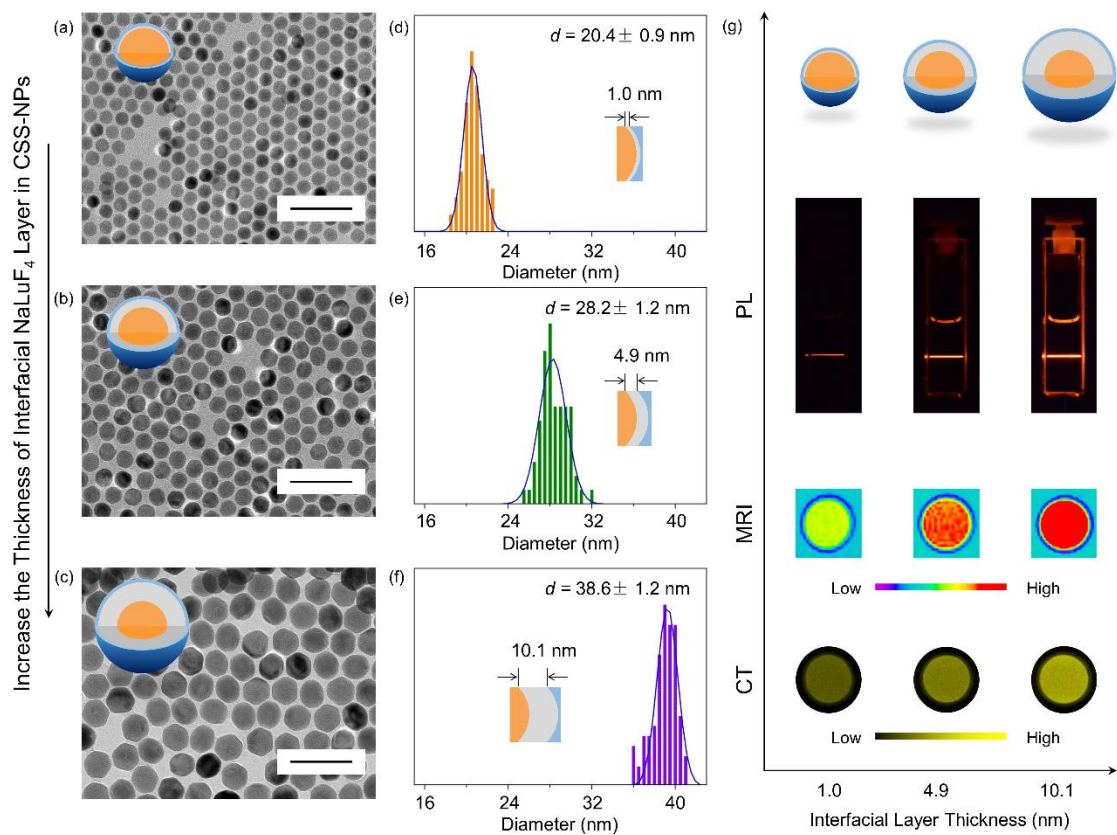


Figure 4.19 (a – c) TEM images of the β -NaYb/ErF₄@NaLuF₄@NaGdF₄ CSS NPs with increasing thickness of the interfacial NaLuF₄ layer. Size distribution analysis of the β -NaYb/ErF₄@NaLuF₄@NaGdF₄ CSS NPs with the thickness of the interfacial NaLuF₄ layer at (d) 1.0 nm, (e) 4.9 nm, and (f) 10.1 nm. (g) Cuvette images, MRI phantom images, and CT phantom images of the β -NaYb/ErF₄@NaLuF₄@NaGdF₄ CSS NPs with the thickness of the interfacial NaLuF₄ layer at 1.0 nm, 4.9 nm, and 10.1 nm.

Table 4.6 The amount of sacrificial α -NaLuF₄ and α -NaGdF₄ NPs used to synthesize β -Yb/Er@Lu@Gd CSS NPs with increasing thickness of interfacial NaLuF₄ layers. The amount of the Yb/Er core NPs was kept at 1 mmol. The amount of α -NaGdF₄ NPs were calculated accordingly to ensure that the thickness of the outmost NaGdF₄ layer in the β -NaYb/ErF₄@NaLuF₄@NaGdF₄ CSS NPs remained as 0.6 nm.

	Amount of core NPs (mmol)	Injected amount of the sacrificial NPs (mmol)	
	β -NaYb/ErF ₄	α -NaLuF ₄	α -NaGdF ₄
Yb/Er@Lu1@Gd	1.0	0.45	0.3
Yb/Er@Lu2@Gd	1.0	3.0	0.6
Yb/Er@Lu3@Gd	1.0	10	1.0

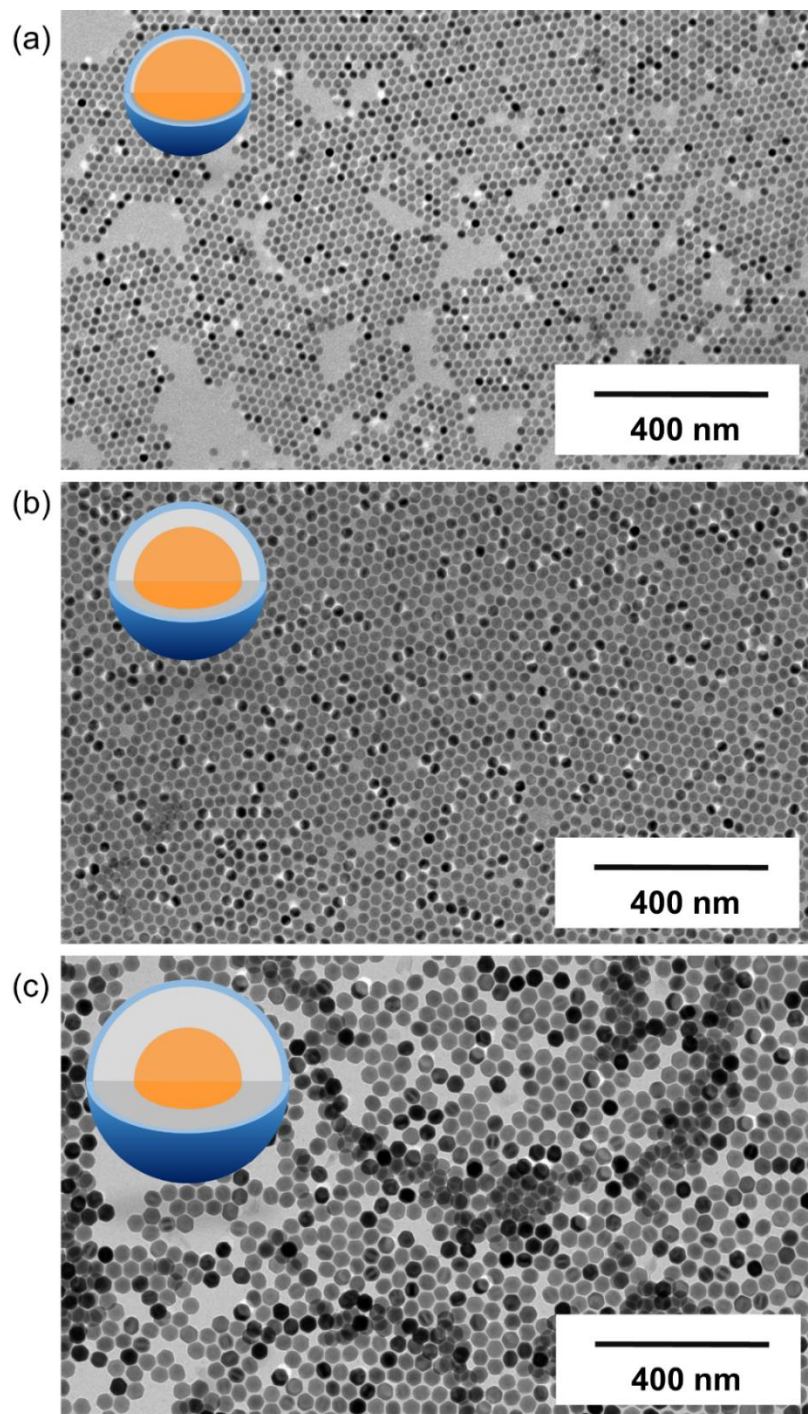


Figure 4.20 Low magnification TEM images of the (a) core, (b) CS, (c) CSS NPs with tunable thickness of the interfacial NaLuF₄ layer.

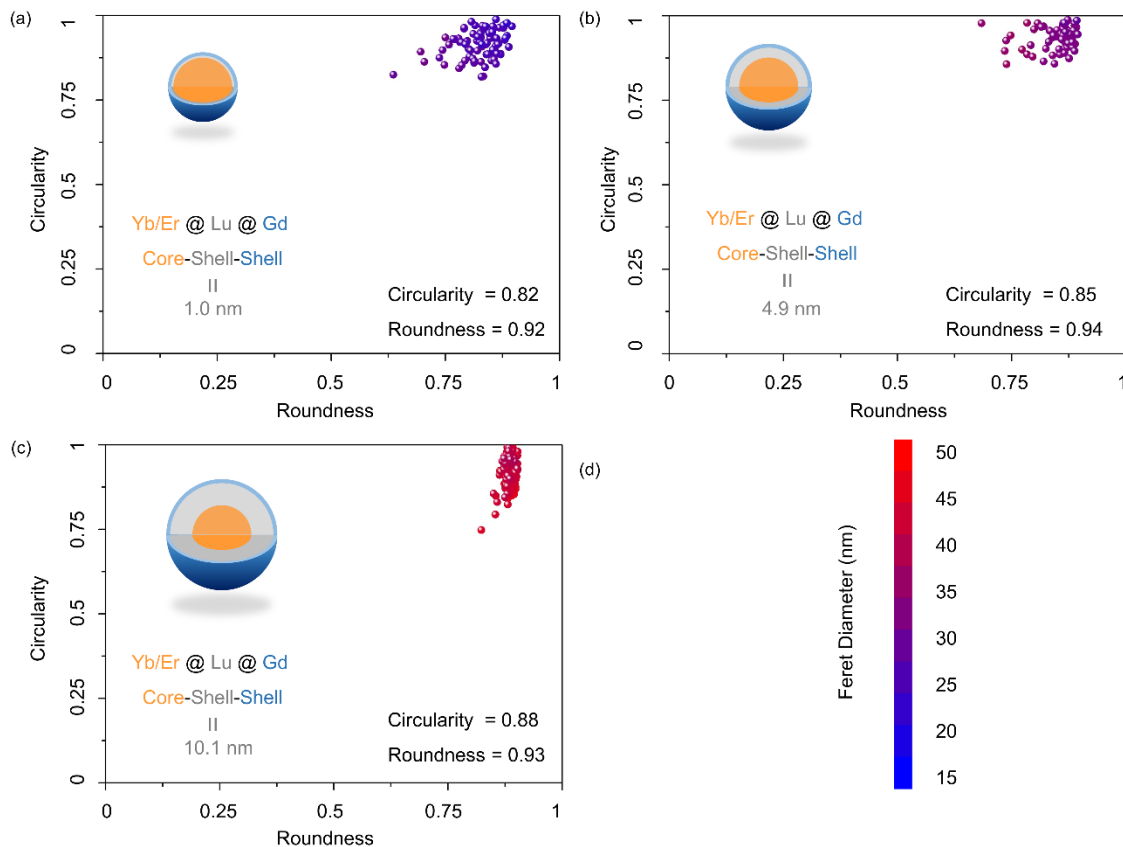


Figure 4.21 Morphological characterization of the (a) core, (b) CS, and (c) CSS NPs with increased interfacial NaLuF₄ layer thickness.

Table 4.7 Molar equivalency of each component in the β -NaYb/ErF₄@NaLuF₄@NaGdF₄ CSS NPs with tunable interfacial NaLuF₄ layers. The obtained molar equivalency is consistent with that in the Table 4.6.

	Radius (nm)	Measured Thickness (nm) of		Molar Equivalency (mmol)		
		NaLuF ₄ Layer	NaGdF ₄ Layer	Er	Lu	Gd
Yb/Er@Lu1@Gd	10.2	1.0	0.6	1.0	0.41	0.27
Yb/Er@Lu2@Gd	14.1	4.9	0.6	1.0	2.96	0.52
Yb/Er@Lu3@Gd	19.3	10.1	0.6	1.0	9.61	0.97

Next, we studied the change of PL emission, MRI relaxivity, and CT contrast of these samples as a function of NaLuF₄ interfacial layer thickness. First, when the thickness of interfacial NaLuF₄ increased from 1.0 nm to 10.1 nm, the upconversion PL was enhanced approximately 13-fold (Figure 4.19g and Figure 4.22). This increase is attributed to the improved shielding of Yb³⁺ and Er³⁺ luminescent centers from the surface by thicker NaLuF₄ layers.⁵⁷ Second, thicker NaLuF₄ layer the MRI relaxivity was enhanced by the β-Yb/Er@Lu CS structures acting as the supporting substrates for outer NaGdF₄ layers. Increasing the interfacial NaLuF₄ layer thickness slowed the NP tumbling,^{52, 64} thus enhancing the MRI relaxivity from 36.6 mM⁻¹s⁻¹ to 51.7 mM⁻¹s⁻¹ (Figure 4.19g and Figure 4.22). Finally, as the thickness of the interfacial NaLuF₄ layer is increased, the mass fraction of Lu³⁺ in a single CSS-NP increased from 25% to 84% (Figure 4.23) enhancing the X-ray attenuation capability for CT (Figure 4.19g and Figure 4.22). These data confirm that the interfacial NaLuF₄ layer is a critical component in the imaging performance of CSS-NP and that modulating the interfacial NaLuF₄ layer promotes the performance of all three imaging modalities simultaneously.

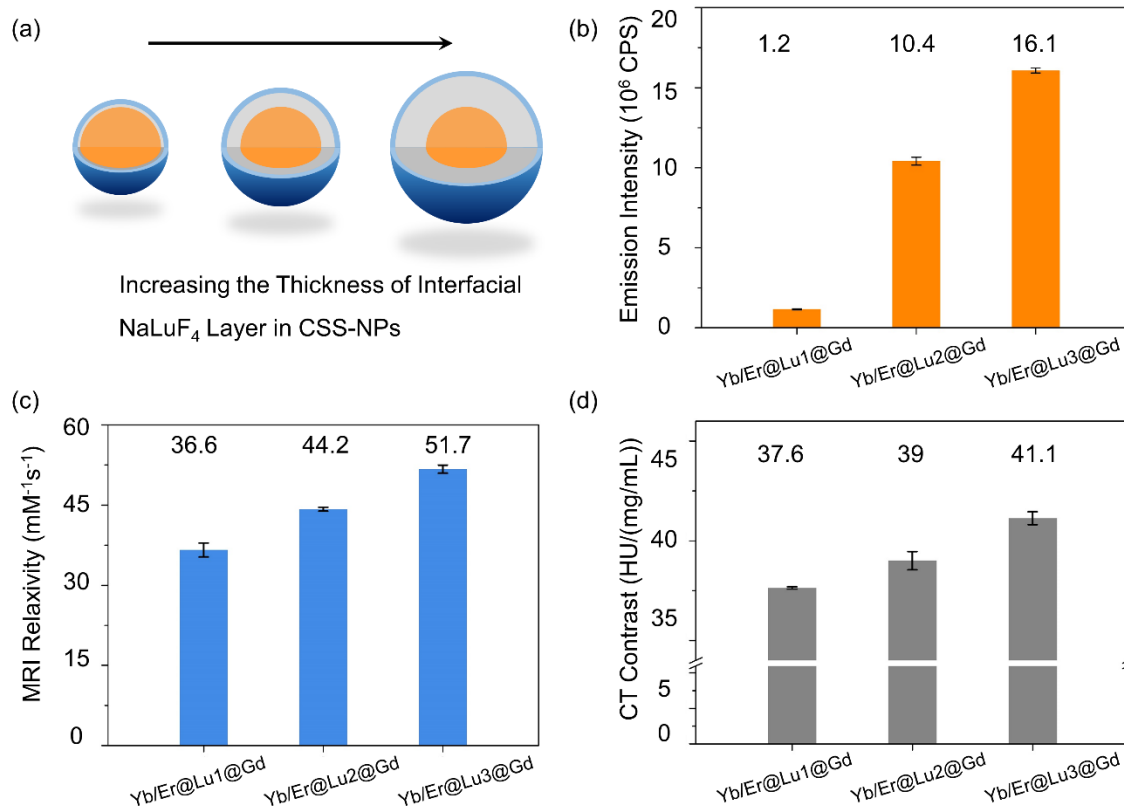


Figure 4.22 Comparison of PL emission intensity, MRI relaxivity, and CT contrast with increasing thickness of the interfacial NaLuF₄ layer.

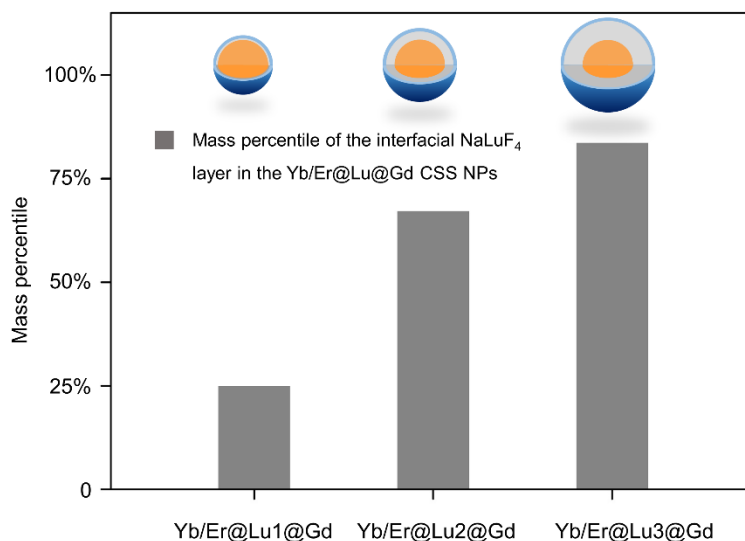


Figure 4.23 Mass percentile change of the interfacial NaLuF₄ layer in the Yb/Er@Lu@Gd CSS NPs with increased amount of sacrificial α - NaLuF₄ NPs deposited on the Yb/Er core NPs.

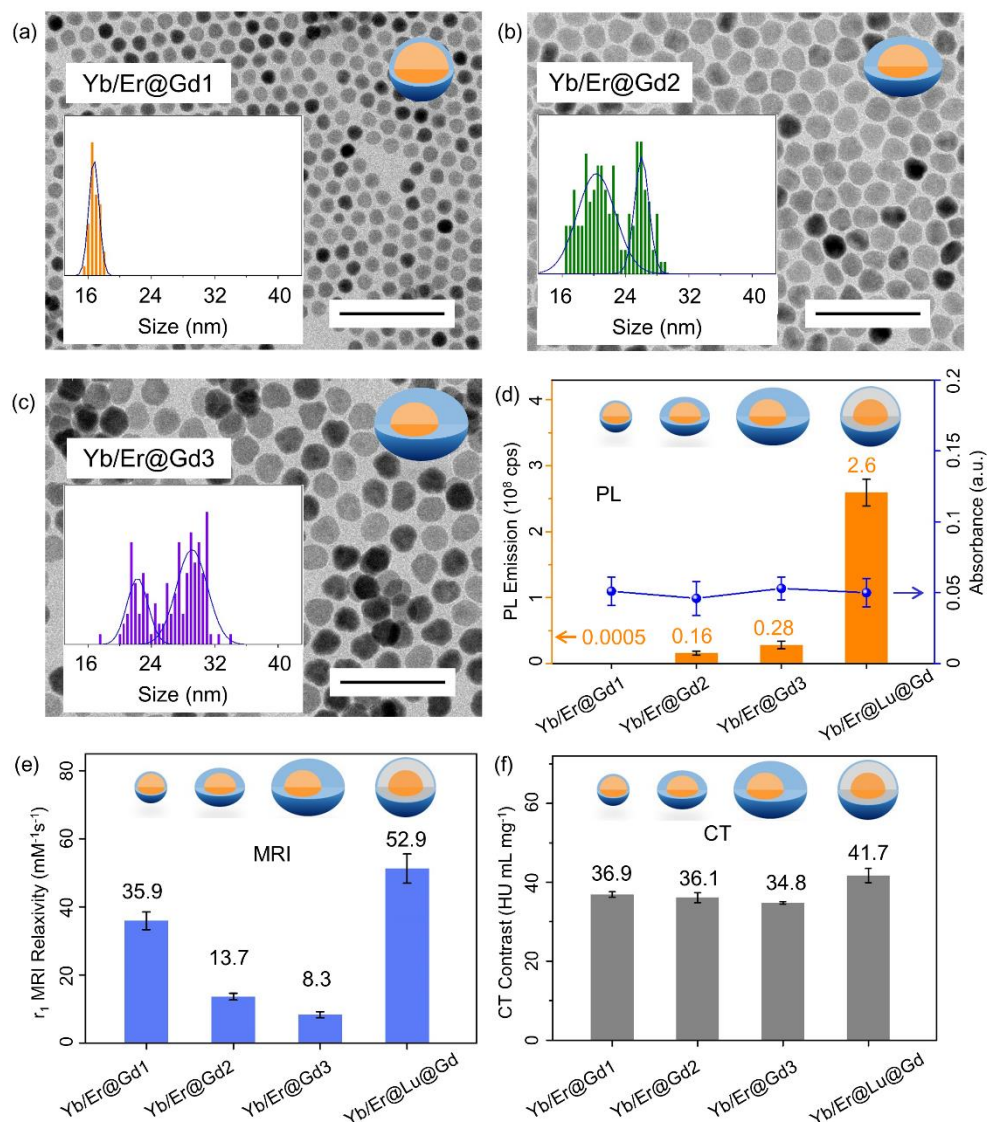


Figure 4.24 (a – c) TEM images of the β -NaYb/ErF₄@NaGdF₄ CS NPs with increasing thickness of the NaGdF₄ layer at the absence of the interfacial NaLuF₄ layer. Comparison of the (d) PL, (e) MRI relaxivity, and (f) CT contrast of β -NaYb/ErF₄@NaGdF₄ CS NPs and β -NaYb/ErF₄@NaLuF₄@NaGdF₄ CSS NPs (The absorbance of each sample remained the same because each sample had the same Yb/Er content while Gd or Lu does not absorb light).

To elucidate the critical role of the interfacial layer further, we deliberately removed the interfacial NaLuF₄ layer in the hetero-epitaxial NP structures (Figure 4.24a – c) and evaluated the performance of β -NaYb/ErF₄@NaGdF₄ (Yb/Er@Gd) CS-NPs as multimodal CAs. Because the lattice size of NaGdF₄ is larger than that of NaYb/ErF₄ (Table 4.1), depositing a NaGdF₄ shell on

the NaYb/ErF₄ core results in a compressive strain of the crystal lattice⁵⁵ and shape deformation in the CS structure as the thickness of the NaGdF₄ shell grows (Figure 4.25). In stark contrast to the β -Yb/Er@Lu@Gd CSS with circularity close to 1, the circularity of β -Yb/Er@Gd CS decreased to 0.57 when approximately 9 mmol NaGdF₄ was deposited on the β -Yb/Er cores resulting in a non-uniform shell (Figure 4.26).

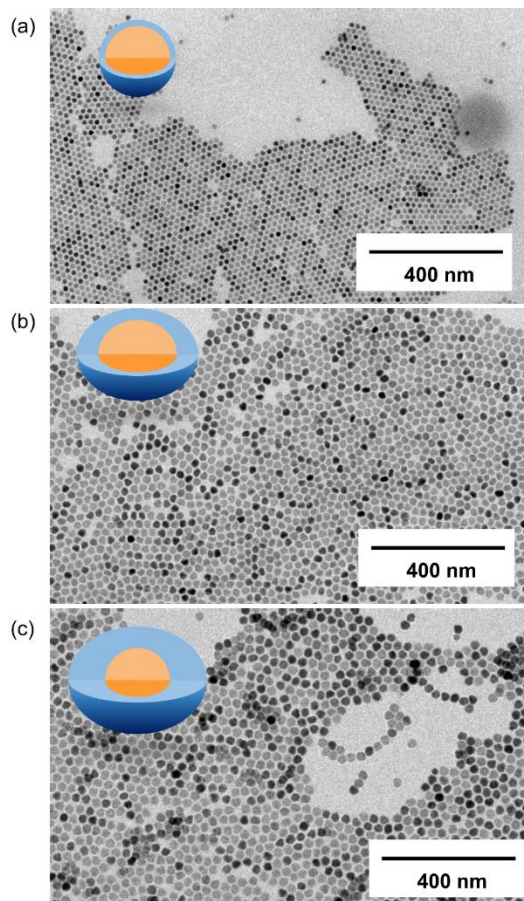


Figure 4.25 Low magnification TEM images of the Yb/Er@Gd1, Yb/Er@Gd2 and Yb/Er@Gd3 CS-NPs with increasing NaGdF₄ shell thickness.

Without the uniform and quasi-spherical CS architecture, the optically active Yb³⁺/Er³⁺ luminescent centers were more susceptible to surface quenching because of the shortened distance between them and the quenchers around the NPs;⁵⁷ therefore, the PL emission intensity of β -Yb/Er@Gd CS was less than 10% of that of β -Yb/Er@Lu@Gd CSS-NPs with the same absorbance

at 980 nm and excitation at the same power density (Figure 4.24d). While the thick NaGdF₄ shell deformed the CS structures and resulted in quenching of PL, it on the other hand reintroduced the limitation on MRI by preventing most of the Gd³⁺ paramagnetic centers from accessing surrounding water protons. As a result, the r_1 MRI relaxivity of the β -Yb/Er@Gd CS-NPs drastically dropped from 35.9 mM⁻¹s⁻¹ to 8.3 mM⁻¹s⁻¹ at 1.5 T with increased thickness of the NaGdF₄ layer (Figure 4.24e). This value is even lower than that of the α -NaGdF₄ sacrificial NPs alone (11.4 mM⁻¹s⁻¹). More critically, we observed that the evolving trend for the PL emission (increasing from 0.0005 to 0.28×10^8 cps) and MRI relaxivity (decreasing from 35.9 mM⁻¹s⁻¹ to 8.3 mM⁻¹s⁻¹) was opposite when we increased the thickness of NaGdF₄ without the interfacial NaLuF₄ layer (Figure 4.24d and 4.24e). This suggests that the PL and MRI properties cannot be optimized simultaneously without the NaLuF₄ interfacial layer in the CSS structures. Finally, the CT contrast of the β -Yb/Er@Gd CS was clearly lower than that of β -Yb/Er@Gd@Lu CSS-NPs because Yb, Er, and Gd all had smaller atomic numbers than Lu (Figure 4.24f). These results conclusively show that the interfacial NaLuF₄ layer in the β -Yb/Er@Gd@Lu CSS-NPs is a critical component in simultaneously enhancing the PL emission, MRI relaxivity, and CT contrast of the CSS-NP CA.

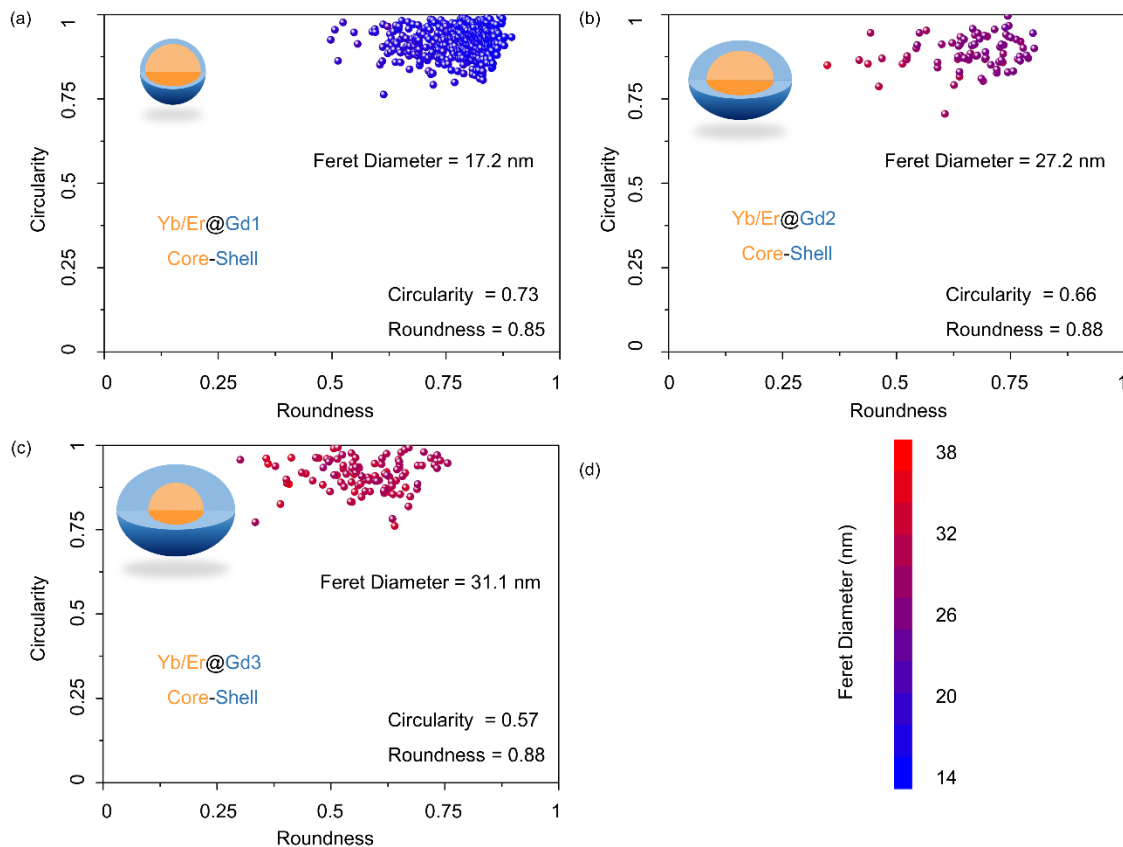


Figure 4.26 Morphological characterization of the (a) core, (b) CS and (c) CSS NPs shown in Figure 4. 24.

4.4 Conclusions

In conclusion, we report Ln hetero-epitaxial CSS-NPs-based multimodal imaging CAs that show simultaneously enhanced performances in PL, MRI, and CT modalities, that is higher than each individual contributing modalities alone. By carefully tuning the interfacial NaLuF₄ layer in the CSS architecture, we demonstrate enhancement of both upconversion and downshifting luminescence by a factor of 10^7 , compared to the core only structure. We also show that the increase in interfacial layer thickness drastically reduces the NP tumbling time ($0.28 \mu\text{s}$ to $12.7 \mu\text{s}$) resulting in enhanced MRI relaxivity from $11.4 \text{ mM}^{-1}\text{s}^{-1}$ to $52.9 \text{ mM}^{-1}\text{s}^{-1}$ at 1.5 T. The overall composite CSS structure with the larger atomic number Lu in the interfacial shell show strong CT

contrast that is 70% higher than the clinical iodine-based CT agents. The described design successfully demonstrates that the performance of each modality can in fact be enhanced in a composite structure rather than being compromised when integrated together. Such multimodal CAs have immense potential impact on future medical diagnostics by earning more availability for imaging in various modalities with a single type of CAs.

4.5 Materials and Methods

Chemicals

Erbium acetate hydrate (99.9%), ytterbium acetate hydrate (99.9%), yttrium acetate hydrate (99.9%), gadolinium oxide (anhydrous, 99.9%), sodium trifluoroacetate (98%), trifluoroacetic acid, 1-octadecene (>90%), oleic acid (>90%), oleylamine (>70%), sodium hydroxide, methanol, chloroform, ethanol, and toluene were all purchased from Sigma. Ammonium fluoride was purchased from Spectrum. Lutetium oxide (anhydrous, 99.9%) was purchased from Alfa Aesar. 1,2-distearoyl-sn-glycero-3-phosphoethanolamine-N-[(polyethylene glycol)-2000] (DSPE-PEG-2000) was purchased from Avanti Lipids. Gadolinium (III) 1, 4, 7, 10-tetraazacyclododecane-1,4,7,10-tetraacetate (Gd-DOTA) was purchased from Macrocyclics. Hexabrix (sodium and meglumine ioxaglate) was purchased from Guerbet. All chemicals were used as received without further purification unless specified.

We synthesized the hexagonal phase (β)- $\text{NaYb}_{0.2}/\text{Er}_{0.8}\text{F}_4@ \text{NaLuF}_4@ \text{NaGdF}_4$ hetero-epitaxial core-shell-shell (CSS) nanoparticles (NPs) by following our previously published procedure. In this procedure, cubic phase (α)- NaLuF_4 (Figure 4.1) and NaGdF_4 (Figure 4.2) NPs were synthesized separately, cleaned, and injected into the β - NaYb/ErF_4 core NPs reaction mixture at high temperature to obtain CSS structures (Figure 4.3).

Synthesis of cubic (α)-NaLuF₄ NPs (Sacrificial shell NPs)

Cubic NaLuF₄ were synthesized according to our previously reported procedure. Briefly, Lu₂O₃ (1 mmol) was dissolved in 50% aqueous trifluoroacetic acid (20 mL), refluxed overnight at 95 °C, and dried overnight at 70 °C remaining ~2 mmol lutetium trifluoroacetate as white powder. Sodium trifluoroacetate (2 mmol), 1-octadecene (12 mL), oleic acid (6 mL), and oleylamine (6 mL) was added to the prepared lutetium trifluoroacetate with vigorous stirring. The obtained yellow slurry was quickly heated to 120 °C under mild vacuum and maintained for 30 min to yield a clear yellow solution. The clear solution was switched under a gentle argon flow, heated to 300 °C rapidly (~15°C/min), and maintained at 300 °C with vigorous stirring until the solution became cloudy. The cloudy solution was kept 300 °C for ~12 min to obtain kinetically-stable α -NaLuF₄ NPs with an average size of ~8.27 nm (Figure 4.1). The synthesized NPs were naturally cooled to room temperature, precipitated by adding ethanol, collected by centrifugation (1900 g, 5 min), and washed with ethanol for several times. The final pellet was then dispersed in hexane (10 mL) as clear and colorless solution, and stored at 37 °C for further use.

Synthesis of cubic (α)-NaGdF₄ NPs (Sacrificial shell NPs)

Cubic (α)-NaGdF₄ were synthesized with the same protocol described above except that Gd₂O₃ (1.0 mmol) was used. The final product were kinetically-stable α -NaGdF₄ NPs with a size of ~6.18 nm (Figure 4.2) dispersed in hexane (10 mL).

Synthesis of hexagonal (β)-NaYb_{0.2}/Er_{0.8}F₄ core NPs

β -NaYb_{0.2}/Er_{0.8}F₄ core NPs were synthesized following our previous protocol with slight modification. Briefly, 0.8 mmol of erbium acetate hydrate, 0.2 mmol ytterbium acetate hydrate, 1-

octadecene (15 mL), and oleic acid (4.5 mL) were mixed, quickly heated to 120 °C under mild vacuum, kept at 120 °C for 45 min, and naturally cooled down to room temperature to yield a pinkish orange solution. A methanol solution (10mL) of ammonium fluoride (4 mmol) and sodium hydroxide (2.5 mmol) was added into the pinkish orange solution to yield a cloudy mixture. The mixture was stirred for 45 min at room temperature and slowly heated (~ 30 min) to 70 °C to remove methanol. The cloudy mixture became progressively clear during the heating process. Afterwards, it was quickly heated to 300 °C (~ 15 °C/min) and maintained at 300 °C for 1 h. Finally, the reaction mixture was cooled down and the NPs were precipitated by adding ethanol, collected by centrifugation (1900 g, 5 min), and washed several times with ethanol. The resulting pellet was then dispersed in chloroform (5 mL) for further studies.

Synthesis of hexagonal (β)-NaYF₄:Yb(18%)/Er(2%) NPs

β -NaYF₄:Yb(18%)/Er(2%) NPs were synthesized using a similar setup except that 0.8 mmol yttrium acetate hydrate, 0.18 mmol of ytterbium acetate hydrate, 0.02 mmol ytterbium, and 6 mL oleic acid were used.

Synthesis of hexagonal (β)-Na Yb_{0.2}/Er_{0.8}F₄@NaLuF₄@NaGdF₄ Hetero-epitaxial NPs

As synthesized sacrificial α -NaLuF₄ NPs (~ 1 mmol, see characterization section for details about quantification) in hexane were mixed with 1 mL 1-octadecene, gently stirred, and placed under a gentle flow of argon to remove hexane leaving NPs dispersed in 1-octadecene. After the β -NaYb/ErF₄ core NPs have been heated at 300 °C for 1 h, 1-octadecene dispersion of sacrificial α -NaLuF₄ NPs was rapidly injected into the solution and allowed to ripen (12-15 min) to yield β -NaYb/ErF₄@NaLuF₄ core-shell (CS) NPs. To generate the thick shell in this study (9.7 nm thick

NaLuF₄ shell on NaYb/ErF₄ core with diameter of 17.2 nm), repeated ($\times 9$) injections and ripening cycles (~ 9.4 mmol α -NaLuF₄ in total, see Table 4.2 for calculation) were performed while carefully maintaining the reaction mixture at 300 °C. After that, 0.96 mmol α -NaGdF₄ NPs were subsequently injected into the solution to yield hetero-epitaxial β -NaYb/ErF₄@NaLuF₄@NaGdF₄ CSS NPs. Finally, the reaction mixture was naturally cooled to room temperature. The CSS NPs were likewise precipitated by adding ethanol, collected by centrifugation (1900 g, 5 min), and washed with ethanol for several times. The resulting pellet was then dispersed in chloroform (5 mL) for further studies.

Synthesis of hexagonal (β)-NaYb/ErF₄@NaLuF₄@NaGdF₄ NPs with tunable thickness in the interfacial NaLuF₄ layer

The procedure was the same with the one above except that different amount of α -NaLuF₄ NPs were injected into the 1 mmol β -NaYb/ErF₄ core NPs solution at high temperature to obtain β -NaYb/ErF₄@NaLuF₄@NaGdF₄ CSS NPs with increasing thickness of interfacial NaLuF₄ layers. The amount of sacrificial α -NaLuF₄ and α -NaGdF₄ NPs used in the synthesis of each sample (Yb/ErG@Lu1@Gd, Yb/ErG@Lu2@Gd, and Yb/ErG@Lu3@Gd) were listed in Table 4.6.

Synthesis of hexagonal (β)-NaErF₄@NaGdF₄ CS NPs

The procedure was the same with that used for the Yb/Er@Lu@Gd CSS NPs except that 9 mmol of α -NaGdF₄ NPs were injected and ripened on the β -NaYb/ErF₄ core NPs without the use of α -NaLuF₄ NPs.

Characterization

The size and uniformity of the NPs were confirmed using transmission electron microscopy (TEM) (FEI, Technai G2 Sphera, operating at 120 kV). One droplet of the NP stock solution was diluted in 1 mL of hexane, drop cast onto a Pelco[®] carbon-coated 400 square mesh copper grid (Ted Pella, Inc.), and air dried for 1 hour before imaging. Scanning electron microscopy (SEM) images were obtained on FEI SFEG UHR SEM. The size distribution of the NPs was extracted from a representative TEM image by measuring at least 100 NPs, and presented as average \pm standard deviation. The energy-dispersive X-ray spectroscopy (EDS) was performed with a Tecnai G2 X-Twin (FEI Co.) instrument operating at 200 kV. Peaks in the EDS spectra were identified by comparison to a library of peaks *via* FEI software. The phase of NPs was determined by powder X-ray diffraction (XRD) using Siemens KFL Cu 2K diffractometer with a resolution of 0.02° and a scanning speed of 1°/min. The peaks in the XRD was reference to JCPDS file # 27-0689. Dynamic light scattering (DLS) measurements were performed using a Zetasizer Nano ZS (Malvern Instruments). Elemental concentration of all samples was determined by digesting the NPs in 70% HNO₃ for at least two days and analyzing on a Perkin Elmer Optima 3000 DV inductively coupled plasma atomic emission spectrometer (ICP-AES). All the photographs were taken with a Nikon[®] D5100 digital camera equipped with an AF-S nikkor 18-55 mm, 1:3.5G-5.6G lens.

Morphological Characterization

The morphological characterization was performed following a previously published protocol. Briefly, a representative TEM image of the each sample was converted to 8-bit binary image through the automatic threshold in ImageJ and outlined. Feret diameters, perimeters, and

areas of NPs were measured automatically using the “analyzed particles” function in ImageJ. The circularity and roundness for all NPs were calculated by ImageJ, *via* the following equations:

$$\text{Roundness} = 4\text{Area}/[\pi(\text{Feret diameter})^2]$$

$$\text{Circularity} = 4\pi\text{Area}/(\text{Perimeter})^2$$

Where the Feret diameter is the major axis of the fitted ellipse that encloses one NP and the perimeter is the length of fitted ellipse around one NP. Since all analyzed samples were larger than 15 nm in diameters, we only collected the outlined NPs with areas larger than 176 nm^2 ($7.5^2 \times 3.14$) to eliminate errors.

Photoluminescence Spectra

Photoluminescent (including both upconversion and downconversion) emission spectra of different samples were collected with a FluoroLog modular spectrofluorometer (Horiba). The samples were excited by either an 808 nm (L808P1WJ, Thorlabs) or 980 nm (L9800P200, Thorlabs) continuous wave laser diode mounted on a temperature controlled laser diode mount (TCLDM9, Thorlabs). Emission in the visible range (400-700 nm) was recorded by the R928 PMT on FluoroLog while the emission in the NIR range (700-1200 nm) was recorded by the R5509 PMT. The R5509 PMT was cooled with excess liquid nitrogen for at least two hours before spectra recording. The integration time was set as 0.5 s. Emission was collected perpendicular to the direction of excitation light. 200 μL chloroform solution of as-synthesized NPs was diluted with toluene (2 mL) to obtain a clear dispersion in a quartz cuvette (path length 1 cm) aiming for relatively low particle concentration suitable for optical measurements. Excitation power density was changed by tuning the controller while maintaining the beam cross-section unchanged. All spectra were corrected with the wavelength-dependent detector sensitivity provided by Horiba.

Emission intensity was calculated by integrating the area under the curve using Origins Lab. The dark counts were subtracted from the integrated emission intensity before determining the enhancement factor.

Phase transfer of NP into water

For the CSS-NPs with diameter of 37.8 nm, 5 mg CSS-NPs (mass of one NP: $\sim 1.69 \times 10^{-13}$ mg, number of NPs in 5 mg: $\sim 3 \times 10^{13}$, ~ 0.05 nmol) in chloroform was mixed with 20 mg DSPE-PEG 2000 ($\sim 7 \times 10^3$ nmol) in a 20 mL screw-neck glass vial. The high molar ratio of DSPE-PEG 2000 to CSS-NPs ($\sim 10^5$) is critical to achieve high MRI relaxivity. and it was kept for phase transfer of all other NPs in this study.

The vial containing the NPs and DSPE-PEG 2000 was left open overnight in a fume hood at room temperature to slowly evaporate chloroform leaving an oily layer at the bottom. The vial was mounted back to a rotary evaporator (Buchi R-205) at 60 °C for 1 h to completely remove excess chloroform. Distilled water (10 mL) was slowly added into the vial and the NPs were transferred to water by sonicating the vial for 5 min (PEGylated NPs). The aqueous solution containing the PEGylated NPs was filtered twice through the 0.22 μm sterile polyethersulfone syringe filters (30 mm diameter, Low Hold-up volume, Olympus Plastics) and the PEGylated NPs were collected by using ultracentrifuge (Optima L-80 XP, Beckman Coulter) with the speed of 45000 rpm ($\sim 184,000g$) at 4 °C for 1 h. The supernatant with excess empty micelles composed of DSPE-PEG 2000 was carefully removed, and the pellet was re-dispersed into 5 mL distilled water and stored at 4 °C for further studies. When a higher concentration of the NPs was needed, the as-prepared aqueous solution was concentrated by centrifuge (3000g, 30 min) through a Vivaspin®

20 Centrifugal Concentrator (100K MWCO, PES) at the Allegra® X-15R Benchtop centrifuge (with a swing-out bucket).

Preparation of the aqueous DOTA solution

DOTA solution was prepared by dissolving 6.527 mg Gd-DOTA into 10 mL DI water to obtain a stock solution of 1 mM and diluted to designated concentrations accordingly before measurement.

MRI Relaxivity measurement at 1.41 Tesla

Longitudinal (T_1) relaxation times of all samples were measured at a Benchtop Bruker Minispec mq-60 relaxometer (60 MHz, 1.41 T at 37 °C). Aqueous dispersion all samples were quantified by ICP-AES and tuned to 0.1 mM Gd^{3+} ionic concentration as the stock solution. The stock solution was diluted to different concentrations (0.05 mM and 0.025 mM) and 200 μ L of each sample was loaded into an NMR tube and measured respectively. For each measurement, application parameters for the relaxometer were: First pulse separation = 10 ms, final pulse separation = 10,000 ms, number of data points = 10, Delay sampling window = 0.05 ms, sampling window = 0.02 ms, time for saturation curve display = 3 s. r_1 MRI relaxivity was calculated by plotting $1/T_1$ against the ionic concentration of Ln^{3+} , fitting the scatter plot, and finding the slope of the fitting.

MRI Phantom studies at 7.0 Tesla

MR phantom images were obtained on a Bruker 7.0 T magnet equipped with Advance II Hardware and a 72 mm quadrature transmit/receive coil. All NPs and DOTA solution (200 μ L)

were loaded into the the 250 μL tubes and the tubes were immobilized into the agarose gel (1% wt) slab (6.5 cm \times 2 cm). The gel slab was scanned in the coil to obtain the cross-section images of all tubes simultaneously. T_1 relaxation time values at 7 T were determined by selecting regions of interest (ROI) using the ParaVision Version 5.1 software, and the fitting parameters were TR = 250.0 ms, TE = 12.6 ms, echo = 1/1, FOV = 6.91 cm/3.12 cm, slice thickness = 2.0 mm/3.0 mm, MTX = 256/116, FA = 180 deg. r_1 MRI relaxivity was also calculated by plotting $1/T_1$ against the ionic concentration of Ln^{3+} , fitting and scatter plot and finding the slope of the fitting.

Computed Tomography

CT contrast was determined on Micro-computed tomography scanner, Skyscan 1076 (Kontich, Belgium). Various aqueous samples in 250 μL tubes (including one tube filled with DI water as control group) were immobilized on a styrofoam stage inside the scanner and exposed to X-rays. Imaging was done at 36 μm isotropic voxel size, applying an electrical potential of 50 kVp and current of 200 μA , and using a 0.5 mm aluminum filter. A beam hardening correction algorithm was applied during image reconstruction. The obtained image intensity of water was set as 0 Hounsfield unit (HU) and air was set as -1000 HU to perform correlation between image intensity and HU values of various samples. Hexabrix (Guerbet, IN) was used as commercial contrast agent for comparison. A 2D orthogonal view of the full tube array was obtained using Dataviewer (Skyscan). The mean attenuation value of each sample was obtained on the cylindrical portion of the tube (5.33 mm height) and using a 3.88 diameter region of interest (ROI) which only covered the solution region and avoided the inner edge of the tube. The analysis was performed using CTAn software (Skyscan).

Surface area of the NPs

Surface area of the NPs (S) was calculated by the following equation

$$S = 4\pi r^2$$

Where r is the average radius of the NPs measured from the TEM images.

For α -NaGdF₄ NPs, $r = 3.1$ nm, therefore $S = 0.12 \mu\text{m}^2$;

For β -NaYb/ErF₄@NaLuF₄@NaGdF₄ NPs, $r = 18.9$ nm, therefore $S = 4.5 \mu\text{m}^2$.

The surfaces of both α -NaGdF₄ NPs and β -NaYb/ErF₄@NaLuF₄@NaGdF₄ NPs were completely cover by NaGdF₄.

Tumbling time of the NPs (τ_R)

Tumbling time of the NPs (τ_R) was calculated by the following equation

$$\tau_R = 4\pi\eta a^3/3k_B T$$

Where η dynamic viscosity = 10^{-3} pa*s, $k_B T = 4 \times 10^{-21}$ J, a is the hydrodynamic radius of the NPs determined by DLS, $T = 298$ K.

Hydrodynamic radius of the α -NaGdF₄ NP is 6.5 nm (Figure 4.17), therefore the $\tau_R = 0.28 \mu\text{s}$;

Hydrodynamic radius of the β -NaYb/ErF₄@NaLuF₄@NaGdF₄ NP is 23 nm (Figure 4.17), therefore the $\tau_R = 12.7 \mu\text{s}$.

Chapter 4, is a reprint of the material as it appears in *Nano Lett.* Sha He, Noah J. J. Johnson, Viet Anh Nguyen Huu, Esther Cory, Yuran Huang, Robert L. Sah, Jess V. Jokerst, and Adah Almutairi, American Chemical Society Press, 2017. The dissertation author was the primary investigator and author of this paper.

4.6 References

1. Kobayashi, H.; Longmire, M. R.; Ogawa, M.; Choyke, P. L., Rational chemical design of the next generation of molecular imaging probes based on physics and biology: mixing modalities, colors and signals. *Chem. Soc. Rev.* **2011**, *40*, 4626-4648.
2. Jokerst, J. V.; Gambhir, S. S., Molecular Imaging with Theranostic Nanoparticles. *Acc. Chem. Res.* **2011**, *44*, 1050-1060.
3. James, M. L.; Gambhir, S. S., A Molecular Imaging Primer: Modalities, Imaging Agents, and Applications. *Physiol. Rev.* **2012**, *92*, 897-965.
4. Kircher, M. F.; de la Zerda, A.; Jokerst, J. V.; Zavaleta, C. L.; Kempen, P. J.; Mitra, E.; Pitter, K.; Huang, R. M.; Campos, C.; Habte, F.; Sinclair, R.; Brennan, C. W.; Mellinghoff, I. K.; Holland, E. C.; Gambhir, S. S., A brain tumor molecular imaging strategy using a new triple-modality MRI-photoacoustic-Raman nanoparticle. *Nat. Med.* **2012**, *18*, 829-U235.
5. Huang, Y. R.; He, S.; Cao, W. P.; Cai, K. Y.; Liang, X. J., Biomedical nanomaterials for imaging-guided cancer therapy. *Nanoscale* **2012**, *4*, 6135-6149.
6. Smith, B. R.; Gambhir, S. S., Nanomaterials for In Vivo Imaging. *Chem. Rev.* **2017**, *117*, 901-986.
7. Della Rocca, J.; Liu, D. M.; Lin, W. B., Nanoscale Metal-Organic Frameworks for Biomedical Imaging and Drug Delivery. *Acc. Chem. Res.* **2011**, *44*, 957-968.
8. Hu, D. H.; Sheng, Z. H.; Zhang, P. F.; Yang, D. Z.; Liu, S. H.; Gong, P.; Gao, D. Y.; Fang, S. T.; Ma, Y. F.; Cai, L. T., Hybrid gold-gadolinium nanoclusters for tumor-targeted NIRF/CT/MRI triple-modal imaging in vivo. *Nanoscale* **2013**, *5*, 1624-1628.
9. Dong, W. J.; Li, Y. S.; Niu, D. C.; Ma, Z.; Liu, X. H.; Gu, J. L.; Zhao, W. R.; Zheng, Y. Y.; Shi, J. L., A Simple Route to Prepare Monodisperse Au NP-Decorated, Dye-doped, Superparamagnetic Nanocomposites for Optical, MR, and CT Trimodal Imaging. *Small* **2013**, *9*, 2500-2508.
10. Xue, S. H.; Wang, Y.; Wang, M. X.; Zhang, L.; Du, X. X.; Gu, H. C.; Zhang, C. F., Iodinated oil-loaded, fluorescent mesoporous silica-coated iron oxide nanoparticles for magnetic resonance imaging/computed tomography/fluorescence trimodal imaging. *Int. J. Nanomedicine* **2014**, *9*, 2527-2538.
11. van Schooneveld, M. M.; Cormode, D. P.; Koole, R.; van Wijngaarden, J. T.; Calcagno, C.; Skajaa, T.; Hilhorst, J.; t Hart, D. C.; Fayad, Z. A.; Mulder, W. J. M.; Meijerink, A., A

- fluorescent, paramagnetic and PEGylated gold/silica nanoparticle for MRI, CT and fluorescence imaging. *Contrast Media Mol. Imaging* **2010**, *5*, 231-236.
12. Miao, Q. Q.; Lyu, Y.; Ding, D.; Pu, K. Y., Semiconducting Oligomer Nanoparticles as an Activatable Photoacoustic Probe with Amplified Brightness for In Vivo Imaging of pH. *Adv. Mater.* **2016**, *28*, 3662-3668.
 13. Pu, K. Y.; Shuhendler, A. J.; Jokerst, J. V.; Mei, J. G.; Gambhir, S. S.; Bao, Z. N.; Rao, J. H., Semiconducting polymer nanoparticles as photoacoustic molecular imaging probes in living mice. *Nat. Nanotechnol.* **2014**, *9*, 233-239.
 14. Cai, W. B.; Chen, X. Y., Nanoplatfoms for targeted molecular imaging in living subjects. *Small* **2007**, *3*, 1840-1854.
 15. Mulder, W. J. M.; Strijkers, G. J.; Van Tilborg, G. A. F.; Cormode, D. P.; Fayad, Z. A.; Nicolay, K., Nanoparticulate Assemblies of Amphiphiles and Diagnostically Active Materials for Multimodality Imaging. *Acc. Chem. Res.* **2009**, *42*, 904-914.
 16. Jokerst, J. V.; Thangaraj, M.; Kempen, P. J.; Sinclair, R.; Gambhir, S. S., Photoacoustic Imaging of Mesenchymal Stem Cells in Living Mice via Silica-Coated Gold Nanorods. *ACS Nano* **2012**, *6*, 5920-5930.
 17. Huynh, E.; Leung, B. Y. C.; Helfield, B. L.; Shakiba, M.; Gandier, J. A.; Jin, C. S.; Master, E. R.; Wilson, B. C.; Goertz, D. E.; Zheng, G., In situ conversion of porphyrin microbubbles to nanoparticles for multimodality imaging. *Nat. Nanotechnol.* **2015**, *10*, 325-332.
 18. Lovell, J. F.; Jin, C. S.; Huynh, E.; Jin, H. L.; Kim, C.; Rubinstein, J. L.; Chan, W. C. W.; Cao, W. G.; Wang, L. V.; Zheng, G., Porphysome nanovesicles generated by porphyrin bilayers for use as multimodal biophotonic contrast agents. *Nat. Mater.* **2011**, *10*, 324-332.
 19. Lemaster, J. E.; Jokerst, J. V., What is new in nanoparticle-based photoacoustic imaging? *Wiley Interdiscip. Rev. Nanomed. Nanobiotechnol.* **2017**, *9*, 11.
 20. Harmsen, S.; Huang, R. M.; Wall, M. A.; Karabeber, H.; Samii, J. M.; Spaliviero, M.; White, J. R.; Monette, S.; O'Connor, R.; Pitter, K. L.; Sastra, S. A.; Saborowski, M.; Holland, E. C.; Singer, S.; Olive, K. P.; Lowe, S. W.; Blasberg, R. G.; Kircher, M. F., Surface-enhanced resonance Raman scattering nanostars for high-precision cancer imaging. *Sci. Transl. Med.* **2015**, *7*, 11.
 21. Rieffel, J.; Chitgupi, U.; Lovell, J. F., Recent Advances in Higher-Order, Multimodal, Biomedical Imaging Agents. *Small* **2015**, *11*, 4445-4461.

22. Louie, A. Y., Multimodality Imaging Probes: Design and Challenges. *Chem. Rev.* **2010**, *110*, 3146-3195.
23. Chen, G. Y.; Qju, H. L.; Prasad, P. N.; Chen, X. Y., Upconversion Nanoparticles: Design, Nanochemistry, and Applications in Theranostics. *Chem. Rev.* **2014**, *114*, 5161-5214.
24. Dong, H.; Du, S. R.; Zheng, X. Y.; Lyu, G. M.; Sun, L. D.; Li, L. D.; Zhang, P. Z.; Zhang, C.; Yan, C. H., Lanthanide Nanoparticles: From Design toward Bioimaging and Therapy. *Chem. Rev.* **2015**, *115*, 10725-10815.
25. Park, Y. I.; Lee, K. T.; Suh, Y. D.; Hyeon, T., Upconverting nanoparticles: a versatile platform for wide-field two-photon microscopy and multi-modal in vivo imaging. *Chem. Soc. Rev.* **2015**, *44*, 1302-1317.
26. Weissleder, R., A clearer vision for in vivo imaging. *Nat. Biotechnol.* **2001**, *19*, 316-317.
27. Cheng, L.; Yang, K.; Zhang, S.; Shao, M. W.; Lee, S. T.; Liu, Z., Highly-Sensitive Multiplexed in vivo Imaging Using PEGylated Upconversion Nanoparticles. *Nano Research* **2010**, *3*, 722-732.
28. Zhao, J.; Jin, D.; Schartner, E. P.; Lu, Y.; Liu, Y.; Zvyagin, A. V.; Zhang, L.; Dawes, J. M.; Xi, P.; Piper, J. A.; Goldys, E. M.; Monroe, T. M., Single-nanocrystal sensitivity achieved by enhanced upconversion luminescence. *Nature Nanotechnology* **2013**, *8*, 729-734.
29. Wang, F.; Banerjee, D.; Liu, Y. S.; Chen, X. Y.; Liu, X. G., Upconversion nanoparticles in biological labeling, imaging, and therapy. *Analyst* **2010**, *135*, 1839-1854.
30. Zhou, J.; Liu, Z.; Li, F. Y., Upconversion nanophosphors for small-animal imaging. *Chem. Soc. Rev.* **2012**, *41*, 1323-1349.
31. Naczynski, D. J.; Sun, C.; Turkcan, S.; Jenkins, C.; Koh, A. L.; Ikeda, D.; Pratz, G.; Xing, L., X-ray-Induced Shortwave Infrared Biomedical Imaging Using Rare Earth Nanoprobes. *Nano Lett.* **2015**, *15*, 96-102.
32. Bottrill, M.; Nicholas, L. K.; Long, N. J., Lanthanides in magnetic resonance imaging. *Chem. Soc. Rev.* **2006**, *35*, 557-571.
33. Lusic, H.; Grinstaff, M. W., X-ray-Computed Tomography Contrast Agents. *Chem. Rev.* **2013**, *113*, 1641-1666.
34. Lee, N.; Choi, S. H.; Hyeon, T., Nano-Sized CT Contrast Agents. *Adv. Mater.* **2013**, *25*, 2641-

2660.

35. Alric, C.; Taleb, J.; Le Duc, G.; Mandon, C.; Billotey, C.; Le Meur-Herland, A.; Brochard, T.; Vocanson, F.; Janier, M.; Perriat, P.; Roux, S.; Tillement, O., Gadolinium chelate coated gold nanoparticles as contrast agents for both X-ray computed tomography and magnetic resonance imaging. *J. Am. Chem. Soc.* **2008**, *130*, 5908-5915.
36. Liu, X. L.; Jiang, H.; Ye, J.; Zhao, C. Q.; Gao, S. P.; Wu, C. Y.; Li, C. H.; Li, J. C.; Wang, X. M., Nitrogen-Doped Carbon Quantum Dot Stabilized Magnetic Iron Oxide Nanoprobe for Fluorescence, Magnetic Resonance, and Computed Tomography Triple-Modal In Vivo Bioimaging. *Adv. Funct. Mater.* **2016**, *26*, 8694-8706.
37. Shen, J. W.; Yang, C. X.; Dong, L. X.; Sun, H. R.; Gao, K.; Yan, X. P., Incorporation of Computed Tomography and Magnetic Resonance Imaging Function into NaYF₄:Yb/Tm Upconversion Nanoparticles for in Vivo Trimodal Bioimaging. *Anal. Chem.* **2013**, *85*, 12166-12172.
38. Tian, G.; Yin, W. Y.; Jin, J. J.; Zhang, X.; Xing, G. M.; Li, S. J.; Gu, Z. J.; Zhao, Y. L., Engineered design of theranostic upconversion nanoparticles for tri-modal upconversion luminescence/magnetic resonance/X-ray computed tomography imaging and targeted delivery of combined anticancer drugs. *J. Mater. Chem. B* **2014**, *2*, 1379-1389.
39. Xia, A.; Chen, M.; Gao, Y.; Wu, D. M.; Feng, W.; Li, F. Y., Gd³⁺ complex-modified NaLuF₄-based upconversion nanophosphors for trimodality imaging of NIR-to-NIR upconversion luminescence, X-Ray computed tomography and magnetic resonance. *Biomaterials* **2012**, *33*, 5394-5405.
40. Wang, L.; Liu, J. H.; Dai, Y. L.; Yang, Q.; Zhang, Y. X.; Yang, P. P.; Cheng, Z. Y.; Lian, H. Z.; Li, C. X.; Hou, Z. Y.; Ma, P. A.; Lin, J., Efficient Gene Delivery and Multimodal Imaging by Lanthanide-Based Upconversion Nanoparticles. *Langmuir* **2014**, *30*, 13042-13051.
41. Zhou, J.; Lu, Z. G.; Shan, G. G.; Wang, S. H.; Liao, Y., Gadolinium complex and phosphorescent probe-modified NaDyF₄ nanorods for T₁- and T₂-weighted MRI/CT/phosphorescence multimodality imaging. *Biomaterials* **2014**, *35*, 368-377.
42. Yang, D. M.; Dai, Y. L.; Liu, J. H.; Zhou, Y.; Chen, Y. Y.; Li, C. X.; Ma, P. A.; Lin, J., Ultra-small BaGdF₅-based upconversion nanoparticles as drug carriers and multimodal imaging probes. *Biomaterials* **2014**, *35*, 2011-2023.
43. González-Béjar, M.; Francés-Soriano, L.; Pérez-Prieto, J., Upconversion Nanoparticles for Bioimaging and Regenerative Medicine. *Front. Bioeng. Biotechnol.* **2016**, *4*, 47.

44. Ni, D. L.; Bu, W. B.; Zhang, S. J.; Zheng, X. P.; Li, M.; Xing, H. Y.; Xiao, Q. F.; Liu, Y. Y.; Hua, Y. Q.; Zhou, L. P.; Peng, W. J.; Zhao, K. L.; Shi, J. L., Single Ho³⁺-Doped Upconversion Nanoparticles for High-Performance T-2-Weighted Brain Tumor Diagnosis and MR/UCL/CT Multimodal Imaging. *Adv. Funct. Mater.* **2014**, *24*, 6613-6620.
45. Li, Y.; Gu, Y. Y.; Yuan, W.; Cao, T. Y.; Li, K.; Yang, S. P.; Zhou, Z. G.; Li, F. Y., Core-Shell NaYbF₄:Tm@CaF₂@NaDyF₄ Nanocomposites for Upconversion/T-2-Weighted MRI/Computed Tomography Lymphatic Imaging. *ACS Appl. Mater. Interfaces* **2016**, *8*, 19208-19216.
46. Zhao, J. B.; Jin, D. Y.; Schartner, E. P.; Lu, Y. Q.; Liu, Y. J.; Zvyagin, A. V.; Zhang, L. X.; Dawes, J. M.; Xi, P.; Piper, J. A.; Goldys, E. M.; Monroe, T. M., Single-nanocrystal sensitivity achieved by enhanced upconversion luminescence. *Nat. Nanotechnol.* **2013**, *8*, 729-734.
47. Han, S. Y.; Deng, R. R.; Xie, X. J.; Liu, X. G., Enhancing Luminescence in Lanthanide-Doped Upconversion Nanoparticles. *Angew. Chem. Int. Ed.* **2014**, *53*, 11702-11715.
48. Su, L. T.; Karuturi, S. K.; Luo, J.; Liu, L.; Liu, X.; Guo, J.; Sum, T. C.; Deng, R.; Fan, H. J.; Liu, X.; Tok, A. I. Y., Photon Upconversion in Hetero-nanostructured Photoanodes for Enhanced Near-Infrared Light Harvesting. *Advanced Materials* **2013**, *25*, 1603-1607.
49. Chen, F.; Bu, W. B.; Zhang, S. J.; Liu, X. H.; Liu, J. N.; Xing, H. Y.; Xiao, Q. F.; Zhou, L. P.; Peng, W. J.; Wang, L. Z.; Shi, J. L., Positive and Negative Lattice Shielding Effects Co-existing in Gd (III) Ion Doped Bifunctional Upconversion Nanoprobes. *Adv. Funct. Mater.* **2011**, *21*, 4285-4294.
50. Johnson, N. J. J.; Oakden, W.; Stanisz, G. J.; Prosser, R. S.; van Veggel, F., Size-Tunable, Ultrasmall NaGdF₄ Nanoparticles: Insights into Their T-1 MRI Contrast Enhancement. *Chem. Mater.* **2011**, *23*, 3714-3722.
51. Cormode, D. P.; Sanchez-Gaytan, B. L.; Mieszawska, A. J.; Fayad, Z. A.; Mulder, W. J. M., Inorganic nanocrystals as contrast agents in MRI: synthesis, coating and introduction of multifunctionality. *NMR Biomed.* **2013**, *26*, 766-780.
52. Werner, E. J.; Datta, A.; Jocher, C. J.; Raymond, K. N., High-Relaxivity MRI Contrast Agents: Where Coordination Chemistry Meets Medical Imaging. *Angew. Chem. Int. Ed.* **2008**, *47*, 8568-8580.
53. Song, Y.; Xu, X. Y.; MacRenaris, K. W.; Zhang, X. Q.; Mirkin, C. A.; Meade, T. J., Multimodal Gadolinium-Enriched DNA-Gold Nanoparticle Conjugates for Cellular Imaging. *Angew. Chem. Int. Ed.* **2009**, *48*, 9143-9147.

54. Caravan, P., Strategies for increasing the sensitivity of gadolinium based MRI contrast agents. *Chem. Soc. Rev.* **2006**, *35*, 512-523.
55. Johnson, N. J. J.; van Veggel, F., Lanthanide-Based Heteroepitaxial Core-Shell Nanostructures: Compressive versus Tensile Strain Asymmetry. *ACS Nano* **2014**, *8*, 10517-10527.
56. Johnson, N. J. J.; Korinek, A.; Dong, C. H.; van Veggel, F., Self-Focusing by Ostwald Ripening: A Strategy for Layer-by-Layer Epitaxial Growth on Upconverting Nanocrystals. *J. Am. Chem. Soc.* **2012**, *134*, 11068-11071.
57. Johnson, N. J. J.; He, S.; Diao, S.; Chan, E. M.; Dai, H. J.; Almutairi, A., Direct Evidence for Coupled Surface and Concentration Quenching Dynamics in Lanthanide-doped Nanocrystals. *J. Am. Chem. Soc.* **2017**, *139*, 3275-3282.
58. Smith, A. M.; Mancini, M. C.; Nie, S. M., Bioimaging Second window for in vivo imaging. *Nat. Nanotechnol.* **2009**, *4*, 710-711.
59. Johnson, N. J. J.; He, S.; Hun, V. A. N.; Almutairi, A., Compact Micellization: A Strategy for Ultrahigh T-1 Magnetic Resonance Contrast with Gadolinium-Based Nanocrystals. *ACS Nano* **2016**, *10*, 8299-8307.
60. Pintacuda, G.; John, M.; Su, X. C.; Otting, G., NMR structure determination of protein-ligand complexes by lanthanide labeling. *Acc. Chem. Res.* **2007**, *40*, 206-212.
61. Caravan, P.; Farrar, C. T.; Frullano, L.; Uppal, R., Influence of molecular parameters and increasing magnetic field strength on relaxivity of gadolinium- and manganese-based T(1) contrast agents. *Contrast Media Mol. Imaging* **2009**, *4*, 89-100.
62. Kim, B. H.; Hackett, M. J.; Park, J.; Hyeon, T., Synthesis, Characterization, and Application of Ultrasmall Nanoparticles. *Chem. Mater.* **2014**, *26*, 59-71.
63. Zarschler, K.; Rocks, L.; Licciardello, N.; Boselli, L.; Polo, E.; Garcia, K. P.; De Cola, L.; Stephan, H.; Dawson, K. A., Ultrasmall inorganic nanoparticles: State-of-the-art and perspectives for biomedical applications. *Nanomed.-Nanotechnol. Biol. Med.* **2016**, *12*, 1663-1701.
64. Avedano, S.; Botta, M.; Haigh, J. S.; Longo, D. L.; Woods, M., Coupling Fast Water Exchange to Slow Molecular Tumbling in Gd³⁺ Chelates: Why Faster Is Not Always Better. *Inorg. Chem.* **2013**, *52*, 8436-8450.

Chapter 5

Compact Micellization: A Strategy for Ultrahigh T_1 Magnetic Resonance Contrast with Gadolinium-Based Nanocrystals

5.1 Abstract

Paramagnetic gadolinium (Gd^{3+})-based nanocrystals (NCs) with a large number of confined gadolinium ions can be expected to heavily enhance the longitudinal (T_1) relaxation of water protons compared to clinical gadolinium complexes with only a single paramagnetic center. However, paramagnetic Gd^{3+} -nanocrystals reported to date show only a modest T_1 relaxivity of $\sim 10 \text{ mM}^{-1}\text{s}^{-1}$ per Gd^{3+} at 1.5 T, only about 3-times higher than clinical Gd^{3+} -complexes. Here we demonstrate a strategy that achieves ultrahigh T_1 relaxivity that is about 25-times higher than clinical Gd^{3+} -complexes by controlling the proximity of water protons to a paramagnetic nanocrystal surface. Using $NaGdF_4$ NCs ($\sim 3 \text{ nm}$) coated with PEG-ylated phospholipid (DSPE-PEG) micelles, we show that the distance of water protons to the NCs surface can be tuned by controlling the NC-micelle sizes. Increasing the ratio of DSPE-PEG to NCs during micellization decreases the size of NC-micelles, enhancing the proximity of water to the NC surface. Using this strategy, we have achieved compact NC-micelles (hydrodynamic diameter, HD $\sim 5 \text{ nm}$) with ultrahigh T_1 relaxivity of $\sim 80 \text{ mM}^{-1}\text{s}^{-1}$ per Gd^{3+} at 1.41 T. The findings reported here demonstrates a nanostructured Gd^{3+} -contrast agent (CA) that simultaneously achieves an ultrahigh T_1 relaxivity approaching theoretical predictions, extremely compact size (HD $< 5 \text{ nm}$), and a biocompatible surface. Our results show the hitherto unknown ultrahigh T_1 relaxation enhancement of water protons in close proximity to a colloidal gadolinium- NC surface that is achievable by precise control of their surface structure.

5.2 Introduction

Magnetic resonance imaging (MRI) is routinely used in medical diagnostics, where the relaxation of water protons exposed to an external magnetic field is used to obtain morphological/anatomical information with high resolution and unlimited tissue penetration. Contrast agents (CAs) shorten the relaxation time of water protons, and gadolinium (Gd^{3+})-complexes are widely used clinically to enhance contrast.¹⁻⁴ While theoretical models predict a relaxivity enhancement of $\sim 80\text{-}100 \text{ mM}^{-1}\text{s}^{-1}$ per Gd^{3+} at clinical field (1.5 T),⁵ clinical Gd^{3+} -complexes in general have only a modest relaxivity of $\sim 3\text{-}5 \text{ mM}^{-1}\text{s}^{-1}$ per Gd^{3+} . This results in a high dosage of gadolinium ($\sim 15 \text{ mg/kg}$ body weight) in clinical scans, raising safety concerns.⁶⁻⁷ The low relaxivity also limits their use in targeted imaging that requires large local concentration of the CAs to observe contrast enhancement.⁸⁻⁹ Thus strategies that enhance the relaxivity of Gd^{3+} -based CAs is both fundamentally and clinically important.

While the relaxation of water protons around a Gd^{3+} -center is a complex interplay of multiple factors,³ strategies to enhance the relaxivity in general is focused on modulating the number of gadolinium bound water (q), optimizing water residence time (τ_M), and enhancing the rotational correlation time (τ_R).⁹ In particular, the ability to enhance the rotational correlation time by coupling Gd^{3+} to larger nanoscale structures have been intensely studied in various platforms such as proteins, dendrimers, liposomes, micelles, nanoparticles, and nanogels.^{1, 10-22} Although these strategies have demonstrated relaxivity enhancement, realizing ultrahigh relaxivities approaching the theoretical predictions ($> 50 \text{ mM}^{-1}\text{s}^{-1}$ per Gd^{3+}) at clinical field (1.5 T) still remains a challenge.²³⁻²⁵ To date it has not been possible to design Gd^{3+} -based nanostructures that simultaneously have a compact size (hydrodynamic size (HD) $< 5 \text{ nm}$, *i.e.* below the renal

threshold for effective clearance),²⁶ ultrahigh relaxivity, and a biocompatible surface, some of the key requirements to realize clinical translation. Here, using colloidal NaGdF₄ nanocrystals (NCs) and PEG-ylated phospholipids, we demonstrate a compact micellization strategy that meets all these key requirements.

The relaxation of water protons near a paramagnetic center is the sum of individual contributions from the inner-sphere (IS), secondary sphere (SS), and outer sphere (OS) water molecules.^{1, 5} The water molecules that are directly bound to the metal center account for the IS, and the water molecules that are diffusing in close proximity account for the SS and OS contributions. While the individual contributions vary depending on the CAs structural composition, it is known that outer sphere contributions around a single paramagnetic center can be significant.^{9, 27} In this context, Gd³⁺-based NCs with a large number of confined paramagnetic ions in a small volume can be expected to significantly affect the relaxation of water protons in close proximity. For example, a 3 nm Gd³⁺-based NC (NaGdF₄) has ~200 Gd³⁺ ions of which 60-80 are surface ions. A collective contribution from these ions should ideally influence the water protons heavily at close proximity to yield large relaxivity values, however Gd³⁺-based NCs reported to date have only a modest relaxivity of <10 mM⁻¹s⁻¹ per Gd³⁺.²⁸⁻³⁶ In this context, we hypothesized that an ideally designed surface structure should address this conundrum, and open possibilities to achieve higher relaxivities than that have been previously demonstrated.

5.3 Results and Discussion

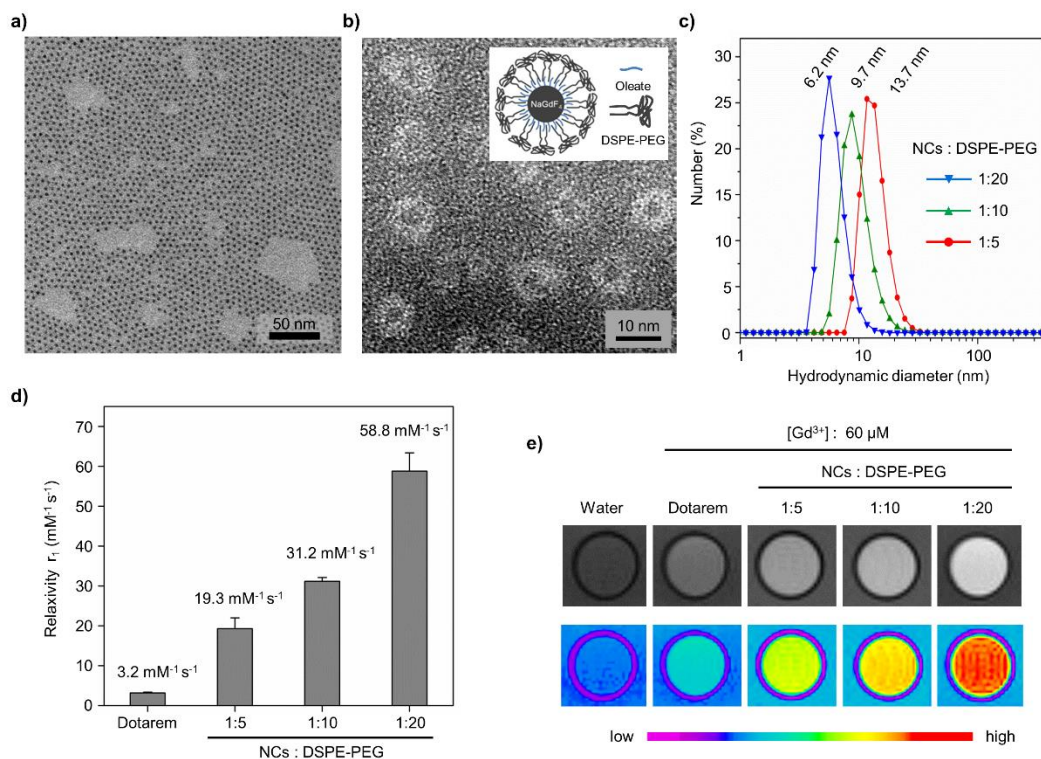


Figure 5.1. (a) TEM image of as synthesized ultrasmall (3 nm) oleate-stabilized NaGdF₄ NCs (b) Representative negative-stained TEM image of DSPE-PEG coated NC-micelles, Inset: Schematic illustration of a NaGdF₄ NC confined within DSPE-PEG micelle. (c) Hydrodynamic size of the NC-micelles at variable NC to DSPE-PEG loading ratio measured by DLS. (d) Longitudinal T₁ relaxivity (per Gd³⁺) of a clinical MRI contrast agent (Dotarem) and the NC-micelles at variable NC to DSPE-PEG loading ratio, at 1.41 T. (e) MRI phantom images of Dotarem and the NC-micelles at identical Gd³⁺ concentration (60 μM), and water.

Highly uniform ultrasmall NaGdF₄ NCs (3 nm) stabilized with oleate ligands as shown in Figure 5.1a were synthesized following a reported procedure³¹ (see Figure 5.2 for size distribution analysis, and TEM images of different NCs used in this study). High quality NCs with very low size distribution requires the use of high temperature and high boiling solvents to precisely control the nucleation and growth.³⁷⁻³⁹ Thus the synthesized NCs have to be transferred to water, and we realized that this step should be critical towards achieving high relaxivity CAs. Coating amphiphilic PEG-ylated phospholipids has been used with a wide range of hydrophobic NCs to be

transferred to water.⁴⁰⁻⁴³ As schematically shown in Figure 5.1b (inset), driven by hydrophobic interactions the PEG-ylated phospholipids (DSPE-PEG-2000) adsorb on the hydrophobic NCs surface while the hydrophilic PEG is exposed to water, generating water dispersible NCs with a biomimetic/biocompatible surface. Given that the relaxation of water protons in close proximity to the NC surface (OS) is determined by the distance of closest approach,⁹ we conceptualized that it is critical to achieve a single NC confined within each micelle that are also extremely compact in size. Multiple NCs confined within the micelles, or micelles with loosely packed PEG-ylated lipids will significantly impact the proximity of the water proton to the NC surface and thus the observed relaxivity.

In this context, we decided to use a solvent exchange method compared to the widely used film hydration method to prepare DSPE-PEG coated NCs.⁴² In the solvent exchange process, the hydrophobic NCs and the PEG-ylated phospholipids dispersed in an organic solvent (chloroform) are first transferred to a miscible common solvent (DMSO), and then subsequently transferred to water (see experimental details in SI), as compared to the abrupt phase transition in film hydration process (thin solid film to water). The sequential steps performed entirely in solution allow for a better control on the surface coating density and coating efficiency with the solvent exchange process.⁴²

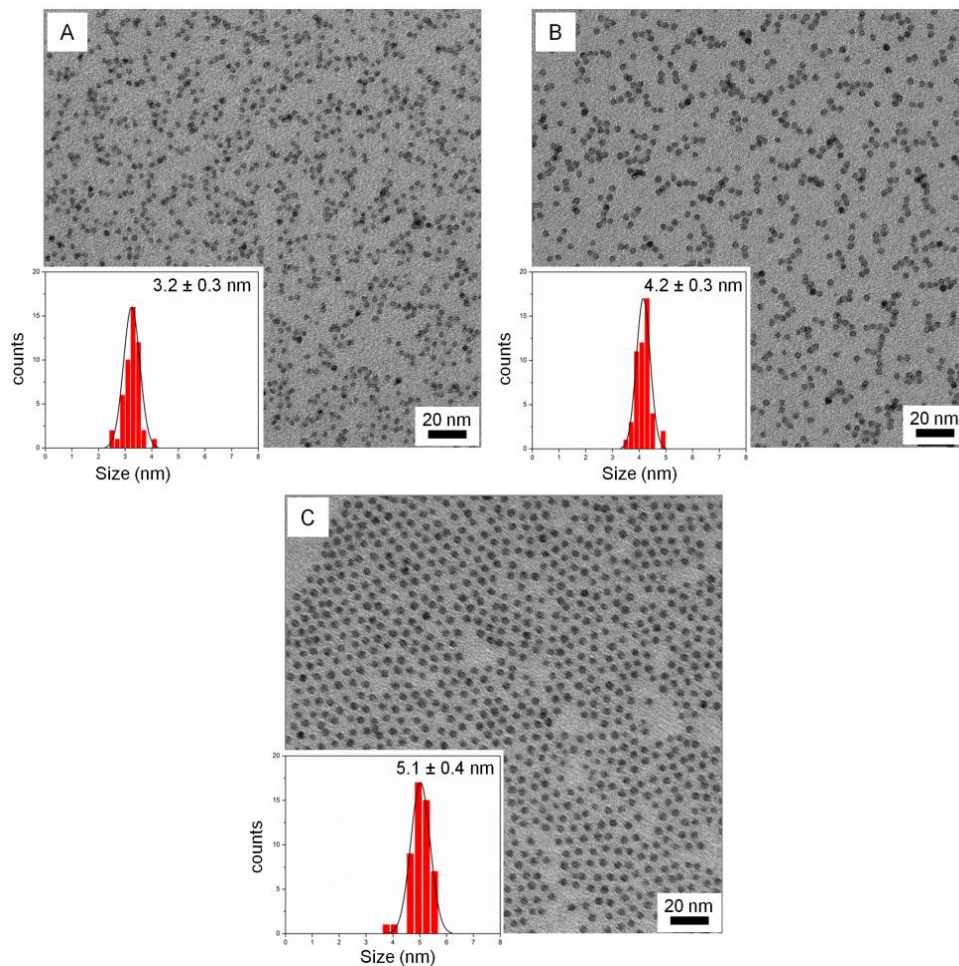


Figure 5.2 Transmission electron microscopy (TEM) images and size distribution of oleate stabilized NaGdF₄ NCs, (A) 3 nm, (B) 4 nm, and (C) 5 nm NaGdF₄:15% Ce³⁺/5% Tb³⁺ NCs.

To prepare compact NC-loaded micelles we hypothesized that the concentration of DSPE-PEG should be a critical factor. To test this hypothesis and to determine the ideal DSPE-PEG concentration, we first investigated the micellization of DSPE-PEG alone at different concentrations (13-267 μ M, see experimental section for details) to generate empty micelles that are within the size range of NCs (\sim 3 nm). Dynamic light scattering (DLS) measurements of the empty micelles (Figure 5.3) show that the micelle sizes decreased (HD diameter: 12.5 to 2.8 nm) with increasing DSPE-PEG concentration (13 to 267 μ M), and that compact micelles of \sim 3 nm can be formed at high DSPE-PEG concentrations. Our observation of such extremely compact

micelles with increasing DSPE-PEG concentration is consistent with previous studies,⁴⁴ and demonstrates that a high DSPE-PEG concentration is critical to achieve compact micelles.

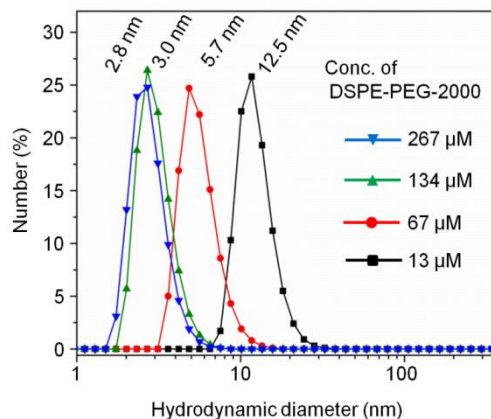


Figure 5.3 Hydrodynamic size of the DSPE-PEG-2000 empty micelles in water prepared at different concentrations measured by DLS.

Based on this we studied the effect of increasing DSPE-PEG concentration in preparing NC-loaded micelles. Using a fixed concentration of NCs (3 nmol), and varying the relative concentration of DSPE-PEG (W/W ratio NC: DSPE-PEG, 1:5, 1:10, and 1:20, that corresponds to ~67, 134, and 267 μM DSPE-PEG-2000) we prepared DSPE-PEG coated NCs using the solvent exchange protocol (see experimental details). A representative negative stained TEM image of DSPE-PEG coated NC micelles is shown in Figure 5.1b. The hydrodynamic size of the DSPE-PEG coated NC micelles decreased from ~14 nm to 6 nm on increasing the loading ratio of NC: DSPE-PEG from 1:5 to 1:20 as shown in Figure 5.1c (see Table 5.1 for average size distributions), confirming the possibility of achieving compact NC-micelles by manipulating the DSPE-PEG concentration during micellization.

Table 5.1 Average hydrodynamic diameter (HD) sizes (number-weighted) and polydispersity index (PDI) of the micelles investigated in this study measured by DLS.

		Hydrodynamic Diameter (HD) nm			
Empty Micelles		[DSPE-PEG-2000]			
		13 μ M	67 μ M	134 μ M	267 μ M
	(HD) nm	12.8 \pm 0.3	5.7 \pm 1.2	2.7 \pm 0.3	2.6 \pm 0.5
	PDI	0.08	0.08	0.07	0.07
Solvent Exchange		NCs : DSPE-PEG-2000			
		1 :5	1 :10	1 :20	1 :40
	(HD) nm	13.6 \pm 0.5	9.5 \pm 0.1	6.8 \pm 0.6	4.2 \pm 0.1
	PDI	0.07	0.08	0.06	0.07
		DSPE-PEG-3000	DSPE-PEG-5000	DMPE-PEG-2000	
	(HD) nm	6.9 \pm 0.5	9.9 \pm 0.1	4.6 \pm 0.1	
	PDI	0.07	0.06	0.05	
		NCs – 4 nm		NCs – 5 nm	
(HD) nm		7.1 \pm 1.7		9.2 \pm 2.2	
PDI		0.07		0.08	
Thin-film Exchange		NCs : DSPE-PEG-2000			
		1 :5	1 :10	1 :20	
	(HD) nm	17.2 \pm 1.6	12.4 \pm 0.6	9.5 \pm 0.6	
	PDI	0.07	0.08	0.07	

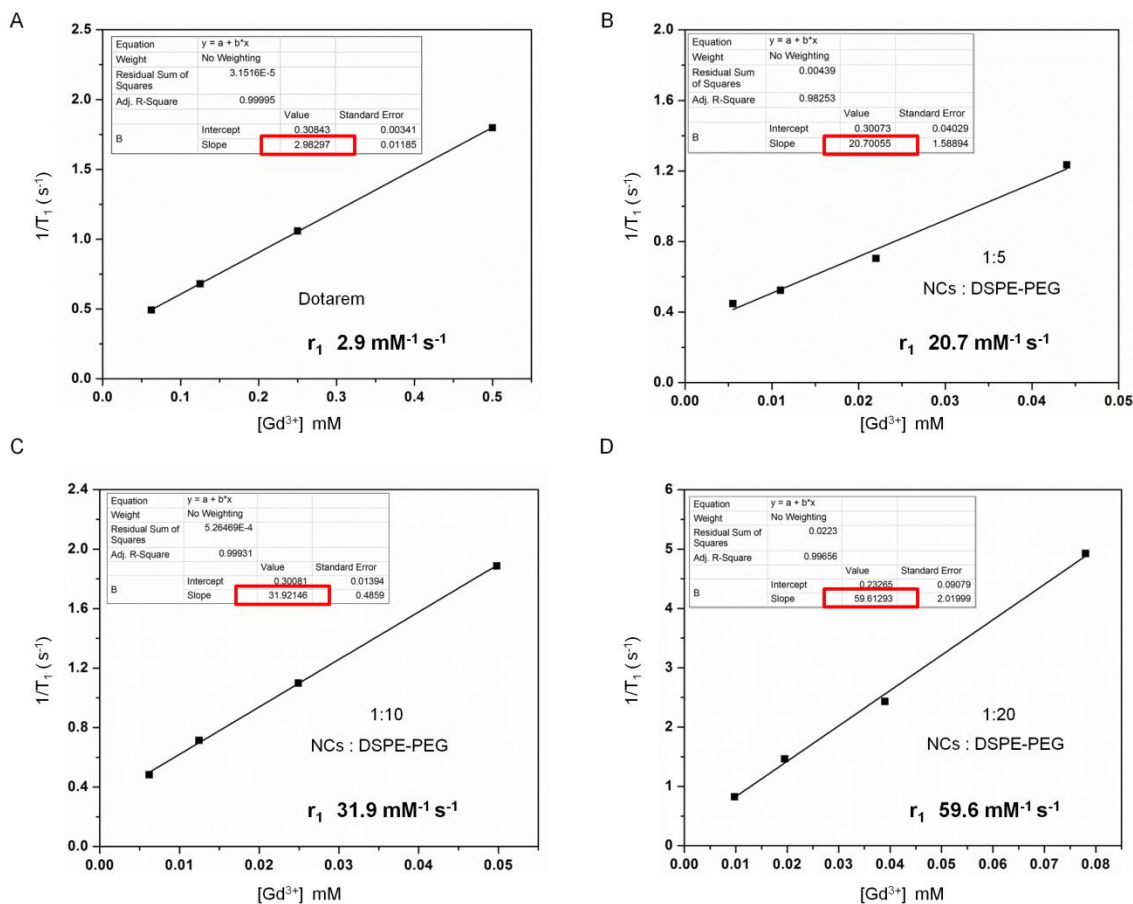


Figure 5.4. Representative concentration dependent T_1 ionic relaxivity plots (1.41 T) of (A) Dotarem, and NC-micelles prepared by solvent exchange with variable NCs to DSPE-PEG ratio (weight/weight ratio) (B) 1:5, (C) 1:10, and (D) 1:20.

We next studied the Gd^{3+} -concentration dependent longitudinal (T_1) relaxation rates of these NC micelles and a commercial Gd^{3+} -complex (Dotarem) using a benchtop relaxometer (60 MHz, 1.41 T @37 °C). While the relaxivity of the clinical complex was only about 3 $\text{mM}^{-1}\text{s}^{-1}$ (per Gd^{3+}), the relaxivity of the NC micelles increased from $\sim 19 \text{mM}^{-1}\text{s}^{-1}$ to 60 $\text{mM}^{-1}\text{s}^{-1}$ (per Gd^{3+}), with increase in DSPE-PEG loading ratio (Figure 5.1d) (see Figure 5.4 for concentration dependent plots, and Table 5.2 for average values). The MRI phantom images of Dotarem, and the NC

micelles at the same Gd^{3+} -concentration ($60 \mu\text{M}$) shown in Figure 5.1e clearly confirm the relaxivity enhancement achievable by controlling the NC-micelle size.

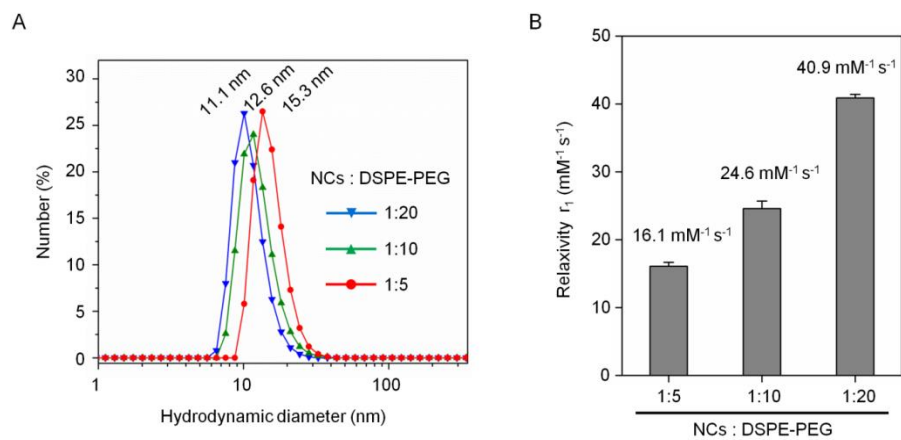


Figure 5.5 NC-micelles with variable NCs to DSPE-PEG ratio (weight/weight ratio) prepared by thin-film hydration method, (A) Hydrodynamic size of NC-micelles in water, and (B) Longitudinal T_1 relaxivity (per Gd^{3+}) of the NC-micelles at 1.41 T.

We also find a similar DSPE-PEG loading ratio dependent relaxivity enhancement with the widely used film hydration method (Figure 5.5 and 5.6), confirming the generality of our observation. However, in all loading ratio the solvent exchange produced more compact micelles and higher relaxivity (Figure 5.7) confirming the higher efficiency and control with this method.⁴²

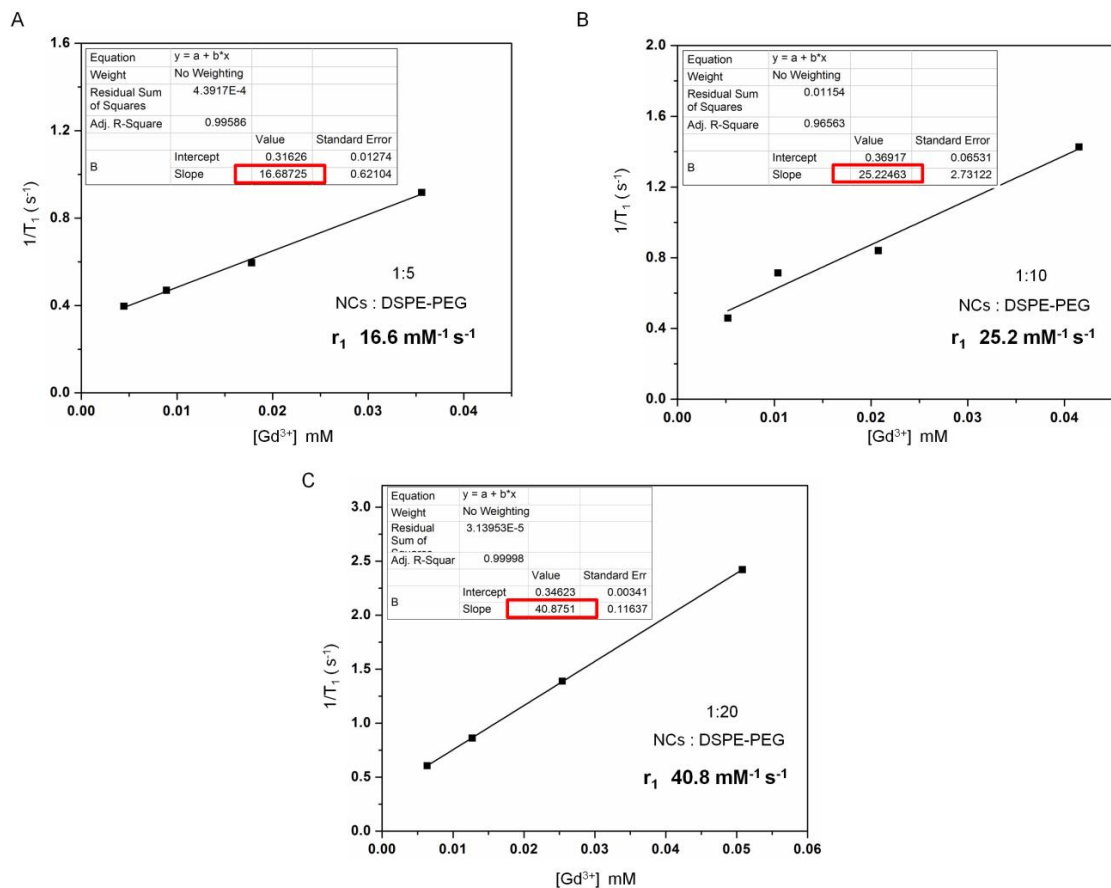


Figure 5.6 Representative concentration dependent T_1 ionic relaxivity plots (1.41 T) of NC-micelles prepared by thin-film hydration method with variable NCs to DSPE-PEG ratio (weight/weight ratio) (A) 1:5, (B) 1:10, and (C) 1:20.

The striking correlation between the observed decrease in NC-micelle size and the extremely large relaxivity enhancement, confirms the strong distance dependent outer sphere relaxivity effect with these NCs. Moreover, the dipole-dipole interaction of the paramagnetic center (Gd^{3+}) and the water protons is strongly distance dependent ($1/r^6$),⁹ which explains the large relaxivity amplification with compact micelles as it enhances the proximity of the water protons to the NC surface.

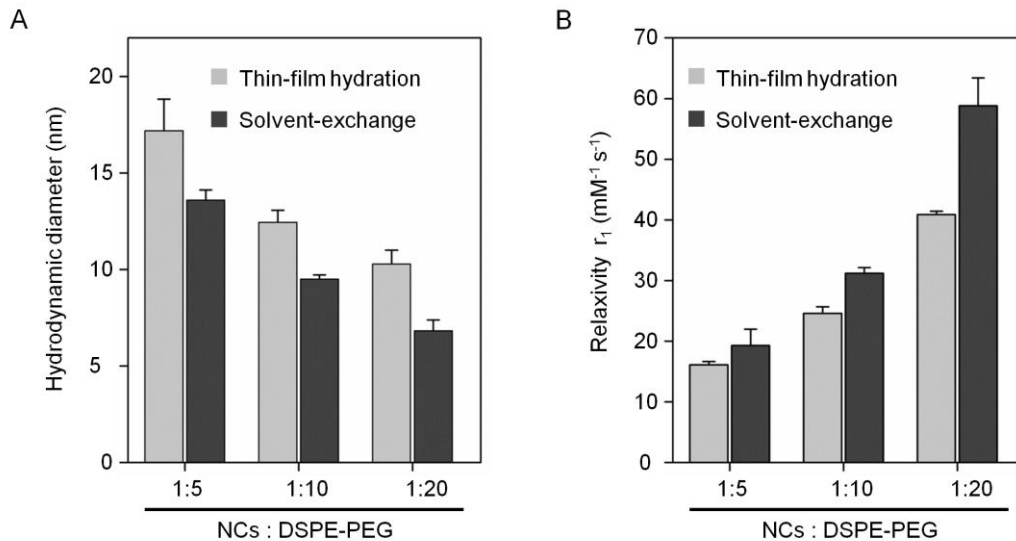


Figure 5.7 Comparison of thin-film hydration and solvent-exchange method with variable NCs to DSPE-PEG ratio (weight/weight ratio), (A) Hydrodynamic size of the NC-micelles, and (B) Longitudinal T₁ relaxivity (per Gd³⁺) of the NC-micelles at 1.41 T.

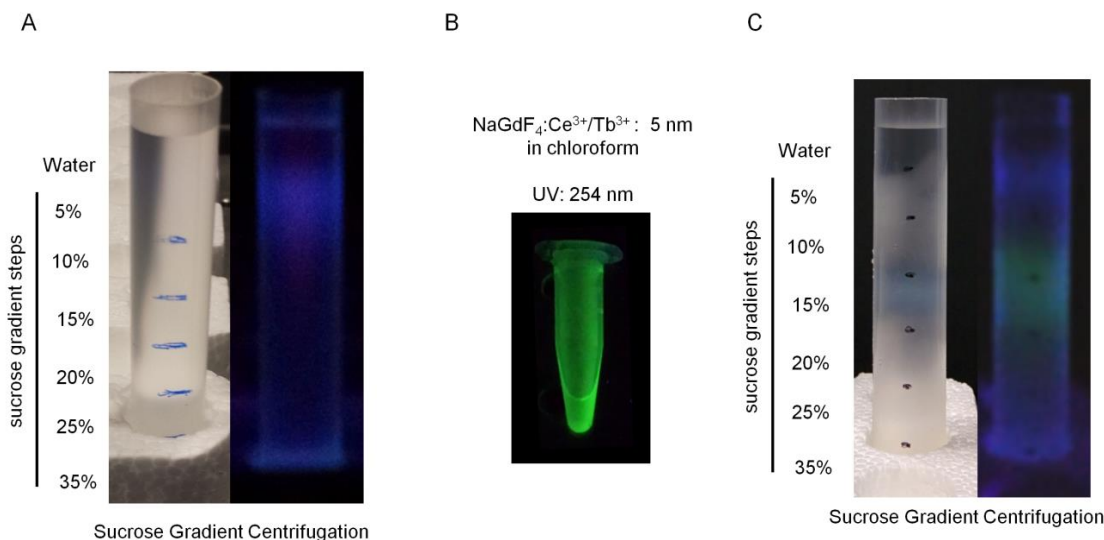


Figure 5.8 Sucrose gradient ultracentrifugation to remove empty micelles (A) Images of the (3 nm) NC-micelles after gradient centrifugation under visible and UV light illumination (see comments below), (B) Dispersion of 5 nm NaGdF₄:15% Ce³⁺/5% Tb³⁺ NCs under UV illumination, and (c) Images of the (5 nm) NC-micelles after gradient centrifugation under visible and UV light illumination.

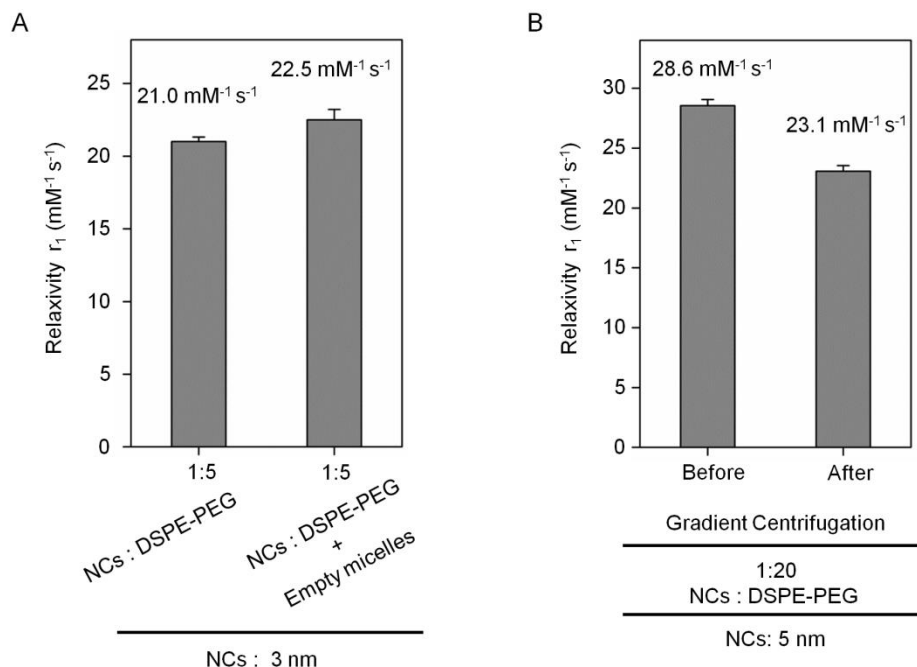


Figure 5.9 Longitudinal T_1 relaxivity (per Gd^{3+}) of the NC-micelles at 1.41 T (A) NC-micelles prepared at 1:5 (NCs to DSPE-PEG weight/weight ratio) and after adding empty micelles prepared at 250 μM DSPE-PEG concentration, and (B) NC-micelles of 5 nm NaGdF_4 :15% Ce^{3+} /5% Tb^{3+} before and after sucrose gradient ultracentrifugation.

To validate the ability to control the water proton proximity to the NC surface and the relaxivity using this strategy, we prepared NC-micelles at a higher loading ratio (NC: DSPE-PEG 1:40). The prepared NC-micelles were purified of empty micelles using sucrose gradient ultracentrifugation (Figure 5.8 and 5.9) and analyzed. The obtained NC-micelles had a more compact size (HD size: 4.2 nm) and enhanced relaxivity of $\sim 80 \text{ mM}^{-1} \text{ s}^{-1}$ per Gd^{3+} that is about 25 times higher than the clinical CA (Figure 5.10a, b and 5.11 for concentration dependent plot). The strikingly large relaxivity enhancement with the compact-NC micelles to that of the clinical CA is clearly observed with the concentration dependent MRI phantom images shown in Figure 5.10c.

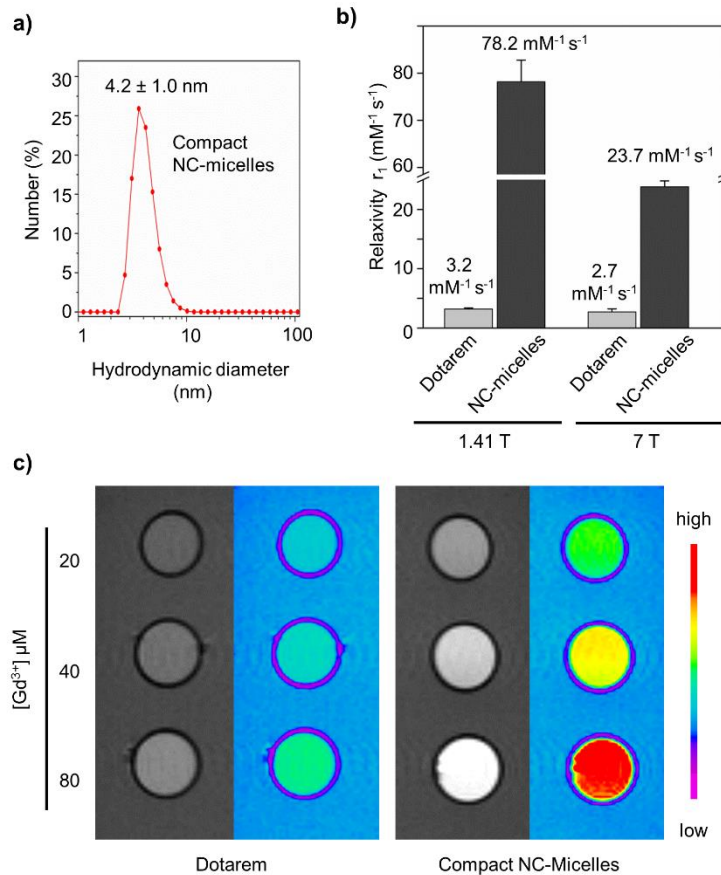


Figure 5.10 (a) Hydrodynamic size of compact NC-micelles prepared from 3 nm NaGdF₄ at NC to DSPE-PEG loading ratio of 1:40 measured by DLS. (b) Longitudinal T_1 relaxivity (per Gd^{3+}) of a clinical MRI contrast agent (Dotarem) and the compact NC-micelles at low (1.41 T) and high field (7 T). (c) Concentration dependent MRI phantom images of the compact Dotarem (left) and compact NC-micelles (right) and their respective color contrasted images.

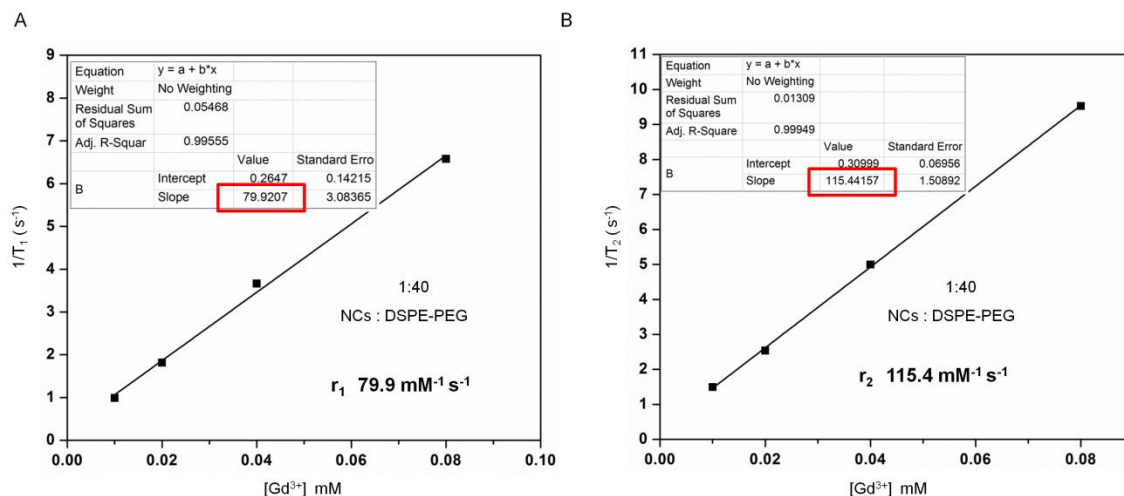


Figure 5.11 Representative concentration dependent ionic relaxivity plots (1.41 T) of compact NC-micelles (NCs to DSPE-PEG ratio weight/weight 1:40), (A) T_1 relaxivity, and (B) T_2 relaxivity.

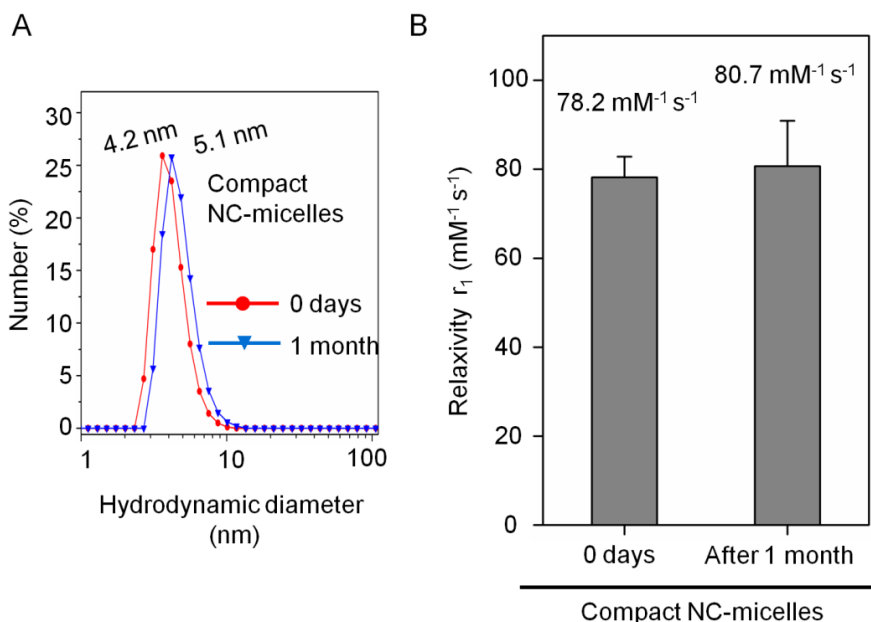


Figure 5.12 Stability of compact-NC micelles stored at 4 °C, (A) Hydrodynamic size of NC-micelles in water, and (B) Longitudinal T_1 relaxivity (per Gd^{3+}) of the NC-micelles at 1.41 T.

It is generally accepted that for clinical utility the final HD size of the NCs need to be below 5 nm, and our results demonstrate the possibility of achieving nanostructured Gd^{3+} -CAs with ultrahigh relaxivity, and HD size below this threshold. These compact NC-micelles are stable over time (Figure 5.12), and have an extremely low r_2/r_1 of 1.5 (see Figure 5.11 for T_2 relaxivity plot,

and Table 5.2 for average values) highlighting their suitability as T₁ CA. Additionally, the enhanced signal-to-noise ratio at high field (> 3T) and the reduced acquisition time has increased interest in finding suitable CAs for high field MRI.^{5,9} We find these compact NC-micelles to have a relaxivity of ~25 mM⁻¹s⁻¹ per Gd³⁺ at 7 T, the highest reported for a Gd³⁺-CA at such a high field (Figure 5.10b and Figure 5.13). Taken together, these findings demonstrate the strong relaxivity enhancement achievable with colloidal Gd³⁺-NCs by controlling their surface structure.

Table 5.2 Average relaxivity values per Gd³⁺ of the micelles investigated in this study.

	Relaxivity (r ₁) mM ⁻¹ s ⁻¹ per Gd ³⁺		(r ₂) mM ⁻¹ s ⁻¹ per Gd ³⁺	
Dotarem	3.2 ± 0.2 (1.41 T)		2.7 ± 0.5 (7 T)	
Solvent Exchange	NCs : DSPE-PEG-2000			
	1 : 5	1 : 10	1 : 20	1 : 40
	19.3 ± 2.7	31.2 ± 1.0	58.8 ± 4.6	78.2 ± 4.6 (r ₁) 116.8 ± 1.6 (r ₂)
	23.7 ± 1.0 (7 T)			
	DSPE-PEG-3000		DSPE-PEG-5000	
	55.4 ± 3.6		54.0 ± 2.5	
DMPE-PEG-2000		DMPE-PEG-2000		
69.4 ± 3.6		69.4 ± 3.6		
NCs – 4 nm		NCs – 5 nm		
39.4 ± 1.0		28.6 ± 0.5		
Thin-film Exchange	NCs : DSPE-PEG-2000			
	1 : 5	1 : 10	1 : 20	
	16.1 ± 0.6	24.6 ± 1.1	40.9 ± 0.5	

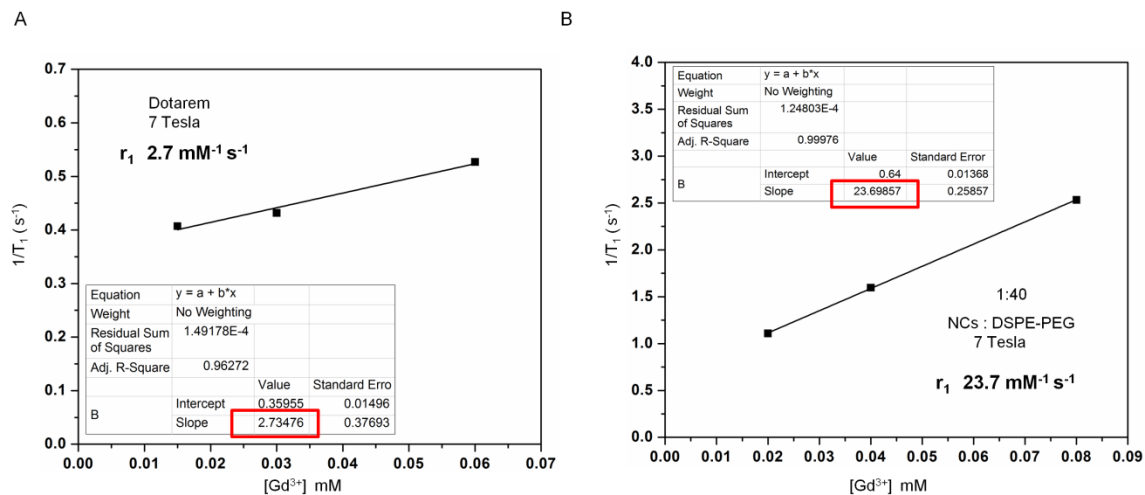


Figure 5.13 Representative concentration dependent T_1 ionic relaxivity plots (7 T) of, (A) Dotarem, and (B) compact NC-micelles (NCs to DSPE-PEG ratio weight/weight 1:40).

To further study the amplified relaxivity enhancement with the compact NC-micelles, we first evaluated the influence of PEG-phospholipid chain length as schematically shown in Figure 5.14a. Using DSPE-PEG with variable PEG length (PEG-2000, 3000, 5000) at same molar concentrations, NC-micelles were prepared and analyzed (see Experimental details in Supporting Information). Increasing the PEG chain length resulted in larger NC-micelles increasing from ~ 6 nm for DSPE-PEG-2000 to ~ 10 nm for DSPE-PEG-5000 (Figure 5.14b). While the NC-micelle sizes increased with increasing the PEG chain length, the relaxivity of the NC-micelles remained almost the same (Figure 5.14c and 5.15), clearly confirming that the relaxivity is independent of the outer PEG chain length. The MRI phantom images of these NC-micelles at identical Gd^{3+} concentration shown in Figure 5.14d further confirm this observation.

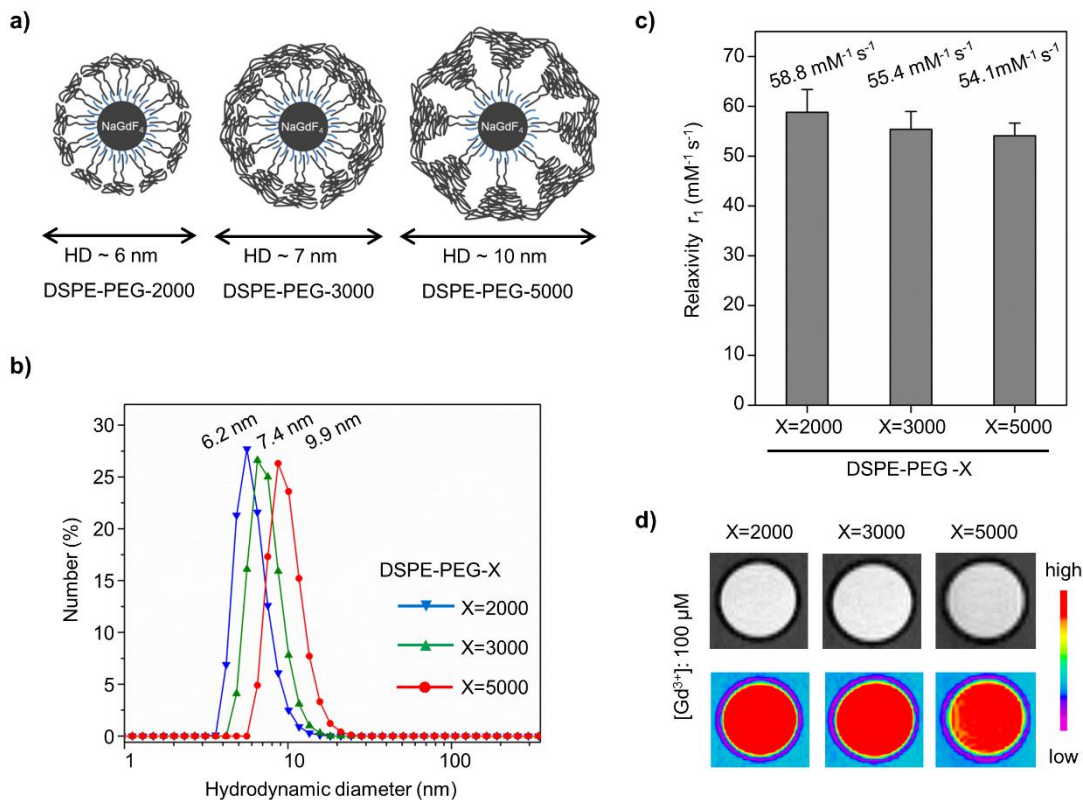


Figure 5.14 (a) Schematic illustration of NaGdF₄ NCs (3 nm) confined within DSPE-PEG micelles with variable PEG chain length and their respective average HD size. (b) Hydrodynamic size of the NC-micelles in water with variable DSPE-PEG-X length (X=2000, 3000, and 5000) measured by DLS. (c) Longitudinal T₁ relaxivity (per Gd³⁺) of the NC-micelles with variable PEG chain length, at 1.41 T. (d) MRI phantom images (top) and color contrasted images (bottom) of the NC-micelles with variable PEG chain length at identical Gd³⁺ concentration (100 μM).

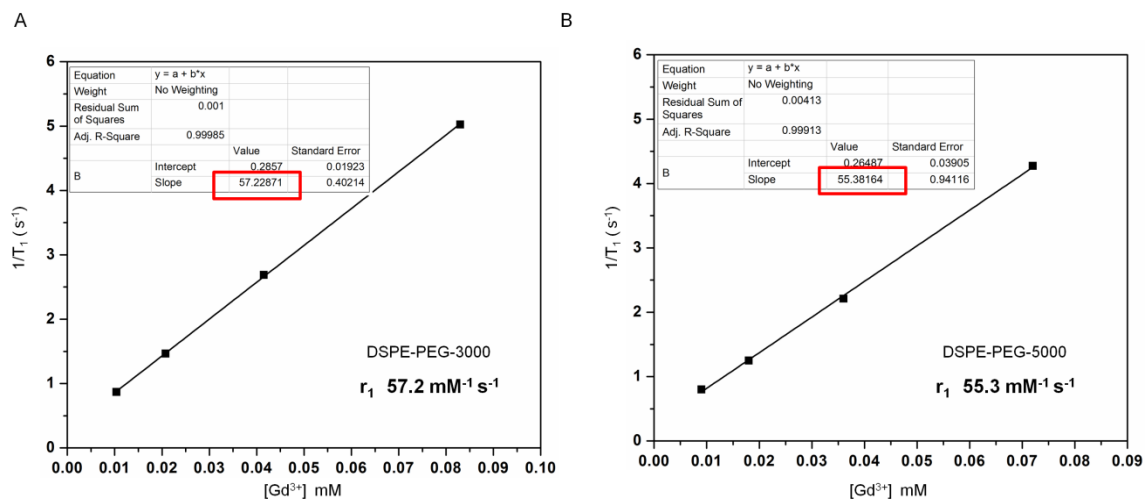


Figure 5.15 Representative concentration dependent ionic relaxivity plots (1.41 T) of NC-micelles with variable DSPE-PEG chain length, (A) DSPE-PEG-3000, and (B) DSPE-PEG-5000.

Considering that the relaxation of water protons with these NC-micelles is determined by the distance of closed approach to the NC surface, which is the interdigitated surface oleate and lipid layer, changing the outer PEG length does not significantly affect the relaxivity. We observe that the slight decrease in relaxivity suggests a slight dilation of the micelle size due to the crowding effect with increasing PEG chain length, however this do not significantly alter the relaxivity and thus the proximity of water to the NC surface. The ability to achieve extremely high relaxivity with various PEG-ylated phospholipids micelles further demonstrate the high degree of control achievable with this strategy in modulating the distance of water protons to the NC surface and also the generality of our method.

We next studied the influence of the size of NaGdF₄ NCs (3, 4, and 5 nm) confined within the DSPE-PEG-2000 micelles on the observed relaxivity as schematically shown in Figure 5.16a. Increasing the NC size from 3 nm to 5 nm resulted in the HD size increase of the NC-micelles from ~6 nm to 9 nm (Figure 5.16b). While the HD size increase of the NC-micelles is comparable to the size increase observed with changing the PEG chain length (Figure 5.14b), the relaxivity

values were however strikingly different for these NC-micelles. Increasing the inner core NC size resulted in lower relaxivity values, and the relaxivity values decreased from $\sim 60 \text{ mM}^{-1}\text{s}^{-1}$ per Gd^{3+} for the 3 nm core to $\sim 30 \text{ mM}^{-1}\text{s}^{-1}$ per Gd^{3+} for the 5 nm NCs (Figure 5.16c, and Figure 5.17 for concentration dependent plots). The MRI phantom images in Figure 5.16d further confirm this size dependent relaxivity, highlighting the importance of smaller NCs with larger surface to volume (S/V) ratio in achieving enhanced relaxivity,³¹ and that the surface ions are the major contributors to relaxivity enhancement.

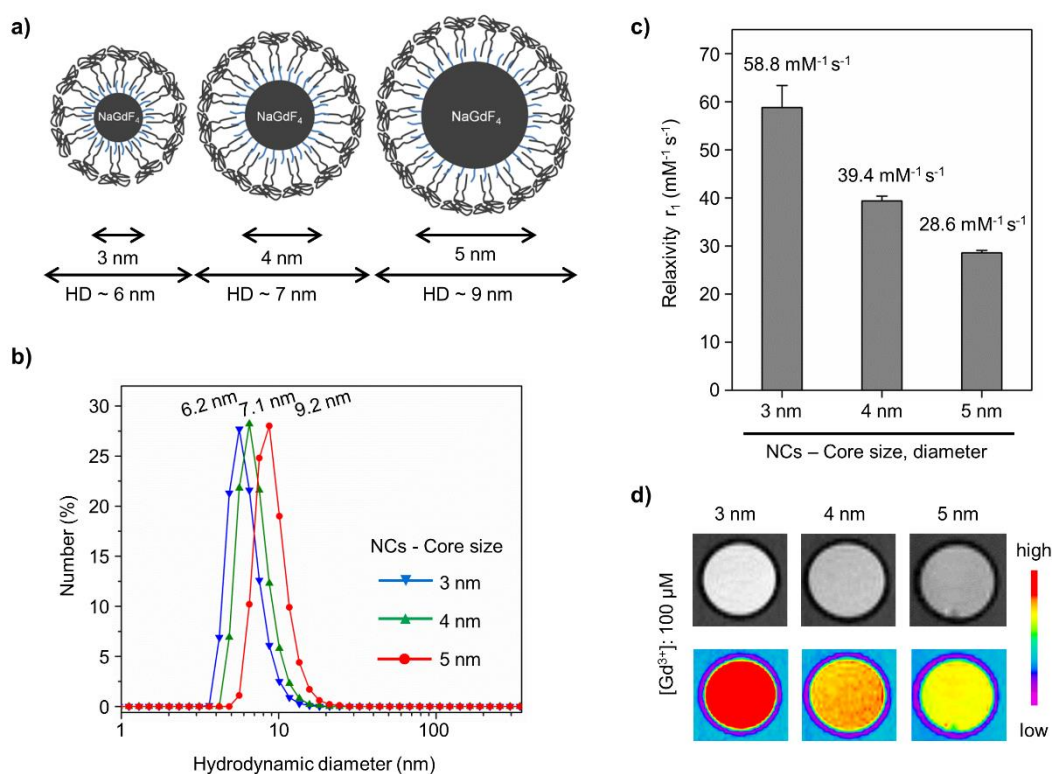


Figure 5.16 (a) Schematic illustration of NaGdF₄ NCs confined within DSPE-PEG micelles with variable core NC size (3, 4, 5 nm) and their respective average HD size. (b) Hydrodynamic size of the NC-micelles in water with variable core size (NCs size = 3, 4, and 5 nm) measured by DLS. (c) Longitudinal T₁ relaxivity (per Gd³⁺) of the NC-micelles with variable core size, at 1.41 T. (d) MRI phantom images (top) and color contrasted images (bottom) of the NC-micelles with variable core size at identical Gd³⁺ concentration (100 μM).

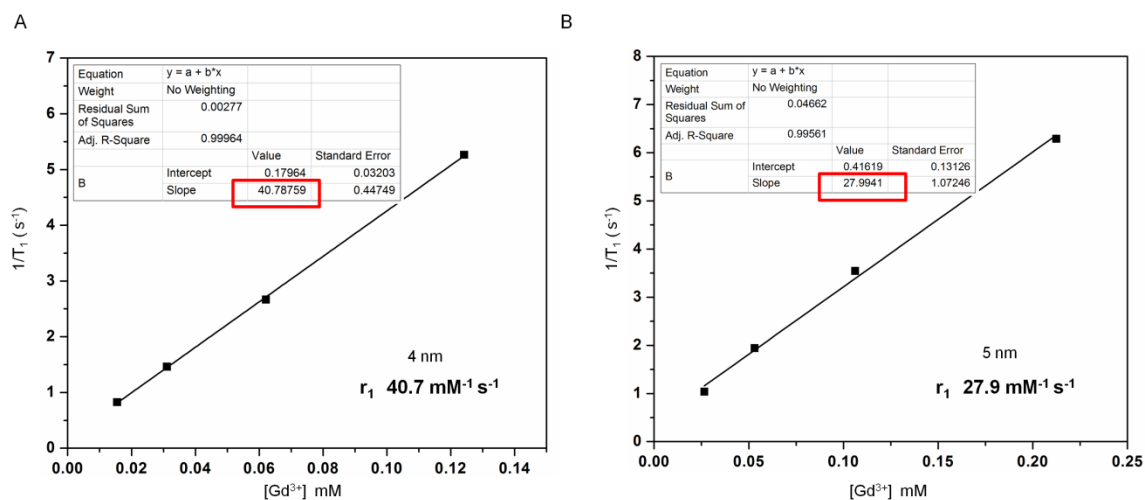


Figure 5.17 Representative concentration dependent ionic relaxivity plots (1.41 T) of NC-micelles with variable core NC size, (A) 4 nm, and (B) 5 nm.

To further evaluate the relaxivity of water protons in proximity to these ultrasmall NaGdF₄ NCs, we prepared NC-Phospholipid-PEG micelles with different phospholipid chain length, C18 (DSPE-PEG), and C14 (DMPE-PEG) as shown in Figure 5.18a (see Materials and Methods for details). As shown in Figure 5.18b, the HD sizes of these NC-micelles were comparable in size (~4 nm), and decreasing the chain length did not decrease the NC-micelle sizes. This suggests that the decrease in hydrophobic chain length result in slightly less propensity to form compact micelles, resulting in slight dilation of the NC-micelles with decreasing phospholipid chain length. The relaxivity values of these micelles were comparable and slightly lower than the compact-NC micelles as shown in Figure 5.18c and 5.19, and further confirmed by the phantom images in Figure 5.18d. Taken together, our ability to achieve extremely large relaxivity enhancement by controlling the surface structure of these NC-micelles with variable lipid coatings clearly confirm the ultrahigh T₁ relaxation enhancement of water protons achievable with colloidal Gd³⁺-based nanocrystals. Based on these results we propose two important criteria to achieve ultrahigh relaxivity with Gd³⁺-based NCs in general, (i) high quality extremely small NCs (< 5 nm) with a

narrow size dispersion, and (ii) a surface coating strategy that achieves compact and individually stabilized NCs in water. We emphasize that further decreasing the NC size, or utilizing a suitable hydrophilic ligand that can achieve "individually" stabilized NCs should further enhance the observed relaxivity, and relaxivity $>100 \text{ mM}^{-1}\text{s}^{-1}$ per Gd^{3+} is achievable with colloidal Gd^{3+} -based NCs.

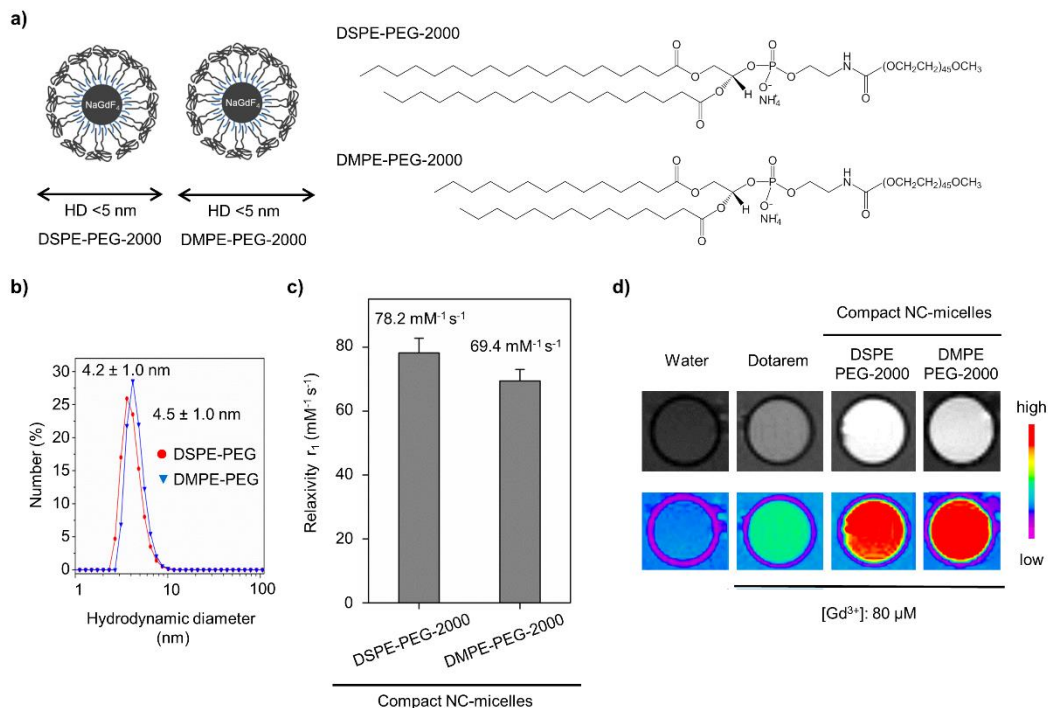


Figure 5.18 (a) Schematic illustration of NaGdF₄ NCs (3 nm) coated with phospholipid-PEG micelles with variable hydrophobic chain length using DSPE-PEG-2000 (C-18) and DMPE-PEG-2000 (C-14) as shown in their molecular structures. (b) Hydrodynamic size of the NC-micelles in water coated with DSPE-PEG-2000 (C-18) and DMPE-PEG-2000 (C-14) measured by DLS. (c) Longitudinal T₁ relaxivity (per Gd^{3+}) of the NC-micelles with different phospholipid-PEG coating, at 1.41 T. (d) MRI phantom images (top) and color contrasted images (bottom) of the NC-micelles and Dotarem at identical Gd^{3+} concentration ($100 \mu\text{M}$), and water for comparison.

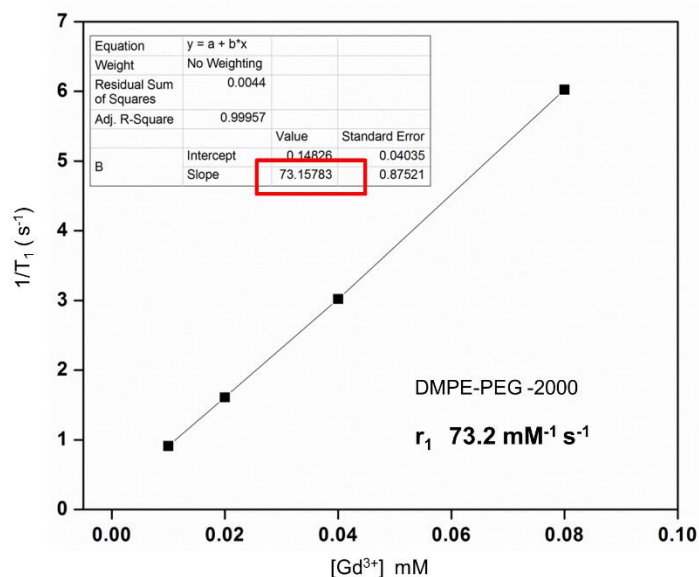


Figure 5.19 Representative concentration dependent ionic relaxivity plot (1.41 T) of NC-micelles with DMPE-PEG-2000 coating.

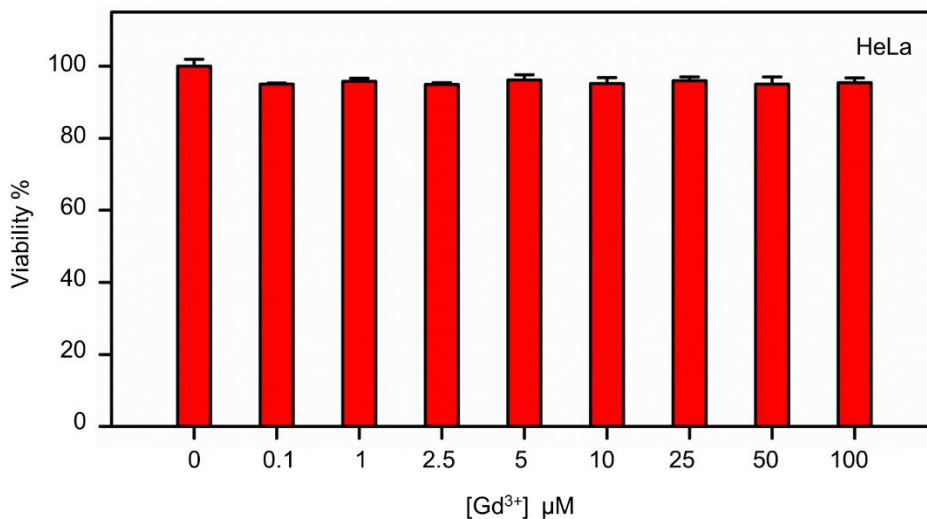


Figure 5.20 *In vitro* cell viability of HeLa cells incubated with compact NaGdF₄:DSPE-PEG-2000 micelles at different concentrations for 24 h.

Finally, we evaluated the *in vitro* performance of these compact-NC micelles using HeLa cells. The cell viability after incubation of these NCs even at high concentrations (100 μM, Gd³⁺) remained high after 24 h, demonstrating minimal toxicity (Figure 5.20). We also observe that the

cell morphology also was not affected at these concentrations (Figure 5.21). MRI images of the NC-micelles incubated cells show the uptake and contrast enhancement overtime (Figure 5.22). The ability to observe MRI contrast enhancement at such low gadolinium concentrations ($< 20 \mu\text{M}$) clearly demonstrate the ability to achieve targeted imaging at low contrast agent dosage. We next quantified the cell uptake of these compact-NC micelles using ICP-AES elemental analysis. We find them to be highly resilient to cell uptake even at elongated incubation times (Table 5.3), as expected for nanocrystals coated with a bio-compatible non-ionic PEG surface.

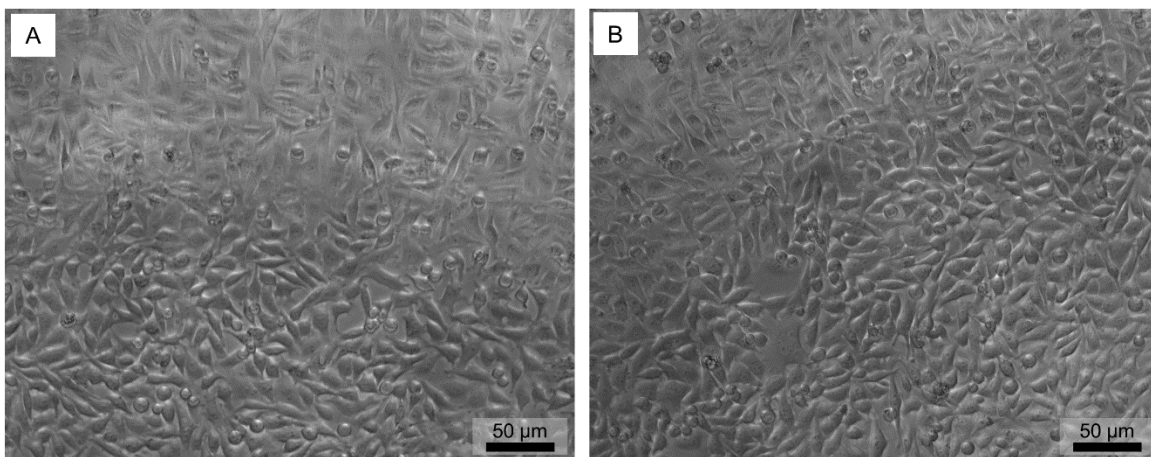


Figure 5.21 Representative optical microscopic images of HeLa cells incubated for 24 h (A) without, and (B) with $\text{NaGdF}_4\text{:DSPE-PEG-2000}$ micelles at $100 \mu\text{M} [\text{Gd}^{3+}]$.

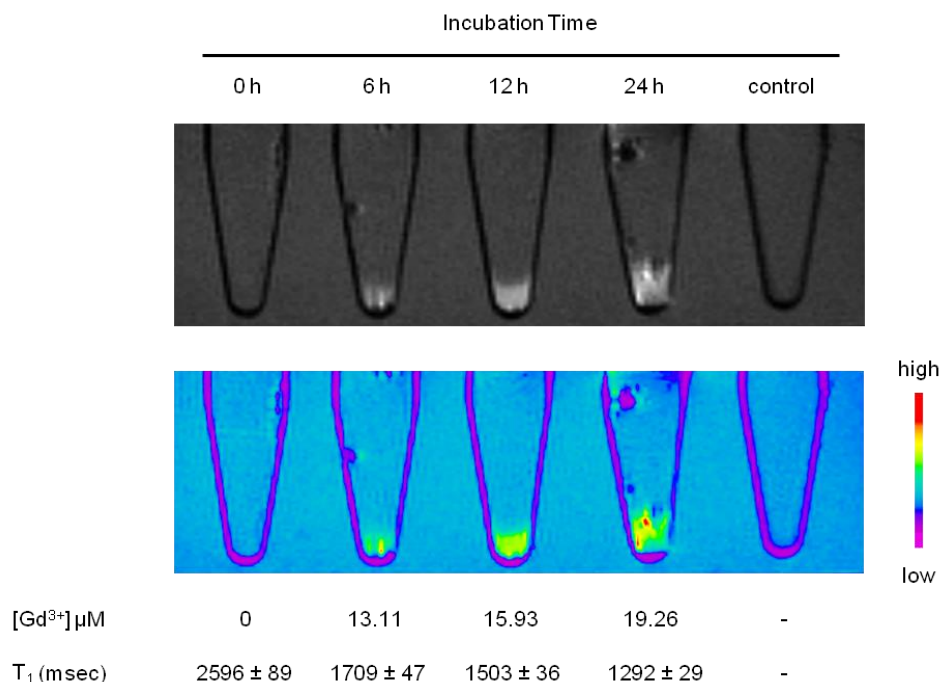


Figure 5.22 MRI phantom images (top) and color contrasted images (bottom) of the HeLa cells incubated with NaGdF₄ NC-micelles with different incubation times.

Table 5.3 ICP-AES analysis summary of HeLa cells incubated with NaGdF₄ NC-micelles.

Cell uptake – ICP-AES analysis summary				
	Incubation Time (h)	6	12	24
Gd ³⁺ Initial concentration = 100 μM	Gd³⁺ concentration from ICP (μM)	4.37	5.31	6.42
Initial volume (96 well plate) = 100 μL	Volume of cell pellet digested (μL)	50	50	50
Gd ³⁺ in each well = 10 ⁻⁸ mol	Gd³⁺ uptake amount (mol)	0.0219x10 ⁻⁸	0.0266x10 ⁻⁸	0.0321x10 ⁻⁸
	Gd³⁺ uptake percentage (%)	2.19	2.66	3.21

Further we evaluated the cell viability of RAW264.7 macrophage cells and find them to be only minimally affected at high gadolinium concentrations (Figure 5.23), similar to previous report.³⁶ Recent work by Shi and coworkers have demonstrated the high *in vivo* compatibility of these class of nanostructures,³⁶ and we expect that our findings should allow for further enhanced

in vivo performance and achieve targeted imaging simultaneously at a very low contrast agent dosage.

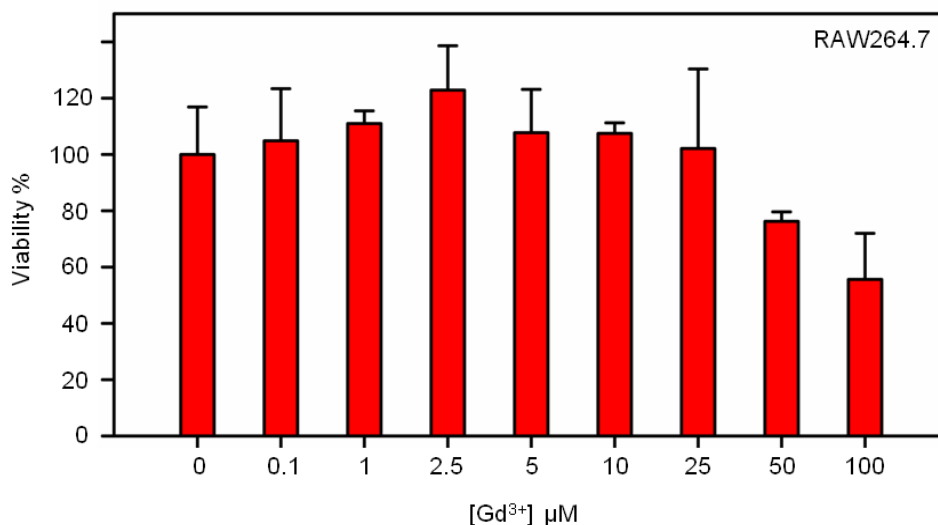


Figure 5.23 *In vitro* cell viability of RAW264.7 cells incubated with compact NaGdF₄:DSPE-PEG-2000 micelles at different concentrations for 24 h.

5.4 Conclusion

In summary, we have demonstrated a strategy to achieve extremely large T_1 relaxivity ($\sim 80 \text{ mM}^{-1}\text{s}^{-1}$ per Gd^{3+} @ 1.41 T) using NaGdF₄ NCs. By modulating the PEG-ylated phospholipid loading, we show that the NC-micelle sizes can be readily controlled to enhance the proximity of water to the NC surface, directly enhancing the relaxivity. This work demonstrates a Gd^{3+} -based nanostructured contrast agent that simultaneously have a compact size (HD ~ 5 nm) below the renal clearance threshold, ultrahigh relaxivity approaching the theoretical predictions,⁵ and a biocompatible PEGylated surface. We expect that our findings will translate to realize targeted MRI imaging with high precision that remains challenging to achieve to date. Finally, given the general utility of PEG-ylated phospholipid coating for a wide range of colloidal NCs, the strategy demonstrated here could be more widely employed to other NCs to achieve compact-sized NC

coating,^{26, 45-47} and also to precisely modulate and enhance their surface related properties at the nanoscale.

5.5 Materials and Methods

Chemicals

Gadolinium chloride hexahydrate (99.999%), gadolinium(III) acetate hydrate (99.9%), cerium(III) acetate hydrate (99.99%), terbium(III) acetate hydrate (99.9%), oleic acid (90%), 1-octadecene (90%), oleylamine (70%) were purchased from Sigma-Aldrich. 1,2-distearoyl-sn-glycero-3-phosphoethanolamine-N-[methoxy (polyethylene glycol)-2000] (ammonium salt) (DSPE-PEG-2000), 1,2-distearoyl-sn-glycero-3-phosphoethanolamine-N-[methoxy (polyethylene glycol)-3000] (ammonium salt) (DSPE-PEG-3000), 1,2-distearoyl-sn-glycero-3-phosphoethanolamine-N-[methoxy (polyethylene glycol)-5000] (ammonium salt) (DSPE-PEG-5000), and 1,2-dimyristoyl-sn-glycero-3-phosphoethanolamine-N-[methoxy (polyethylene glycol)-2000] (ammonium salt) (DMPE-PEG-2000) were purchased from Avanti Polar Lipids. Sodium hydroxide from Fisher Scientific, ammonium fluoride from Spectrum, and all chemicals were used as received.

Synthesis of NaGdF₄ nanocrystals (3 nm)

The synthesis was done following a previously reported procedure with slight modifications. In a typical synthesis, gadolinium chloride hexahydrate (1.0 mmol), oleic acid (4 mL), and 1-octadecene (15 mL) were taken in a 100 mL flask and heated to 140 °C under vacuum for 1 h and cooled to room temperature. To this solution at room temperature, methanol solution (10 mL) of ammonium fluoride (4 mmol) and sodium hydroxide (2.5 mmol) was added and stirred

for 1 h. The reaction vessel was then heated to 70 °C to remove methanol and subsequently heated to 275 °C (~10°C/min) under argon and maintained for 40 min and then cooled to room temperature. The nanocrystals (NCs) were precipitated by addition of ethanol, collected by centrifugation (1900 g, 5 min), washed with ethanol and dispersed in chloroform.

Synthesis of NaGdF₄:Ce³⁺(15%)/Tb³⁺(5%) doped NCs (5 nm)

They were synthesized using acetate salts in the respective molar ratio to a total of 0.75 mmol, oleic acid (8 mL), oleylamine (8 mL), and 1-octadecene (16 mL) in a 100 mL flask and heated to 120 °C under vacuum for 45 min and cooled to room temperature. To this solution at room temperature, methanol solution (10 mL) of ammonium fluoride (4 mmol) and sodium hydroxide (2.5 mmol) was added and stirred for 30 min. The reaction vessel was then heated to 70 °C to remove methanol and subsequently heated to 300 °C (~10°C/min) under argon and maintained for 15 min and then cooled to room temperature. The NCs were precipitated by addition of ethanol, collected by centrifugation (1900 g, 5 min), washed with ethanol and dispersed in chloroform.

Undoped NaGdF₄ (4 nm)

NCs were synthesized as described above, except gadolinium acetate (0.75 mmol) was used and the reaction was done at 300 °C under argon and maintained for 40 min.

Phospholipid-PEG micelles (Empty micelles)

Empty micelles were prepared using DSPE-PEG-2000 at different concentrations. Chloroform dispersion (1 mL) of DSPE-PEG-2000 with variable amounts (150, 750, 1500, 3000

µg) was prepared and to that 4 mL DMSO was added and the chloroform removed under vacuum in a rotary evaporator for 1 h at 35 °C. This gives a molar concentration of DSPE-PEG in DMSO to be about 15, 70, 135, and 270 µM with increasing concentration. The DMSO solution was then placed in a clean glass vial and 16 mL of water was added rapidly, followed by three rounds of centrifugation using Vivaspin-20 centrifugal filters (50kDa MWCO, and 3000xg/30 min) to replace the DMSO completely with water. The final concentrate was diluted to a total volume of 5 mL using deionized water, and filtered through a 0.2 µm syringe filter.

Phospholipid-PEG coated NC-micelles through solvent exchange

Solvent exchange method was adapted from a reported protocol with modifications. The dispersion of NCs in chloroform (1 mg/ mL) was first prepared based on ICP-AES analysis of the original stock solution. In all the exchange experiments, the concentration of NCs (number of NCs) was kept to ~3 nmol. For the 3 nm NCs, 150 µL of the NCs dispersed in chloroform (1 mg/ml) was added to DSPE-PEG-2000 in chloroform (850 µL). The amount of DSPE-PEG in chloroform was based on weight ratio of the NCs to the lipid (1:5, 1:10, 1:20, and 1:40). To the NCs/DSPE-PEG mixture in chloroform, DMSO (4 mL) was added dropwise and left on a shaker at room temperature for 30 min. The chloroform was then completely removed under vacuum in a rotary evaporator for 1 h at 35 °C. The DMSO solution was then placed in a clean glass vial and 16 mL of water was added rapidly, followed by three rounds of centrifugation using Vivaspin-20 centrifugal filters (50kDa MWCO, and 3000xg/30 min) to replace the DMSO completely with water. The final concentrate was diluted to a total volume of 5 mL using deionized water, and filtered through a 0.2 µm syringe filter.

For the phospholipid-PEG coating with different PEG chain lengths (DSPE-PEG-2000/3000/5000), the amount of phospholipid-PEG was maintained at the same molar amount (1.25 μmol), which corresponds to weight ratio of the NCs to the DSPE-PEG-2000 (1:20). The transfer protocol was followed as described above (for DSPE-PEG-3000 and DSPE-PEG-5000, 100kDa MWCO Vivaspin-20 centrifugal filters, and 3000xg/30 min was used).

For the undoped NaGdF_4 (4 nm) and $\text{NaGdF}_4:\text{Ce}^{3+}(15\%)/\text{Tb}^{3+}(5\%)$ (5 nm) NCs, the amount of NCs used was 3 nmol as before, $\sim 350\mu\text{L}$ of the NCs dispersed in chloroform (1 mg/ml) was added to DSPE-PEG-2000 in chloroform. The weight ratio of the NCs to the lipid was 1:10. The transfer protocol was followed as described above.

For the phospholipid-PEG coating with DMPE-PEG-2000, the amount of phospholipid-PEG was maintained at the same molar amount as used in the DSPE-PEG-2000 coating, which corresponds to weight ratio of the NCs to the DSPE-PEG-2000 (1:40). The transfer protocol was followed as described above with no deviations.

Gradient centrifugation

Phospholipid-PEG coated NC-micelles obtained from the three rounds of centrifugal filtration was diluted to 1 mL using deionized water. A sucrose step gradient was prepared (Polyallomer centrifuge tubes, Beckman Coulter) with 1.5 mL steps of 5, 10, 15, 20, 25, 35, 45% sucrose and the NC-micelles dispersion (1 mL) was added to the top, and centrifuged at 24,000 rpm ($\sim 100,000$ g, SW41Ti rotor) for 18 h. For the 5 nm $\text{NaGdF}_4:\text{Ce}^{3+}(15\%)/\text{Tb}^{3+}(5\%)$, the green emission under UV (254 nm) irradiation was used to locate (Figure 5.8) and remove the NC-micelles free of empty micelles. For the 3 nm NCs, the sucrose band around 5-10 wt% was removed as NC-micelles (see comments below Figure 5.8). The sucrose dispersion of NC-micelles

was subsequently dialyzed against water at 4 °C overnight (Float-A-Lyzer, 8-10 kDa, Spectrum Labs). The NC-micelle solution was then concentrated using centrifugal filtration (50kDa MWCO, and 3000xg/30 min), and diluted to 4 mL and filtered through a 0.2 µm syringe filter. All NC-micelle dispersions and empty micelles were stored at 4 °C immediately after preparation.

Phospholipid-PEG coated NC-micelles through film hydration

150 µL of the NCs (3 nm) dispersed in chloroform (1 mg/ml) was added to DSPE-PEG-2000 in chloroform (25 mg/mL). The weight ratio of the NCs to DSPE-PEG-2000 was 1:5, 1:10, and 1:20. The glass vial was left overnight in the fume hood to slowly evaporate chloroform and then placed in a rotary evaporator at 50 °C for 20 min under vacuum. To the obtained thin film, 10 mL of water was added and sonicated for 1-2 min and placed in a rotary evaporator for 10 min under vacuum. The dispersion was then filtered through a 0.2 µm syringe filter.

Cytotoxicity studies

HeLa/RAW264.7 cells were seeded 12h prior to incubation on tissue culture treated 96-well plates (Corning) at 10,000 cells/well in phosphate-free RPMI 1640 (MP Biomedicals) medium (DMEM for the RAW264.7 cells), supplemented with 10% Fetal Bovine Serum (Omega Scientific), 2 mM L-Glutamine (Thermo Fisher) and 1% penicillin/streptomycin (Thermo Fisher). Compact DSPE-PEG coated NC-micelles with varying concentrations (0-100 µM Gd³⁺) in cell culture media (3 wells for each condition) were added to the cells and incubated for 24 h at 37 °C in 5% CO₂. Finally, the cells were washed with cell culture media, and metabolic activity of cells was tested using the alamarBlue assay (Thermo Fisher) according to kit instructions. To quantify

viability, fluorescence ($\lambda_{\text{ex}} = 560 \text{ nm}$, $\lambda_{\text{em}} = 585 \text{ nm}$) of each well was measured using a plate reader (SpectraMax M5, Molecular Devices) 2 h after adding the alamarBlue agent.

Characterization

Transmission Electron Microscopy (TEM) images of the oleate-stabilized NCs was obtained from a FEI Tecnai Spirit microscope operating at 120 kV. The hexane dispersion of the NCs was drop cast on a carbon-coated (400 mesh Cu) grid and air-dried before imaging. Size and size distribution analysis from the TEM images were obtained by measuring ~50 NCs. Negative-stained TEM images of the DSPE-PEG coated NCs were obtained from a FEI Sphera microscope operating at 200 kV. The NaGdF₄:Ce³⁺(15%)/Tb³⁺(5%) (5 nm) NC-micelles purified by sucrose gradient ultracentrifugation in water was drop cast on a glow discharged carbon-coated (400 mesh Cu) grid dried under vacuum overnight, and stained with 2 wt% phosphotungstic acid before imaging. Dynamic Light Scattering (DLS) measurements to determine the hydrodynamic diameter sizes were performed using a Zetasizer Nano ZS (Malvern Instruments). Hydrodynamic size data were obtained from number weighted size distribution analysis and reported as mean of triplicate measurements of the same sample \pm s.d. Polydispersity index (PDI) were obtained from the s.d. and mean size of each individual measurement and averaged. Gadolinium ion concentration was determined using a Perkin Elmer Optima 3000DV inductively coupled plasma atomic emission spectrometer (ICP-AES), the NC and NC-micelle dispersions were digested in 70% HNO₃ for at least two days before analysis. Similarly cells incubated with the nanocrystals were digested with 70% HNO₃ for a week, diluted and analyzed by ICP-AES for determining the gadolinium concentration. Longitudinal (T₁) and transverse relaxation (T₂) times of the NC-micelle dispersions were obtained using a benchtop Bruker Minispec mq 60 relaxometer (60 MHz,

1.41 T at 37 °C). MR phantom images were obtained on a Bruker 7.0 T magnet equipped with Avance II hardware and a 72 mm quadrature transmit/receive coil. The NC-micelle dispersions in 200 μ L tubes were immobilized in agarose gel and imaged. For cell images, the cells incubated with the nanocrystals were detached from the culture plates, mixed with 2% agarose gel and deposited into 200 μ L tubes. To that, 1% agarose gel was carefully deposited on top and then imaged. T_1 relaxivity values at 7T was determined by selecting regions of interest (ROI) using the ParaVision Version 5.1 software, the fitting parameters were TR = 250.0 ms, TE = 12.6 ms, echo = 1/1, FOV = 6.11 cm/3.09 cm, slice thickness = 2 mm/3 mm, MTX = 256/116. The hydrodynamic diameter (number-weighted) sizes and relaxivity values from triplicate measurements are tabulated in Table 5.1 and 5.2 respectively.

Chapter 5, is a reprint of the material as it appears in *ACS Nano*. Noah J. J. Johnson, Sha He, Viet Anh Nguyen Huu, and Adah Almutairi, American Chemical Society Press, 2016. The dissertation author was the primary investigator and author of this paper.

5.6 References

1. Aime, S.; Botta, M.; Fasano, M.; Terreno, E., Lanthanide(III) Chelates for NMR Biomedical Applications. *Chem. Soc. Rev.* **1998**, *27*, 19-29.
2. Bottrill, M.; Kwok, L.; Long, N. J., Lanthanides in Magnetic Resonance Imaging. *Chem. Soc. Rev.* **2006**, *35*, 557-571.
3. Caravan, P.; Ellison, J. J.; McMurry, T. J.; Lauffer, R. B., Gadolinium(III) Chelates as MRI Contrast Agents: Structure, Dynamics, and Applications. *Chem. Rev.* **1999**, *99*, 2293-2352.
4. Lauffer, R. B., Paramagnetic Metal Complexes as Water Proton Relaxation Agents for NMR Imaging: Theory and Design. *Chem. Rev.* **1987**, *87*, 901-927.
5. Caravan, P.; Farrar, C. T.; Frullano, L.; Uppal, R., Influence of Molecular Parameters and Increasing Magnetic Field Strength on Relaxivity of Gadolinium- and Manganese-Based T₁ Contrast Agents. *Contrast Media Mol. Imaging* **2009**, *4*, 89-100.
6. Chen, R.; Ling, D.; Zhao, L.; Wang, S.; Liu, Y.; Bai, R.; Baik, S.; Zhao, Y.; Chen, C.; Hyeon, T., Parallel Comparative Studies on Mouse Toxicity of Oxide Nanoparticle- and Gadolinium-Based T₁ MRI Contrast Agents. *ACS Nano* **2015**, *9*, 12425-12435.
7. Penfield, J. G.; Reilly, R. F., What Nephrologists Need to Know About Gadolinium. *Nat. Clin. Pract. Nephrol.* **2007**, *3*, 654-668.
8. Botta, M.; Tei, L., Relaxivity Enhancement in Macromolecular and Nanosized GdIII-Based MRI Contrast Agents. *Eur. J. Inorg. Chem.* **2012**, *2012*, 1945-1960.
9. Caravan, P., Strategies for Increasing the Sensitivity of Gadolinium Based MRI Contrast Agents. *Chem. Soc. Rev.* **2006**, *35*, 512-523.
10. Anderson, E. A.; Isaacman, S.; Peabody, D. S.; Wang, E. Y.; Canary, J. W.; Kirshenbaum, K., Viral Nanoparticles Donning a Paramagnetic Coat: Conjugation of MRI Contrast Agents to the MS2 Capsid. *Nano Lett.* **2006**, *6*, 1160-1164.
11. Andreozzi, E.; Wang, P.; Valenzuela, A.; Tu, C.; Gorin, F.; Dhenain, M.; Louie, A., Size-Stable Solid Lipid Nanoparticles Loaded with Gd-DOTA for Magnetic Resonance Imaging. *Bioconjugate Chem.* **2013**, *24*, 1455-1467.
12. Chan, M.; Lux, J.; Nishimura, T.; Akiyoshi, K.; Almutairi, A., Long-Lasting and Efficient Tumor Imaging Using a High Relaxivity Polysaccharide Nanogel Magnetic Resonance Imaging Contrast Agent. *Biomacromolecules* **2015**, *16*, 2964-2971.

13. Cormode, D. P.; Skajaa, T.; van Schooneveld, M. M.; Koole, R.; Jarzyna, P.; Lobatto, M. E.; Calcagno, C.; Barazza, A.; Gordon, R. E.; Zanzonico, P.; Fisher, E. A.; Fayad, Z. A.; Mulder, W. J. M., Nanocrystal Core High-Density Lipoproteins: A Multimodality Contrast Agent Platform. *Nano Lett.* **2008**, *8*, 3715-3723.
14. Datta, A.; Hooker, J. M.; Botta, M.; Francis, M. B.; Aime, S.; Raymond, K. N., High Relaxivity Gadolinium Hydroxypyridonate–Viral Capsid Conjugates: Nanosized MRI Contrast Agents. *J. Am. Chem. Soc.* **2008**, *130*, 2546-2552.
15. Floyd, W. C.; Klemm, P. J.; Smiles, D. E.; Kohlgruber, A. C.; Pierre, V. C.; Mynar, J. L.; Fréchet, J. M. J.; Raymond, K. N., Conjugation Effects of Various Linkers on Gd(III) MRI Contrast Agents with Dendrimers: Optimizing the Hydroxypyridinonate (HOPO) Ligands with Nontoxic, Degradable Esteramide (EA) Dendrimers for High Relaxivity. *J. Am. Chem. Soc.* **2011**, *133*, 2390-2393.
16. Moriggi, L.; Cannizzo, C.; Dumas, E.; Mayer, C. R.; Ulianov, A.; Helm, L., Gold Nanoparticles Functionalized with Gadolinium Chelates as High-Relaxivity MRI Contrast Agents. *J. Am. Chem. Soc.* **2009**, *131*, 10828-10829.
17. Pierre, V. C.; Botta, M.; Raymond, K. N., Dendrimeric Gadolinium Chelate with Fast Water Exchange and High Relaxivity at High Magnetic Field Strength. *J. Am. Chem. Soc.* **2005**, *127*, 504-505.
18. Song, Y.; Xu, X.; MacRenaris, K. W.; Zhang, X.-Q.; Mirkin, C. A.; Meade, T. J., Multimodal Gadolinium-Enriched DNA–Gold Nanoparticle Conjugates for Cellular Imaging. *Angew. Chem., Int. Ed.* **2009**, *121*, 9307-9311.
19. Werner, E. J.; Datta, A.; Jocher, C. J.; Raymond, K. N., High-Relaxivity MRI Contrast Agents: Where Coordination Chemistry Meets Medical Imaging. *Angew. Chem., Int. Ed.* **2008**, *47*, 8568-8580.
20. Huang, C.-H.; Nwe, K.; Al Zaki, A.; Brechbiel, M. W.; Tsourkas, A., Biodegradable Polydisulfide Dendrimer Nanoclusters as MRI Contrast Agents. *ACS Nano* **2012**, *6*, 9416-9424.
21. Lacerda, S.; Bonnet, C. S.; Pallier, A.; Villette, S.; Foucher, F.; Westall, F.; Buron, F.; Suzenet, F.; Pichon, C.; Petoud, S.; Tóth, É., Lanthanide-Based, Near-Infrared Luminescent and Magnetic Lipoparticles: Monitoring Particle Integrity. *Small* **2013**, *9*, 2662-2666.
22. Lux, J.; Chan, M.; Vander Elst, L.; Schopf, E.; Mahmoud, E.; Laurent, S.; Almutairi, A., Metal chelating crosslinkers form nanogels with high chelation stability. *J. Mater. Chem. B* **2013**, *1*, 6359-6364.

23. Ananta, J. S.; Godin, B.; Sethi, R.; Moriggi, L.; Liu, X.; Serda, R. E.; Krishnamurthy, R.; Muthupillai, R.; Bolskar, R. D.; Helm, L.; Ferrari, M.; Wilson, L. J.; Decuzzi, P., Geometrical Confinement of Gadolinium-Based Contrast Agents in Nanoporous Particles Enhances T₁ Contrast. *Nat. Nanotechnol.* **2010**, *5*, 815-821.
24. Pierre, V. C.; Allen, M. J.; Caravan, P., Contrast Agents for MRI: 30+ Years and Where Are We Going? *JBIC, J. Biol. Inorg. Chem.* **2014**, *19*, 127-131.
25. Rotz, M. W.; Culver, K. S. B.; Parigi, G.; MacRenaris, K. W.; Luchinat, C.; Odom, T. W.; Meade, T. J., High Relaxivity Gd(III)-DNA Gold Nanostars: Investigation of Shape Effects on Proton Relaxation. *ACS Nano* **2015**, *9*, 3385-3396.
26. Soo Choi, H.; Liu, W.; Misra, P.; Tanaka, E.; Zimmer, J. P.; Itty Ipe, B.; Bawendi, M. G.; Frangioni, J. V., Renal Clearance of Quantum Dots. *Nat. Biotechnol.* **2007**, *25*, 1165-1170.
27. Aime, S.; S. Batsanov, A.; Botta, M.; S. Dickins, R.; Faulkner, S.; E. Foster, C.; Harrison, A.; A. K. Howard, J.; M. Moloney, J.; J. Norman, T.; Parker, D.; Royle, L.; A. Gareth Williams, J., Nuclear Magnetic Resonance, Luminescence and Structural Studies of Lanthanide Complexes with Octadentate Macrocyclic Ligands Bearing Benzylphosphinate Groups. *J. Chem. Soc., Dalton Trans.* **1997**, 3623-3636.
28. Bridot, J.-L.; Faure, A.-C.; Laurent, S.; Rivière, C.; Billotey, C.; Hiba, B.; Janier, M.; Jossierand, V.; Coll, J.-L.; Vander Elst, L.; Muller, R.; Roux, S.; Perriat, P.; Tillement, O., Hybrid Gadolinium Oxide Nanoparticles: Multimodal Contrast Agents for In Vivo Imaging. *J. Am. Chem. Soc.* **2007**, *129*, 5076-5084.
29. Chen, F.; Bu, W.; Zhang, S.; Liu, J.; Fan, W.; Zhou, L.; Peng, W.; Shi, J., Gd³⁺-Ion-Doped Upconversion Nanoprobes: Relaxivity Mechanism Probing and Sensitivity Optimization. *Adv. Funct. Mater.* **2013**, *23*, 298-307.
30. Hifumi, H.; Yamaoka, S.; Tanimoto, A.; Citterio, D.; Suzuki, K., Gadolinium-Based Hybrid Nanoparticles as a Positive MR Contrast Agent. *J. Am. Chem. Soc.* **2006**, *128*, 15090-15091.
31. Johnson, N. J. J.; Oakden, W.; Stanisiz, G. J.; Scott Prosser, R.; van Veggel, F. C. J. M., Size-Tunable, Ultrasmall NaGdF₄ Nanoparticles: Insights into Their T₁ MRI Contrast Enhancement. *Chem. Mater.* **2011**, *23*, 3714-3722.
32. Na, H. B.; Hyeon, T., Nanostructured T₁ MRI Contrast Agents. *J. Mater. Chem.* **2009**, *19*, 6267-6273.
33. Na, H. B.; Song, I. C.; Hyeon, T., Inorganic Nanoparticles for MRI Contrast Agents. *Adv. Mater.* **2009**, *21*, 2133-2148.

34. Park, J. Y.; Baek, M. J.; Choi, E. S.; Woo, S.; Kim, J. H.; Kim, T. J.; Jung, J. C.; Chae, K. S.; Chang, Y.; Lee, G. H., Paramagnetic Ultrasmall Gadolinium Oxide Nanoparticles as Advanced T₁ MRI Contrast Agent: Account for Large Longitudinal Relaxivity, Optimal Particle Diameter, and In Vivo T₁ MR Images. *ACS Nano* **2009**, *3*, 3663-3669.
35. Park, Y.; Kim, H. M.; Kim, J. H.; Moon, K. C.; Yoo, B.; Lee, K. T.; Lee, N.; Choi, Y.; Park, W.; Ling, D.; Na, K.; Moon, W. K.; Choi, S. H.; Park, H. S.; Yoon, S. Y.; Suh, Y. D.; Lee, S. H.; Hyeon, T., Theranostic Probe Based on Lanthanide-Doped Nanoparticles for Simultaneous In Vivo Dual-Modal Imaging and Photodynamic Therapy. *Advanced Materials* **2012**, *24*, 5755-5761.
36. Xing, H.; Zhang, S.; Bu, W.; Zheng, X.; Wang, L.; Xiao, Q.; Ni, D.; Zhang, J.; Zhou, L.; Peng, W.; Zhao, K.; Hua, Y.; Shi, J., Ultrasmall NaGdF₄ Nanodots for Efficient MR Angiography and Atherosclerotic Plaque Imaging. *Adv. Mater.* **2014**, *26*, 3867-3872.
37. Murray, C. B.; Norris, D. J.; Bawendi, M. G., Synthesis and Characterization of Nearly Monodisperse CdE (E = Sulfur, Selenium, Tellurium) Semiconductor Nanocrystallites. *J. Am. Chem. Soc.* **1993**, *115*, 8706-8715.
38. Park, J.; An, K.; Hwang, Y.; Park, J.-G.; Noh, H.-J.; Kim, J.-Y.; Park, J.-H.; Hwang, N.-M.; Hyeon, T., Ultra-Large-Scale Syntheses of Monodisperse Nanocrystals. *Nat. Mater.* **2004**, *3*, 891-895.
39. Wang, F.; Deng, R.; Liu, X., Preparation of Core-Shell NaGdF₄ Nanoparticles Doped with Luminescent Lanthanide Ions to be Used as Upconversion-Based Probes. *Nat. Protoc.* **2014**, *9*, 1634-1644.
40. Dubertret, B.; Skourides, P.; Norris, D. J.; Noireaux, V.; Brivanlou, A. H.; Libchaber, A., In Vivo Imaging of Quantum Dots Encapsulated in Phospholipid Micelles. *Science* **2002**, *298*, 1759-1762.
41. Prantner, A. M.; Chen, J.; Murray, C. B.; Scholler, N., Coating Evaluation and Purification of Monodisperse, Water-Soluble, Magnetic Nanoparticles Using Sucrose Density Gradient Ultracentrifugation. *Chem. Mater.* **2012**, *24*, 4008-4010.
42. Tong, S.; Hou, S.; Ren, B.; Zheng, Z.; Bao, G., Self-Assembly of Phospholipid-PEG Coating on Nanoparticles through Dual Solvent Exchange. *Nano Lett.* **2011**, *11*, 3720-3726.
43. Tong, S.; Hou, S.; Zheng, Z.; Zhou, J.; Bao, G., Coating Optimization of Superparamagnetic Iron Oxide Nanoparticles for High T₂ Relaxivity. *Nano Lett.* **2010**, *10*, 4607-4613.
44. Vuković, L.; Khatib, F. A.; Drake, S. P.; Madriaga, A.; Brandenburg, K. S.; Král, P.; Onyuksel,

- H., Structure and Dynamics of Highly PEG-ylated Sterically Stabilized Micelles in Aqueous Media. *J. Am. Chem. Soc.* **2011**, *133*, 13481-13488.
45. Kim, B. H.; Lee, N.; Kim, H.; An, K.; Park, Y. I.; Choi, Y.; Shin, K.; Lee, Y.; Kwon, S. G.; Na, H. B.; Park, J.-G.; Ahn, T.-Y.; Kim, Y.-W.; Moon, W. K.; Choi, S. H.; Hyeon, T., Large-Scale Synthesis of Uniform and Extremely Small-Sized Iron Oxide Nanoparticles for High-Resolution T₁ Magnetic Resonance Imaging Contrast Agents. *J. Am. Chem. Soc.* **2011**, *133*, 12624-12631.
46. Kim, B. H.; Hackett, M. J.; Park, J.; Hyeon, T., Synthesis, Characterization, and Application of Ultrasmall Nanoparticles. *Chem. Mater.* **2014**, *26*, 59-71.
47. Ma, L.; Tu, C.; Le, P.; Chitoor, S.; Lim, S. J.; Zahid, M. U.; Teng, K. W.; Ge, P.; Selvin, P. R.; Smith, A. M., Multidentate Polymer Coatings for Compact and Homogeneous Quantum Dots with Efficient Bioconjugation. *J. Am. Chem. Soc.* **2016**, *138*, 3382-3394.